CONVERSION MATERIALS FOR RECHARGEABLE BATTERIES, 2nd Edition

EDITED BY: Feixiang Wu, Shengkui Zhong, Junchao Zheng and Danni Lei
PUBLISHED IN: Frontiers in Chemistry and Frontiers in Materials

frontiers Research Topics

ISSN 1664-8714
ISBN 978-2-88966-196-1
DOI 10.3389/978-2-88966-196-1

About Frontiers

Frontiers is more than just an open-access publisher of scholarly articles: it is a pioneering approach to the world of academia, radically improving the way scholarly research is managed. The grand vision of Frontiers is a world where all people have an equal opportunity to seek, share and generate knowledge. Frontiers provides immediate and permanent online open access to all its publications, but this alone is not enough to realize our grand goals.

Frontiers Journal Series

The Frontiers Journal Series is a multi-tier and interdisciplinary set of open-access, online journals, promising a paradigm shift from the current review, selection and dissemination processes in academic publishing. All Frontiers journals are driven by researchers for researchers; therefore, they constitute a service to the scholarly community. At the same time, the Frontiers Journal Series operates on a revolutionary invention, the tiered publishing system, initially addressing specific communities of scholars, and gradually climbing up to broader public understanding, thus serving the interests of the lay society, too.

Dedication to Quality

Each Frontiers article is a landmark of the highest quality, thanks to genuinely collaborative interactions between authors and review editors, who include some of the world's best academicians. Research must be certified by peers before entering a stream of knowledge that may eventually reach the public - and shape society; therefore, Frontiers only applies the most rigorous and unbiased reviews.
Frontiers revolutionizes research publishing by freely delivering the most outstanding research, evaluated with no bias from both the academic and social point of view. By applying the most advanced information technologies, Frontiers is catapulting scholarly publishing into a new generation.

What are Frontiers Research Topics?

Frontiers Research Topics are very popular trademarks of the Frontiers Journals Series: they are collections of at least ten articles, all centered on a particular subject. With their unique mix of varied contributions from Original Research to Review Articles, Frontiers Research Topics unify the most influential researchers, the latest key findings and historical advances in a hot research area! Find out more on how to host your own Frontiers Research Topic or contribute to one as an author by contacting the Frontiers Editorial Office: researchtopics@frontiersin.org

CONVERSION MATERIALS FOR RECHARGEABLE BATTERIES, 2nd Edition

Topic Editors:
Feixiang Wu, Central South University, China
Shengkui Zhong, Soochow University, China
Junchao Zheng, Central South University, China
Danni Lei, Sun Yat-sen University, China

Publisher's note: In this 2nd edition, the following article has been updated: Wang X, Jiang Q, Zhang Y, Yuan N and Tang J (2020) High Efficient and Environment Friendly Plasma-Enhanced Synthesis of Al2O3-Coated LiNi1/3Co1/3Mn1/3O2 With Excellent Electrochemical Performance. *Front. Chem.* 8:72. doi: 10.3389/fchem.2020.00072

Citation: Wu, F., Zhong, S., Zheng, J., Lei, D., eds. (2020). Conversion Materials for Rechargeable Batteries, 2nd Edition. Lausanne: Frontiers Media SA. doi: 10.3389/978-2-88966-196-1

Table of Contents

05 ***Heterostructured SnO_2-SnS_2@C Embedded in Nitrogen-Doped Graphene as a Robust Anode Material for Lithium-Ion Batteries***
Hui Li, Bao Zhang, Xu Wang, Jie Zhang, Tianhui An, Zhiying Ding, Wanjing Yu and Hui Tong

17 ***Spray-Drying Synthesis of $LiFeBO_3$/C Hollow Spheres With Improved Electrochemical and Storage Performances for Li-Ion Batteries***
Yulei Sui, Wei Chen, Shibao Tang, Ling Wu, Binjue Wang, Huacheng Li, Wei Li and Shengkui Zhong

25 ***Fabrication of $Li_4Ti_5O_{12}$@CN Composite With Enhanced Rate Properties***
Hui Xiao, Xiaobing Huang, Yurong Ren, Xiang Ding and Shibiao Zhou

32 ***The Effects of Reversibility of H2-H3 Phase Transition on Ni-Rich Layered Oxide Cathode for High-Energy Lithium-Ion Batteries***
Jie Chen, Huiping Yang, Tianhao Li, Chaoyang Liu, Hui Tong, Jiaxin Chen, Zengsheng Liu, Lingfeng Xia, Zhaoyong Chen, Junfei Duan and Lingjun Li

42 ***Concentrated LiODFB Electrolyte for Lithium Metal Batteries***
Juan Yu, Na Gao, Jiaxin Peng, Nani Ma, Xiaoyan Liu, Chao Shen, Keyu Xie and Zhao Fang

50 ***Controlled Synthesis of $Ni_xCo_yS_4$/rGO Composites for Constructing High-Performance Asymmetric Supercapacitor***
Mingxia Dong, Zhixing Wang, Jiexi Wang, Huajun Guo, Xinhai Li and Guochun Yan

61 ***Flexible $Li[Li_{0.2}Ni_{0.13}Co_{0.13}Mn_{0.54}]O_2$/Carbon Nanotubes/Nanofibrillated Celluloses Composite Electrode for High-Performance Lithium-Ion Battery***
Yan Li, Han Zhang, Zhe Xiao and Renheng Wang

69 ***Synthesis and Electrochemical Performance of ZnSe Electrospinning Nanofibers as an Anode Material for Lithium Ion and Sodium Ion Batteries***
Peng Zhou, Mingyu Zhang, Liping Wang, Qizhong Huang, Zhean Su, Liewu Li, Xiaodong Wang, Yuhao Li, Chen Zeng and Zhenghao Guo

79 ***Toward High-Performance Li Metal Anode via Difunctional Protecting Layer***
Jinlei Gu, Chao Shen, Zhao Fang, Juan Yu, Yong Zheng, Zhanyuan Tian, Le Shao, Xin Li and Keyu Xie

88 ***Electrochemical Analysis for Enhancing Interface Layer of Spinel $LiNi_{0.5}Mn_{1.5}O_4$ Using p-Toluenesulfonyl Isocyanate as Electrolyte Additive***
Zhe Xiao, Renheng Wang, Yan Li, Yiling Sun, Shuting Fan, Keyu Xiong, Han Zhang and Zhengfang Qian

96 ***Facile One-Step Hydrothermal Synthesis of $Na_3V_2(PO_4)_2F_3$@C/CNTs Tetragonal Micro-Particles as High Performance Cathode Material for Na-Ion Batteries***
Hao Guo, Yong Hu, Xiaoping Zhang, Rongliang Zhang, Dong Hou, Yulei Sui and Ling Wu

104 ***Graphene-Modified 3D Copper Foam Current Collector for Dendrite-Free Lithium Deposition***

Juan Yu, Yangyang Dang, Maohui Bai, Jiaxin Peng, Dongdong Zheng, Junkai Zhao, Linbo Li and Zhao Fang

114 ***Effect of Aging-Induced Dioxolane Polymerization on the Electrochemistry of Carbon-Coated Lithium Sulfide***

Lucas Lodovico, Alberto Varzi and Stefano Passerini

120 ***Fluorine-Doped Carbon Coated $LiFePO_{3.938}F0_{.062}$ Composites as Cathode Materials for High-Performance Lithium-Ion Batteries***

Zhixiong Yan, Dequan Huang, Xiaoping Fan, Fenghua Zheng, Qichang Pan, Zhaoling Ma, Hongqiang Wang, Youguo Huang and Qingyu Li

132 ***High Efficient and Environment Friendly Plasma-Enhanced Synthesis of Al_2O_3-Coated $LiNi_{1/3}Co_{1/3}Mn_{1/3}O_2$ With Excellent Electrochemical Performance***

Xinzhi Wang, Qianqian Jiang, Yichi Zhang, Nannan Yuan and Jianguo Tang

frontiers in Chemistry

ORIGINAL RESEARCH
published: 14 May 2019
doi: 10.3389/fchem.2019.00339

Heterostructured SnO_2-SnS_2@C Embedded in Nitrogen-Doped Graphene as a Robust Anode Material for Lithium-Ion Batteries

*Hui Li[1], Bao Zhang[1], Xu Wang[1], Jie Zhang[1], Tianhui An[1], Zhiying Ding[2], Wanjing Yu[1] and Hui Tong[1]**

[1] School of Metallurgy and Environment, Central South University, Changsha, China, [2] School of Chemistry and Chemical Engineering, Central South University, Changsha, China

Tin-based anode materials with high capacity attract wide attention of researchers and become a strong competitor for the next generation of lithium-ion battery anode materials. However, the poor electrical conductivity and severe volume expansion retard the commercialization of tin-based anode materials. Here, SnO_2-SnS_2@C nanoparticles with heterostructure embedded in a carbon matrix of nitrogen-doped graphene (SnO_2-SnS_2@C/NG) is ingeniously designed in this work. The composite was synthesized by a two-step method. Firstly, the SnO_2@C/rGO with a nano-layer structure was synthesized by hydrothermal method as the precursor, and then the SnO_2-SnS_2@C/NG composite was obtained by further vulcanizing the above precursor. It should be noted that a carbon matrix with nitrogen-doped graphene can inhibit the volume expansion of SnO_2-SnS_2 nanoparticles and promote the transport of lithium ions during continuous cycling. Benefiting from the synergistic effect between nanoparticles and carbon matrix with nitrogen-doped graphene, the heterostructured SnO_2-SnS_2@C/NG further fundamentally confer improved structural stability and reaction kinetics for lithium storage. As expected, the SnO_2-SnS_2@C/NG composite exhibited high reversible capacity (1201.2 mA h g^{-1} at the current rate of 0.1 A g^{-1}), superior rate capability and exceptional long-life stability (944.3 mAh g^{-1} after 950 cycles at the current rate of 1.0 A g^{-1}). The results demonstrate that the SnO_2-SnS_2@C/NG composite is a highly competitive anode material for LIBs.

Keywords: SnO_2-SnS_2, heterostructure, nitrogen-doped graphene, nanoparticle, anode

OPEN ACCESS

Edited by:
Danni Lei,
Sun Yat-sen University, China

Reviewed by:
Renheng Wang,
Shenzhen University, China
Xunhui Xiong,
South China University of Technology, China

***Correspondence:**
Hui Tong
huitong@csu.edu.cn

Specialty section:
This article was submitted to Electrochemistry, a section of the journal Frontiers in Chemistry

Received: *19 March 2019*
Accepted: *25 April 2019*
Published: *14 May 2019*

Citation:
Li H, Zhang B, Wang X, Zhang J, An T, Ding Z, Yu W and Tong H (2019) Heterostructured SnO_2-SnS_2@C Embedded in Nitrogen-Doped Graphene as a Robust Anode Material for Lithium-Ion Batteries. Front. Chem. 7:339. doi: 10.3389/fchem.2019.00339

INTRODUCTION

In recent years, with the widespread use of portable electronic products and electric vehicles, lithium-ion battery technology needs to be rapidly upgraded (Armand and Tarascon, 2008; Wang et al., 2017a,b, 2019; Chen J. et al., 2018; Zheng et al., 2018; Tong et al., 2019). At present, the main problems faced by lithium-ion batteries (LIBs) are as follows: energy density, cycle life, safety and cost. These problems are mainly related to the anode and cathode of the battery. As far as anode materials are concerned, commercial graphite on the market today is unable to meet the increasing energy density requirements due to its lower capacity (about 372 mAh g^{-1}) (Chen et al., 2018b; Xiao et al., 2018). In the past few decades, researchers developed many high-capacity and structurally

stable anode materials, among which tin oxide anode materials with low discharge potential and natural abundance, received extensive attention and become a strong competitor for the next generation of lithium-ion battery anode materials (Chou et al., 2009; Sahoo and Ramaprabhu, 2018; Woo et al., 2018; Ye et al., 2019). Besides, owing to the conversion reaction ($SnO_2 + 4Li^+ + 4e^- \rightarrow Sn + 2Li_2O$) and alloying reaction ($Sn + 4.4Li^+ + 4.4e^- \leftrightarrow Li_{4.4}Sn$), SnO_2 anodes possess a high theoretical capacity (1,494 mAh g^{-1}) for lithium storage (Hu et al., 2017; Shao et al., 2017; Wang et al., 2018).

However, two main problems that delay the commercialization process of SnO_2 anodes are poor conductivity and severe volume expansion. Researchers have done a lot of research work to solve these problems, and the most effective strategy at present is to combine with carbon materials (Du et al., 2014; Chen et al., 2018d; Hou et al., 2018; Li et al., 2018), which is indeed a great strategy. The introduction of carbon can limit the size of the material to obtain nanomaterials (Wang et al., 2013; Chen et al., 2018c). Nanoparticles can effectively reduce the absolute volume change of each particle, greatly improving the structural stability of the material. Furthermore, the charge-diffusion path of ions and electrons are greatly shortened and a large number of electrochemically active sites existed in nanoparticles (Ying and Han, 2017). On the other hand, the introduction of carbon can greatly improve the electrical conductivity of the material and enhance the structural stability of the material. Compared with other carbon materials, graphene has a two-dimensional layer structure with a single atomic thickness, remarkable structural flexibility, excellent electrical conductivity, high mechanical strength, and a large specific surface area. Therefore, graphene has obvious advantages in the application of electrode materials, and is an ideal substrate for dispersing and limiting active substances (Chen et al., 2018a; Li et al., 2019).

Recently, some researchers propose that the charge transfer kinetics can be enhanced by constructing a reasonable heterogeneous structure with built-in driving force (Jiang et al., 2017; Li et al., 2018; Ren et al., 2018). The synergistic effect of ion/electron transport originating from solid-solid heterojunctions is particularly important for electrode performance of essentially enhanced kinetics. In this context, superior electrochemical performance was demonstrated for SnS/SnO_2 (Li et al., 2018), MoS_2/SnS_2 (Jiang et al., 2017), $MnMoO_4/CoMoO_4$ (Chen H. et al., 2014), and Fe_2O_3/Mn_2O_3 (Ren et al., 2018). SnS_2 is a CdI2 type layered structure material with a large interlayer spacing (0.5899 nm) and a narrow band gap (Xu et al., 2015). Moreover, since the bond energy of Sn-S is weaker than the bond energy of Sn-O, this will promote the conversion of SnS_2 to Sn (Zhang S. et al., 2017; Wu et al., 2019). Therefore, the conversion reaction kinetics can be greatly improved by constructing a heterostructure between SnO_2 and SnS_2. Whereas, the development of synergistic ultra-fine heterogeneous interface lithium storage materials still faces enormous challenges.

Herein, we propose a facile and scalable fabrication approach of heterostructured SnO_2-SnS_2@carbon/nitrogen-doped reduced graphene oxide (SnO_2-SnS_2@C/NG) composite. In this hierarchical structure, the as-prepared SnO_2-SnS_2 nanoparticles were intimately embedded in carbon matrix with nitrogen-doped graphene, constructing an intimate cross-link conductive framework. Apart from the heterojunction structure of SnO_2-SnS_2, the carbon matrix with nitrogen-doped graphene accommodates the volume variation and facilitates the transport of lithium ions during continuous lithation/delithation cycling. The SnO_2-SnS_2@C/NG composite with hierarchical structure can fundamentally possess enhanced kinetics and reaction reversibility, thereby ensuring the stable cycling life.

EXPERIMENTAL SECTION

Preparation of SnO_2-SnS_2@C/NG Composite

All chemical reagents in this experiment are of analytical grade. The preparation method of SnO_2@C/reduced graphene oxide (SnO_2@C/rGO) refers to our previous report (Li et al., 2019). Firstly, 30 mL of graphene oxide (GO) solution (0.5 mg mL^{-1}) was added to the beaker, and then 0.25 g of $SnCl_2$ and 0.15 g of sodium alginate were thoroughly dispersed in the above GO solution, and slowly added to 30 mL of deionized water to form uniform solution. Secondly, the resulting solution was then hydrothermally treated at 180°C for 12 h. After that, the obtained gray powder was calcined at 450°C for 1 h under Ar atmosphere to obtain SnO_2@C/rGO composite. Finally, 0.2 g of the obtained precursor and 0.4 g of thioacetamide were added to 50 ml of deionized water, and hydrothermally treated at 200°C for 15 h to obtain the desired SnO_2-SnS_2@C/NG composite. SnO_2-SnS_2@C was prepared using the above method with 0.3 g of sodium alginate, and without using GO solution. SnO_2@C was prepared using the above method with 0.3 g of sodium alginate, and without using GO solution and no further vulcanization.

Characterization

The structure of SnO_2-SnS_2 composite was determined by X-ray diffraction (XRD, Bruker D8) with Cu Kα radiation. The degree of the disorder of carbon was detected by Raman spectroscopy (HORIBA, Jobin-Yvon Lab RAM Aramis). The form of various elements in the SnO_2-SnS_2@C/NG was characterized by X-ray photoelectron spectroscopy (XPS, K-Alpha). The macroscopic morphology of the composite was observed by scanning electron microscopy (SEM, Zeiss Gemini DSM 982) and the microscopic morphology of the composite was observed by transmission electron microscopy (TEM, FEI Tecnai, G2 F20 STWIN). Thermogravimetric analyses (TGA, NETZSCH STA 409PG/PC) of the composites were performed in air with a heating rate of 5°C min^{-1}.

The electrochemical properties of the composites were evaluated using CR2025 cells. The composite material, conductive carbon (SP) and polyvinylidene fluoride (weight ratio 7:2:1) were dispersed in N-methylpyrrolidinone, and uniformly mixed to prepare a slurry. The slurry was uniformly coated on a copper foil current collector and dried at 120°C overnight, and the dried electrode sheets were controlled to have a loading density of 1.1–1.5 mg cm^{-2}. The CR2025 batteries were assembled in a closed glove box, in which lithium tablets

were used as the counter electrodes, and 1 M $LiPF_6$ in ethylene carbonate and dimethyl carbonate (1:1, vol) was used as the electrolyte. The galvanostatic discharge/charging performances were tested by the battery test system (CT2001A, LAND) and the measured potential range was from 0.01 to 3.0 V. Cyclic voltammetry curves (CV, 0.01–3.0 V) and electrochemical impedance spectroscopy (EIS, 0.01–10^5 Hz) were recorded by electrochemical workstation measurements (CHI1000C, CH Instruments).

RESULTS AND DISCUSSION

The representative fabrication process of heterostructured SnO_2-SnS_2@C/NG is presented in **Scheme 1**. Firstly, the SnO_2@C/rGO composite was synthesized by hydrothermal method, using sodium alginate and GO to produce carbon matrix (C/rGO). Then, SnO_2 was partially vulcanized and grapheme was doped by nitrogen under hydrothermal reaction to finally obtain SnO_2-SnS_2@C/NG composite with a heterostructure structure, in which the thioacetamide works as a vulcanizing agent and a nitrogen dopant.

X-ray diffraction (XRD) patterns were collected to reveal the phase structures of the as-prepared SnO_2-SnS_2@C/NG and SnO_2-SnS_2@C composites. As exhibited in **Figure 1A**, the sharp diffraction peaks for both samples were consistent with SnO_2 (PDF No#21-1250) and SnS_2 (PDF#22-0951), respectively. The strong diffraction peaks represent a high degree of crystallinity of the composite. The results indicate that the composites consisted of SnO_2 and SnS_2 mixtures. Additionally, no obvious peaks indexed into carbon were observed, suggesting the amorphous state of carbon and graphene. SnO_2@C sample (**Figure S1A**) was consistent with SnO_2 (PDF No#88-0287). To demonstrate the existence of graphene in composites, Raman spectroscopy at the range of 800–3.200 cm^{-1} were collected in **Figure 1B**. It shows two obvious peaks at 1,337 and 1,583 cm^{-1}, assigning to the disorder of carbon materials for D-band and characteristic of sp^2 hybridized carbon for G-band (Liu et al., 2010; Zhang et al., 2016). Compared with the SnO_2-SnS_2@C and SnO_2@C (**Figure S1B**) (I_D/I_G = 0.72 and 0.71), the I_D/I_G ratio in SnO_2-SnS_2@C/NG (1.20) was much higher, suggesting that the existence of graphene, which is beneficial for the rapid electron transport. In addition, it can be found in the spectra that the SnO_2-SnS_2@C/NG composite had two distinct peaks at 2670.3 and 2916.1 cm^{-1} due to the 2D and S3 bands, respectively (Liu et al., 2010). Notably, the symmetric 2D band indicates the presence of a single layer of graphene in the SnO_2-SnS_2@C/NG composite (Shah et al., 2017). To determine the carbon and SnS_2 content, TGA was estimated in air, as displayed in **Figure 1C**. As can be seen from the figure, the weight loss can be divided into three stages, which are divided into the following: the first stage is room temperature to 250°C, the second stage is 250 to 450°C, and the third stage is 450 to 600°C. The weight loss in the first stage is due to the release of adsorbed water. The weight loss in the second stage corresponds to the conversion of SnS_2 to SnO_2 ($SnS_2+3O_2 = SnO_2+SO_2\uparrow$) (Lu et al., 2018), meanwhile, SnO_2-SnS_2@C and SnO_2-SnS_2@C/NG composites lost weights of 8.04 and 11.05 wt%, respectively. It can be calculated that the contents of the SnS_2 in SnO_2-SnS_2@C and SnO_2-SnS_2@C/NG composites material are 45.75 and 62.88 wt%, respectively, and the content of SnO_2 produced from those are 37.71 and 51.83 wt%, respectively. The weight loss in the third stage is ascribed to the oxidation of carbon, resulting in weight losses of 5.85 and 6.83 wt% for the SnO_2-SnS_2@C and SnO_2-SnS_2@C/NG composites, respectively. Until the last stage, the remaining products were all SnO_2, and the SnO_2-SnS_2@C and SnO_2-SnS_2@C/NG composites retain 82.98 and 79.39 wt% (This contains two parts of SnO_2: one part is the original SnO_2 in the composites and the other part is the SnO_2 converted from SnS_2), respectively. Furthermore, it is inferred the specific composition of each component in the composite, as listed in **Table 1**. Surface chemical elements of SnO_2-SnS_2@C and SnO_2-SnS_2@C/NG composites were characterized by XPS analyses (**Figure 1D**). The S, O, Sn, and C elements were found in both composites in the full spectrum of XPS. Compared with SnO_2-SnS_2@C, it can be observed that SnO_2-SnS_2@C/NG had a

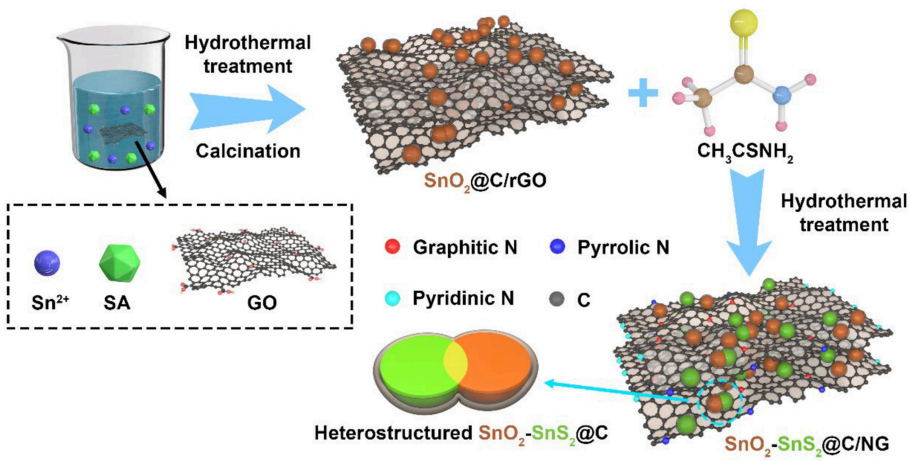

SCHEME 1 | Schematic illustration of the preparation process of SnO_2-SnS_2@C/NG composite.

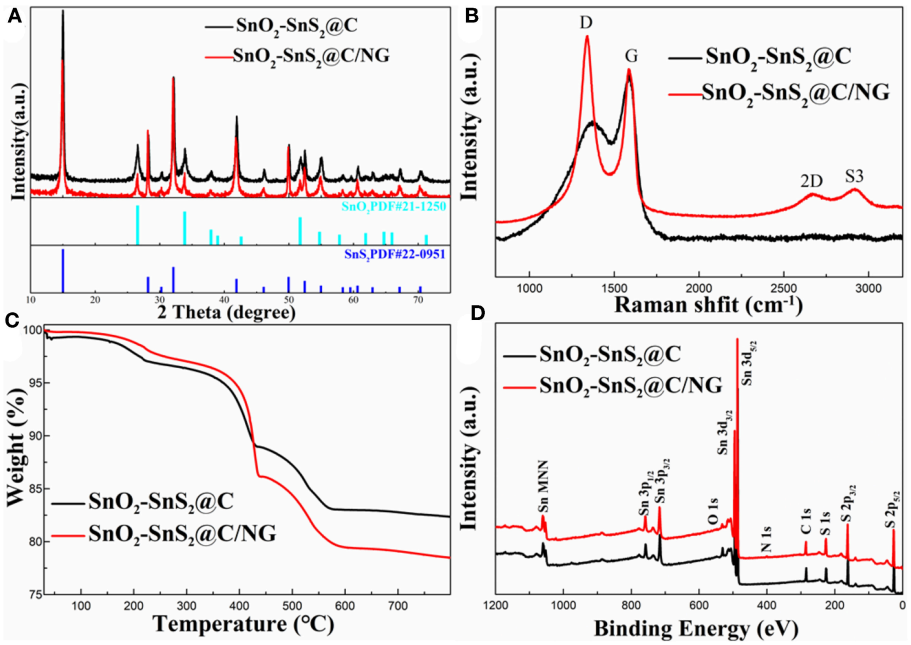

FIGURE 1 | (A) XRD patterns, **(B)** Raman spectra, **(C)** TGA curves, and **(D)** XPS spectra of SnO_2-SnS_2@C and SnO_2-SnS_2@C/NG composites.

TABLE 1 | Contents of each component in the composites.

	SnO_2 (wt%)	SnS_2 (wt%)	Carbon (wt%)
SnO_2@C (**Figure S1C**)	90.56	0	5.80
SnO_2-SnS_2@C	45.27	45.75	5.85
SnO_2-SnS_2@C/NG	62.88	27.56	6.83

weak intensity peak of N 1s at 400 cm^{-1}, suggesting that the N element has been doped into the graphene lattice.

To obtain more information about the chemical state of the elements in the prepared SnO_2-SnS_2@C/NG composite, High-resolution XPS spectra are depicted in **Figure 2**. As shown in **Figure 2A**, the high-resolution Sn 3d XPS spectrum of the SnO_2-SnS_2@C/NG composite can be fitted to the intensity peaks at 487.2 and 495.6 eV, respectively, confirmed that tin in the composite exists in the form of Sn^{4+} (Lu et al., 2018). The C 1s spectrum is applied to further analyze the carbon form in the SnO_2-SnS_2@C/NG composite. As observed in **Figure 2B**, the high-resolution C 1s XPS spectrum of SnO_2-SnS_2@C/NG can be fitted to three peaks located at 284.7, 285.5, and 286.9 eV for C=C, C-N, and C-O, respectively (Li et al., 2018). The relative weak intensity of the C-O peak indicates that the oxide in the graphene is partially reduced. Besides, the presence of C-N peak further demonstrates nitrogen doping into the graphene lattice, which opens the band gap, adjusts the conductivity type, changes the electronic structure, and increases the free carrier density in the graphene, thereby improving the conductivity of SnO_2-SnS_2@C/NG electrodes. By fitting the high-resolution N 1s spectrum (**Figure 2C**), it can be found that N 1s spectrum can be divided into three peaks located in at 400.0, 401.8, and 402.7 eV, corresponding to the pyridinic, pyrrolic, and graphitic nitrogen atoms, respectively (Wu et al., 2018). **Figure 2D** shows the O 1s spectrum of the SnO_2-SnS_2@C/NG composite, which can be fitted into four types of oxygen-containing bond units located at 530.9, 531.2, 532.5, and 534.9 eV, respectively. The peaks at 530.9, 531.2 and 532.5 eV correspond to O-Sn^{4+}, H-O-H, and C-O-C bonds, respectively. Notably, the peak at 534.9 eV corresponds to the S-Sn^{4+}-O bond, which is a strong evidence of the presence of a heterojunction in the composite (Zhang et al., 2018). This confirmed the presence of a chemical bond between SnO_2 and SnS_2 particles.

The morphology and detailed structural feature of the prepared composite were observed by SEM, TEM and HRTEM. As can be observed in **Figure 3a**, the morphology of the SnO_2-SnS_2@C/NG composite shows an orderly lamination structure, forming a fluffy gap between the layers, which is very beneficial to the infiltration of the electrolyte. The ultrafine SnO_2-SnS_2 nanoparticles embedded into the crumpled carbon matrix, thereby forming tremendous voids in the composite. Due to the uniform distribution of nanosized particles, which are hardly observed from the SEM image (**Figure 3b**). In the absence of graphene-involved combination, the particles of the SnO_2-SnS_2@C composite were agglomerated into microspheres of 200–300 μm diameter (**Figure S2A**). TEM is also applied to characterize the detailed structural feature of SnO_2-SnS_2@C/NG composite. As presented in **Figure 3c**, it can be clearly observed that the nanoparticles are perfectly wrapped by a single layer of graphene sheet. The graphene sheet in the figure also has void spaces and wrinkles, which can significantly suppress

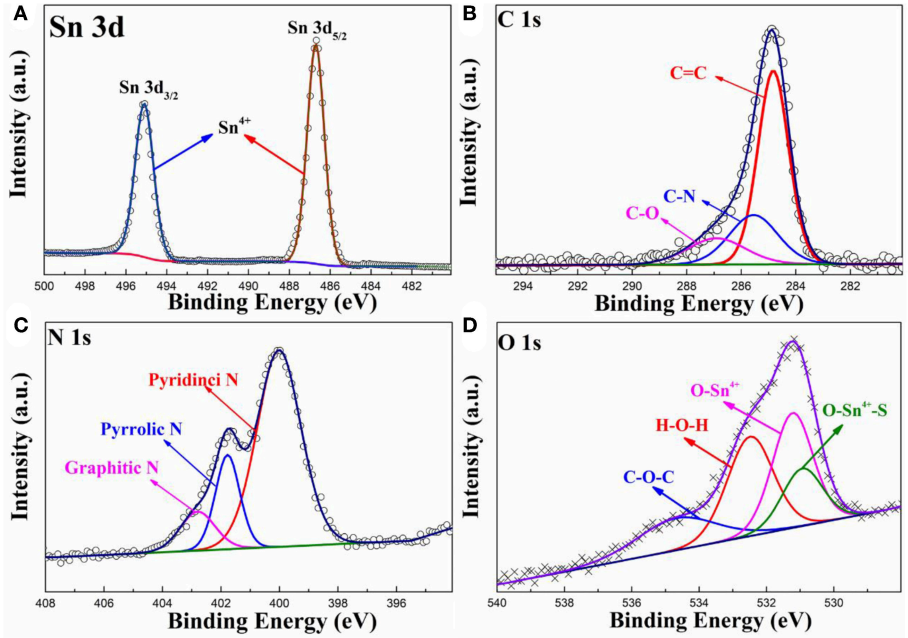

FIGURE 2 | High-resolution XPS spectra of **(A)** Sn 3d, **(B)** C 1s, **(C)** N 1s, and **(D)** O 1s spectra for SnO_2-SnS_2@C/NG composite.

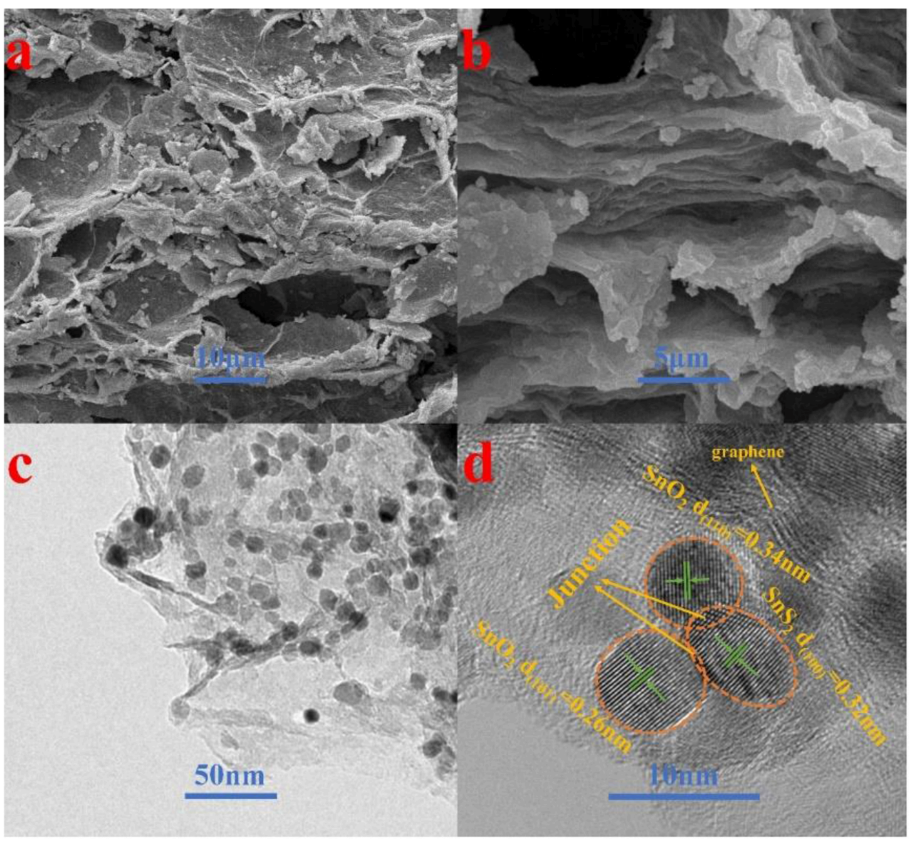

FIGURE 3 | (a,b) SEM, **(c)** TEM, and **(d)** HRTEM images of SnO_2-SnS_2@C/NG composite.

the volume expansion of the nanoparticles and enhance the conductivity of the composites. Under the observation of TEM, it is found that the microspheres of SnO_2-SnS_2@C composite (**Figure S2B**) are composed of primary particles of about 100–500 nm, and the surface of the primary particles is covered with an amorphous carbon. **Figure 3d** clearly depicts the nanoparticles with the diameter of 5–10 nm and high degree of crystallization, which are uniformly embedded in graphene with a curved lattice fringe of 0.424 nm. The particle in nanometer size can significantly shorten the lithium diffusion path and greatly improve the rate performance of the composite. Meanwhile, **Figure 3d** also displays the obvious several small nanocrystals with lattice spacings of 0.26, 0.34 and 0.32 nm, corresponding to (101) and (110) planes of SnO_2 and (100) plane of SnS_2, respectively (Shi and Lu, 2014; Chen et al., 2015; Shan et al., 2015; Yin et al., 2017). More importantly, as denoted in **Figure 3d**, the heterojunctions are formed in the overlapped junction regions. In **Figure S2C**, the heterojunction phenomenon of SnO_2-SnS_2@C can also be found. The formation of heterojunctions composed of (101) plane of SnO_2, (100) plane of SnS_2, and (110) plane of SnO_2, which strongly confirms the existence of heterogeneous SnO_2-SnS_2. Such a hierarchical structure is imperative for circumventing the self-aggregation of Sn-based nanoparticles, as well as the Sn and/or Li_xSn nanoparticles produced during cycling. Additionally, EDS mapping illustrates the homogeneous distribution of C, N, O, S, and Sn elements on the SnO_2-SnS_2@C/NG composite, as presented in **Figure 4**, which is consistent with the TEM analysis. The characterization of various physical and chemical means suggests that SnO_2-SnS_2@C/NG composite is a well-designed hierarchical structure, in which heterojunctions composed of SnO_2 and SnS_2 ultrafine nanoparticles are encapsulated in nitrogen-doped graphene sheets.

In order to explore the mechanism reaction of the composite during the charging and discharging process, the CV curve in the first three cycles of SnO_2-SnS_2@C/NG electrode was studied, as shown in **Figure 5A**. During the first scan of the cathodic process, the peaks at 1.87 and 1.70 V are attributed to the Li deintercalation in the SnS_2 layer, and there was no phase decomposition in this process, so the corresponding peaks were not found in the subsequent cycle (Yin et al., 2017). Decomposition of SnS_2 to metallic tin and Li_2S results in a peak at 1.29 V. The conversion of SnO_2 and SnO to Sn produced a cathode peak at around 0.92 V and formed a synchronous products of Li_2O and SEI film (Chen et al., 2015). The strong cathode peak at 0.18 V is attributed to Li_xSn produced by the alloying reaction of elemental tin and lithium ions, and peak at the same potential was also observed in subsequent cycles, indicating that the alloying reaction here is reversible. In the anodic scan process, the strong peak at 0.5 V is caused by the de-alloying of Li_xSn, corresponding to the 0.18 V peak in the cathodic scan. The peak at 1.86 V is attributed to the oxidation and sulfurization of Sn to SnO_2 and SnS_2, respectively. The peak at 2.35 V is related to partial decomposition of Li_2S, which also produces the first small irreversible capacity (Lu et al., 2018). It is worth noting that due to phase decomposition and structural collapse, the cathodic peak of 1.29 V in the first cycle shifted to 1.36 V in the subsequent cycle (Lu et al., 2018). Meanwhile, **Figure 5B** shows the first three discharge/charge curves of the SnO_2-SnS_2@C/NG composite, with a voltage window of 0.01–3.0 V and a current rate of 0.1 A g^{-1}, which is consistent with the CV results. The first discharge/charge capacity achieved 1727.2 and 1201.2 mAh g^{-1}, respectively, with initial coulombic efficiency of 69.54%. The excess capacity may come from the formation of SEI film on the surface of active materials, lithium-insertion reaction in acetylene black and interfacial storage, which is similar to the phenomena of other Sn-based anodes (Chen Y. et al., 2014; Fu et al., 2018; Li et al., 2019). The low initial coulombic efficiency is mainly due to the formation of SEI films, which is usually observed for the nanosized anode materials (Liu et al., 2014; Yang et al., 2018), whereas the coulombic efficiency approached 99.9% in the following cycles. In contrast, the initial charge capacity for SnO_2-SnS_2@C reached 812.4 mAh g^{-1} under the

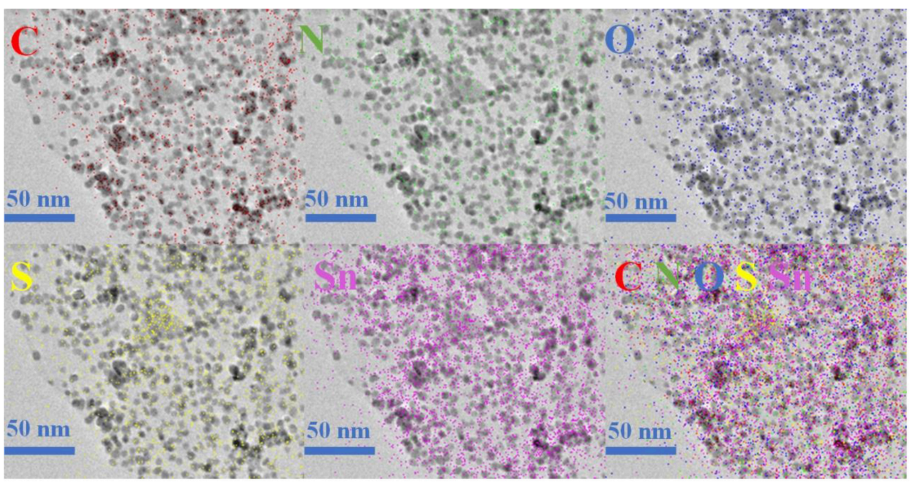

FIGURE 4 | EDS mapping images of SnO_2-SnS_2@C/NG composite.

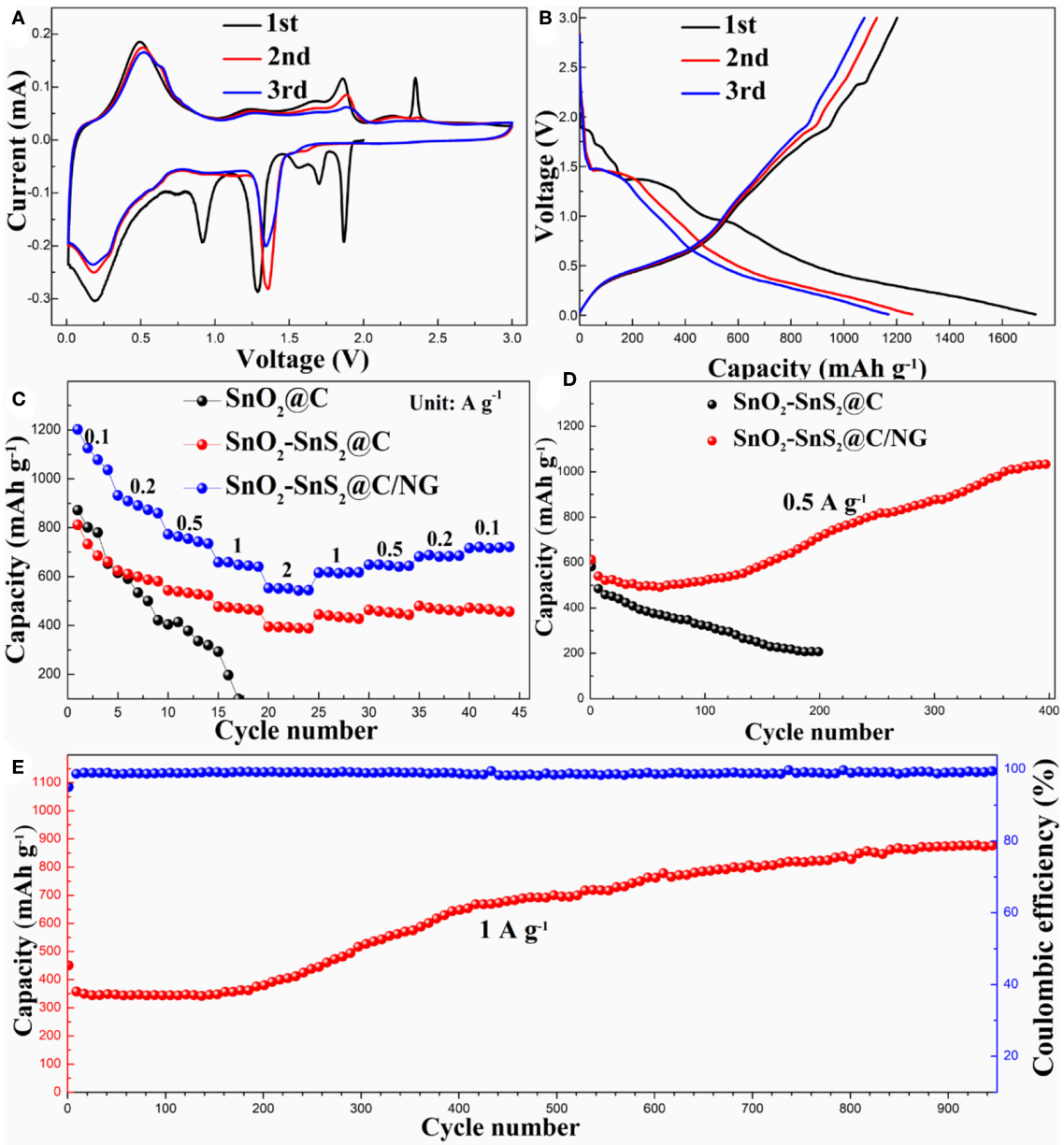

FIGURE 5 | (A) CV profiles and **(B)** the charge/discharge curves in the initial three cycles for SnO_2-SnS_2@C/NG composite. **(C)** Rate capabilities and **(D)** cycle performances for SnO_2-SnS_2@C and SnO_2-SnS_2@C/NG composites at current rate of 0.5 A g^{-1}, and **(E)** long cycling property for SnO_2-SnS_2@C/NG composite at current rate of 1 A g^{-1}.

same condition (**Figure S3**), which is relatively lower than that of SnO_2-SnS_2@C/NG.

As depicted in **Figure 5C**, the rate capabilities of the composite electrodes were performed at various current rates ranging from 0.1 to 2 A g^{-1}. The SnO_2-SnS_2@C electrodes delivered stable capacities of 815.7, 628.6, 544.5, 478.6, and 395.8 mAh g^{-1} at the rates of 0.1, 0.2, 0.5, 1, and 2 A g^{-1}, respectively. When current rate returned to 0.1 A g^{-1}, it recovered to 475.7 mAh g^{-1}. In contrast, the rate performance of the SnO_2@C electrode was relatively poorer, as its capacity dropped sharply when the current density increased until the cell failed. The possible reason is that the heterojunction in the SnO_2-SnS_2@C composite can significantly improve the conductivity, resulting in an increase in rate performance. Apparently, the rate performance of SnO_2-SnS_2@C/NG composite was the best. The SnO_2-SnS_2@C/NG electrodes delivered stable capacities of 1206.7, 936.3, 777.3, 666.3, and 559.0 mAh g^{-1} at the rates of 0.1, 0.2, 0.5, 1, and 2 A g^{-1}, respectively. When the current rate returns to 0.1 A g^{-1}, it still can recover to 724.1 mAh g^{-1}. The SnO_2-SnS_2@C/NG composite also exhibited the best

cycle performance. The capacity of SnO_2-SnS_2@C/NG composite electrode at current rate of 0.5 A g^{-1} reached 717.6 mAh g^{-1} after 200 cycles and gradually increased to 1039.4 mAh g^{-1} after 400 cycles (**Figure 5D**). In addition, the charge and discharge curves for the 400th cycle of the SnO_2-SnS_2@C/NG composite are shown in the **Figure S4**. The capacity ratio in the voltage of 2.0–3.0 V was about 42%, which may be related to the reversible formation of the polymer gel-like film. However, the SnO_2-SnS_2@C electrode exhibited a low capacity of 208.0 mA h g^{-1} at 0.5 A g^{-1} after 200 cycles. Remarkably, at the high current rate of 1 A g^{-1} (**Figure 5E**), the SnO_2-SnS_2@C/NG electrode still performed well after 950 cycles, exhibiting a strong reversible capacity of 944.3 mAh g^{-1}, with the stabilized coulombic efficiency of around 99.5% throughout the whole cycling, confirming the merits of SnO_2-SnS_2@C/NG composite during the long-term cycling. In contrast with previous reported anodes materials, the SnO_2-SnS_2@C/NG composite exhibits outstanding cycle stability at higher current rates and

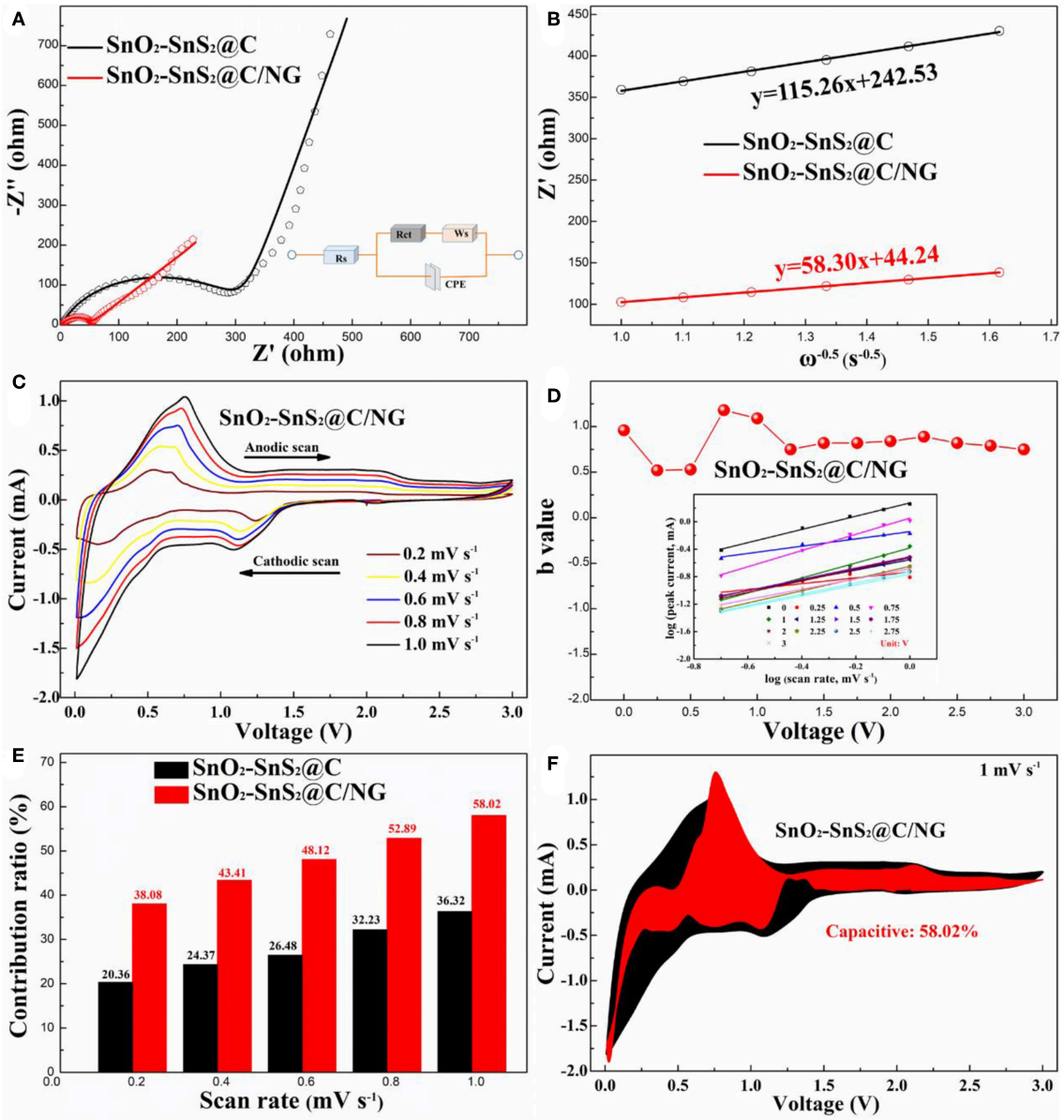

FIGURE 6 | (A) Nyquist plots and corresponding fitted curves of SnO_2-SnS_2@C and SnO_2-SnS_2@C/NG electrodes before cycles (the inset is the modified equivalent circuit); **(B)** Nyquist plots and corresponding relationship between the real resistance (Z') and angular frequency ($\omega^{-0.5}$) for SnO_2-SnS_2@C and SnO_2-SnS_2@C/NG electrodes; **(C)** CV curves of SnO_2-SnS_2@C/NG electrode at different scan rates from 0.2–1.0 mV s^{-1}; **(D)** b values plotted against cell voltage of SnO_2-SnS_2@C/NG electrode for cathodic scans; **(E)** the percentage of the capacitance contribution for SnO_2-SnS_2@C and SnO_2-SnS_2@C/NG at different scan rates; **(F)** CV curve of SnO_2-SnS_2@C/NG at a sweep rate of 1.0 mV s^{-1}, and the estimated capacitive current contribution is shown in the shaded region.

exhibits outstanding electrochemical performance (as shown in **Table S1**). It is noteworthy that the capacity had a slightly decrease during the first 50 cycles, then gradually increased during the subsequent cycles, and finally maintaining a stable performance. This phenomenon is attributed to the electrode activation and reversible formation of the polymer gel-like film, followed by the continuous reconstruction of SEI film on the surface of nanomaterials (Wang et al., 2013; Zhou et al., 2013; Liu et al., 2014).

In order to gain a deep understanding of the excellent electrochemical properties and to evaluate the lithium storage kinetics and charge transfer capacity of the composites, the SnO_2-SnS_2@C and SnO_2-SnS_2@C/NG electrodes were investigated by EIS. As displayed in **Figure 6A**, all Nyquist plots consist of a depressed semicircle at high frequency and a straight drift at low-medium frequency, which can be perfect fitted with an equivalent circuit as displayed in the insert of **Figure 6A**. Compared with charge-transfer resistance (R_{ct}) of SnO_2-SnS_2@C (323.6 Ω), the R_{ct} of SnO_2-SnS_2@C/NG (47.37 Ω) is much smaller. Furthermore, the lithium-ion diffusion coefficient (D_{Li+}) can be further calculated according to the following equations (Yi et al., 2017; Zhang B. et al., 2017; Tong et al., 2018) (R, gas constant; T, absolute temperature; A, surface area; n, average reacted electrons; F, Faraday constant; C, Li^+ concentration, respectively):

$$D_{Li}^{+} = R^2T^2/2A^2n^4F^4C^2\sigma^2 \quad (1)$$

$$Z' = R_s + R_{ct} + \sigma\omega^{1/2} \quad (2)$$

in which, σ can be calculated by the plot of Z' vs. $\omega^{-0.5}$ (angular frequency) as depicted in **Figure 6B**. Therefore, the calculated values of D_{Li}^{+} listed in **Table S2** imply the rapid diffusion of lithium ions and excellent reaction kinetics of the SnO_2-SnS_2@C/NG electrode.

In order to further explore the excellent rate performance of the SnO_2-SnS_2@C/NG electrode, CV analyses at various scan rates from 0.2 to 1 mV s^{-1} were carried out (**Figure 6C**). Considering that SnO_2-SnS_2@C/NG is superior than SnO_2-SnS_2@C in high-rate performance and fast lithium ion transport, the pseudocapacitance contribution of SnO_2-SnS_2@C/NG may be more than that of SnO_2-SnS_2@C during charge/discharge process. In this case, the ratios of capacitive contribution can be further quantitatively quantified by separating the current response (*i*) at a fixed potential (V) into capacitive contribution (k_1v) and

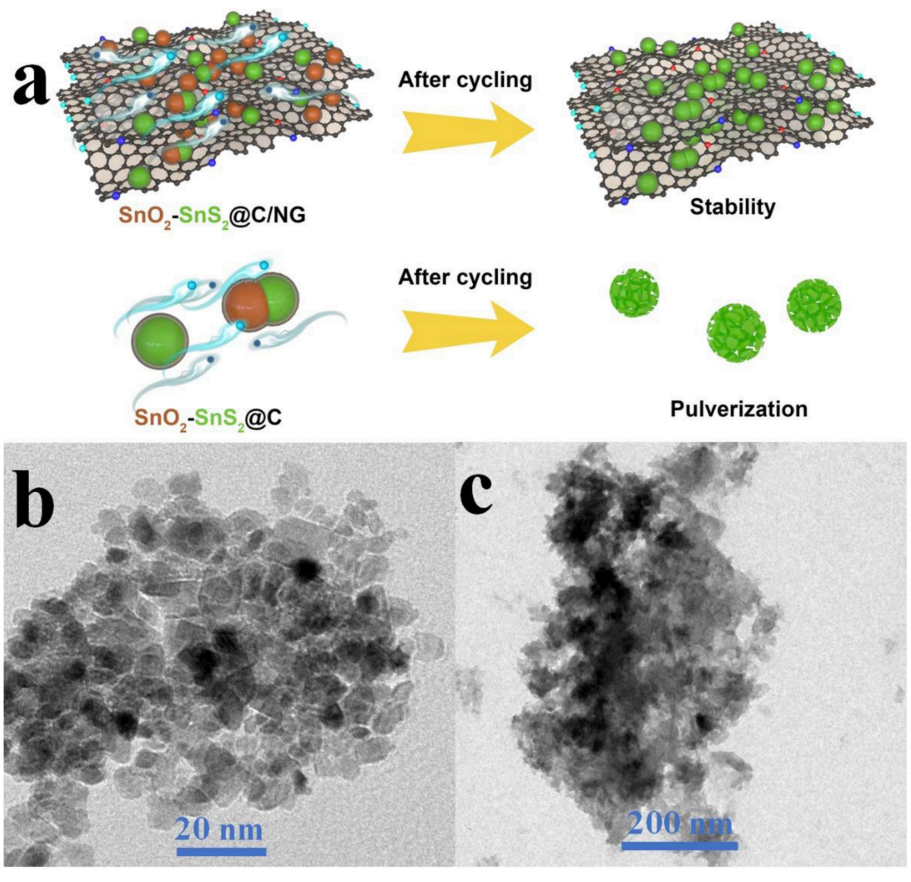

FIGURE 7 | (a) Schematic illustration of the robust structure for SnO_2-SnS_2@C/NG and SnO_2-SnS_2@C composites. TEM images of **(b)** SnO_2-SnS_2@C/NG and **(c)** SnO_2-SnS_2@C composites after cycling test.

diffusion-controlled contribution ($k_2v^{1/2}$), according to the following equation:

$$i = k_1v + k_2v^{1/2} = av^b \quad (3)$$

in which, a and b present adjustable values. It must be noted that there is no proportional relationship between the measured current (i) and the square root of the scan rate (v) at a certain potential, suggesting the redox process can hardly be assigned to entire ion-diffusion control. The value of b is usually between 0.5 and 1, where 0.5 represents the diffusion control process and 1.0 illustrates the ideal pseudocapacitive behavior according to previous mechanism (Zhao et al., 2017). As displayed in **Figure 6D**, by fitting log(i) and log(v) at various redox potentials, several b values >0.8 can be obtained therefrom, demonstrating a dominated pseudocapacitive-controlled contribution process for the SnO_2-SnS_2@C/NG electrode. Furthermore, the contribution of total pseudocapacitive at a specific scan rate can be accurately calculated by the following equation ((Zhao et al., 2017); Zhang et al., 2018):

$$i(V)/v^{1/2} = k_1v^{1/2} + k_2 \quad (4)$$

By carefully comparing the capacity contributions at different scan rates (**Figure 6E**), it is not difficult to conclude that the percentage of pseudocapacitive contribution increases gradually as the scan rate increases, and the lithiation/delithiation reaction of the SnO_2-SnS_2@C/NG composite gradually becomes capacitive control, and the pseudocapacitive-controlled contribution ratios of the SnO_2-SnS_2@C/NG composite are always higher than those of the SnO_2-SnS_2@C composite. As highlighted in **Figure 6F**, when the scan rate is 1 mV s^{-1}, nearly 58.02% of the total current (red region) is attributed to the pseudocapacitive contribution for the SnO_2-SnS_2@C/NG electrode, which is the maximum at all scan rates.

The distinct pseudocapacitive behavior and enhanced reaction kinetic proved by EIS results are originated from the synergistic effect of SnO_2-SnS_2 heterojunction incorporated into the highly conductive N-doped graphene. The ultrafine SnO_2-SnS_2 nanoparticles can provide shorten transport distance of lithium ions, especially the formation of heterojunctions at the interface of SnO_2-SnS_2 nanoparticles effectively enhance the electronic transmission, which greatly promote the rate capability. Furthermore, nitrogen-doped graphene also plays a key role in lithium ion and electronic conductivity, which can build highly-conductive framework among the dispersive nanoparticles with integrity architecture, efficiently facilitating the lithium transport path and thus resulting in the excellent electrochemical performance.

The nitrogen-doped graphene nanosheets interconnect the nanoparticles and act as cushions for its volume expansion during long-term lithiation/delithiation process, further enhancing the structural stability and improving the life-cycle of entire electrode, as schematically illustrated in **Figure 7a**. The correlations between cycling properties and structural features for the as-prepared SnO_2-SnS_2@C/NG and SnO_2-SnS_2@C composites were characterized by TEM tests after 400th cycle at the current rate of 0.5 A g^{-1}. As presented in **Figure 7b**, the flake morphology of SnO_2-SnS_2@C/NG was well-maintained after long-term cycling. The repeated volume expansion is effectively restricted by the robust architecture of the carbon matrix, in which the amorphous carbon locks the SnO_2-SnS_2 nanoparticles on the nitrogen-doped graphene sheets, inhibiting its severe volume variation. In comparison, SnO_2-SnS_2@C composite without incorporation of graphene suffer from the particle pulverization and agglomeration after continuous cycling (**Figure 7c**), and the nanoparticles are easily detached from the current collector, which leads to the unstable structure and severe electrode degradation with bad cycling performance. Furthermore, the repeated formation of thick SEI films overlying on the surface SnO_2-SnS_2 particles has adverse effects on the reversibility of conversion reaction, directly impeding the lithium ion and electron transfer and resulting in the continuous capacity decrease. All results indicate that heterostructured SnO_2-SnS_2@C/NG composite demonstrates enhanced structural stability and superior electrochemical performance.

CONCLUSIONS

In this work, the well-designed SnO_2-SnS_2@C/NG composite was ingeniously fabricated by a facile approach, in which the heterojunction of SnO_2-SnS_2 was created and embedded into the carbon matrix with highly conductive nitrogen-doped graphene nanosheets. As expected, SnO_2-SnS_2@C/NG composite exhibited a high reversible capacity (1201.2 mA h g^{-1} at current rate of 0.1 A g^{-1}), superior rate capability and long-life stability (1039.4 mAh g^{-1} after 400 cycles at current rate of 0.5 A g^{-1}, and 944.3 mAh g^{-1} after 950 cycles at current rate of 1.0 A g^{-1}). The excellent electrochemical properties may be ascribed to the following reasons. The lithium ion diffusion path is shortened in SnO_2-SnS_2 nanoparticles with ultrafine size, and reversibility and reaction kinetics are enhanced through the introduction of heterostructure. Meanwhile, the nitrogen-doped graphene sheets improve the electronic conductivity and structural stability, which can effectively accommodate the volume variation and maintain the steady formation of SEI films without particle pulverization. This strategy contributes a new insight for preparing the high-performance electrode materials for LIBs.

DATA AVAILABILITY

The raw data supporting the conclusions of this manuscript will be made available by the authors, without undue reservation, to any qualified researcher.

AUTHOR CONTRIBUTIONS

HL carried out the experiment and wrote the manuscript. XW, JZ, and TA participated in the experiment. BZ, ZD and WY contributed to the

discussion. HT supervised the experiment and proofread the manuscript.

ACKNOWLEDGMENTS

This work was supported by National Natural Science Foundation of China (Grant No. 51502350, 51772334, and 51702367), China Postdoctoral Science Foundation (Grant No. 2016M592447), The International Postdoctoral Exchange Fellowship Program (Grant No. 155212), and Hunan Provincial Innovation Foundation for Postgraduate (CX2017B060).

SUPPLEMENTARY MATERIAL

The Supplementary Material for this article can be found online at: https://www.frontiersin.org/articles/10.3389/fchem.2019.00339/full#supplementary-material

REFERENCES

Armand, M., and Tarascon, J. M. (2008). Building better batteries. *Nature* 451, 652–657. doi: 10.1038/451652a

Chen, C.-Y., Yokoshima, T., Nara, H., Momma, T., and Osaka, T. (2015). One-step hydrothermal synthesis of SnS_2/SnO_2/C hierarchical heterostructures for li-ion batteries anode with superior rate capabilities. *Electrochim. Acta* 183, 78–84. doi: 10.1016/j.electacta.2015.05.079

Chen, H., Hu, L., Chen, M., Yan, Y., and Wu, L. (2014). Nickel-cobalt layered double hydroxide nanosheets for high-performance supercapacitor electrode materials. *Adv. Funct. Mater.* 24, 934–942. doi: 10.1002/adfm.201301747

Chen, H., Huang, Y., Mao, G., Tong, H., Yu, W., Zheng, J., et al. (2018a). Reduced graphene oxide decorated $Na_3V_2(PO_4)_3$ microspheres as cathode material with advanced sodium storage performance. *Front. Chem.* 6:174. doi: 10.3389/fchem.2018.00174

Chen, H., Zhang, B., Cao, Y., Wang, X., Yao, Y., Yu, W., et al. (2018b). ZnS nanoparticles embedded in porous honeycomb-like carbon nanosheets as high performance anode material for lithium ion batteries. *Ceramics Int.* 44, 13706–13711. doi: 10.1016/j.ceramint.2018.04.211

Chen, H., Zhang, B., Wang, X., Dong, P., Tong, H., Zheng, J. C., et al. (2018c). CNT-decorated $Na_3V_2(PO_4)_3$ microspheres as a high-rate and cycle-stable cathode material for sodium ion batteries. *ACS Appl. Mater. Interfaces* 10, 3590–3595. doi: 10.1021/acsami.7b16402

Chen, H., Zhang, B., Zhang, J., Yu, W., Zheng, J., Ding, Z., et al. (2018d). *In-situ* grown SnS_2 nanosheets on rGO as an advanced anode material for lithium and sodium ion batteries. *Front. Chem.* 6:629. doi: 10.3389/fchem.2018.00629

Chen, J., Li, L., Wu, L., Yao, Q., Yang, H., Liu, Z., et al. (2018). Enhanced cycle stability of $Na_{0.9}Ni_{0.45}Mn_{0.55}O_2$ through tailoring O3/P2 hybrid structures for sodium-ion batteries. *J. Power Sources* 406, 110–117. doi: 10.1016/j.jpowsour.2018.10.058

Chen, Y., Song, B., Chen, R. M., Lu, L., and Xue, J. (2014). A study of the superior electrochemical performance of 3 nm SnO_2 nanoparticles supported by graphene. *J. Mater. Chem. A*, 2, 5688–5695. doi: 10.1039/C3TA14745B

Chou, W.-Y., Yeh, B.-L., Cheng, H.-L., Sun, B.-Y., Cheng, Y. C., Lin, Y.-S., et al. (2009). Organic complementary inverters with polyimide films as the surface modification of dielectrics. *Organ. Electronics* 10, 1001–1005. doi: 10.1016/j.orgel.2009.03.017

Du, F. H., Liu, Y. S., Long, J., Zhu, Q. C., Wang, K. X., Wei, X., et al. (2014). Incorporation of heterostructured Sn/SnO nanoparticles in crumpled nitrogen-doped graphene nanosheets for application as anodes in Lithium-ion batteries. *Chem. Commun.* 50, 9961–9964. doi: 10.1039/C4CC04187A

Fu, S., Wu, Q., He, S., Tong, S., Yang, X., Meng, Y., et al. (2018). Ultrafine SnO_2 nanocrystals self-anchored in carbon for stable lithium storage. *ChemElectroChem* 5, 2341–2347. doi: 10.1002/celc.201800631

Hou, C. X., Tai, Z. X., Zhao, L. L., Zhai, Y. J., Hou, Y., Fan, Y. Q., et al. (2018). High performance MnO@C microcages with a hierarchical structure and tunable carbon shell for efficient and durable lithium storage. *J. Mater. Chem. A* 6, 9723–9736. doi: 10.1039/C8TA02863J

Hu, L. L., Yang, L. P., Zhang, D., Tao, X. S., Zeng, C., Cao, A. M., et al. (2017). Designed synthesis of SnO_2-C hollow microspheres as an anode material for lithium-ion batteries. *Chem. Commun.* 53, 11189–11192. doi: 10.1039/C7CC05747D

Jiang, Y., Guo, Y., Lu, W., Feng, Z., Xi, B., Kai, S., et al. (2017). Rationally incorporated MoS_2/SnS_2 nanoparticles on graphene sheets for lithium-ion and sodium-ion batteries. *ACS Appl. Mater. Interfaces* 9, 27697–27706. doi: 10.1021/acsami.7b06572

Li, H., Zhang, B., Zhou, Q., Zhang, J., Yu, W., Ding, Z., et al. (2019). Dual-carbon confined SnO_2 as ultralong-life anode for Li-ion batteries. *Ceramics Int.* 45, 7830–7838. doi: 10.1016/j.ceramint.2019.01.090

Li, M., Deng, Q., Wang, J., Jiang, K., Shang, L., Hu, Z., et al. (2018). *In-situ* gas reduction in reversible SnS-SnO_2@N-doped graphene anodes for high-rate and lasting lithium storage. *J. Alloys Compounds* 769, 1007–1018. doi: 10.1016/j.jallcom.2018.08.038

Liu, J., Li, W., and Manthiram, A. (2010). Dense core-shell structured SnO_2/C composites as high performance anodes for lithium ion batteries. *Chem. Commun.* 46, 1437–1439. doi: 10.1039/b918501a

Liu, Z., Cao, Z., Deng, B., Wang, Y., Shao, J., Kumar, P., et al. (2014). Ultrafast and scalable laser liquid synthesis of tin oxide nanotubes and its application in lithium ion batteries. *Nanoscale* 6, 5853–5858. doi: 10.1039/C3NR06444A

Lu, X., Liu, D., Han, T., Zhu, M., Ryu, S. O., and Huang, J. (2018). A facile synthesis of sandwich-structured SnS_2@reduced graphene oxide with high performance for lithium-ion battery anode. *J. Alloys Compounds* 765, 1061–1071. doi: 10.1016/j.jallcom.2018.06.245

Ren, W., Liu, D., Sun, C., Yao, X., Tan, J., Wang, C., et al. (2018). Nonhierarchical heterostructured Fe_2O_3/Mn_2O_3 porous hollow spheres for enhanced lithium storage. *Small* 14:1800659. doi: 10.1002/smll.201800659

Sahoo, M., and Ramaprabhu, S. (2018). One-pot environment-friendly synthesis of boron doped graphene-SnO_2 for anodic performance in Li ion battery. *Carbon* 127, 627–635. doi: 10.1016/j.carbon.2017.11.056

Shah, M. S., a. S., Lee, J., Park, A. R., Choi, Y., Kim, W.-J., et al. (2017). Ultra-fine SnO_2 nanoparticles doubly embedded in amorphous carbon and reduced graphene oxide (rGO) for superior lithium storage. *Electrochim. Acta* 224, 201–210. doi: 10.1016/j.electacta.2016.12.049

Shan, J., Liu, Y., Liu, P., Huang, Y., Su, Y., Wu, D., et al. (2015). Nitrogen-doped carbon-encapsulated SnO_2-SnS/graphene sheets with improved anodic performance in lithium ion batteries. *J. Mater. Chem. A* 3, 24148–24154. doi: 10.1039/C5TA06617D

Shao, Q., Tang, J., Sun, Y., Li, J., Zhang, K., Yuan, J., et al. (2017). Unique interconnected graphene/SnO_2 nanoparticle spherical multilayers for lithium-ion battery applications. *Nanoscale* 9, 4439–4444. doi: 10.1039/C6NR09689A

Shi, W., and Lu, B. (2014). Nanoscale Kirkendall effect synthesis of echinus-like SnO_2@SnS_2 nanospheres as high performance anode material for lithium ion batteries. *Electrochim. Acta* 133, 247–253. doi: 10.1016/j.electacta.2014.04.013

Tong, H., Dong, P., Zhang, J., Zheng, J., Yu, W., Wei, K., et al. (2018). Cathode material $LiNi_{0.8}Co_{0.1}Mn_{0.1}O_2$/$LaPO_4$ with high electrochemical performance for lithium-ion batteries. *J. Alloys Compounds* 764, 44–50. doi: 10.1016/j.jallcom.2018.06.020

Tong, H., Zhou, Q., Zhang, B., Wang, X., Yao, Y., Ding, Z., et al. (2019). A novel core-shell structured nickel-rich layered cathode material for high-energy lithium-ion batteries. *Eng. Sci.* doi: 10.30919/es8d502

Wang, G., Xiong, X., Xie, D., Fu, X., Ma, X., Li, Y., et al. (2019). Suppressing dendrite growth by a functional electrolyte additive for robust Li metal anodes. *Energy Storage Mater.* doi: 10.1016/j.ensm.2019.02.026

Wang, H., Jiang, X., Chai, Y., Yang, X., and Yuan, R. (2018). Sandwich-like C@SnO_2/Sn/void@C hollow spheres as improved anode materials for lithium ion batteries. *J. Power Sources* 379, 191–196. doi: 10.1016/j.jpowsour.2018.01.054

Wang, L., Wang, D., Dong, Z., Zhang, F., and Jin, J. (2013). Interface chemistry engineering for stable cycling of reduced GO/SnO_2 nanocomposites for lithium ion battery. *Nano Lett.* 13, 1711–1716. doi: 10.1021/nl400269d

Wang, R., Li, X., Wang, Z., and Han, Z. (2017a). Electrochemical analysis graphite/electrolyte interface in lithium-ion batteries: p-Toluenesulfonyl isocyanate as electrolyte additive. *Nano Energy* 34, 131–140. doi: 10.1016/j.nanoen.2017.02.037

Wang, R., Wang, Z., Li, X., and Han, Z. (2017b). Electrochemical analysis the influence of Propargyl Methanesulfonate as electrolyte additive for spinel LTO interface layer. *Electrochim. Acta* 241, 208–219. doi: 10.1016/j.electacta.2017.04.125

Woo, H., Wi, S., Kim, J., Kim, J., Lee, S., Hwang, T., et al. (2018). Complementary surface modification by disordered carbon and reduced graphene oxide on SnO_2 hollow spheres as an anode for Li-ion battery. *Carbon* 129, 342–348. doi: 10.1016/j.carbon.2017.12.015

Wu, L., Zheng, J., Wang, L., Xiong, X., Shao, Y., Wang, G., et al. (2019). PPy-encapsulated SnS_2 nanosheets stabilized by defects on a TiO_2 support as a durable anode material for lithium-ion batteries. *Angew. Chem. Int. Ed.* 58, 811–815. doi: 10.1002/anie.201811784

Wu, N., Du, W., Gao, X., Zhao, L., Liu, G., Liu, X., et al. (2018). Hollow SnO_2 nanospheres with oxygen vacancies entrapped by a N-doped graphene network as robust anode materials for lithium-ion batteries. *Nanoscale* 10, 11460–11466. doi: 10.1039/C8NR02290A

Xiao, B., Zhang, B., Zheng, J.-C., Tang, L.-B., An, C.-S., He, Z.-J., et al. (2018). Nano-micro structure VO_2/CNTs composite as a potential anode material for lithium ion batteries. *Ceramics Int.* 44, 13113–13121. doi: 10.1016/j.ceramint.2018.04.133

Xu, K., Li, N., Zeng, D., Tian, S., Zhang, S., Hu, D., et al. (2015). Interface bonds determined gas-sensing of SnO_2-SnS_2 hybrids to ammonia at room temperature. *ACS Appl. Mater. Interfaces* 7, 11359–11368. doi: 10.1021/acsami.5b01856

Yang, J., Chen, S., Tang, J., Tian, H., Bai, T., and Zhou, X. (2018). Rod-like hierarchical Sn/SnO_x@C nanostructures with enhanced lithium storage properties. *Appl. Surface Sci.* 435, 203–209. doi: 10.1016/j.apsusc.2017.11.085

Ye, X., Lin, Z., Liang, S., Huang, X., Qiu, X., Qiu, Y., et al. (2019). Upcycling of electroplating sludge into ultrafine Sn@C nanorods with highly stable lithium storage performance. *Nano Lett.* 19, 1860–1866. doi: 10.1021/acs.nanolett.8b04944

Yi, L., Liu, L., Guo, G., Chen, X., Zhang, Y., Yu, S., et al. (2017). Expanded graphite@SnO_2@polyaniline composite with enhanced performance as anode materials for lithium ion batteries. *Electrochim. Acta* 240, 63–71. doi: 10.1016/j.electacta.2017.04.012

Yin, L., Chai, S., Huang, J., Kong, X., and Pan, L. (2017). Preparation of hierarchical SnS_2/SnO_2 anode with enhanced electrochemical performances for lithium-ion battery. *Electrochim. Acta* 238, 168–177. doi: 10.1016/j.electacta.2017.03.183

Ying, H., and Han, W. Q. (2017). Metallic Sn-based anode materials: application in high-performance lithium-ion and sodium-ion batteries. *Adv. Sci.* 4:1700298. doi: 10.1002/advs.201700298

Zhang, B., Dong, P., Tong, H., Yao, Y., Zheng, J., Yu, W., et al. (2017). Enhanced electrochemical performance of $LiNi_{0.8}Co_{0.1}Mn_{0.1}O_2$ with lithium-reactive Li_3VO_4 coating. *J. Alloys Compounds* 706, 198–204. doi: 10.1016/j.jallcom.2017.02.224

Zhang, M., Sun, Z., Zhang, T., Sui, D., Ma, Y., and Chen, Y. (2016). Excellent cycling stability with high SnO_2 loading on a three-dimensional graphene network for lithium ion batteries. *Carbon* 102, 32–38. doi: 10.1016/j.carbon.2016.02.032

Zhang, S., Zhao, H., Yue, L., Wang, Z., and Mi, J. (2017). Fixed-bed assisted synthesis SnO_2/SnS_2/CNTs composite for enhanced sodium storage performance. *J. Alloys Compounds* 717, 127–135. doi: 10.1016/j.jallcom.2017.05.055

Zhang, Y., Yang, J., Zhang, Y., Li, C., Huang, W., Yan, Q., et al. (2018). Fe_2O_3/SnSSe hexagonal nanoplates as lithium-ion batteries anode. *ACS Appl. Mater. Interfaces* 10, 12722–12730. doi: 10.1021/acsami.8b01537

Zhao, C., Yu, C., Zhang, M., Sun, Q., Li, S., Banis, M. N., et al. (2017). Enhanced sodium storage capability enabled by super wide-interlayer-spacing MoS_2 integrated on carbon fibers. *Nano Energy* 41, 66–74. doi: 10.1016/j.nanoen.2017.08.030

Zheng, J.-C., Yang, Z., He, Z.-J., Tong, H., Yu, W.-J., and Zhang, J.-F. (2018). *In situ* formed $LiNi_{0.8}Co_{0.15}Al_{0.05}O_2$@$Li_4SiO_4$ composite cathode material with high rate capability and long cycling stability for lithium-ion batteries. *Nano Energy* 53, 613–621. doi: 10.1016/j.nanoen.2018.09.014

Zhou, X., Wan, L. J., and Guo, Y. G. (2013). Binding SnO_2 nanocrystals in nitrogen-doped graphene sheets as anode materials for lithium-ion batteries. *Adv. Mater.* 25, 2152–2157. doi: 10.1002/adma.201300071

Conflict of Interest Statement: The authors declare that the research was conducted in the absence of any commercial or financial relationships that could be construed as a potential conflict of interest.

frontiers in Chemistry

ORIGINAL RESEARCH
published: 28 May 2019
doi: 10.3389/fchem.2019.00379

Spray-Drying Synthesis of $LiFeBO_3$/C Hollow Spheres With Improved Electrochemical and Storage Performances for Li-Ion Batteries

Yulei Sui[1], Wei Chen[1], Shibao Tang[1], Ling Wu[1], Binjue Wang[1], Huacheng Li[2], Wei Li[3] and Shengkui Zhong[1]**

[1] School of Iron and Steel, Soochow University, Suzhou, China, [2] Citic Dameng Mining Industries Limited, Chongzuo, China, [3] Guangxi Key Laboratory of Electrochemical and Magnetochemical Functional Materials, Guilin University of Technology, Guili, China

$LiFeBO_3$/C cathode material with hollow sphere architecture is successfully synthesized by a spray-drying method. SEM and TEM results demonstrate that the micro-sized $LiFeBO_3$/C hollow spheres consist of $LiFeBO_3$@C particles and the average size of $LiFeBO_3$@C particles is around 50–100 nm. The thickness of the amorphous carbon layer which is coated on the surface of $LiFeBO_3$ nanoparticles is about 2.5 nm. $LiFeBO_3$@C particles are connected by carbon layers and formed conductive network in the $LiFeBO_3$/C hollow spheres, leading to improved electrical conductivity. Meanwhile, the hollow structure boosts the Li^+ diffusion and the carbon layers of $LiFeBO_3$@C particles protect $LiFeBO_3$ from moisture corrosion. Consequently, synthesized $LiFeBO_3$/C sample exhibits good electrochemical properties and storage performance.

Keywords: Li-ion batteries, $LiFeBO_3$, hollow sphere, cathode materials, spray drying

OPEN ACCESS

Edited by:
Juchen Guo,
University of California, Riverside, United States

Reviewed by:
Qiaobao Zhang,
Xiamen University, China
Biao Gao,
Wuhan University of Science and Technology, China

****Correspondence:***
Ling Wu
lwu@suda.edu.cn
Shengkui Zhong
zhongshengkui@suda.edu.cn

Specialty section:
This article was submitted to Electrochemistry, a section of the journal Frontiers in Chemistry

Received: *29 March 2019*
Accepted: *09 May 2019*
Published: *28 May 2019*

Citation:
Sui Y, Chen W, Tang S, Wu L, Wang B, Li H, Li W and Zhong S (2019) Spray-Drying Synthesis of $LiFeBO_3$/C Hollow Spheres With Improved Electrochemical and Storage Performances for Li-Ion Batteries. Front. Chem. 7:379. doi: 10.3389/fchem.2019.00379

INTRODUCTION

With the development of electric vehicles in the twenty-first century, Li-ion batteries (LIBs) play an increasingly important role in modern society (Nayak et al., 2018; Wu et al., 2019) and various cathode materials are developed (Ma et al., 2015; Zheng et al., 2018a,b; Yang et al., 2019). Recently, borate-based materials ($LiMBO_3$, M = Fe, Mn, and Co) have received wide attention in the field of LIBs (Lin et al., 2012; Tao et al., 2013). Compared with the commonly used phosphate-based materials ($LiMPO_4$, M = Fe, Mn, and Co), borate groups ($LiMBO_3$, M = Fe, Mn, and Co) with a low specific weight show higher capacities. For instance, the theoretical capacity of $LiMnBO_3$ is 222 mAh g^{-1}, whereas the phosphate counterpart, $LiMnPO_4$, is limited to 170 mAh g^{-1} (Moskon et al., 2016; Zhang et al., 2017). Moreover, the volume changes of borate-based materials during charging-discharging process are less than those of phosphate-based materials so that they usually show good structural stability (Loftager et al., 2017). Among various borate-based cathode materials, $LiFeBO_3$ with the theoretical capacity of 220 mAh g^{-1} presents moderate working voltage, relatively high intrinsic conductivity, and good structural stability (Michalski et al., 2017). Therefore, $LiFeBO_3$ is considered as a potential cathode material for LIBs. However, there is only one-dimensional (1D) pathway for Li^+ diffusing in the $LiFeBO_3$ crystal, which leading to low electronic and ionic conductivity (Dong et al., 2008; Kalantarian et al., 2013). Furthermore, $LiFeBO_3$ is highly sensitive to moisture so that surface poisoning by H_2O molecules of air would seriously disrupt its electrochemical properties (Gu et al., 2017). These problems make it

challenging to achieve $LiFeBO_3$-based materials with high reversible specific capacity and good storage performance. In order to improve the electrochemical performance of $LiFeBO_3$-based materials, various strategies have been introduced, such as metal-ions doping, conductive carbon coating, and nano-architecturing (Aravindan and Umadevi, 2012; Afyon et al., 2013; Le Roux et al., 2015; Sin et al., 2015). Among these methods, carbon coating is a promising and effective way to improve the properties of $LiFeBO_3$, which attributes to the improved conductivity and the prevention of moisture corrosion. For example, Li et al. reported that the carbon coated $LiFeBO_3$ nanoparticles exhibit the improved first discharge capacities of 190.4 and 106.6 mAh g^{-1} at 0.1 and 1°C rate, respectively (Li et al., 2015). The $LiFeBO_3$/C prepared by Zhang et al. also indicated carbon coating is an effective way to improve the properties of $LiFeBO_3$. However, the rate capability and storage performance of $LiFeBO_3$ are still not satisfied (Zhang et al., 2014). Therefore, achieving homogeneous carbon coated $LiFeBO_3$ cathode materials with high electrochemical properties and good storage performance is still a challenge right now.

Herein, $LiFeBO_3$/C with hollow porous sphere architecture is successfully synthesized by spray-drying method at the temperature as low as 450°C (Li et al., 2015). Amorphous carbon layer which was produced by polyethylene glycol 6,000 (PEG-6000) decomposition is coated on the surface of $LiFeBO_3$ nanoparticles. The $LiFeBO_3$@C particles are connected together and formed $LiFeBO_3$/C hollow porous spheres. The obtained $LiFeBO_3$/C sample with distinctive architecture shows the improved electrochemical and storage performances as cathode for LIBs.

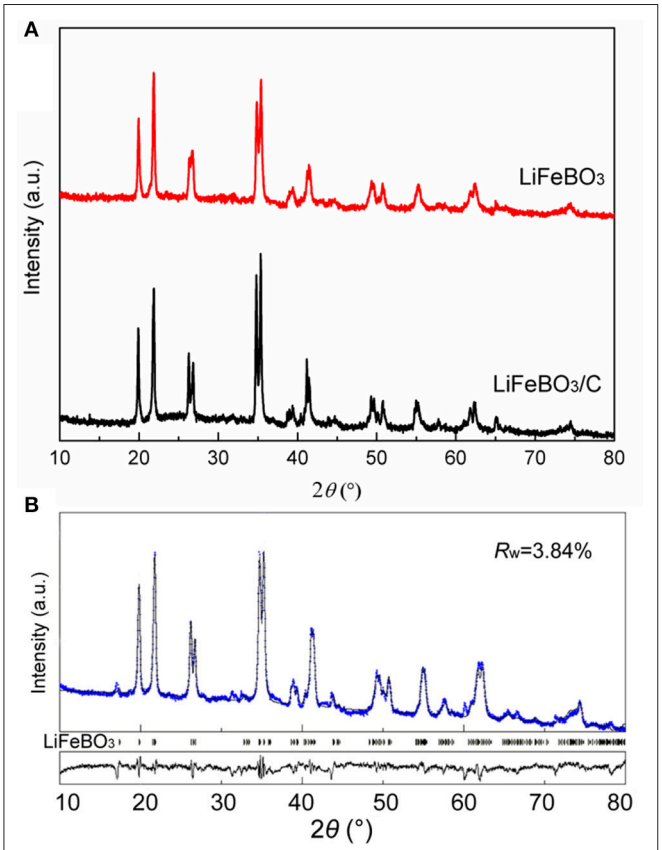

FIGURE 1 | (A) XRD patterns of the as-prepared $LiFeBO_3$/C and $LiFeBO_3$; **(B)** Rietveld refinement XRD pattern of the as-prepared $LiFeBO_3$/C.

TABLE 1 | Results of structural analysis obtained from X-ray Rietveld refinement of $LiFeBO_3$/C.

Atom	Site	*x*	*Y*	*z*	Occupancy
Li1	8f	0.6175	0.5429	0.1539	0.48
Li2	8f	0.6573	0.4782	0.0605	0.52
Fe1	8f	0.1372	0.3332	0.1392	0.72
Fe2	8f	0.1835	0.3435	0.0915	0.28
B1	8f	0.1592	0.6431	0.1043	1
O1	8f	0.3877	0.1737	0.0891	1
O2	8f	0.7673	0.3031	0.1497	1
O3	8f	0.3229	0.5376	0.1216	1
Lattice parameters		a (Å)	b (Å)	c (Å)	β (°)
Sample		5.1662	8.9141	10.1700	91.25

EXPERIMENTAL

Synthesis of $LiFeBO_3$/C and $LiFeBO_3$

Firstly, $LiNO_3$, 1.38g $LiNO_3$, 8.08g $Fe(NO_3)_3{\cdot}9H_2O$, and 1.24g H_3BO_3 were weighed and dissolved gradually in deionized water under stirring, and the mixed solution was named solution A. Meanwhile, 1.22 g PEG-6000 was dropped and dissolved in deionized water under stirring to form solution B. Then the solution B was added into the solution A and stirred carefully. A homogeneous sol was obtained when the mixed solution has been stirred at 80°C for 1 h. The precursor of $LiFeBO_3$/C was synthesized using the obtained sol as raw material via a spray drying process. The inlet and outlet air temperatures are 200 and

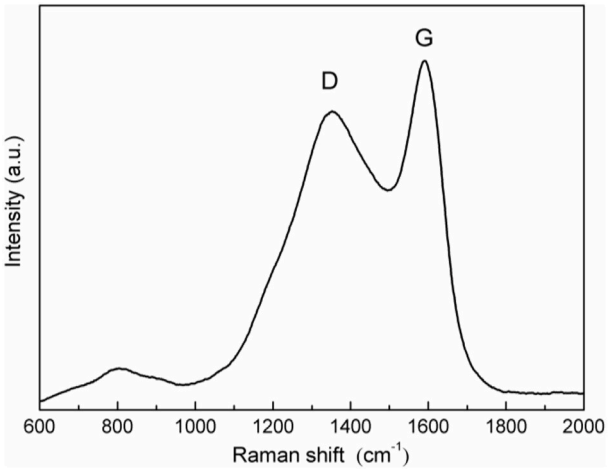

FIGURE 2 | Raman spectra of the as-prepared $LiFeBO_3$/C.

100°C during the spray drying process with the air pressure of 0.25 MPa. The as-obtained precursor was calcined at 350°C (3 h), followed by crystallized at 450°C for 10 h in an argon atmosphere, and the final $LiFeBO_3$/C was obtained. For contrast, the $LiFeBO_3$ sample was also prepared by the similar synthetic process but without PEG-6000. All the chemical regents employed in this work were of analytic grade.

Characterization

The structure of $LiFeBO_3$/C and $LiFeBO_3$ samples was investigated by XRD (Rigaku/Ultima-IV) and Raman micro-spectroscopy. And the range of XRD and Raman spectroscopic analysis is $2\theta = 10 \sim 80^\circ$ and 600–2,000 cm^{-1}, respectively. Morphology and microstructure of $LiFeBO_3$/C and $LiFeBO_3$ samples were investigated by SEM (JSM/6380LV) and TEM (TecnaiG220). C-S analysis (Eltar) was used to determine the carbon content of samples.

Electrochemical Measurements

The electrochemical measurements were performed in coin-type cells (CR2025) with lithium metal as the negative electrode. The positive electrodes were prepared by mixing as-prepared $LiFeBO_3$/C or $LiFeBO_3$ powder, acetylene black (99.9%, Sinopharm Chemial Reagent Co., Ltd.) and polyvinylidene fluoride (PVDF, 99.9%, Sinopharm Chemial Reagent Co., Ltd. the weight ratio is 80:10:10) in N-methylpyrolline onto an Al foil and dried at 120°C for 4 h in vacuum oven. Then the coin-type cells were assembled in a glove box filled with high purity argon. 1M $LiPF_6$ solution in a mixture of ethylene carbonate and dimethyl carbonate with 1:1 volumetric ratio was used as electrolyte (Sinopharm Chemial Reagent Co., Ltd.). The cells

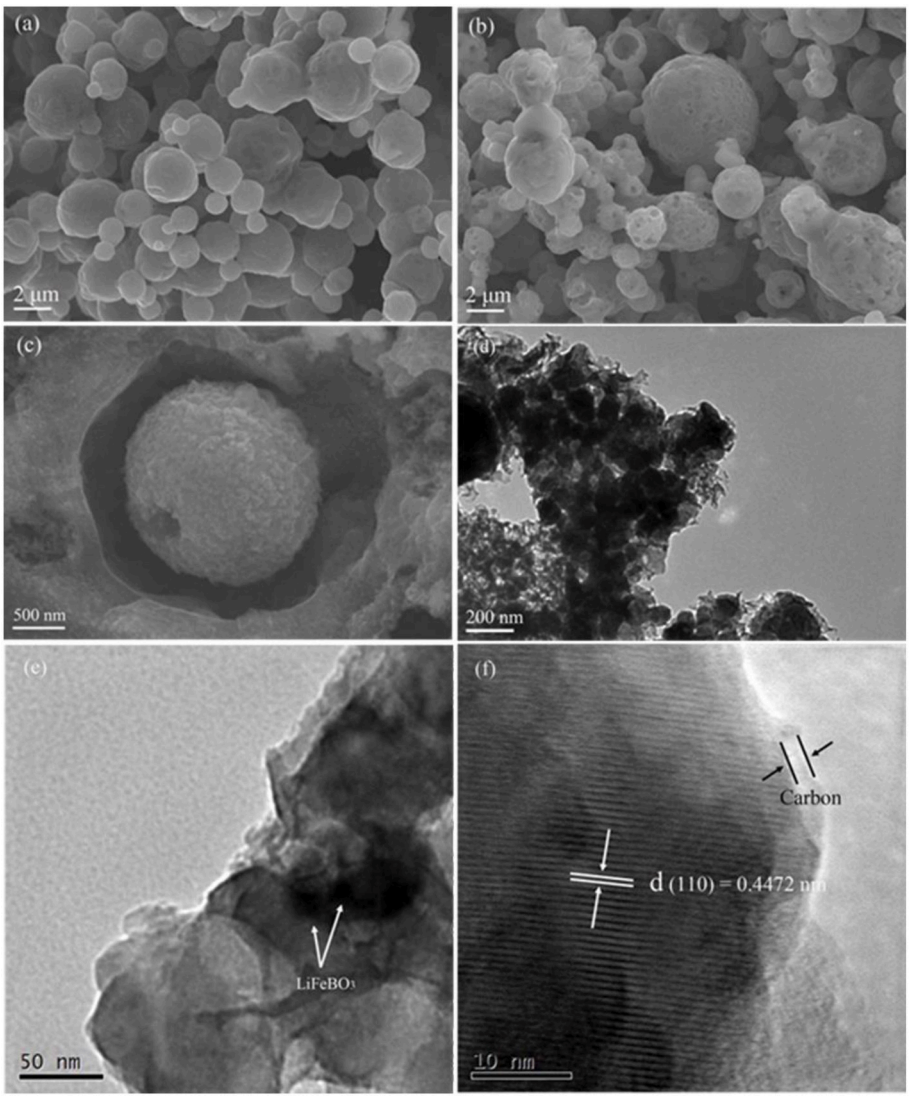

FIGURE 3 | SEM images of the as-prepared $LiFeBO_3$ **(a)** and $LiFeBO_3$/C **(b,c)**; TEM images of the as-prepared $LiFeBO_3$/C **(d–f)**.

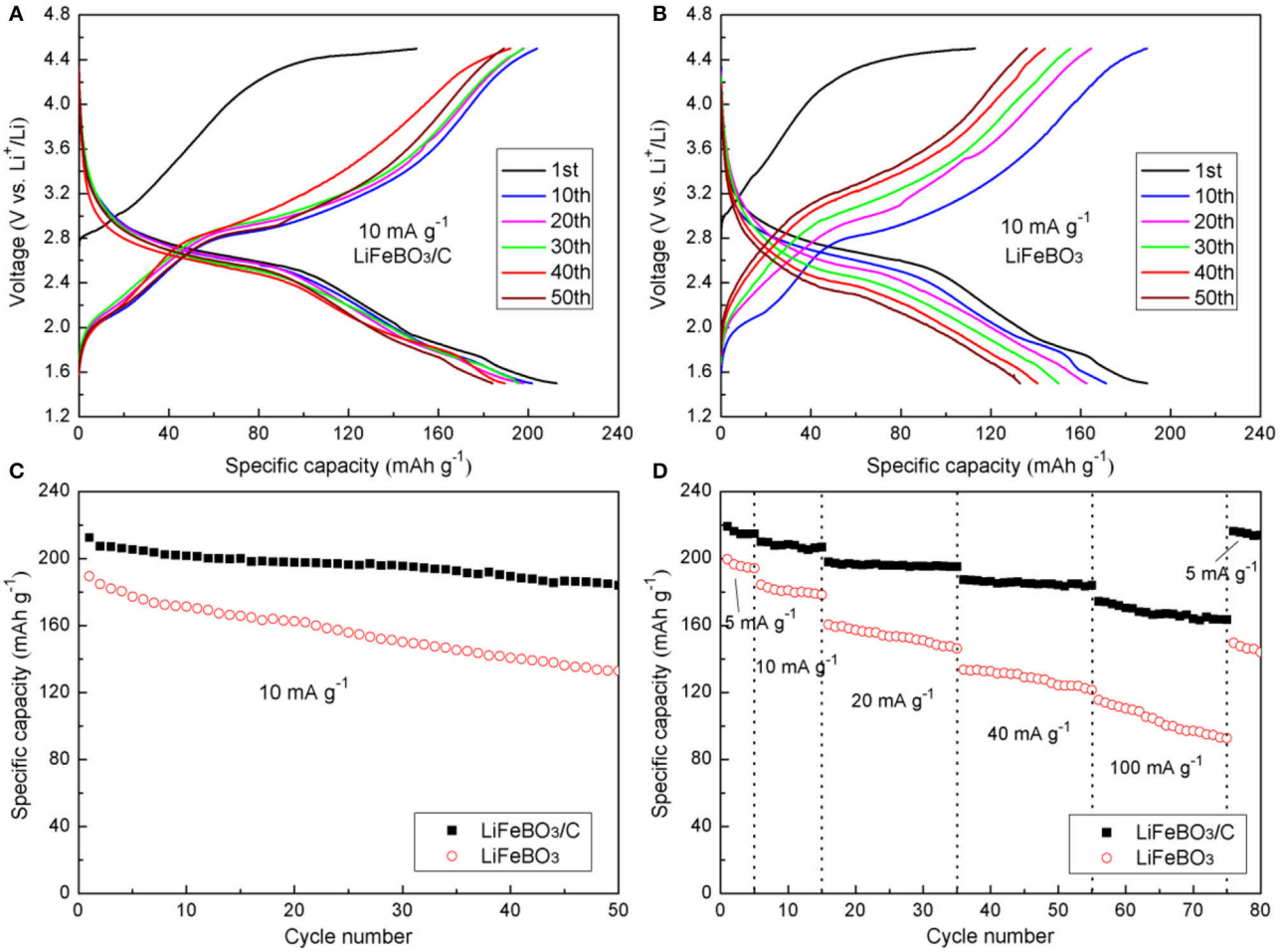

FIGURE 4 | Charge-discharge curves of the $LiFeBO_3$/C **(A)** and $LiFeBO_3$ **(B)** at the current density of 10 mA g^{-1}; **(C)** Cycle performance of $LiFeBO_3$/C and $LiFeBO_3$ at the current density of 10 mA g^{-1}; **(D)** Rate capability of $LiFeBO_3$/C and $LiFeBO_3$ at various current densities.

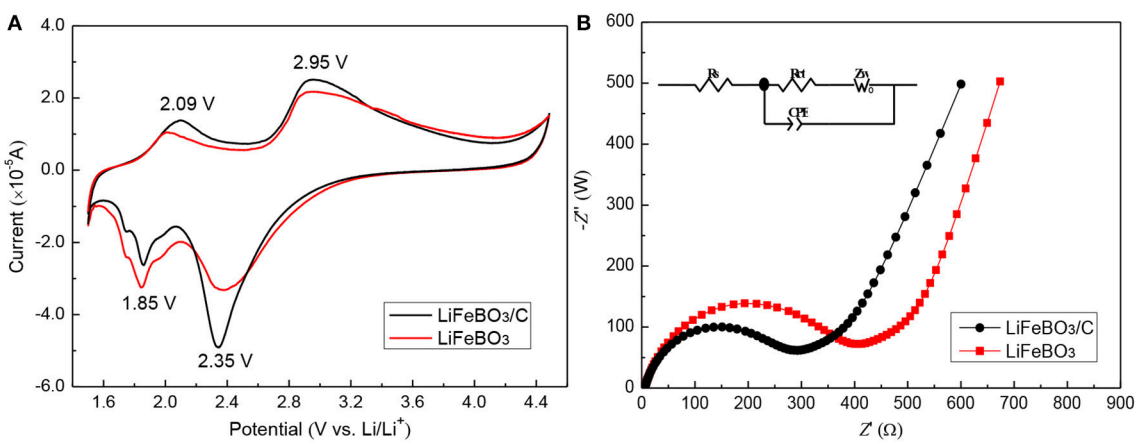

FIGURE 5 | (A) Cyclic voltammetry profiles of $LiFeBO_3$/C and $LiFeBO_3$ at the scan rate of 0.1 mV s^{-1}; **(B)** Electrochemical impedance spectra of as-prepared $LiFeBO_3$/C and $LiFeBO_3$.

were tested in the voltage range of 1.5–4.5 V under various charge/discharge current densities from 5 to 100 mA g^{-1} at room temperature. The electrochemical impedance spectroscopy (EIS) and the cyclic voltammetry (CV) was both measured by a CHI 660D workstation.

RESULTS AND DISCUSSION

XRD patterns of the synthesized LiFeBO$_3$/C and LiFeBO$_3$ samples are shown in **Figure 1A**. Obviously, the LiFeBO$_3$ with monoclinic structure is well-crystallized. XRD patterns of two samples are similar, indicating the combination of LiFeBO$_3$ and carbon has little influence on the crystal structure. Although the amount of carbon in the LiFeBO$_3$/C composites is 4.9 wt. % (proved by C-S analysis), the diffraction peak of carbon is not detected from the XRD patterns, implying the carbon in the LiFeBO$_3$/C composite is amorphous.

In order to further clarify the crystal structure and lattice parameters of the synthesized LiFeBO$_3$/C, XRD data was refined by Rietveld method (Rietveld, 1967) using Maud software (Lutterotti, 2011), and the Rietveld refinement XRD pattern and atoms positions and occupancy for Li and Fe atoms in LiFeBO$_3$/C investigated. As can be seen from **Figure 1B** and **Table 1**, the sharp peaks of the sample can be identified as monoclinic LiFeBO$_3$ with space group of C2/c and the structure is crystallized well. Meanwhile, the observed and calculated patterns match well, and the reliability factors are good. In accordance with the refinement results, the lattice parameters of LiFeBO$_3$ are $a = 5.1662$ Å, $b = 8.9141$ Å, $c = 10.1700$ Å, $\beta = 91.25^{\circ}$, agreeing well with the reported literature (Zhang et al., 2014).

Figure 2 represents the Raman spectroscopy of the as-prepared LiFeBO$_3$/C sample. As can be seen from **Figure 2**, the broad peak observed at 1,354 cm^{-1} correspond to the D (disordered) band of carbon while the broad peak located at 1,590 cm^{-1} agreeing well with G (graphitized) band of sp^2 type carbon (Liu et al., 2015; Zhu et al., 2017). The strong D-peak further reveals that the carbon is amorphous, which is in agreement with the XRD result.

SEM and TEM were employed to analyze morphology and micro-structure of the synthesized LiFeBO$_3$ and LiFeBO$_3$/C. As shown in **Figure 3a**, the LiFeBO$_3$ sample displays a spherical shape with a size distribution in the range of 1–4 μm and the surface is compact. While, the LiFeBO$_3$/C sample exhibits hollow spherical shape with a rough and porous surface layer (**Figures 3b,c**). The comparison of the darker outer shell and the lighter central regions indicates that the LiFeBO$_3$/C spheres present porous and hollow internal structure (**Figure 3d**), which is consistent with the SEM results. As shown in **Figure 3c**, it is obvious that the spherical LiFeBO$_3$/C are actually consist of numerous primary nanoparticles. **Figure 3e** shows that nano-sized primary LiFeBO$_3$ particles are well wrapped by thick carbon layer. This carbon-coated layer is benefit to prevent LiFeBO$_3$ from moisture corrosion. As we can see from **Figure 3f**, the lattice fringe with an interior planar distance of 0.4472 nm is correspond well to (1 1 0) crystal planes of LiFeBO$_3$. The coating layer with the thickness of 2.5 nm could be assigned to the amorphous carbon, so that LiFeBO$_3$@C shows a core-shell structure. In addition, the carbon-coated layer and conductive carbon network can improve the conductivity of LiFeBO$_3$-based cathode material, which is also benefit to the electrochemical performances.

TABLE 2 | Parameters obtained from equivalent circuit fitting of EIS data.

Sample	R_s(Ω)	R_{ct}(Ω)	j_o(mA cm^{-2})
LiFeBO$_3$	6.03	354.12	7.26×10^{-5}
LiFeBO$_3$/C	5.79	238.60	10.78×10^{-5}

In the potential (*vs.* Li/Li$^+$) range of 1.5–4.5 V, the cells were charged/discharged at 10 mA g^{-1}, and the curves of the as-synthesized LiFeBO$_3$/C and LiFeBO$_3$ samples are exhibited in **Figures 4A,B**, respectively. It is noted that the initial charge curves of both samples show obviously higher voltage plateau than the subsequent cycles, which mainly due to the high polarization before cycling. This phenomenon is very similar to cases of LiMnBO$_3$ and LiCoBO$_3$ (Afyon et al., 2014; Tang et al., 2015). The charge plateau (∼3.2 V) and the discharge plateau (∼2.8 V) in the voltage profiles correspond to the plateaus of LiFeBO$_3$. There is a reduced thermodynamic potential for the degraded LiFeBO$_3$ phase so that a short discharge plateau ∼1.8 V appeared in the discharge profiles (Bo et al., 2012).

The cycling performances of the as-prepared LiFeBO$_3$/C and LiFeBO$_3$ samples at 10 mA g^{-1} are shown in **Figure 4C**. The initial discharge specific capacities of LiFeBO$_3$/C and LiFeBO$_3$ are 212.4 and 189.5 mAh g^{-1}, respectively. The specific capacity of LiFeBO$_3$/C is as high as 184.1 mAh g^{-1} while the specific capacity of LiFeBO$_3$ is only 132.9 mAh g^{-1} after 50 cycles, indicating the LiFeBO$_3$/C sample has a better cyclic stability. **Figure 4D** displays the rate capability of the as-prepared LiFeBO$_3$/C and LiFeBO$_3$ samples under different current densities. The initial capacity of the as-prepared LiFeBO$_3$/C is 219.2 mAh g^{-1} at 5 mA g^{-1}, which is approximately 98.7% of the theoretical capacity. When the current density is increased up to 40 and 100 mA g^{-1}, the LiFeBO$_3$/C sample holds a stable reversible capacity of 187.3 and 175.8 mAh g^{-1}, respectively. However, the discharge capacity of LiFeBO$_3$ at 40 and 100 mA g^{-1} are only 144.5 and 115.5 mAh g^{-1}, respectively. If the current density returns back to 5 mA g^{-1} after 75 cycles test, and 98.6% of the initial discharge specific capacity (216.3 mAh g^{-1}) can be recovered for LiFeBO$_3$/C but only 75.1% was recovered for LiFeBO$_3$ electrode (149.6 mAh g^{-1}), implying the LiFeBO$_3$/C sample has a better capacity recovery ability than LiFeBO$_3$. The improved electrochemical performances can be attributed to the special hollow sphere structure and network of amorphous carbon layer. The conductivity is improved by the network of amorphous carbon layer and the volume expansion during the charge and discharge progresses is againsted due to the special hollow sphere architecture provides a flexible structure, so that the electrochemical performance of the synthesized cathode is improved (Li et al., 2013).

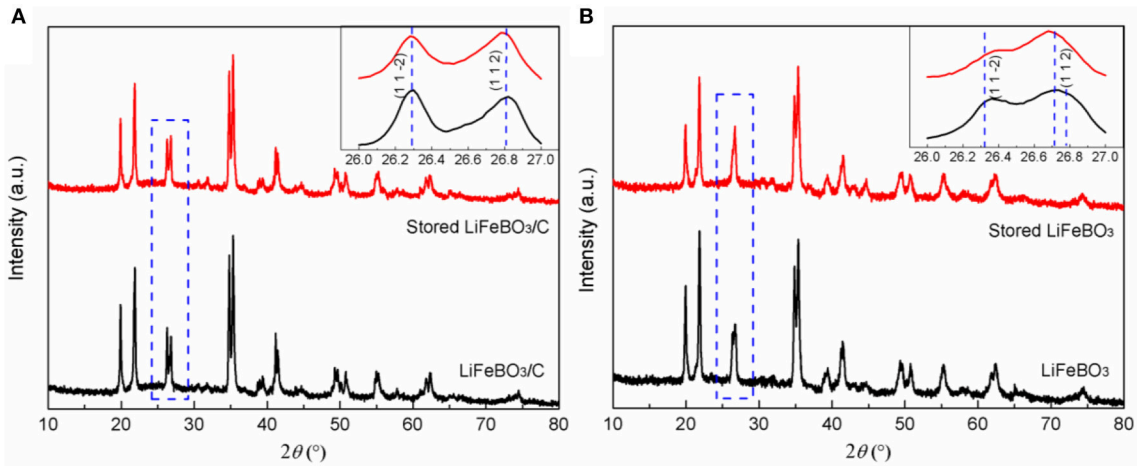

FIGURE 6 | XRD patterns of LiFeBO$_3$/C **(A)** and LiFeBO$_3$ **(B)** before and after storing for 6 months (air exposure at room temperature).

Figure 5A shows the cyclic voltammetry (CV) of the as-prepared LiFeBO$_3$/C and LiFeBO$_3$ samples. The oxidation/reduction peaks located at ∼2.95/2.35 V correspond to the phase transition between LiFeBO$_3$ and FeBO$_3$. It is clearly observed that LiFeBO$_3$/C sample shows sharper peaks and larger areas than LiFeBO$_3$, implying the synthesized LiFeBO$_3$/C has a better reversibility. In addition, a couple of oxidation/reduction peaks are located at ∼2.09/1.85 V, and these patterns can be ascribed to the degradation of LiFeBO$_3$ (Afyon et al., 2014).

In order to analyze the conductivity of the as-prepared LiFeBO$_3$/C and LiFeBO$_3$ samples, the EIS tests (**Figure 5B**) are measured in our study. Then the EIS data is fitted with Z-view software using an equivalent circuit, and the related parameters are listed in **Table 2**. R_s, Z_w, and R_{ct} in the equivalent circuit (insert **Figure 5B**) represent the resistance of the electrolyte, Warburg impedance and charge transfer resistance, respectively. The R_{ct} of LiFeBO$_3$/C (238.6 Ω) is lower than that of LiFeBO$_3$ (354.1 Ω), implying the charge transfer speed during the charge and discharge processes of electrode is significantly improved. The exchange current density (j_0) of synthesized LiFeBO$_3$/C and LiFeBO$_3$ is calculated by the following equation, respectively.

$$j_0 = \frac{RT}{nFR_{ct}}$$

Where T and n refer to the temperature and the electrons number, respectively. The exchange current density (j_0) of LiFeBO$_3$/C (10.78×10^{-4} mA cm^{-2}) is higher than that of LiFeBO$_3$ (7.26×10^{-5} mA cm^{-2}), which indicates that LiFeBO$_3$/C has a better electrode reaction reversibility than LiFeBO$_3$.

To evaluate the storage stability, LiFeBO$_3$/C and LiFeBO$_3$ samples were stored in air exposure for 6 months. XRD patterns of the LiFeBO$_3$/C and LiFeBO$_3$ samples before and after storage are shown in **Figure 6**. Gratifyingly, the stored LiFeBO$_3$/C sample also remains its original crystal structure, verifying high storage stability of LiFeBO$_3$/C, as shown in **Figure 6A**. However, the XRD pattern of LiFeBO$_3$ changed after storing 6 months. As can be seen from **Figure 6B**, the intensity of (1 1 2) peak tends to increase while the intensity of (1 1 2) peak tends to decrease, and the two peaks prone to overlap each other. This phenomenon can be attributed to phase changing of LiFeBO$_3$ from monoclinic to orthorhombic structure with air corrosion (Bo et al., 2012; Chen et al., 2015).

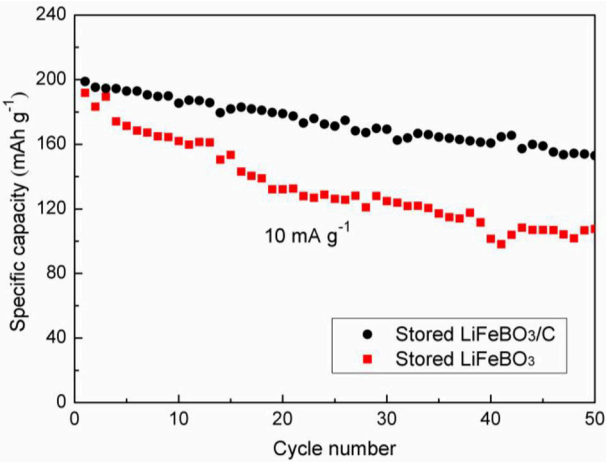

FIGURE 7 | Cycling performances of the LiFeBO$_3$/C and LiFeBO$_3$ after storing for 6 months.

After 6 months of storage, the cycling performances of LiFeBO$_3$/C and LiFeBO$_3$ samples are investigated, and the results are shown in **Figure 7**. The capacity of the stored LiFeBO$_3$/C is as high as 198.9 mAh g^{-1} and there is 76.9% capacity retention after 50 cycles. However, the

stored $LiFeBO_3$ delivers a capacity of 191.7 mAh g^{-1} and only 56.1% capacity retention after 50 cycles. Obviously, the stored $LiFeBO_3$/C shows higher stability and cycling performance than the stored $LiFeBO_3$. In summary, carbon coating and structural modification improve the conductivity of $LiFeBO_3$, shorten the Li^+ diffusion/conduction path and protect $LiFeBO_3$ from moisture corrosion, thus leading to good electrochemical performance.

CONCLUSIONS

$LiFeBO_3$/C hollow sphere is successfully synthesized by a facile spray-drying method. Primary $LiFeBO_3$@C particles are connected by carbon layers and formed $LiFeBO_3$/C hollow spheres with improved electrical conductivity. Meanwhile, the hollow porous structure boosts the Li^+ diffusion and the carbon layers of $LiFeBO_3$@C particles protect $LiFeBO_3$ from moisture corrosion. Therefore, the synthesized $LiFeBO_3$/C sample shows good electrochemical performances and improved storage performance. This work is conducive to obtaining promising and high-performance cathode materials for LIBs.

DATA AVAILABILITY

The raw data supporting the conclusions of this manuscript will be made available by the authors, without undue reservation, to any qualified researcher.

AUTHOR CONTRIBUTIONS

YS, ST, and WC did the main experiment and write the manuscript. LW and BW envolved the discussion of the experiment and revised the manuscript. HL and WL assisted the material synthesis. LW and SZ made the research plan. SZ and LW also provided the financial support.

FUNDING

This study was supported by the National Natural Science Foundation of China (51574168, 51574170, and 51774207), Guangxi Key Laboratory of Electrochemical and Magnetochemical Functional Materials (EMFM20182202), and Major Projects for Science & Technology Development of Guangxi Province, China (AA16380043).

REFERENCES

Afyon, S., Kundu, D., Krumeich, F., and Nesper, R. (2013). Nano-$LiMnBO_3$, a high-capacity cathode material for Li-ion batteries. *J. Power Sources* 224, 145–151. doi: 10.1016/j.jpowsour.2012.09.099

Afyon, S., Mensing, C., Krumeich, F., and Nesper, R. (2014). The electrochemical activity for nano-$LiCoBO_3$ as a cathode material for Li-ion batteries. *Solid State Ionics* 256, 103–108. doi: 10.1016/j.ssi.2014.01.010

Aravindan, V., and Umadevi, M. (2012). Synthesis and characterization of novel $LiFeBO_3$/C cathodes for lithium batteries. *Ionics* 18, 27–30. doi: 10.1007/s11581-011-0594-7

Bo, S. H., Wang, F., Janssen, Y., Zeng, D. L., Nam, K. W., Xu, W. Q., et al. (2012). Degradation and (de)lithiation processes in the high capacity battery material $LiFeBO_3$. *J. Mater. Chem.* 22, 8799–8809. doi: 10.1039/c2jm16436a

Chen, Z. X., Cao, L. F., Chen, L., Zhou, H. H., Zheng, C. M., Xie, K., et al. (2015). Mesoporous $LiFeBO_3$/C hollow spheres for improved stability lithium ion battery cathodes. *J. Power Sources* 298, 355–362. doi: 10.1016/j.jpowsour.2015.08.073

Dong, Y. Z., Zhao, Y. M., Shi, Z. D., An, X. N., Fu, P., and Chen, L. (2008). The structure and electrochemical performance of $LiFeBO_3$ as a novel Li-battery cathode material. *Electrochim. Acta*. 53, 2339–2345. doi: 10.1016/j.electacta.2007.09.050

Gu, X. F., Ting, M., and Zhi, S. (2017). Sol-gel synthesis of nanostructure $LiFeBO_3$/C lithium-ion cathode materials with high storage capacity. *J. Sol-Gel. Sci. Techn.* 81, 362–366. doi: 10.1007/s10971-016-4264-0

Kalantarian, M. M., Asgari, S., and Mustarelli, P. (2013). A theoretical approach to evaluate the rate capability of Li-ion battery cathode materials. *J. Mater. Chem. A* 2, 107–115. doi: 10.1039/C3TA13387G

Le Roux, B., Bourbon, C., Lebedev, O. I., Colin, J. F., and Pralong, V. (2015). Synthesis and characterization of the $LiMnBO_3$-$LiCoBO_3$ solid solution and its use as a lithium-ion cathode material. *Inorg. Chem.* 54, 5273–5279. doi: 10.1021/acs.inorgchem.5b00260

Li, S. L., Xu, L. Q., Li, G. D., Wang, M., and Zhai, Y. J. (2013). *In-situ* controllable synthesis and performance investigation of carbon-coated monoclinic and hexagonal $LiMnBO_3$ composites as cathode materials in lithium-ion batteries. *J. Power Sources* 236, 54–60. doi: 10.1016/j.jpowsour.2013.02.027

Li, Z., Wang, Y., Hu, Q., Yang, Y., Wu, Z., and Ban, C. (2015). Improved electrochemical performance of carbon-coated $LiFeBO_3$ nanoparticles for lithium-ion batteries. *J. Nanosci. Nanotechno.* 15, 7186–7190. doi: 10.1166/jnn.2015.10555

Lin, Z. P., Zhao, Y. J., and Zhao, Y. M. (2012). First-principles study of the structural, magnetic, and electronic properties of $LiMBO_3$ (M=Mn, Fe, Co). *Phys. Lett. A* 376, 179–184. doi: 10.1016/j.physleta.2011.08.018

Liu, Y., Xu, X., Wang, M., Lu, T., Sun, Z., and Pan, L. (2015). Nitrogen-doped carbon nanorods with excellent capacitive deionization ability. *J. Mater. Chem. A* 3, 17304–17311. doi: 10.1039/C5TA 03663A

Loftager, S., Garcialastra, J. M., and Vegge, T. (2017). A density functional theory study of the carbon-coating effects on lithium iron borate battery electrodes. *Phys. Chem. Chem. Phys.* 19, 2087–2094. doi: 10.1039/C6CP06312H

Lutterotti, L. (2011). *Maud version 2.91*. Avliable online at: https://www.softpedia.com/get/Science-CAD/Maud.shtml (accessed March, 2019)

Ma, T., Muslim, A., and Su, Z. (2015). Microwave synthesis and electrochemical properties of lithium manganese borate as cathode for lithium ion batteries. *J. Power Sources* 282, 95–99. doi: 10.1016/j.jpowsour.2015.02.013

Michalski, P. P., Pietrzak, T. K., Nowinski, J. L., Wasiucionek, M., and Garbarczyk, J. E. (2017). Novel nanocrystalline mixed conductors based on $LiFeBO_3$ glass. *Solid State Ionics* 302, 40–44. doi: 10.1016/j.ssi.2016.12.002

Moskon, J., Pivko, M., Jerman, I., Tchernychova, E., Zabukovec Logar, N., Selih, V. S., et al. (2016). Cycling stability and degradation mechanism of $LiMnPO_4$ based electrodes. *J. Power Sources* 303, 97–108. doi: 10.1016/j.jpowsour.2015.10.094

Nayak, P. K., Yang, L., Brehm, W., and Adelhelm, P. (2018). From Lithium-ion to sodium-ion batteries: advantages, challenges, and surprises. *Angew. Chem. Int. Edit.* 57, 102–120. doi: 10.1002/anie.201703772

Rietveld, H. M. (1967). Line profiles of neutron powder-diffraction peaks for structure refinement. *Acta Cryst.* 22, 151–152. doi: 10.1107/S0365110X67000234

Sin, B. C., Singh, L., Lee, K. E., Kim, M., Cho, M., Yarger, J. L., et al. (2015). Enhanced electrochemical performance of $LiFe_{0.4}Mn_{0.6}(PO_4)_{1-x}(BO_3)_x$ as cathode material for lithium ion batteries. *J. Electroanal. Chem.* 756, 56–60. doi: 10.1016/j.jelechem.2015.08.012

Tang, A. P., He, D. H., He, Z. Q., Xu, G. R., Song, H. S., and Peng, R. H. (2015). Electrochemical performance of $LiMnBO_3$/C composite synthesized by a combination of impregnation and precipitation followed by annealing. *J. Power Sources* 275, 888–892. doi: 10.1016/j.jpowsour.2014.11.087

Tao, L., Neilson, J. R., Melot, B. C., Mcqueen, T. M., Masquelier, C., and Rousse, G. (2013). Magnetic structures of $LiMBO_3$ (M = Mn, Fe, Co) lithiated transition metal borates. *Inorg. Chem*. 52, 11966–11974. doi: 10.1021/ic401671m

Wu, L., Zheng, J., Wang, L., Xiong, X., Shao, Y., Wang, G., et al. (2019). PPy-encapsulated SnS_2 nanosheets stabilized by defects on a TiO_2 support as a durable anode material for lithium-ion batteries. *Angew. Chem. Int. Edit*. 58, 811–815. doi: 10.1002/anie.201811784

Yang, H., Wu, H. H., Ge, M., Li, L., Yuan, Y., Yao, Y., et al. (2019). Simultaneously dual modification of Ni-rich layered oxide cathode for high-energy lithium-ion batteries. *Adv. Funct. Mater*. 29:1808825. doi: 10.1002/adfm.201808825

Zhang, B., Ming, L., Zheng, J. C., Zhang, J. F., Shen, C., Han, Y. D., et al. (2014). Synthesis and characterization of multi-layer core-shell structural $LiFeBO_3$/C as a novel Li-battery cathode material. *J. Power Sources* 261, 249–254. doi: 10.1016/j.jpowsour.2014.03.082

Zhang, B., Zhu, Y. S., Yu, W. J., Zhang, J. F., and An, C. S. (2017). Facile synthesis of carbon-encapsulated $LiMnBO_3$ composite by the sol-gel method as a lithium-ion battery cathode material. *J. Alloys. Compd*. 704, 343–347. doi: 10.1016/j.jallcom.2017.02.058

Zheng, J. C., Yang, Z., He, Z. J., Tong, H., Yu, W. J., and Zhang, J. F. (2018a). In situ formed $LiNi_{0.8}Co_{0.15}Al_{0.05}O_2$@$Li_4SiO_4$ composite cathod material with high rate capability and long cycling stability for lithium-ion batteries. *Nano Energy* 53, 613–621. doi: 10.1016/j.nanoen.2018.09.014

Zheng, J. C., Yang, Z., Wang, P. B., Tang, L. B., An, C. S., and He, Z. J. (2018b). Multiple linkage modification of lithium-rich layered oxide $Li_{1.2}Mn_{0.54}Ni_{0.13}Co_{0.13}O_2$ for lithium ion battery. *ACS Appl. Mater. Inter*. 10, 31324–31329. doi: 10.1021/acsami.8b09256

Zhu, Y. E., Yang, L. P., Sheng, J., Chen, Y. N., Gu, H. C., Wei, J. P., et al. (2017). Fast sodium storage in TiO_2@CNT@C nanorods for high-performance Na-ion capacitors. *Adv. Energy Mater*. 7:1701222. doi: 10.1002/aenm.201701222

Conflict of Interest Statement: The authors declare that the research was conducted in the absence of any commercial or financial relationships that could be construed as a potential conflict of interest.

frontiers in Chemistry

ORIGINAL RESEARCH
published: 14 June 2019
doi: 10.3389/fchem.2019.00432

Fabrication of $Li_4Ti_5O_{12}$@CN Composite With Enhanced Rate Properties

Hui Xiao[1], Xiaobing Huang[2], Yurong Ren[1]*, Xiang Ding[2] and Shibiao Zhou[2]*

[1] School of Materials Science and Engineering, Jiangsu Collaborative Innovation Center of Photovolatic Science and Engineering, Changzhou University, Changzhou, China, [2] Hunan Province Cooperative Innovation Center for The Construction and Development of Dongting Lake Ecological Economic Zone, College of Chemistry and Materials Engineering, Hunan University of Arts and Science, Changde, China

Folic acid is first time applied as a carbon-nitrogen precursor to fabricate $Li_4Ti_5O_{12}$@CN composites via ball milling Nano-TiO_2, Li_2CO_3 and folic acid with ethanol as solvent, and then followed by heating treatment in argon. XRD, SEM, TEM, XPS, charge-discharge test and EIS are used to evaluate the influence of N-doped carbon coating on its structure, morphologies and electrochemical property. It is demonstrated that the N-doped carbon coated $Li_4Ti_5O_{12}$ composite exhibits superior high-rate performance compared with pure $Li_4Ti_5O_{12}$. It possesses a high discharge capacity of 174, 165 mAh g^{-1} at 0.5 and 10 C, respectively. Additionally, an initial specific capacity of 96.2% is obtained after 200 cycles at 10 C. The remarkable performance might be put down to the N-doped carbon layer providing efficiently electron conductive network and nanosized decreasing lithium ion diffusion path.

Keywords: Li-ion batteries, anode material, folic acid, $Li_4Ti_5O_{12}$, N-doped carbon coating

OPEN ACCESS

Edited by:
Junchao Zheng,
Central South University, China

Reviewed by:
Zhian Zhang,
Central South University, China
Ling Wu,
Soochow University, China

****Correspondence:***
Xiaobing Huang
hxb220170@126.com
Yurong Ren
ryrchem@163.com

Specialty section:
This article was submitted to Electrochemistry, a section of the journal Frontiers in Chemistry

Received: *20 March 2019*
Accepted: *27 May 2019*
Published: *14 June 2019*

Citation:
Xiao H, Huang X, Ren Y, Ding X and Zhou S (2019) Fabrication of $Li_4Ti_5O_{12}$@CN Composite With Enhanced Rate Properties. Front. Chem. 7:432. doi: 10.3389/fchem.2019.00432

INTRODUCTION

In the past few years, carbon materials have been regarded as the most commercially valued lithium battery anode material (Ma et al., 2016; Long et al., 2017; Li et al., 2019; Wu et al., 2019). Unfortunately, its low lithiation potential (~0.2 V vs. Li^+/Li) will result in the activation of dendritic lithium, thus further creating safety problems. Moreover, insufficient diffusion coefficient of lithium ion and large volume change will result in poor rate performance and cycle stability (Han et al., 2018; Yi et al., 2018). Therefore, it is essential to find alternative anodes with excellent electrochemical properties and outstanding safety characteristics. Among the reported alternative candidates, Spinel lithium titanium ($Li_4Ti_5O_{12}$) is suggested as a potential anode material used in lithium-ion batteries (LIBs) due to the following reasons: (i) The higher flat discharge and charge plateau (1.55 V vs. Li^+/Li) can prevent lithium metal dendrites from evolving during the electrochemical reaction process (Wang S. et al., 2017). (ii) Small volume expansion provides superior cycle stability and reversibility among charge and discharge process (Tian et al., 2017; Wang Q. et al., 2017). Nevertheless, its small lithium ion diffusion coefficients (10^{-9} ~10^{-13} cm^2 S^{-1}) and weak electrical conductivity (~10^{-13} S cm^{-1}) (Jiang et al., 2017), resulting in serious electrode polarization and poor capability at high current density, has been considered as the main bottleneck of its commercial application for high-power LIBs. In order to overcover this problem, several strategies have been suggested by researchers, including synthesis of $Li_4Ti_5O_{12}$ with porous structure (Lu et al., 2017), coating the surface of $Li_4Ti_5O_{12}$ particles with conductive materials

(Tang et al., 2017), construction of nanoscale particle size (Chiu et al., 2017), and introduction of metal and nonmetal ion into $Li_4Ti_5O_{12}$ (Chen et al., 2017; Cheng et al., 2017; Liang et al., 2017).

Thin carbon coating on the surface of $Li_4Ti_5O_{12}$ particles has been considered as an effective method to enhance its electrochemical properties in all reported literatures, since the carbon coating can both improve the surface electron conductivity and inhibit the growth of primary particles in the heat treatment process, this further leads to faster lithium ion diffusion. Very recently, the introduction of nitrogen-doped carbon to modify the electrode materials has been received more and more attention. It is well-known that N atoms can provide additional electrons to further increase the conductivity of the coated carbon layer (Jiang et al., 2017; Xu et al., 2017).In addition, N-doped is favorable to reduce the barrier of energy of lithium-ion penetration and enhance reaction sites (Xiong et al., 2018). We have just proposed folic acid as a new carbon nitrogen precursor to prepare $Na_3V_2(PO_4)_3$@CN composite material, it possesses excellent rate performance and excellent cycling performance when used as cathode electrode of sodium ion batteries. In this work, a similar strategy was suggested to prepared $Li_4Ti_5O_{12}$@CN composite. It is well-expected that the as-prepared $Li_4Ti_5O_{12}$@CN sample will possess excellent electrochemical characters.

EXPERIMENTAL

Material Preparation

$Li_4Ti_5O_{12}$@CN composite was synthesized via a solid-state process, and the detail process was described as following. Firstly, 2.2281 g of Li_2CO_3 (99.5%),5.9985 g of TiO_2 (99.9%) and 1 g of folic acid were mixed by ball milling in ethyl alcohol for 6 h. Secondly, the solvent was evaporated by drying the ready-prepared mixture at 80°C for 2 h. Thirdly, the synthesized precursor was heated under argon atmosphere at 750°C for 8 h. For comparison, pure $Li_4Ti_5O_{12}$ was also synthesized via the similar method without using folic acid as the starting material.

Characterization of Materials

X-ray diffraction instrument was used to investigate the structure and composition of both as-prepared $Li_4Ti_5O_{12}$ samples. The surface chemical states of $Li_4Ti_5O_{12}$@CN were identified by XPS. SEM was used for observing morphologies of the two ready-prepared $Li_4Ti_5O_{12}$ samples. N-doped carbon layer was further investigated by TEM. Elemental analyzer was carried out to investigate the content of carbon and nitrogen for $Li_4Ti_5O_{12}$@CN composite. Four-point probe method was used to investigate the electronic conductivities of both $Li_4Ti_5O_{12}$ samples.

Electrochemical Measurements

The fabricated working electrodes consisted of as-synthesized $Li_4Ti_5O_{12}$ sample, LA-132 and Super-P in a weight ratio of 85:5:10. The mixture was uniformly casted onto the aluminum foil and then dried in vacuum. CR2032 coin type cells were prepared in glove box with filled argon by composing of lithium piece as the counter electrode, 1 mol/L $LiPF_6$ in EC/DEC/DMC (1:1:1 in volume) as the electrolyte. Celgard 2400 as the separator,. LAND CT2001 system were used to investigate the charge-discharge experiments between the potential range of 1–3V. Electrochemical impedance spectra (EIS) were investigated by using CHI600E electrochemical station in a frequency range of $10^{-2} - 10^5$ Hz.

RESULTS AND DISCUSSION

Crystal structure of both as-obtained $Li_4Ti_5O_{12}$ samples was characterized via XRD, and the results are plotted in **Figure 1**. It clearly verifies that the dominating diffraction peaks of both as-synthesized $Li_4Ti_5O_{12}$ samples are in consistence with the base peaks of spinel $Li_4Ti_5O_{12}$ (PDF No.49-0207), demonstrating that the nitrogen-doped carbon layer coating process has little effect on the formation of spinel $Li_4Ti_5O_{12}$ (Li et al., 2013a; Chang et al., 2014; Wang P. et al., 2017). Perhaps due to the amorphous morphology of carbon, the diffraction peak relative to carbon was not observed (Xu et al., 2017; Liu et al., 2018). The detail of the enlarged peak corresponding to $Li_4Ti_5O_{12}$ (111) plane was described in **Figure 1B**. As clearly found that the central position of this peak shifts to larger angles after N-doped carbon coating, suggesting that nitrogen atoms possibly doped into the $Li_4Ti_5O_{12}$ lattice and form a new thin layer of TiN_x, similar phenomenon was also reported by Li et al. (Zhang et al., 2013). In addition, the intensity of the peaks in $Li_4Ti_5O_{12}$@CN composite is lower than that of pure $Li_4Ti_5O_{12}$, indicating that the N-doped carbon coating on the surface of $Li_4Ti_5O_{12}$ will prevent the growth of particles. In order to investigate the content of carbon and nitrogen in $Li_4Ti_5O_{12}$@CN composite, elemental analysis measurement is carried out. The content of carbon and nitrogen for $Li_4Ti_5O_{12}$@CN composite is 1.46 and 0.24%, respectively.

The obtained results of surface chemical state of $Li_4Ti_5O_{12}$@CN composite evaluated by X-ray photoelectron spectroscopy (XPS) are given in **Figure 2**. Li1s, Ti2p, O1s, C1s, and N1s peaks are observed from the XPS spectra of $Li_4Ti_5O_{12}$@CN composite (**Figure 2A**). The high-resolution N1s of $Li_4Ti_5O_{12}$@CN composite is demonstrated in **Figure 2B**. As illustrated in **Figure 2B**, pyridine (N_1), pyrrole (N_2) and graphitic (N_3) correspond to peaks centered at 398.2, 399.8, and 401.4eV, respectively. (Li H. et al., 2014; Long et al., 2015; Wang et al., 2015). The above results clearly showed that nitrogen-doping is successfully introduced in the carbon layer by using folic acid as a carbon-nitrogen precursor, which might result in produce the flaws in the symmetric offset spread of aromatic rings carbon, and thus further increase the diffusion of Li^+ in the interface (Li et al., 2013a; Wang et al., 2015). Additionally, a peak at about 397 eV being attributed to the interaction energy of TiN is observed in **Figure 2B**, indicating that titanium nitride (TiN) phase is created during the sintering process (Wan et al., 2012). As well-accepted, the existence of TiN with a metallic conductivity will improve electronic conductivity (Li H. et al., 2014). The high-resolution Ti2p of $Li_4Ti_5O_{12}$@CN composite is depicted in **Figure 2C**. Clearly, two peaks appeared at approximately 464.2 and 458.5eV are

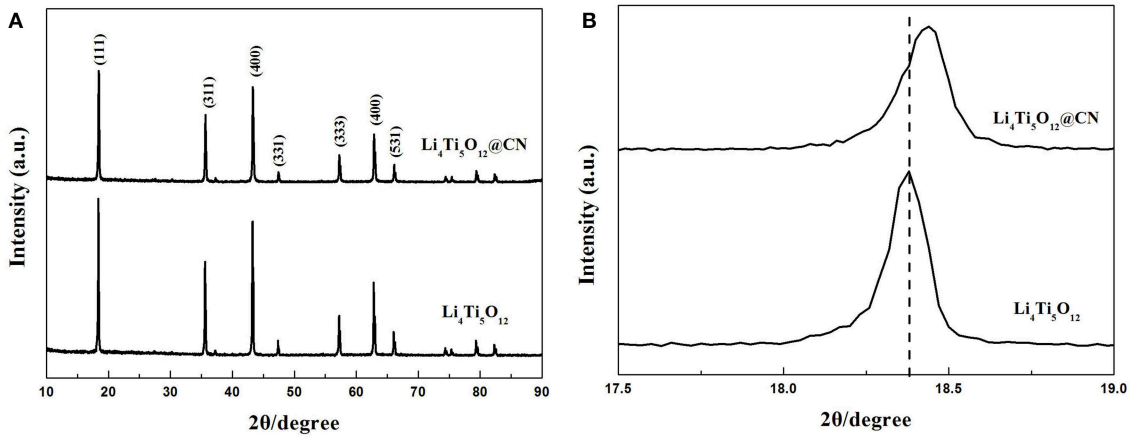

FIGURE 1 | (A) X-ray diffraction profiles of $Li_4Ti_5O_{12}$ and $Li_4Ti_5O_{12}$@CN composite, **(B)** Enlarged (111) peak of $Li_4Ti_5O_{12}$ and $Li_4Ti_5O_{12}$@CN composite.

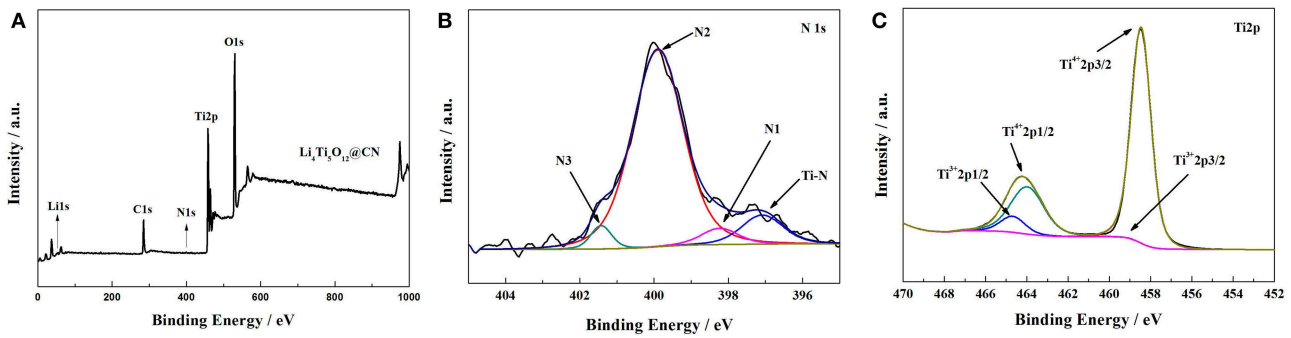

FIGURE 2 | (A) X-ray photoelectron spectroscopy survey spectra of $Li_4Ti_5O_{12}$@CN composite, **(B)** high-resolution XPS spectra of N1s, **(C)** high-resolution XPS spectra of Ti2p.

observed, which represents to peaks of Ti 2p1/2 and Ti 2p3/2 of Ti^{4+} in the sample (Li et al., 2014). In addition, two extra peaks located at about 459 and 464.7eV are detected, corresponding to the peaks of Ti 2p1/2 and Ti 2p3/2 of Ti^{3+} in the sample, respectively, which suggests that Ti^{3+} sites were introduced in the $Li_4Ti_5O_{12}$@CN composite due to the reduced ability of N-doped carbon. Similar phenomena were also demonstrated in previous reports (Wan et al., 2012; Ming et al., 2014). It further verified that the titanium nitride (TiN) phase was formed.

The different morphology and particle size between $Li_4Ti_5O_{12}$ and $Li_4Ti_5O_{12}$@CN composites were investigated by SEM characterization. The results are shown in **Figure 3**. As clearly demonstrated in **Figure 3**, $Li_4Ti_5O_{12}$@CN composite possesses a much smaller particle size than that of $Li_4Ti_5O_{12}$. It is well-accepted that *in situ* N-doped carbon coating will well-prohibit the $Li_4Ti_5O_{12}$ particles from growing into larger crystals (Wang C. et al., 2014). The SEM results agree well with the XRD results. To further verify this prediction, the specific surface area of both as-obtained $Li_4Ti_5O_{12}$ samples was investigated. $Li_4Ti_5O_{12}$@CN composite and pure $Li_4Ti_5O_{12}$ possess a specific surface area of 12.75 and 7.08 $m^2\ g^{-1}$, respectively. Generally, much smaller particles of $Li_4Ti_5O_{12}$@CN composite gives the larger specific surface area. As well-accepted that fabrication of material with much smaller particle size and larger specific surface area will decrease the lithium ion diffusion pathways and thus enhance the kinetics of lithiation/delithiation (Long et al., 2015). The carbon-nitrogen layer of $Li_4Ti_5O_{12}$@CN composite was further studied by TEM characterization and results are demonstrated in **Figure 4**. It was found that a carbon-nitrogen layer with a thickness of 2 to 5 nm is formed on the exterior of $Li_4Ti_5O_{12}$. The electronic conductivities of the as-synthesized $Li_4Ti_5O_{12}$ samples were confirmed by four-point probe method. Pure $Li_4Ti_5O_{12}$ and $Li_4Ti_5O_{12}$@CN composite have the electronic conductivities of 7.67×10^{-5} and 1.06×10^{-2} S cm^{-1}, respectively.

The first charge-discharge cycle for as-synthesized $Li_4Ti_5O_{12}$ and $Li_4Ti_5O_{12}$@CN composite at a rate of 0.5 C between a voltage range of 1–3V are described in **Figure 5**. Both as-prepared $Li_4Ti_5O_{12}$ samples possess a voltage plateau at ∼1.55V, suggesting a two-phase reaction is carried out on the basis of the redox pair of Ti^{3+}/Ti^{4+} (Wang et al., 2012; Wang B. et al., 2014). However, the potential separation between the charge and discharge curves of $Li_4Ti_5O_{12}$@CN composite material is much smaller than that of $Li_4Ti_5O_{12}$, indicating that the $Li_4Ti_5O_{12}$@CN electrode has less polarization and better reaction kinetics, which

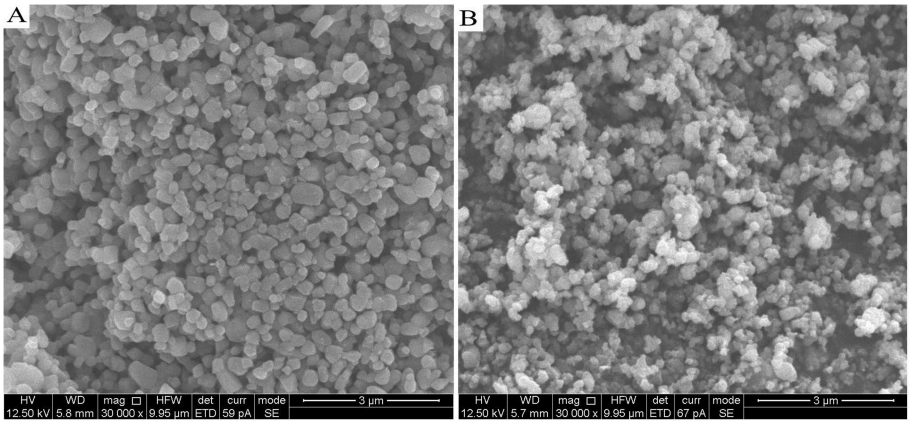

FIGURE 3 | SEM pictures of $Li_4Ti_5O_{12}$ and $Li_4Ti_5O_{12}$@CN composite.

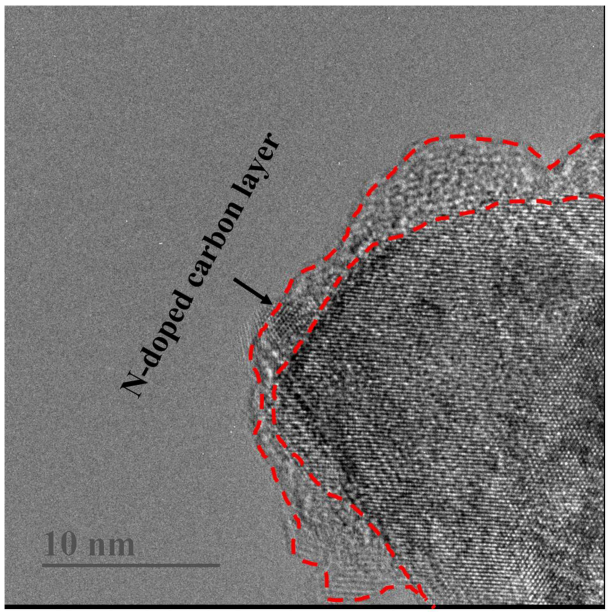

FIGURE 4 | TEM image of $Li_4Ti_5O_{12}$@CN composite.

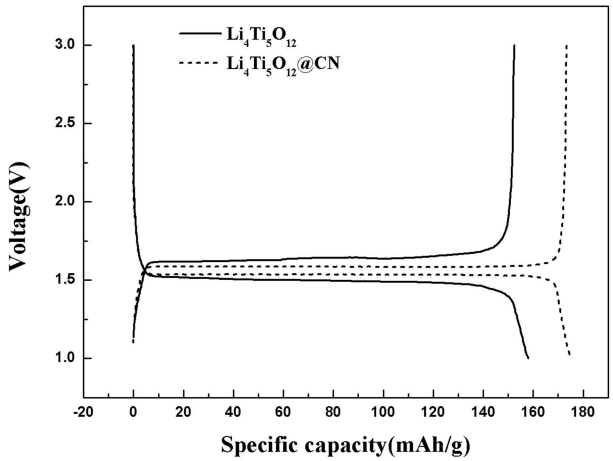

FIGURE 5 | The first charge-discharge cycles for $Li_4Ti_5O_{12}$ and $Li_4Ti_5O_{12}$@CN composite at 0.2 C.

demonstrates that the enhancement of electrical conductivity of $Li_4Ti_5O_{12}$ after introducing N-doped carbon coating (Li et al., 2013a; Zhang et al., 2014).

The rate capabilities of $Li_4Ti_5O_{12}$@CN composite and $Li_4Ti_5O_{12}$ are shown in **Figure 6**. Pure $Li_4Ti_5O_{12}$ obtained a discharge capacity of 158 mAh g^{-1} at a low rate of 0.5 C, and the capacity decreases remarkably as the rate increased from 0.5 to 1, 2, 5, and 10 C, respectively. Especially, its discharge capacity is only 79 mAh g^{-1} at 10 C. The poor rate properties of pure $Li_4Ti_5O_{12}$ could be due to its poor conductivity. While much-improved discharge capacity at each rate for $Li_4Ti_5O_{12}$@CN composite in comparison with pure $Li_4Ti_5O_{12}$. At 0.5, 5, and 10 C, its discharge capacity were 174, 168, and 165 mAh g^{-1}, respectively. The superior rate properties of $Li_4Ti_5O_{12}$@CN composite could be due to three reasons: (i) As demonstrated in SEM results (Seen in **Figure 4**), the smaller particle size for $Li_4Ti_5O_{12}$@CN composite is favorable for the faster Li^+ diffusion and further enhancement of kinetic coefficient of lithium ion embedded into $Li_4Ti_5O_{12}$ structure (Long et al., 2015). (ii) The electronic conductivity of $Li_4Ti_5O_{12}$ is deemed to be enhanced by N-doped carbon coating (Xu et al., 2017), and the defects in the carbon layer caused by N-doping facilitate Li^+ migration in the interface (Li et al., 2013b). (iii) The electronic conductivity properties of $Li_4Ti_5O_{12}$ will be further increased with the existence of TiN_x in the composite.

The cyclic property of $Li_4Ti_5O_{12}$@CN composite at a rate of 10 C is depicted in **Figure 7**. As clearly seen, the initial discharge capacity of $Li_4Ti_5O_{12}$@CN composite is 165 mAh g^{-1}, and 96.2% of its capacity is obtained after 200 cycles, suggesting that the as-synthesized $Li_4Ti_5O_{12}$@CN composite possesses good cycle stability.

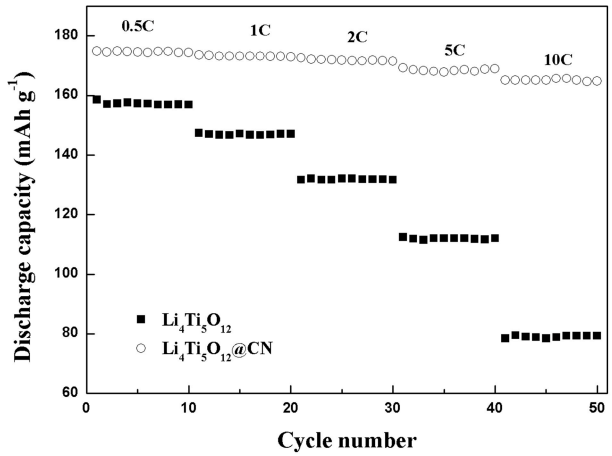

FIGURE 6 | Rate property of $Li_4Ti_5O_{12}$ and $Li_4Ti_5O_{12}$@CN composite at different rates from 0.5 C to10 C.

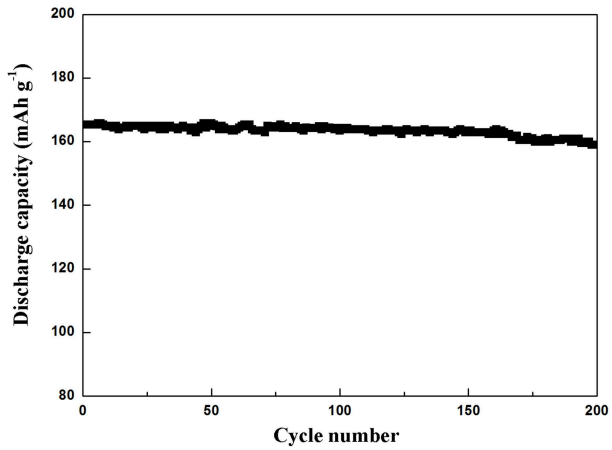

FIGURE 7 | Cycle property of $Li_4Ti_5O_{12}$@CN composite at 10 C.

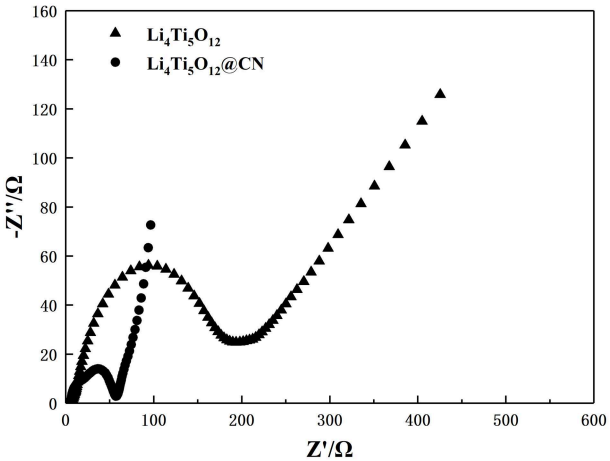

FIGURE 8 | Nyquist plots of $Li_4Ti_5O_{12}$ and $Li_4Ti_5O_{12}$@CN composite.

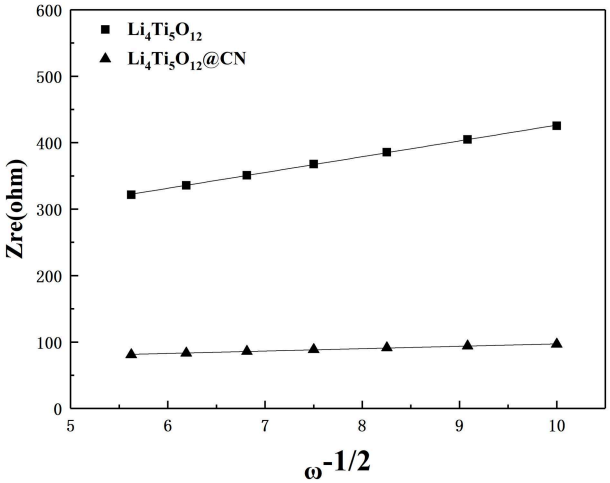

FIGURE 9 | Relation Z_{re} and $\omega^{-1/2}$ in between at the low frequency region.

To further investigate the effect of N-doped carbon coating on electrode behavior, electrochemical impedance spectroscopy measurements were performed on $Li_4Ti_5O_{12}$ and $Li_4Ti_5O_{12}$@CN electrodes, and the results are plotted in **Figure 8**. Obviously, each electrode exhibits a similar profile with a straight line at the low frequency region and a depressed semicircle at the high-middle frequency range, being correlated with Li-ion diffusion and charges transfer resistance (Rct) in the electrode/electrolyte interface, respectively (Zheng et al., 2018; An et al., 2019; He et al., 2019; Lv et al., 2019; Xiao et al., 2019; Zhou et al., 2019). As obtained from **Figure 8**, $Li_4Ti_5O_{12}$@CN electrode exhibits much smaller charge-transfer resistance of 52 Ω than that of 194 Ω for pure $Li_4Ti_5O_{12}$ electrode, suggesting the improved electronic conductivity of $Li_4Ti_5O_{12}$@CN composite in comparison with pure $Li_4Ti_5O_{12}$ caused by the highly electronic conductive coating with N-doped carbon as well as the presence of TiN_x phase (Zhou et al., 2017). According to the following equation, the Li-ion diffusion coefficient of both as-prepared $Li_4Ti_5O_{12}$ samples can be obtained:

$$D = R^2T^2/2A^2n^4F^4C^2\sigma^2 \quad (1)$$

$$Z_{re} = R_D + R_L + \sigma\omega^{-1/2} \quad (2)$$

The value of σ for both samples could be obtained from the lines described in **Figure 9**. Based on the above equations and the results from **Figure 9**, the obtained lithium ion diffusion coefficient for $Li_4Ti_5O_{12}$ and $Li_4Ti_5O_{12}$@CN composite is 6.58×10^{-11} and 2.89×10^{-9} cm^2 s^{-1}, respectively. There is no doubt that the $Li_4Ti_5O_{12}$@CN electrode has a larger Li-ion diffusion coefficient due to the smaller particle size and the carbon layer defect of the $Li_4Ti_5O_{12}$@CN composite, indicating that a valid enhancement of the diffusion kinetics of $Li_4Ti_5O_{12}$ after the

introduction of the N-doped carbon coating. Based on the above results and discussion, coating with N-doped carbon can dramatically improve the lithium ion and conductive property. Consequently, $Li_4Ti_5O_{12}$@CN composite has much improved electrochemical performance in compassion with pure $Li_4Ti_5O_{12}$.

CONCLUSIONS

In this study, N-doped carbon-coated $Li_4Ti_5O_{12}$ is prepared with folic acid as a carbon-nitrogen source. $Li_4Ti_5O_{12}$@CN composite has the outstanding reversible capacity, high rate capability in compassion with pure $Li_4Ti_5O_{12}$. The discharge capacity of the $Li_4Ti_5O_{12}$@CN composite at 10 C was 165 mAh g^{-1}, and the initial specific capacity remained at 96.2% after 200 cycles. The superior properties of $Li_4Ti_5O_{12}$@CN composite could be owing to the improved electronic conductivity caused by the N-doped carbon layer and the TiN phase as well as enhanced Li-ion diffusion coefficient rising from the smaller particle size and the defects in the carbon layer.

DATA AVAILABILITY

The raw data supporting the conclusions of this manuscript will be made available by the authors, without undue reservation, to any qualified researcher.

AUTHOR CONTRIBUTIONS

XH and YR contributed conception and design of the study. HX carried out experiments and wrote the manuscript. XD performed analyzed experimental results. SZ revised the manuscript.

FUNDING

This project was financially supported by the National Nature Science Foundation of China (Nos. 21771062, 21576030 and U1607127), the Research Fund of Hunan Provincial Education Department (18A366), the Opening Project of Material Corrosion and Protection Key Laboratory of Sichuan Province of China (No. 2018CL15).

REFERENCES

An, C. S., Yuan, Y. F., Zhang, B., Tang, L. B., Xiao, B., Lu, J., et al. (2019). Graphene wrapped $FeSe_2$ nano-microspheres with high pseudocapacitive contribution for enhanced na-ion storage. *Adv. Energy Mater*. 2019:1900356. doi: 10.1002/aenm.201900356

Chang, L. J., Luo, S. H., Zhang, H. L., Qi, X. W., Wang, Z. Y., Liu, Y. G., et al. (2014). Synthesis and performance of $Li_4Ti_5O_{12}$ anode materials using the PVP-assisted combustion method. *Chin. Chem. Lett*. 25, 1569–1572. doi: 10.1016/j.cclet.2014.09.002

Chen, C., Liu, X., Ai, C., and Wu, Y. (2017). Enhanced lithium storage capability of $Li_4Ti_5O_{12}$ anode material with low content Ce modification. *J. Alloy. Compd.* 714, 71–78. doi: 10.1016/j.jallcom.2017.04.184

Cheng, Q., Tang, S., Liu, C., Lan, Q., Zhao, J., Liang, J., et al. (2017). Preparation and electrochemical performance of $Li_{4-x}Mg_xTi_5O_{12}$ as anode materials for lithium-ion battery. *J. Alloy. Compd*. 722, 229–234. doi: 10.1016/j.jallcom.2017.06.040

Chiu, H. C., Lu, X., Zhou, J., Gu, L., Reid, J., Gauvin, R., et al. (2017). Annealing-regulated elimination of residual strain-induced structural relaxation for stable high-power $Li_4Ti_5O_{12}$ nanosheet anodes. *Nano Energy* 32, 533–541. doi: 10.1016/j.nanoen.2016.12.063

Han, X., Gui, X., Yi, T. F., Li, Y. W., and Yue, C. B. (2018). Recent progress of $NiCo_2O_4$-based anodes for high-performance lithium-ion batteries. *Curr. Opin. Solid State Mater. Sci*. 22, 109–126. doi: 10.1016/j.cossms.2018.05.005

He, Z., Li, M., Li, Y., Li, C., Yi, Z., Zhu, J., et al. (2019). ZrO_2 nanoparticle embedded carbon nanofibers by electrospinning technique as advanced negative electrode materials for vanadium redox flow battery. *Electrochim Acta* 309, 166–176. doi: 10.1016/j.electacta.2019.04.100

Jiang, C., Liu, S., Lian, Q., Zhao, J., Ding, W., Yu, Z., et al. (2017). Nitrogen-doped carbon-coated hierarchical $Li_4Ti_5O_{12}$-TiO_2 hybrid microspheres as excellent high rate anode of Li-ion battery. *Ceram. Int*. 43, 11354–11360. doi: 10.1016/j.ceramint.2017.05.341

Li, H., Shen, L., Wang, J., Ding, B., Nie, P., Xu, G., et al. (2014). Design of a nitrogen-doped, carbon-coated $Li_4Ti_5O_{12}$ nanocomposite with a core-shell structure and its application for high-rate lithium-ion batteries, *ChemPlusChem* 79, 128–133. doi: 10.1002/cplu.201300316

Li, H., Shen, L., Yin, K., Ji, J., Wang, J., Wang, X., et al. (2013b). Facile synthesis of N-doped carbon-coated $Li_4Ti_5O_{12}$ microspheres using polydopamine as a carbon source for high rate lithium ion batteries. *J. Mater. Chem. A* 1, 7270–7276. doi: 10.1039/c3ta10623c

Li, H., Shen, L., Zhang, X., Wang, J., Nie, P., Che, Q., et al. (2013a). Nitrogen-doped carbon coated $Li_4Ti_5O_{12}$ nanocomposite: superior anode materials for rechargeable lithium ion batteries. *Power Sour. J.* 221, 122–127. doi: 10.1016/j.jpowsour.2012.08.032

Li, R., Xiao, W., Miao, C., Fang, R., Wang, Z., and Zhang, M. (2019). Sphere-like SnO_2/TiO_2 composites as high-performance anodes for lithium ion batteries. *Ceramics Int.* 45, 13530–13535. doi: 10.1016/j.ceramint.2019.04.059

Li, X., Lin, H., Cui, W., Xiao, Q., and Zhao, J. (2014). Fast solution-combustion synthesis of nitrogen-modified $Li_4Ti_5O_{12}$ nanomaterials with improved electrochemical performance. *ACS Appl. Mater. Interfaces* 6, 7895–7901. doi: 10.1021/am501220f

Liang, Q., Cao, N., Song, Z., Gao, X., Hou, L., Guo, T., et al. (2017). Co-doped $Li_4Ti_5O_{12}$ nanosheets with enhanced rate performance for lithium-ion batteries. *Electrochim. Acta* 251, 407–414. doi: 10.1016/j.electacta.2017.08.121

Liu, H., Su, C., Li, X., and Guo, Y. (2018). Fabrication of N-doped carbon-coated $Li_4Ti_{5-x}Co_xO_{12}$ anode for lithium-ion batteries. *Solid State Ionics* 320, 113–117. doi: 10.1016/j.ssi.2018.02.035

Long, D. H., Jeong, M. G., Lee, Y. S., Choi, W., Lee, J. K., Oh, I. H., et al. (2015). Coating lithium titanate with nitrogen-doped carbon by simple refluxing for high-power lithium-ion batteries. *ACS Appl. Mater. Interfaces* 7, 10250–10257. doi: 10.1021/acsami.5b00776

Long, W., Fang, B., Ignaszak, A., Wu, Z., Wang, Y. J., and Wilkinson, D. (2017). Biomass-derived nanostructured carbons and their composites as anode materials for lithium ion batteries. *Chem. Soc. Rev*. 46, 7176–7190. doi: 10.1039/C6CS00639F

Lu, M., Yang, H., Zhang, Y., Wang, G., and Zhuang, S. (2017). Novel insights into the charge/discharge characteristics of spherical porous $Li_4Ti_5O_{12}$ co-coated with carbon and metal. *Power Sour. J.* 349, 52–56. doi: 10.1016/j.jpowsour.2017.03.027

Lv, Y. R., Zhang, L., Cheng, G., Wang, P. F., Zhang, T. Z., Wang, L., et al. (2019). Preparation of carbon nanosheet by molten salt route and its application in catalyzing VO^{2+}/VO_2^+ redox reaction. *J. Electrochem.* 166, A953–A959. doi: 10.1149/2.0371906jes

Ma, Z., Cui, Y., Xiao, X., Deng, Y., Song, X., Zuo, X., et al. (2016). A reconstructed graphite-like carbon micro/nano-structure with higher capacity and comparative voltage plateau of graphite. *J. Mater. Chem. A* 4, 11462–11471. doi: 10.1039/C6TA02195F

Ming, H., Ming, J., Li, X., Zhou, Q., Wang, H., Jin, L., et al. (2014). Hierarchical $Li_4Ti_5O_{12}$ particles co-modified with C&N towardsenhanced

performance in lithium-ion battery applications. *Electrochim. Acta* 116, 224–229. doi: 10.1016/j.electacta.2013.11.038

Tang, B., Li, A., Tong, Y., Song, H., Chen, X., Zhou, J., et al. (2017). Carbon-coated $Li_4Ti_5O_{12}$ tablets derived from metal-organic frameworks as anode material for lithium-ion batteries. *J. Alloy. Compd.* 708, 6–13. doi: 10.1016/j.jallcom.2017.02.279

Tian, Q., Chen, P., Zhang, Z., and Yang, L. (2017). Achievement of significantly improved lithium storage for novel clew-like $Li_4Ti_5O_{12}$ anode assembled by ultrafine nanowires. *Power Sour. J.* 350, 49–55. doi: 10.1016/j.jpowsour.2017.03.065

Wan, Z., Cai, R., Jiang, S., and Shao, Z. (2012). Nitrogen- and TiN-modified $Li_4Ti_5O_{12}$: one-step synthesis and electrochemical performance optimization. *J. Mater. Chem.* 22, 17773–17781. doi: 10.1039/c2jm33346e

Wang, B., Wang, J., Cao, J., Ge, H., and Tang, Y. (2014). Nitrogen-doped $Li_4Ti_5O_{12}$ nanosheets with enhanced lithium storage properties. *Power Sources J.* 266, 150–154. doi: 10.1016/j.jpowsour.2014.05.009

Wang, C., Li, H., Fu, A., Liu, J., Ye, W., Guo, P., et al. (2014). An RAPET approach to *in situ* synthesis of carbon modified $Li_4Ti_5O_{12}$ anode nanocrystals with improved conductivity. *N. Chem. J.* 38, 616–623. doi: 10.1039/C3NJ01319G

Wang, F., Luo, L., Du, J., Guo, L., Lia, B., and Ding, Y. (2015). Nitrogen-doped carbon decorated $Li_4Ti_5O_{12}$ composites as anode materials for high performance lithium-ion batteries. *RSC Adv.* 5, 46359–46365. doi: 10.1039/C5RA05989E

Wang, L., Zhang, Z., Liang, G., Ou, X., and Xu, Y. (2012). Synthesis and electrochemical performance of $Li_4Ti_5O_{12}$/C composite by a starch sol assisted method. *Powder Technol.* 215–216, 79–84. doi: 10.1016/j.powtec.2011.09.011

Wang, P., Zhang, G., Cheng, J., You, Y., Li, Y. K., Ding, C., et al. (2017). Facile Synthesis of Carbon-coated spinel $Li_4Ti_5O_{12}$/rutile-TiO_2 composites as an improved anode material in full lithium-ion batteries with $LiFePO_4$@N-doped carbon cathode. *ACS Appl. Mater. Interfaces* 9, 6138–6143. doi: 10.1021/acsami.6b15982

Wang, Q., Zhang, J., Liu, W., Xie, X., and Xia, B. (2017). Quantitative investigation of the gassing behavior in cylindrical $Li_4Ti_5O_{12}$ batteries. *Power Sour. J.* 343, 564–570. doi: 10.1016/j.jpowsour.2017.01.073

Wang, S., Yang, Y., Quan, W., Hong, Y., Zhang, Z., Tang, Z., et al. (2017). Ti^{3+}-free three-phase $Li_4Ti_5O_{12}/TiO_2$ for high-rate lithium ion batteries: capacity and conductivity enhancement by phase boundaries. *Nano Energy* 32, 294–301. doi: 10.1016/j.nanoen.2016.12.052

Wu, L., Zheng, J., Wang, L., Xiong, X. H., Shao, Y. Y., Wu, M. H. et al. (2019). PPy-encapsulated SnS_2 nanosheets stabilized by defects on a TiO_2 support as a durable anode material for lithium-ion batteries. *Angew. Chem. Int. Ed.* 58, 811–815. doi: 10.1002/anie.201811784

Xiao, B., Wang, P. B., He, Z. J., Yang, Z., Tang, L. B., Zheng, J. C., et al. (2019). Effect of MgO and TiO2 coating on the electrochemical performance of li-rich cathode materials for lithium-ion Batteries. *Energy Technol.* 2019:1800829. doi: 10.1002/ente.201800829

Xiong, Q. Q., Lou, J. J., Teng, X. J., Lu, X. X., Liu, S. Y., Chi, H. Z., et al. (2018). Controllable synthesis of N-C@$LiFePO_4$ nanospheres as advanced cathode of lithium ion batteries. *J. Alloy. Compd.* 743, 377–382. doi: 10.1016/j.jallcom.2018.01.350

Xu, G., Quan, X., Gao, H., Li, J., Cai, Y., Cheng, X., et al. (2017). Facile spray drying route for large scale nitrogen-doped carbon-coated $Li_4Ti_5O_{12}$ anode material in lithium-ion batteries. *Solid State Ionics* 304, 40–45. doi: 10.1016/j.ssi.2017.03.018

Yi, T. F., Zhu, Y. R., Tao, W., Luo, S. H., Xie, Y., and Li, X. F. (2018). Recent advances in the research of $MLi_2Ti_6O_{14}$ (M=2Na, Sr, Ba, Pb) anode materials for Li-ion batteries. *Power Sour. J.* 399, 26–41. doi: 10.1016/j.jpowsour.2018.07.086

Zhang, H., Deng, Q., Mou, C., Huang, Z., Wang, Y., Zhou, A., et al. (2013). Surface structure and high-rate performance of spinel $Li_4Ti_5O_{12}$ coated with N-doped carbon as anode material for lithium-ion batteries. *Power Sour. J.* 239, 538–545. doi: 10.1016/j.jpowsour.2013.03.013

Zhang, J., Zhang, J., Peng, Z., Cai, W., Yu, L., Wu, Z., et al. (2014). Outstanding rate capability and long cycle stability induced by homogeneous distribution of nitrogen doped carbon and titanium nitride on the surface and in the bulk of spinel lithium titanate. *Electrochim. Acta* 132, 230–238. doi: 10.1016/j.electacta.2014.03.007

Zheng, J. C., Yang, Z., He, Z. J., Tong, H., Yu, W. J., and Zhang, J. F. (2018). *In situ* formed $LiNi_{0.8}Co_{0.15}Al_{0.05}O_2$@$Li_4SiO_4$ composite cathode material with high rate capability and long cycling stability for lithium-ion batteries. *Nano Energy* 53, 613–621. doi: 10.1016/j.nanoen.2018.09.014

Zhou, C. X., Wang, P. B., Zhang, B., Tang, L. B., Tong, H. J., and Zheng, J. C. (2019). Formation and effect of residual lithium compounds on Li-rich cathode material $Li_{1.35}[Ni_{0.35}Mn_{0.65}]O_2$. *ACS Appl. Mater. Interfaces* 11, 11518–11523. doi: 10.1021/acsami.9b01806

Zhou, K., Fan, X., Chen, W., Chen, F., Wei, X., Li, A., et al. (2017). Nitrogen-doped $Li_4Ti_5O_{12}$/carbon hybrids derived from inorganic polymer for fast lithium storage. *Electrochim. Acta* 247, 132–138. doi: 10.1016/j.electacta.2017.06.175

Conflict of Interest Statement: The authors declare that the research was conducted in the absence of any commercial or financial relationships that could be construed as a potential conflict of interest.

frontiers in Chemistry

ORIGINAL RESEARCH
published: 16 July 2019
doi: 10.3389/fchem.2019.00500

The Effects of Reversibility of H2-H3 Phase Transition on Ni-Rich Layered Oxide Cathode for High-Energy Lithium-Ion Batteries

*Jie Chen[1†], Huiping Yang[1†], Tianhao Li[1], Chaoyang Liu[1], Hui Tong[2], Jiaxin Chen[1], Zengsheng Liu[1], Lingfeng Xia[1], Zhaoyong Chen[1], Junfei Duan[1] and Lingjun Li[1,3]**

[1] School of Materials Science and Engineering, Changsha University of Science and Technology, Changsha, China, [2] School of Metallurgy and Environment, Central South University, Changsha, China, [3] Hunan Provincial Key Laboratory of Modeling and Monitoring on the Near-Earth Electromagnetic Environments, Changsha University of Science and Technology, Changsha, China

OPEN ACCESS

Edited by:
Shengkui Zhong,
Soochow University, China

Reviewed by:
Yunjian Liu,
Jiangsu University, China
Haisheng Fang,
Kunming University of Science and Technology, China

***Correspondence:**
Lingjun Li
lingjun.li@csust.edu.cn

[†] These authors have contributed equally to this work as co-first authors

Specialty section:
This article was submitted to Electrochemistry, a section of the journal Frontiers in Chemistry

Received: 13 June 2019
Accepted: 01 July 2019
Published: 16 July 2019

Citation:
Chen J, Yang H, Li T, Liu C, Tong H, Chen J, Liu Z, Xia L, Chen Z, Duan J and Li L (2019) The Effects of Reversibility of H2-H3 Phase Transition on Ni-Rich Layered Oxide Cathode for High-Energy Lithium-Ion Batteries. Front. Chem. 7:500. doi: 10.3389/fchem.2019.00500

Although $LiNi_{0.8}Co_{0.1}Mn_{0.1}O_2$ is attracting increasing attention on account of its high specific capacity, the moderate cycle lifetime still hinders its large-scale commercialization applications. Herein, the Ti-doped $LiNi_{0.8}Co_{0.1}Mn_{0.1}O_2$ compounds are successfully synthesized. The $Li(Ni_{0.8}Co_{0.1}Mn_{0.1})_{0.99}Ti_{0.01}O_2$ sample exhibits the best electrochemical performance. Under the voltage range of 2.7–4.3 V, it maintains a reversible capacity of 151.01 $mAh{\cdot}g^{-1}$ with the capacity retention of 83.98% after 200 cycles at 1 C. Electrochemical impedance spectroscopy (EIS) and differential capacity profiles during prolonged cycling demonstrate that the Ti doping could enhance both the abilities of electronic transition and Li ion diffusion. More importantly, Ti doping can also improve the reversibility of the H2-H3 phase transitions during charge-discharge cycles, thus improving the electrochemical performance of Ni-rich cathodes.

Keywords: lithium ion batteries, cathode materials, $LiNi_{0.8}Co_{0.1}Mn_{0.1}O_2$, Ti-doped, phase transitions

INTRODUCTION

With the rapid development of renewable energy of wind and solar power, the large-scale energy storage system has become more and more important (Manthiram et al., 2016; Chen et al., 2018; Wu et al., 2018; Wu C. et al., 2019; Xia et al., 2019). Among them, lithium ion batteries have been powering our daily life from mobile phones to electric vehicles (EVs), due to their high energy density, long cycle life and environmental friendly (Chen et al., 2014; Li et al., 2018; Wu L. et al., 2019; Ye et al., 2019). With the rapid development of high-performance silicon-carbon composite anodes (Su et al., 2018; Xiao et al., 2018), cathode materials become the technological bottleneck for obtaining high performance lithium-ion batteries (Myung et al., 2016; Chen Z. et al., 2017; Xu et al., 2017; Zheng et al., 2019). Among the various types of layered cathodes, $LiNi_{0.8}Co_{0.1}Mn_{0.1}O_2$ (NCM) is attracting an increasing amount of attention on account of its high specific capacity and low cost, compared to traditional $LiCoO_2$ material (Zhang et al., 2012; Li et al., 2016a; Chen M. et al., 2017; Yang et al., 2019).

However, the long-term capacity retention of NCM is not satisfactory for large-scale application, which can be ascribed to the undesired side reactions between the highly reactive species Ni^{4+} and liquid electrolyte at the interface of the cathodes, triggering the irreversible phase transition from initial layered R-3m phase to spinel Fd-3m phase and further to the rock-salt phase (Nam et al., 2013; Lin et al., 2014a,b). Worse yet, the NiO passivation layer will increase the impedance, hindering the electrochemical kinetics, and resulting in the deterioration of electrochemical performance (Meng et al., 2017; Ryu et al., 2018a).

During the extraction of Lithium-ion, Ni-rich materials undergoes a series of phase transitions: The original layered structure (H1) transforms to the monoclinic phase (M), the second hexagonal phase (H2), and the third hexagonal phase (H3) (He et al., 2018; Gao et al., 2019; Wu et al., 2019a). It has been reported that the H2-H3 transition will cause detrimental lattice shrinkage along the c-direction, resulting in the volume change and the local stress accumulation, and further leading to the microcracks generation and propagation in secondary particles (Lee et al., 2014; Sun and Manthiram, 2017; Yoon et al., 2018). Ryu et al. (2018b) reported the cross-sectional SEM images of the charged $LiNi_{0.90}Co_{0.05}Mn_{0.05}O_2$ particles, numerous cracks emanating from the particle core and some cracks traverse across the entire particle and nearly fracture the secondary particle. The produced cracks create fresh surface where phase transitions and corrosion as well as side reactions occur, thereby further accelerating the structural degradation of the cathodes.

Such severe structural collapse affected by mechanical strain associated with the poor irreversibility of the H2-H3 phase transition during cycling. Cations substitutions have been regarded as promising way to overcome these challenges and enhance the structural stability of Ni-rich materials (Xia et al., 2018; Li et al., 2019; Susai et al., 2019; Weigel et al., 2019). Wu et al. (2019b) demonstrated that by doping Ti^{4+} in $LiNi_{0.9}Co_{0.1}O_2$ materials, the improved reversibility of the H2-H3 phase transitions and the lossless H3 phase suppress the generation of microcracks and structural degradations. It is also reported that, by doping with boron, the $LiNi_{0.9}Co_{0.05}Mn_{0.05}O_2$ shows no visible cracks, which is consistent with its good reversibility of H2-H3, attesting to the beneficial effect of boron doping and enables deflection of the internal strain posed by the phase transition (Park et al., 2018).

In this work, the structural and electrochemical performances of Ti-doped $LiNi_{0.8}Co_{0.1}Mn_{0.1}O_2$ (0, 0.5, 1, 2%) have been systematically studied. The Ti doping can keep the layered structure materials with one phase. Among them, the $Li(Ni_{0.8}Co_{0.1}Mn_{0.1})_{0.99}Ti_{0.01}O_2$ sample exhibits the best electrochemical performance. Within a voltage window of 2.7–4.3 V, the $Li(Ni_{0.8}Co_{0.1}Mn_{0.1})_{0.99}Ti_{0.01}O_2$ sample maintains a reversible capacity of 151.01 $mAh{\cdot}g^{-1}$ with 83.98% capacity retention after 200 cycles, corresponding 0.08% decay per cycle. The improved electrochemical performance can be ascribed to the enhanced abilities of electronic transition and Li ion diffusion. More importantly, the reversibility of H2-H3 phase transitions and the lossless H3 phase during prolonged cycling can also improve the electrochemical performance of Ni-rich cathodes.

EXPERIMENTAL SECTION

Materials Synthesis

The pristine $LiNi_{0.8}Co_{0.1}Mn_{0.1}O_2$ (denoted as NCM) spherical material was synthesized by solid-state method. Stoichiometric ratio of $LiOH{\cdot}H_2O$ and $Ni_{0.8}Co_{0.1}Mn_{0.1}(OH)_2$ precursor were mixed and ground in an agate mortar. Then, under oxygen atmosphere, the mixtures were precalcined at 480°C for 5 h and calcined at 830°C for 12 h with a heating rate of $5°C{\cdot}min^{-1}$. Next, the sample was cooled to room temperature naturally in a tube furnace.

The 0.5, 1, 2 mol% Ti-doped NCM (denoted as Ti-0.5, Ti-1, Ti-2) samples were prepared by the following steps. Firstly, the stoichiometric amount of $C_{16}H_{36}O_4Ti$ was dissolved into 60 mL absolute ethanol, then stirring continuously in water bath at the temperature of 60°C. Secondly, the $LiOH{\cdot}H_2O$ were added to the solution and kept stirring for about 30 min, subsequently the $Ni_{0.8}Co_{0.1}Mn_{0.1}(OH)_2$ precursor was added. Afterward, the mixed solution was dried overnight at 120°C. Finally, the Ti-doped samples were obtained by calcining under the same condition as NCM.

Materials Characterization

The crystalline structures of all the samples were determined by X-ray diffraction (XRD, Bruker D8 advance) using Cu Kα radiation in the 2θ range of 10–90° with a scan rate of $5°{\cdot}min^{-1}$ and operated at 40 kV and 40 mA. Scanning electron microscopy (SEM, Nova NanoSEM-230) was performed to observe the particle morphologies of samples. The microstructures of the NCM and Ti-1 samples were examined by high-resolution transmission electron microscopy (HRTEM, FEI Talso 200s).

Electrochemical Measurements

The electrochemical properties were measured using a CR2025 coin-type half cell. The working electrodes were prepared by mixing the active materials, acetylene black, and polyvinylidenedifluoride (PVDF) with a weight ratio of 8:1:1 in N-methyl-2-pyrrolidone (NMP). The resulting slurry was cast uniformly onto aluminum foil, followed by drying at 120°C in a vacuum oven for 4 h and pouched. The typical mass loading of positive electrode was about 2.3 $mg{\cdot}cm^{-2}$ with an electrode diameter of 12 mm. 1 M $LiPF_6$ dissolved in a solution of dimethyl carbonate (DMC), ethylene carbonate (EC), and ethyl methyl carbonate (EMC) (volume ratio = 1:1:1) was used as the electrolyte. All the cells were assembled in an Ar-filled glovebox where the moisture and oxygen content is under 0.1 ppm by using a lithium metal anode and separator (Celgard 2500 polyethylene). Then, the cells were silenced before electrochemically tests. Electrochemical tests were performed on NEWARE BTS7.6 battery test system between 2.7 and 4.3 V vs. Li/Li^+ at room temperature (25°C). The cycling performance was initially charged and discharged at 0.1 C (18 $mA{\cdot}g^{-1}$) with 2 cycles, then charged and discharged at 1 C in the subsequent cycles. The cyclic voltammetry (CV) was measured at a scan

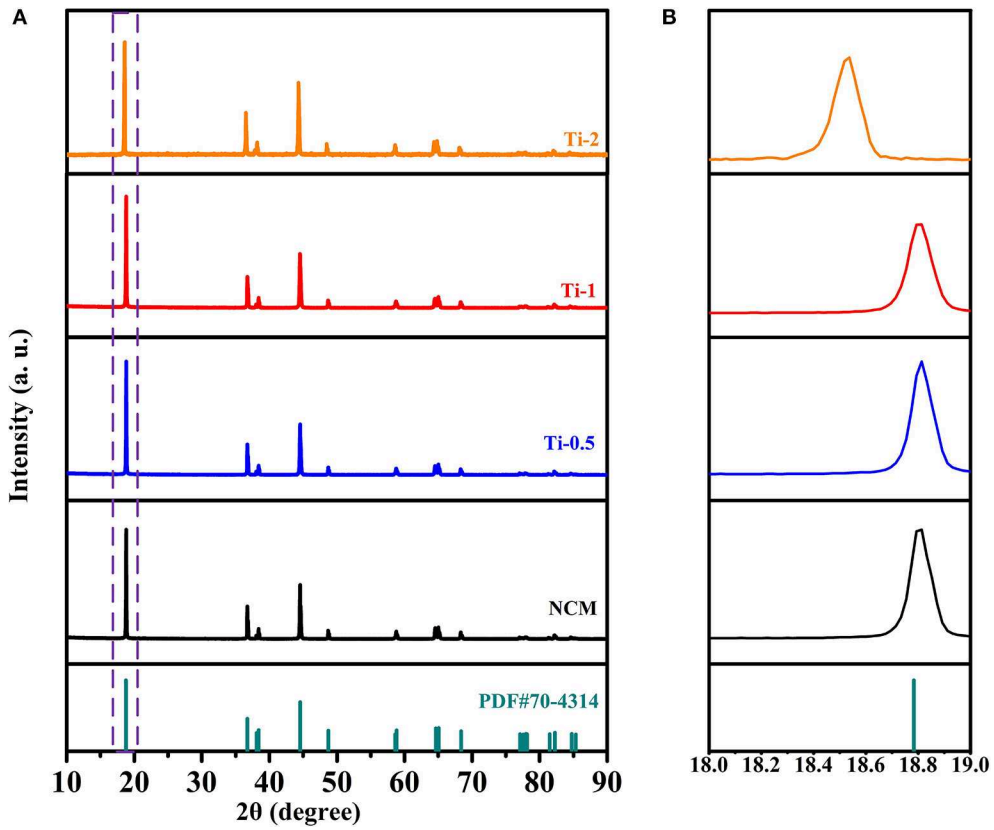

FIGURE 1 | (A) XRD patterns of NCM, Ti-0.5, Ti-1, and Ti-2; **(B)** Corresponding enlarged patterns of (003) peak between 18 and 19°.

TABLE 1 | Lattice parameters of all samples obtained by XRD analysis.

Samples	a (Å)	c (Å)	V (Å^3)
NCM	2.86390	14.16697	100.63
Ti-0.5	2.86714	14.16738	100.78
Ti-1	2.86805	14.16898	100.87
Ti-2	2.86914	14.17678	100.89

rate of 0.1 mV·s^{-1} within 2.7–4.5 V through an electrochemical workstation (Solartron 1470E). Electrochemical impedance spectroscopy (EIS) tests were conducted in the frequency range of 10^{-3}-10^5 Hz.

RESULTS AND DISCUSSION

The structure characteristics of the NCM and Ti-doped NCM samples are analyzed by XRD measurements as shown in **Figure 1A**. All the diffraction peaks of all samples can be well indexed to the hexagonal α-$NaFeO_2$ layered structure (PDF#70-4314) with R-3m space group, and no secondary phase is observed, indicating that Ti^{4+} is successfully incorporated into the bulk structure. Furthermore, the clear splitting of (006)/(102) and (108)/(110) couples for all samples manifest a well-developed layered structure. The partial magnified patterns in **Figure 1B** displays that the (003) diffraction peaks shift to a lower angle with increasing Ti-doped content, demonstrating lattice expansion caused by the successfully dopant of Ti^{4+}. The result can also be proved by the increase of lattice parameter c and the cell volume as shown in **Table 1**.

The morphologies of the pristine NCM and Ti-1 samples are shown in **Figures 2a,d**. The pristine and modified samples images exhibit very similar morphology. It is found that the secondary particles are spherical with the size is ∼12 μm in diameter, which are composed of densely packed primary particles. Apparently, the result indicates that Ti doping cannot change the particle morphology and particle size. To further investigate the effect of Ti doping on the microstructure of NCM sample, the HRTEM images of NCM (**Figures 2b,c**) and Ti-1 (**Figures 2e,f**) are performed. As shown, the rectangle region is selected as representative to observe the atomic-scale crystal structure, and the fast fourier transform (FFT) of the selected region are shown on the right. The FFT image of the NCM demonstrates that layered phase (space group R-3m) is successfully formed. For the Ti-1 sample, the diffraction spots of the corresponding FFT can be assigned to the (104) lattice plane, indicating that the microstructure cannot be changed by 1% Ti doping.

Electrochemical properties of the pristine and Ti-doped NCM samples are tested in lithium-ion half-cells at room temperature. **Figure 3A** shows the initial charge/discharge profiles of all

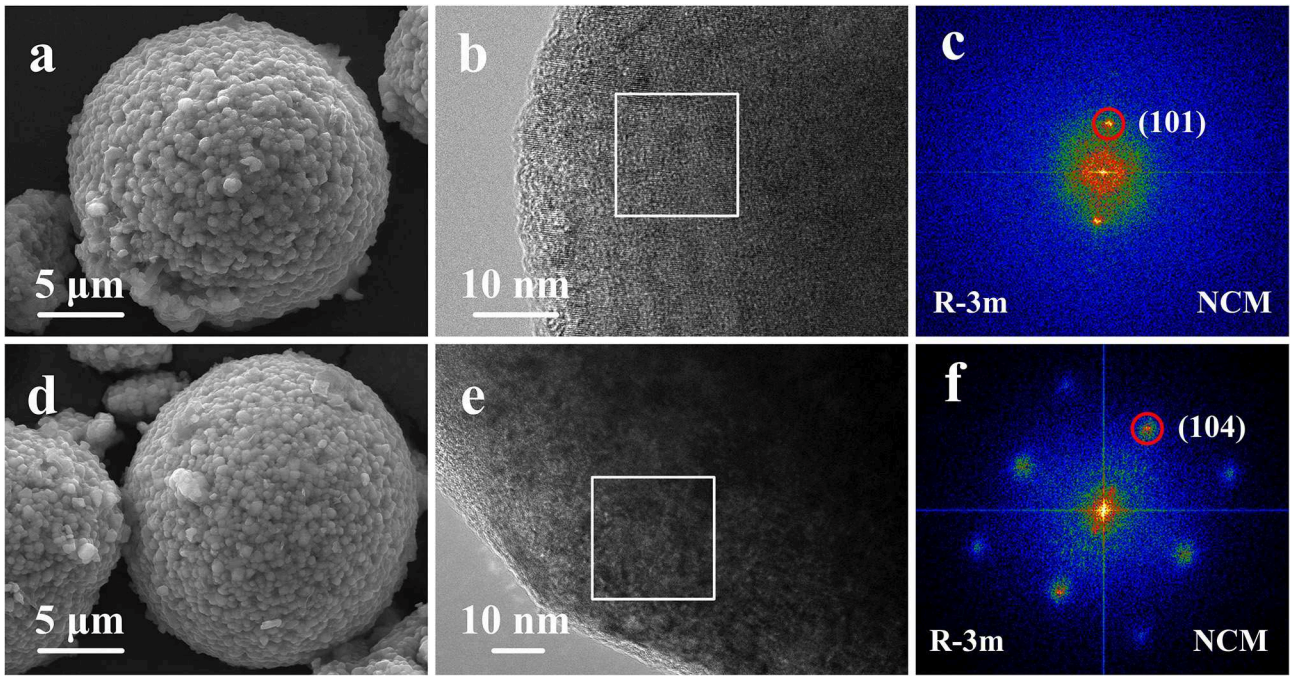

FIGURE 2 | SEM images of the pristine NCM **(a)**, Ti-1 **(d)**; HRTEM images and Corresponding FFT images of the pristine NCM **(b,c)** and Ti-1 **(e,f)**.

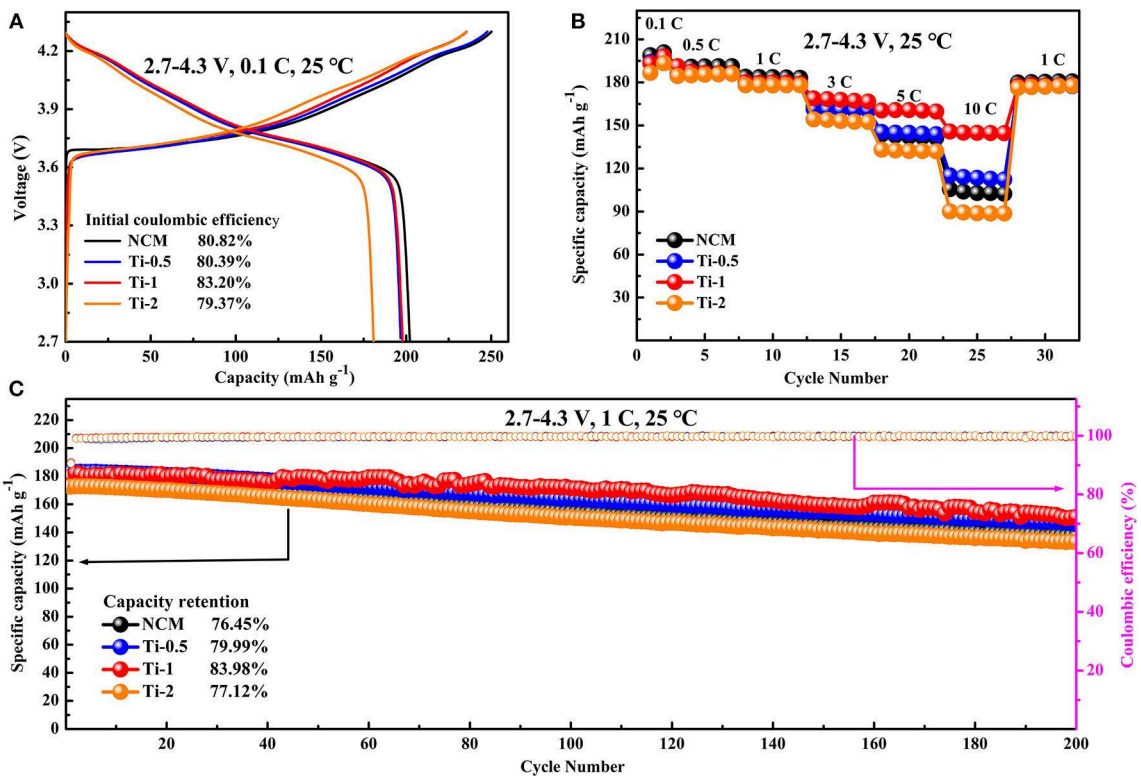

FIGURE 3 | Electrochemical performance of all electrodes in the voltage range of 2.7–4.3 V at room temperature: **(A)** Initial charge-discharge profiles at 0.1 C. **(B)** Rate capabilities at various current densities. **(C)** Cycling performance at a current rate of 1 C.

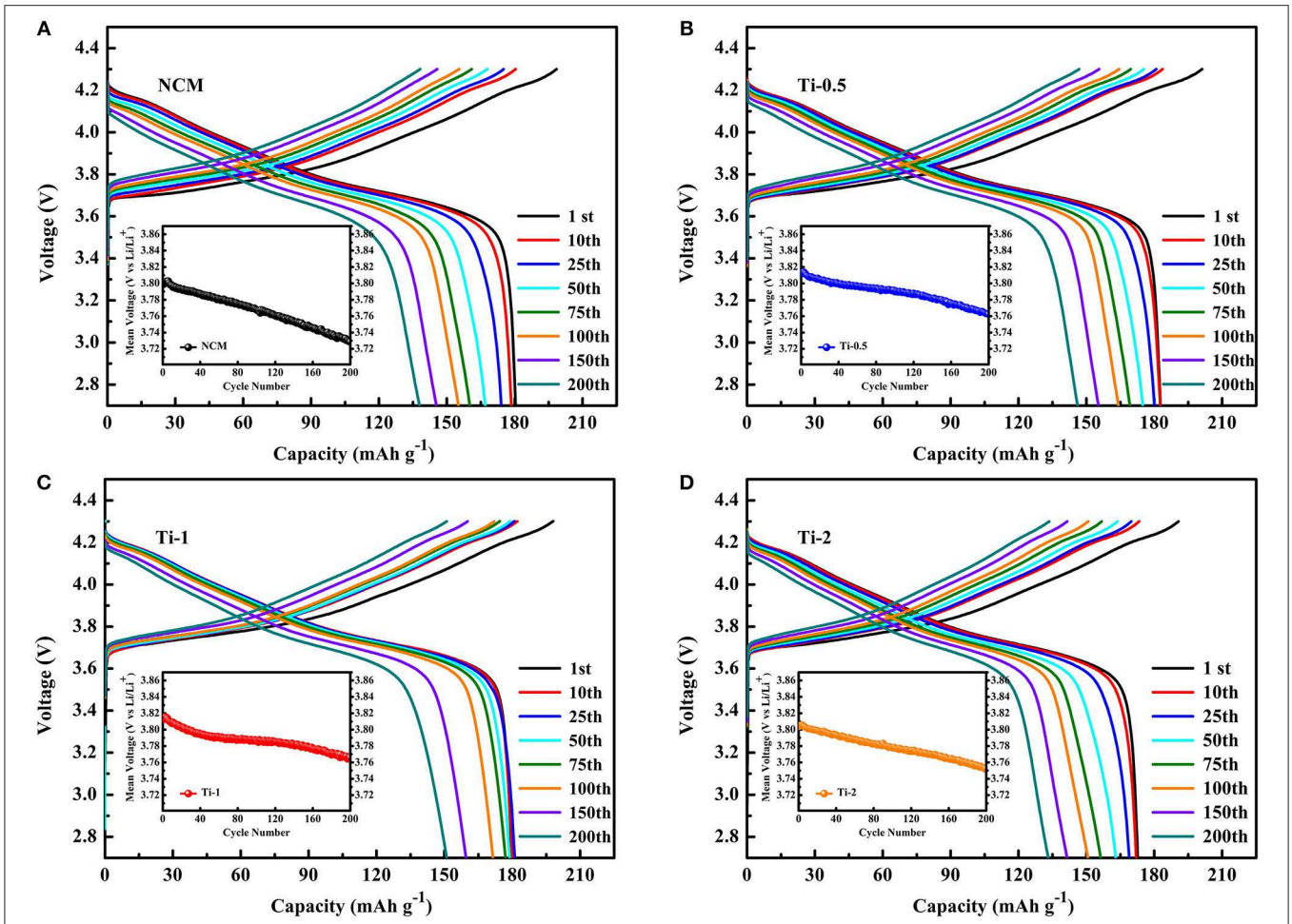

FIGURE 4 | Charge-discharge curves of NCM **(A)**, Ti-0.5 **(B)**, Ti-1 **(C)**, and Ti-2 **(D)** at different cycle number (insets are the midpoint voltage vs. cycle numbers).

electrodes between 2.7 and 4.3 V at the rate of 0.1 C. It can be observed that all the discharge profiles are similar to each other. The initial discharge specific capacity is decreased slightly from 202.24 to 180.95 mAh·g^{-1} with the increasing of Ti amounts. However, the Ti-1 electrode shows the higher Coulombic efficiency of 83.20% than NCM electrode showing Coulombic efficiency of 80.82%, most probably owing to that suitable Ti doping can reduce the irreversible capacity.

The rate performances of the pristine and Ti-doped NCM electrodes at the current density ranging from 0.1 to 10 C are presented in **Figure 3B**. Comparing to the NCM electrode, the Ti-0.5 and Ti-1 electrodes show improved rate capability. Particularly, the Ti-1 electrode maintains a reversible capacity of 145.71 mAh·g^{-1} at high current rates of 10 C, while the NCM cathodes only deliver a specific capacity of 105.52 mAh·g^{-1}. The remarkable rate property is mainly related to the slight enlargement along c axis by Ti doping, which benefits the fast Li ion diffusion. In addition, the cycling performances of all electrodes are compared at 1 C rate in the range of 2.7–4.3 V. As can be seen in **Figure 3C**, the NCM electrode shows fast capacity degradation from 179.03 to 136.88 mAh·g^{-1} after 200 cycles, corresponding to 76.45% capacity retention with 0.118% decay per cycle. In comparison, the Ti-doped electrodes possess the higher capacity retention than pristine electrode, specifically, the Ti-1 electrode maintains 151.01 mAh·g^{-1} with 83.98% capacity retention after 200 cycles, corresponding 0.08% decay per cycle.

Figure 4 shows the charge-discharge curves of NCM, Ti-0.5, Ti-1, Ti-2 electrodes at different cycle number, respectively. It is distinctly observed that the reversible capacity and discharge voltage plateau of the NCM electrode declined rapidly with increasing cycle, while the Ti-1 electrode shows stable charge-discharge curves and discharge capacity, indicating that suitable Ti doping can effectively improve the cycle stability of NCM and alleviate the voltage reduction during cycling.

To further understand the different charge-discharge behavior of the NCM and Ti-doped electrodes, the differential capacity (dQ/dV) curves are shown in **Figure 5**. All curves display three couples of redox peaks, which are ascribed to the phase transition of hexagonal (H1) to monoclinic (M), monoclinic (M) to hexagonal (H2), and hexagonal (H2) to hexagonal (H3) during the delithiation/lithiation processes. As shown in **Figure 5A**, the oxidation peaks for the pristine NCM shift to high potential

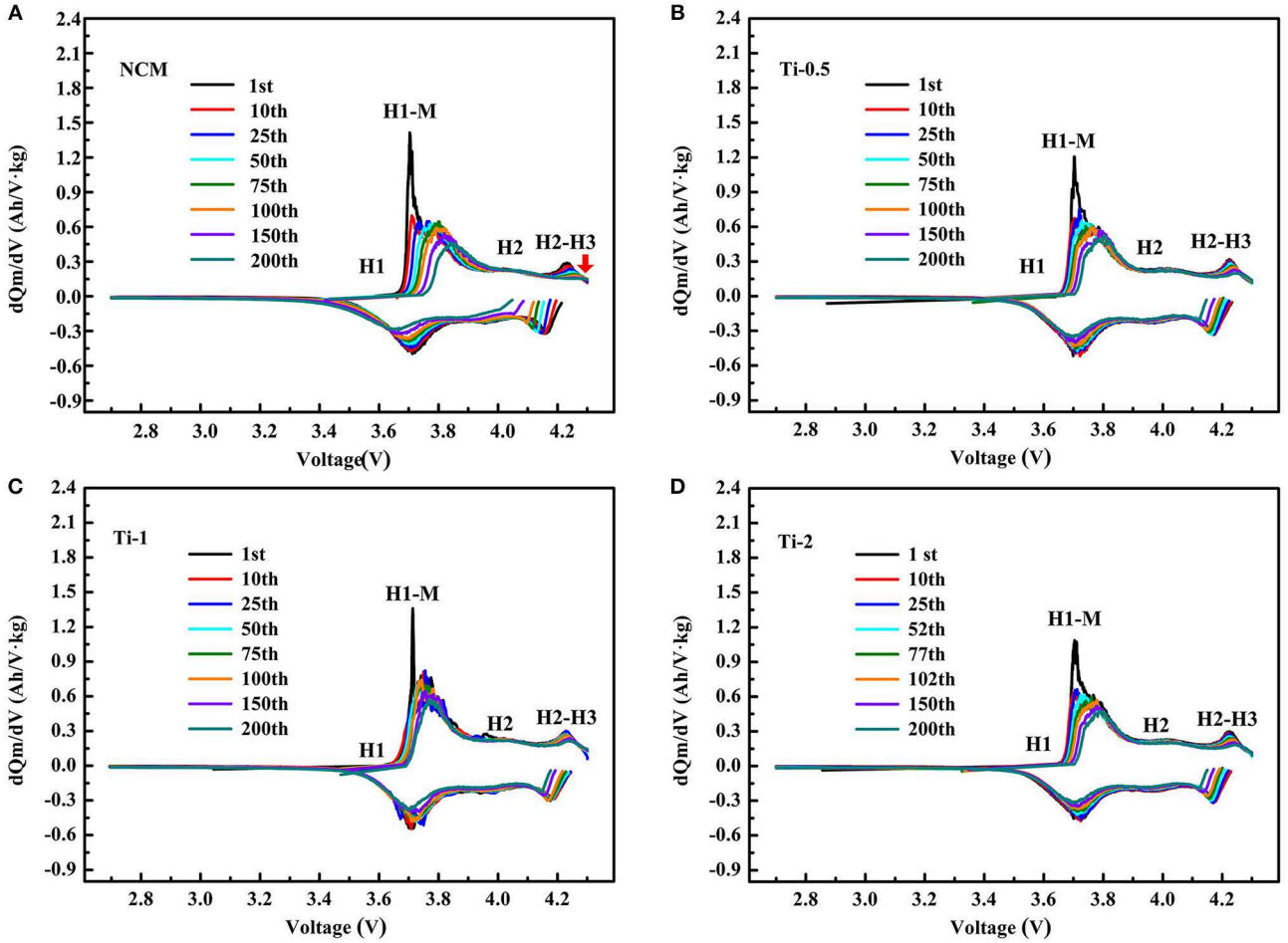

FIGURE 5 | Differential capacity vs. cell potential curves of different numbers for the NCM **(A)**, Ti-0.5 **(B)**, Ti-1 **(C)**, and Ti-2 **(D)** electrodes.

significantly, while the reduction peaks shift to low potential during cycling, and the corresponding peaks areas are greatly decreased. As shows, the poor reversibility of H2-H3 phase transition and gradually loss of H3 phase associated with poor structural stability of NCM, should take responsibility for the faster capacity drop of the NCM sample. In contrast, the voltage hysteresis for the Ti-doped electrodes is substantially suppressed. For Ti-1, the negligible change of overlap of dQ/dV curves within 200 cycles suggests the lower polarization and better H2-H3 reversibility of the modified electrodes. In conclusion, the Ti-doped electrodes exhibit improved electrochemical properties, which can be attributed to the better structural stability due to the enhanced reversibility of H2-H3 phase transition.

To understand the relationship between electrochemical degradation and resistance parameters, EIS measurements are conducted for all samples in a charged state of 4.3 V after different cycle numbers. **Figures 6A–C** show the Nyquist plots of the electrodes and corresponding equivalent circuit at the fresh cells, after 5 and 200 cycles, respectively. The curves consist of a semicircle and a sloped line in **Figure 6A**. The semicircle is regarded as the charge transfer resistance (R_{ct}) and the followed sloped line relates to the Warburg impedance (Z_w). Moreover, the intercept with real axis (Z') is assigned to the solution resistance (R_s). Differently, **Figures 6B,C** display an increased semicircle in the high-frequency region, which can be ascribed to the film resistance (R_f) due to the solid electrolyte interface (SEI) film formed on the electrode during high-voltage cycling. The fitting results of the electrodes based on the equivalent circuit are summarized in **Table 2**. The R_{ct} of the NCM electrode in the fresh cell is 96.5 Ω, and the resistance increases dramatically after 200 cycles (1372 Ω). In comparison, the Ti-doped electrodes exhibit more stable values of R_{ct} during cycling, implying better structural stability. According to the relationships between Z'_{re} and $\omega^{-1/2}$ in the low-frequency region (**Figure 6D**), the lithium ion diffusion coefficient (D_{Li+}) is calculated and the results are listed in **Table 2** (Li et al., 2015, 2016b; Liu et al., 2019; Zhu et al., 2019). Notably, the Ti-1 electrode shows highest D_{Li+} values than that of the NCM electrode after 200 cycles, contributing to the best rate property among all electrodes. The EIS results demonstrate that the Ti-doped samples exhibit better

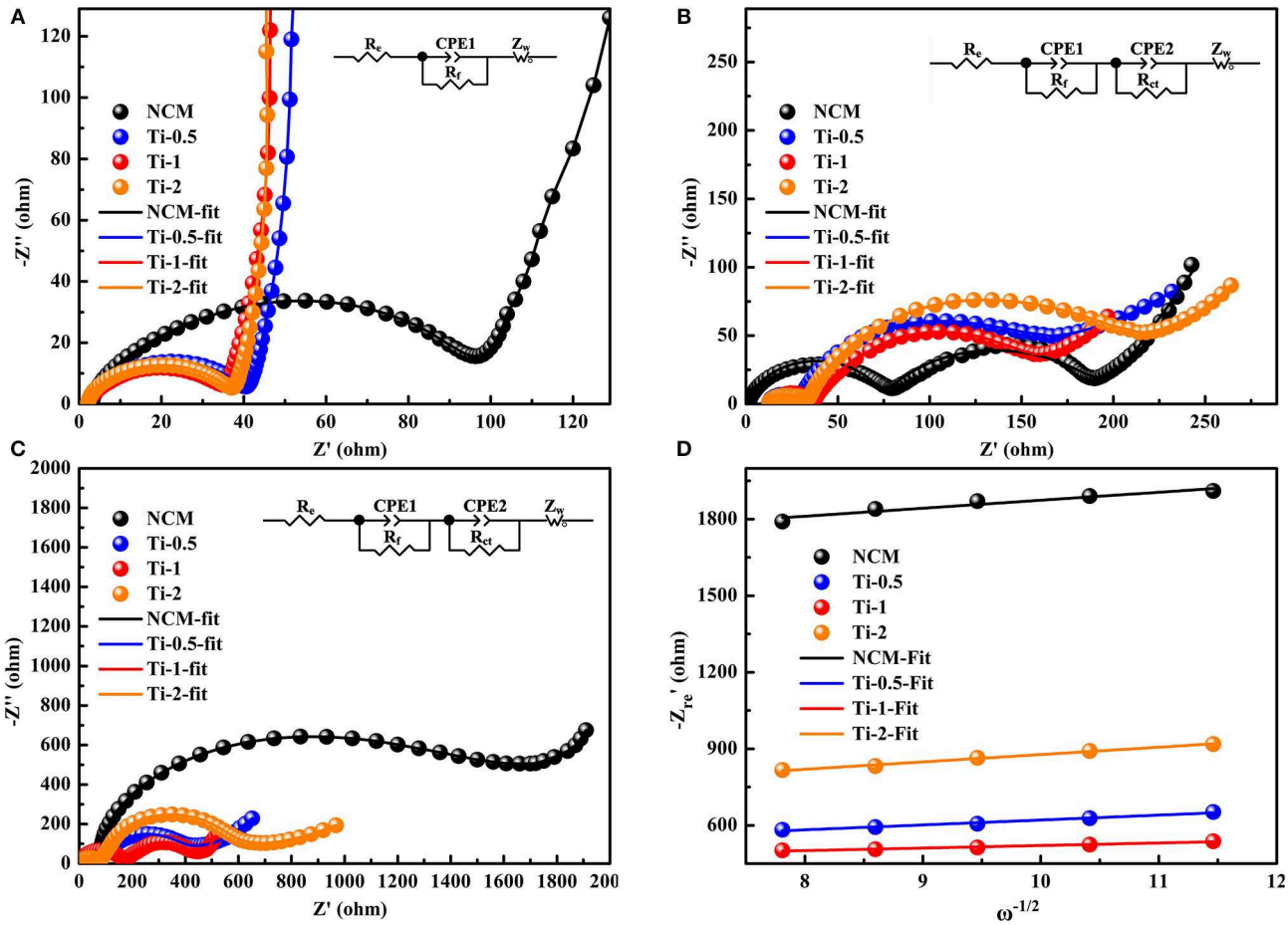

FIGURE 6 | Nyquist plots of **(A)** as-prepared electrodes before cycling, **(B)** all electrodes at the charge state of 4.3V after 5th, **(C)** all electrodes at the charge state of 4.3V after 200th (insets are the equivalent circuit models), **(D)** the relationships between Z'_{re} and $\omega^{-1/2}$ based on the 200th cycles.

TABLE 2 | The values of R_f, R_{ct}, and D_{Li}^+ for as-prepared electrodes and cycled electrode.

Samples	As-prepared	5th		200th		
	R_{ct} (Ω)	R_f (Ω)	R_{ct} (Ω)	R_f (Ω)	R_{ct} (Ω)	D_{Li}^+ ($cm^2\ s^{-1}$)
NCM	96.5	71.24	121.7	85	1372	7.13×10^{-13}
Ti-0.5	39.3	31.3	102.1	87	351	7.79×10^{-13}
Ti-1	37.2	32.4	103.2	155	263	2.01×10^{-12}
Ti-2	35.3	31.7	163.2	124	445	7.19×10^{-13}

kinetic behavior than those of the NCM, which can be related to the outstanding structural stability by the modification of Ti doping.

To study the redox behavior associated with phase transition during battery operation, Cyclic voltammetry (CV) is employed at a scan rate of 0.1 $mV{\cdot}s^{-1}$ between 2.7 and 4.5 V. **Figures 7A–D** illustrate the first three CV curves of all samples, respectively. For these CV curves, three pairs of oxidation/reduction peaks are observed, which can be assigned to the phase transitions from H1 to M, H2 and H3. It is worth noting that the H2-H3 phase transition can induce sharp lattice contraction along c axis, result in the anisotropic changes of cell volume (Yang and Xia, 2016; Xu et al., 2019). Apparently, the peak intensity of the phase transition of H2-H3 gradually become weaker with increasing Ti concentration, implying that the Ti doping could suppress the detrimental phase transition during charging/discharging cycles. In other words, the structural stability of the NCM is improved by Ti doping.

CONCLUSION

To address the problem related to the structural degradations of NCM, Ti is intentionally introduced to enhance the structural stability and electrochemical performance of $LiNi_{0.8}Co_{0.1}Mn_{0.1}O_2$. The Ti-doped $LiNi_{0.8}Co_{0.1}Mn_{0.1}O_2$ (0, 0.5, 1, 2%) composites are successfully synthesized via one-step calcination method. Among them, the $Li(Ni_{0.8}Co_{0.1}Mn_{0.1})_{0.99}Ti_{0.01}O_2$ sample exhibits the best electrochemical performance, it maintains a reversible capacity of 151.01 $mAh{\cdot}g^{-1}$ after 200 cycles at 1 C with

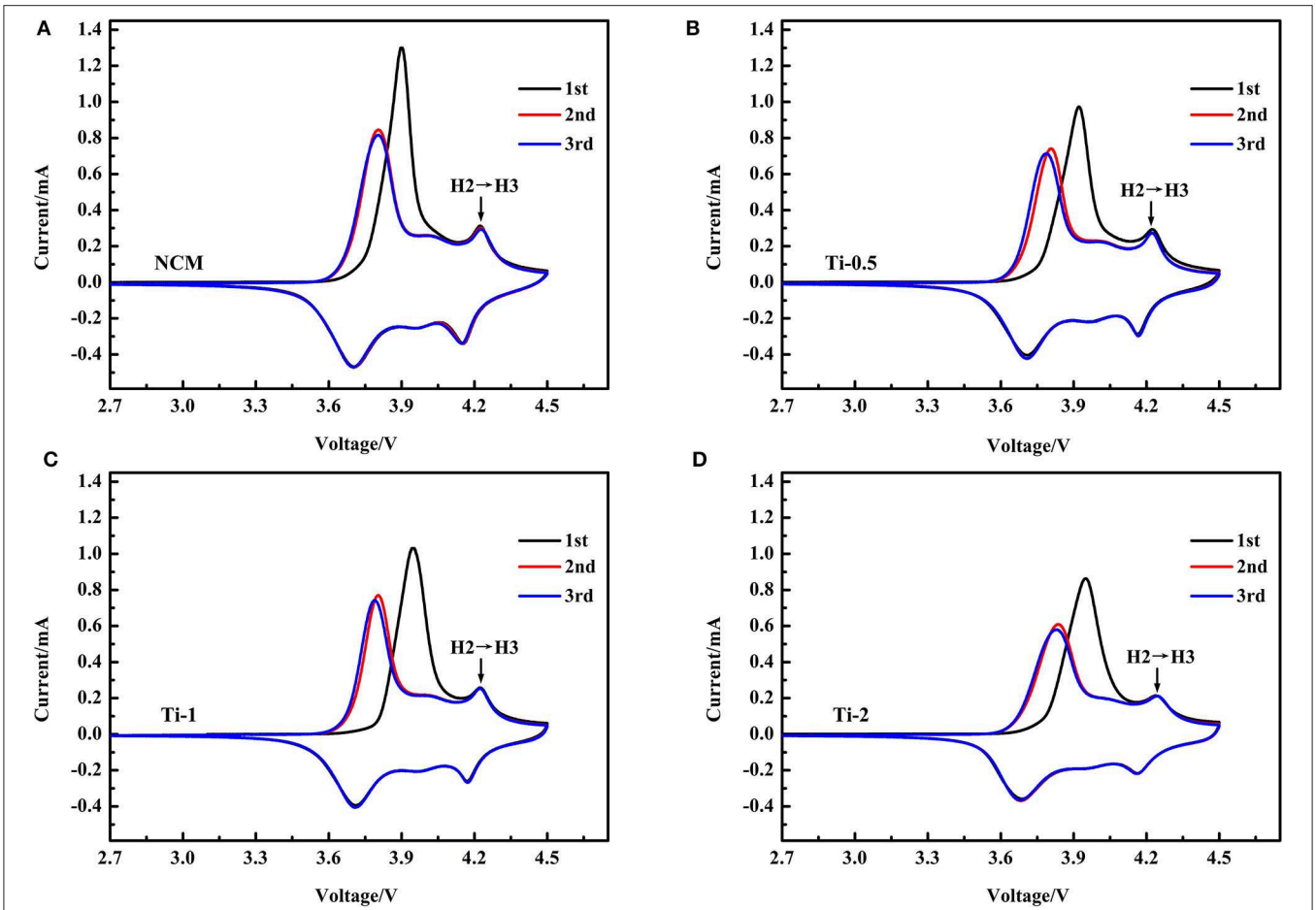

FIGURE 7 | CV curves of NCM **(A)**, Ti-0.5 **(B)**, Ti-1 **(C)**, and Ti-2 **(D)** for first three cycles in the voltage range of 2.7–4.5 V.

83.98% capacity retention. The superior electrochemical performance can be ascribed to two aspects: (1) the enhanced reversibility of H2-H3 phase transitions and the lossless H3 phase during prolonged cycling; (2) the lower electrochemical impedance and the improved Li-ion diffusion ability.

DATA AVAILABILITY

All datasets generated for this study are included in the manuscript/supplementary files.

AUTHOR CONTRIBUTIONS

LL, JieC, and HY: conceived the idea. JieC, HY, and LL: prepared all materials. JieC, HY, and TL: conducted SEM experiments. CL, JiaC, ZL, and LX: conducted XRD experiments. LL, JieC, and HY: analyzed the data. JieC and HY: wrote the manuscript. HT, ZC, and JD: commented on the manuscript. LL: supervised the implementation of the project.

FUNDING

This work was supported by the National Natural Science Foundation of China (Grant Nos. 51774051 and 51502350), this work was also supported by the Changsha City Fund for Distinguished and Innovative Young Scholars (Grant No. KQ1707014), the Hunan Provincial Natural Science Foundation of China (No. 2018JJ2428), the Scientific Research Fund of Hunan Provincial Education Department (No. 17B002), and the Key Laboratory of Modeling and Monitoring on the Near-Earth Electromagnetic Environments (No. 20170109).

REFERENCES

Chen, J., Li, L., Wu, L., Yao, Q., Yang, H., Liu, Z., et al. (2018). Enhanced cycle stability of $Na_{0.9}Ni_{0.45}Mn_{0.55}O_2$ through tailoring O3/P2 hybrid structures for sodium-ion batteries. *J. Power Sources* 406, 110–117. doi: 10.1016/j.jpowsour.2018.10.058

Chen, M., Zhao, E., Chen, D., Wu, M., Han, S., Huang, Q., et al. (2017). Decreasing Li/Ni disorder and improving the electrochemical performances

of Ni-Rich $LiNi_{0.8}Co_{0.1}Mn_{0.1}O_2$ by Ca doping. *Inorg. Chem.* 56, 8355–8362. doi: 10.1021/acs.inorgchem.7b01035

Chen, Z., Xu, M., Du, B., Zhu, H., Xie, T., and Wang, W. (2014). Morphology control of lithium iron phosphate nanoparticles by soluble starch-assisted hydrothermal synthesis. *J. Power Sources* 272, 837–844. doi: 10.1016/j.jpowsour.2014.09.019

Chen, Z., Yan, X., Xu, M., Cao, K., Zhu, H., Li, L., et al. (2017). Building honeycomb-like hollow microsphere architecture in a bubble template reaction for high-performance lithium-rich layered oxide cathode materials. *ACS Appl. Mater. Interfaces* 9, 30617–30625. doi: 10.1021/acsami.7b07542

Gao, S., Zhan, X., and Cheng, Y.-T. (2019). Structural, electrochemical and Li-ion transport properties of Zr-modified $LiNi_{0.8}Co_{0.1}Mn_{0.1}O_2$ positive electrode materials for Li-ion batteries. *J. Power Sources* 410–411, 45–52. doi: 10.1016/j.jpowsour.2018.10.094

He, T., Lu, Y., Su, Y., Bao, L., Tan, J., Chen, L., et al. (2018). Sufficient utilization of zirconium ions to improve the structure and surface properties of nickel-rich cathode materials for lithium-ion batteries. *ChemSusChem* 11, 1639–1648. doi: 10.1002/cssc.201702451

Lee, E. J., Chen, Z., Noh, H. J., Nam, S. C., Kang, S., Kim, D. H., et al. (2014). Development of microstrain in aged lithium transition metal oxides. *Nano Lett.* 14, 4873–4880. doi: 10.1021/nl5022859

Li, H., Zhou, P., Liu, F., Li, H., Cheng, F., and Chen, J. (2019). Stabilizing nickel-rich layered oxide cathodes by magnesium doping for rechargeable lithium-ion batteries. *Chem. Sci.* 10, 1374–1379. doi: 10.1039/C8SC03385D

Li, L., Chen, Z., Zhang, Q., Xu, M., Zhou, X., Zhu, H., et al. (2015). A hydrolysis-hydrothermal route for the synthesis of ultrathin $LiAlO_2$-inlaid $LiNi_{0.5}Co_{0.2}Mn_{0.3}O_2$ as a high-performance cathode material for lithium ion batteries. *J. Mater. Chem. A* 3, 894–904. doi: 10.1039/C4TA05902F

Li, L., Xu, M., Yao, Q., Chen, Z., Song, L., Zhang, Z., et al. (2016a). Alleviating surface degradation of nickel-rich layered oxide cathode material by encapsulating with nanoscale Li-ions/electrons superionic conductors hybrid membrane for advanced Li-ion batteries. *ACS Appl. Mater. Interfaces* 8, 30879–30889. doi: 10.1021/acsami.6b09197

Li, L., Yao, Q., Zhu, H., Chen, Z., Song, L., and Duan, J. (2016b). Effect of Al substitution sites on $Li_{1-x}Al_x(Ni_{0.5}Co_{0.2}Mn_{0.3})_{1-y}Al_yO_2$ cathode materials for lithium ion batteries. *J. Alloys Compd.* 686, 30–37. doi: 10.1016/j.jallcom.2016.05.333

Li, M., Lu, J., Chen, Z., and Amine, K. (2018). 30 years of lithium-ion batteries. *Adv. Mater. Weinheim.* 30, 1800561–1800584. doi: 10.1002/adma.201800561

Lin, F., Markus, I. M., Nordlund, D., Weng, T.-C., Asta, M. D., Xin, H. L., et al. (2014a). Surface reconstruction and chemical evolution of stoichiometric layered cathode materials for lithium-ion batteries. *Nat. Commun.* 5, 3529–3537. doi: 10.1038/ncomms4529

Lin, F., Nordlund, D., Weng, T.-C., Zhu, Y. E., Ban, C., Richards, R. M., et al. (2014b). Phase evolution for conversion reaction electrodes in lithium-ion batteries. *Nat. Commun.* 5, 3358–3366. doi: 10.1038/ncomms4358

Liu, D., Fan, X., Li, Z., Liu, T., Sun, M., Qian, C., et al. (2019). A cation/anion co-doped $Li_{1.12}Na_{0.08}Ni_{0.2}Mn_{0.6}O_{1.95}F_{0.05}$ cathode for lithium ion batteries. *Nano Energy* 58, 786–796. doi: 10.1016/j.nanoen.2019.01.080

Manthiram, A., Knigth, J. C., Myung, S.-T., Oh, S.-M., and Sun, Y.-K. (2016). Nickel-rich and lithium-rich layered oxide cathodes: progress and perspectives. *Adv. Energy Mater.* 6, 1501010–1501032. doi: 10.1002/aenm.201501010

Meng, K., Wang, Z., Guo, H., and Li, X. (2017). Enhanced cycling stability of $LiNi_{0.8}Co_{0.1}Mn_{0.1}O_2$ by reducing surface oxygen defects. *Electrochim. Acta* 234, 99–107. doi: 10.1016/j.electacta.2017.03.054

Myung, S.-T., Maglia, F., Park, K.-J., Yoon, C. S., Lamp, P., Kim, S.-J., et al. (2016). Nickel-rich layered cathode materials for automotive lithium-ion batteries: achievements and perspectives. *ACS Energy Lett.* 2, 196–223. doi: 10.1021/acsenergylett.6b00594

Nam, K.-W., Bak, S.-M., Hu, E., Yu, X., Zhou, Y., Wang, X., et al. (2013). Combining *in situ* synchrotron x-ray diffraction and absorption techniques with transmission electron microscopy to study the origin of thermal instability in overcharged cathode materials for lithium-ion batteries. *Adv. Funct. Mater.* 23, 1047–1063. doi: 10.1002/adfm.201200693

Park, K.-J., Jung, H.-G., Kuo, L.-Y., Kaghazchi, P., Yoon, C. S., and Sun, Y.-K. (2018). Improved cycling stability of $Li[Ni_{0.90}Co_{0.05}Mn_{0.05}]O_2$ through microstructure modification by boron doping for Li-ion batteries. *Adv. Energy. Mater.* 8, 1801202–1801210. doi: 10.1002/aenm.201801202

Ryu, H.-H., Park, K.-J., Yoon, C. S., and Sun, Y.-K. (2018b). Capacity fading of Ni-Rich $Li[Ni_xCo_yMn_{1-x-y}]O_2$ ($0.6 \leq x \leq 0.95$) cathodes for high-energy-density lithium-ion batteries: bulk or surface degradation? *Chem. Mater.* 30, 1155–1163. doi: 10.1021/acs.chemmater.7b05269

Ryu, H. H., Park, G. T., Yoon, C. S., and Sun, Y. K. (2018a). Microstructural degradation of Ni-Rich $Li[Ni_xCo_yMn_{1-x-y}]O_2$ cathodes during accelerated calendar aging. *Small* 14, 1803179–1803186. doi: 10.1002/smll.201803179

Su, M., Wan, H., Liu, Y., Xiao, W., Dou, A., Wang, Z., et al. (2018). Multi-layered carbon coated Si-based composite as anode for lithium-ion batteries. *Powder Technol.* 323, 294–300. doi: 10.1016/j.powtec.2017.09.005

Sun, H.-H., and Manthiram, A. (2017). Impact of microcrack generation and surface degradation on a nickel-rich layered $Li[Ni_{0.9}Co_{0.05}Mn_{0.05}]O_2$ cathode for lithium-ion batteries. *Chem. Mater.* 29, 8486–8493. doi: 10.1021/acs.chemmater.7b03268

Susai, F. A., Kovacheva, D., Chakraborty, A., Kravchuk, T., Ravikumar, R., Talianker, M., et al. (2019). Improving performance of LiNi0.8Co0.1Mn0.1O2 cathode materials for lithium-ion batteries by doping with molybdenum-ions: theoretical and experimental studies. *ACS Appl. Energy Mater.* 2, 4521–4534. doi: 10.1021/acsaem.9b00767

Weigel, T., Schipper, F., Erickson, E. M., Susai, F. A., Markovsky, B., and Aurbach, D. (2019). Structural and electrochemical aspects of LiNi0.8Co0.1Mn0.1O2 cathode materials doped by various cations. *ACS Energy Lett.* 4, 508–516. doi: 10.1021/acsenergylett.8b02302

Wu, C., Lou, X., and Jia, C. (2019). Porous Ni-Mo-Co hydroxide nanoflakes on carbon cloth for supercapacitor application. *J. Nanosci. Nanotechnol.* 19, 272–276. doi: 10.1166/jnn.2019.16450

Wu, F., Li, Q., Chen, L., Lu, Y., Su, Y., Bao, L., et al. (2019a). Use of Ce to reinforce the interface of Ni-rich $LiNi_{0.8}Co_{0.1}Mn_{0.1}O_2$ cathode materials for lithium-ion batteries under high operating voltage. *ChemSusChem* 12, 935–943. doi: 10.1002/cssc.201802304

Wu, F., Liu, N., Chen, L., Su, Y., Tan, G., Bao, L., et al. (2019b). Improving the reversibility of the H2-H3 phase transitions for layered Ni-rich oxide cathode towards retarded structural transition and enhanced cycle stability. *Nano Energy* 59, 50–57. doi: 10.1016/j.nanoen.2019.02.027

Wu, L., Shi, S., Zhang, X., Yang, Y., Liu, J., Tang, S., et al. (2018). Room-temperature pre-reduction of spinning solution for the synthesis of $Na_3V_2(PO_4)_3$/C nanofibers as high-performance cathode materials for Na-ion batteries. *Electrochim. Acta* 274, 233–241. doi: 10.1016/j.electacta.2018.04.122

Wu, L., Zheng, J., Wang, L., Xiong, X., Shao, Y., Wang, G., et al. (2019). PPy-encapsulated SnS_2 nanosheets stabilized by defects on a TiO_2 support as a durable anode material for lithium-ion batteries. *Angew. Chem. Int. Ed Engl.* 58, 811–815. doi: 10.1002/anie.201811784

Xia, L., Zhang, Q., Wu, C., Liu, Y., Ding, M., Ye, J., et al. (2019). Graphene coated carbon felt as a high-performance electrode for all vanadium redox flow batteries. *Surf. Coat. Technol.* 358, 153–158. doi: 10.1016/j.surfcoat.2018.11.024

Xia, Y., Zheng, J., Wang, C., and Gu, M. (2018). Designing principle for Ni-rich cathode materials with high energy density for practical applications. *Nano Energy* 49, 434–452. doi: 10.1016/j.nanoen.2018.04.062

Xiao, Z., Xia, N., Song, L., Li, L., Cao, Z., and Zhu, H. (2018). Synthesis of yolk–shell-structured Si@C nanocomposite anode material for lithium-ion battery. *J. Elect Mater.* 47, 6311–6318. doi: 10.1007/s11664-018-6513-1

Xu, M., Fei, L., Lu, W., Chen, Z., Li, T., Liu, Y., et al. (2017). Engineering hetero-epitaxial nanostructures with aligned Li-ion channels in Li-rich layered oxides for high-performance cathode application. *Nano Energy* 35, 271–280. doi: 10.1016/j.nanoen.2017.03.051

Xu, X., Huo, H., Jian, J., Wang, L., Zhu, H., Xu, S., et al. (2019). Radially oriented single-crystal primary nanosheets enable ultrahigh rate and cycling properties of $LiNi_{0.8}Co_{0.1}Mn_{0.1}O_2$ cathode material for lithium-ion batteries. *Adv. Energy. Mater.* 9, 1803963–1803971. doi: 10.1002/aenm.201803963

Yang, H., Wu, H. H., Ge, M., Li, L., Yuan, Y., Yao, Q., et al. (2019). Simultaneously dual modification of Ni-rich layered oxide cathode for high-energy lithium-ion batteries. *Adv. Funct. Mater.* 29, 1808825–1808837. doi: 10.1002/adfm.201808825

Yang, J., and Xia, Y. (2016). Suppressing the phase transition of the layered Ni-rich oxide cathode during high-voltage cycling by introducing low-content Li_2MnO_3. *ACS Appl. Mater. Interfaces* 8, 1297–1308. doi: 10.1021/acsami.5b09938

Ye, X., Lin, Z., Liang, S., Huang, X., Qiu, X., Qiu, Y., et al. (2019). Upcycling of electroplating sludge into ultrafine Sn@C nanorods with highly stable lithium storage performance. *Nano Lett.* 19, 1860–1866. doi: 10.1021/acs.nanolett.8b04944

Yoon, C. S., Ryu, H.-H., Park, G.-T., Kim, J.-H., Kim, K.-H., and Sun, Y.-K. (2018). Extracting maximum capacity from Ni-rich $Li[Ni_{0.95}Co_{0.025}Mn_{0.025}]O_2$ cathodes for high-energy-density lithium-ion batteries. *J. Mater. Chem. A* 6, 4126–4132. doi: 10.1039/C7TA11346C

Zhang, B., Li, L., and Zheng, J. (2012). Characterization of multiple metals (Cr, Mg) substituted $LiNi_{0.8}Co_{0.1}Mn_{0.1}O_2$ cathode materials for lithium ion battery. *J. Alloys Compd.* 520, 190–194. doi: 10.1016/j.jallcom.2012.01.004

Zheng, S., Liu, D., Tao, L., Fan, X., Liu, K., Liang, G., et al. (2019). Electrochemistry and redox characterization of rock-salt-type lithium metal oxides $Li_{1+z/3}Ni_{1/2-z/2}Ti_{1/2+z/6}O_2$ for Li-ion batteries. *J. Alloys Compd.* 773, 1–10. doi: 10.1016/j.jallcom.2018.09.261

Zhu, C., Wei, D., Wu, Y., Zhang, Z., Zhang, G., Duan, J., et al. (2019). Controllable construction of interconnected SnO_x/N-doped carbon/carbon composite for enhanced-performance lithium-ion batteries anodes. *J. Alloys Compd.* 778, 731–740. doi: 10.1016/j.jallcom.2018.11.233

Conflict of Interest Statement: The authors declare that the research was conducted in the absence of any commercial or financial relationships that could be construed as a potential conflict of interest.

frontiers in Chemistry

ORIGINAL RESEARCH
published: 18 July 2019
doi: 10.3389/fchem.2019.00494

Concentrated LiODFB Electrolyte for Lithium Metal Batteries

Juan Yu[1], *Na Gao*[1], *Jiaxin Peng*[1], *Nani Ma*[1], *Xiaoyan Liu*[2], *Chao Shen*[2], *Keyu Xie*[2] *and Zhao Fang*[1]*

[1] School of Metallurgical Engineering, Xi'an University of Architecture and Technology, Xi'an, China, [2] State Key Laboratory of Solidification Processing, Center for Nano Energy Materials, School of Materials Science and Engineering, Northwestern Polytechnical University and Shaanxi Joint Laboratory of Graphene (NPU), Xi'an, China

Nowadays, lithium (Li) metal batteries arouse widespread concerns due to its ultrahigh specific capacity (3,860 mAh g^{-1}). However, the growth of Li dendrites has always limited their industrial development. In this paper, the use of concentrated electrolyte with lithium difluoro(oxalate)borate (LiODFB) salt in 1, 2-dimethoxyethane (DME) enables the good cycling of a Li metal anode at high Coulombic efficiency (up to 98.1%) without dendrite growth. Furthermore, a Li/Li cell can be cycled at 1 mA cm^{-2} for over 3,000 h. Besides, compared to conventional $LiPF_6$-carbonate electrolyte, Li/$LiFePO_4$ cells with 4 M LiODFB-DME exhibit superior electrochemical performances, especially at high temperature (65°C). These outstanding performances can be certified to the increased availability of Li^+ concentration and the merits of LiODFB salt. We believe that the concentrated LiODFB electrolyte is help to enable practical applications for Li metal anode in rechargeable batteries.

Keywords: Li-metal batteries, concentrated electrolyte, LiODFB, high temperature, dendrites free

OPEN ACCESS

Edited by:
Junchao Zheng,
Central South University, China

Reviewed by:
Haisheng Fang,
Kunming University of Science and Technology, China
Chaoyi Chen,
Guizhou University, China
Ying Hong Yang,
Northeastern University, China

***Correspondence:**
Zhao Fang
fangzhao@xauat.edu.cn

Specialty section:
This article was submitted to Electrochemistry, a section of the journal Frontiers in Chemistry

Received: *21 April 2019*
Accepted: *26 June 2019*
Published: *18 July 2019*

Citation:
Yu J, Gao N, Peng J, Ma N, Liu X, Shen C, Xie K and Fang Z (2019) Concentrated LiODFB Electrolyte for Lithium Metal Batteries. Front. Chem. 7:494. doi: 10.3389/fchem.2019.00494

INTRODUCTION

In the past several decades, Li-ion batteries have played successful role in the consumable electronic device market (Etacheri et al., 2011; Goodenough and Kim, 2014). However, the limited specific capacity of the graphite anode limits its wider applications. The theoretical capacity of graphite is only 372 mAh g^{-1}, so it is difficult to achieve the urgent need for high-energy density batteries to adapt to the electrical miniaturization trend (Placke et al., 2017). Based on this reason, the Li metal batteries (LMBs) have attracted wide attention because of its high theoretical specific capacity of 3,860 mAh g^{-1}, small density of 0.534 g cm^{-3} and the relatively negative electrochemical potential (−3.040 V vs. Li/Li^+) (Zhamu et al., 2012). However, the shortcomings of LMBs are also a headache, such as unsatisfied Coulombic efficiency (CE) and dendritic Li growth. In addition, poor cycle performance caused by Li dendrites seriously affected the commercial development of LMBs.

Significant efforts have been made in the past to solve these problems, including prepare the current collector (Yang et al., 2015; Liang et al., 2016; Zhang et al., 2016; Shi et al., 2017), *ex-situ* protective coating of Li anode (Thompson et al., 2011; Kozen et al., 2015), introduce the battery intermediate protective layer (Liang et al., 2015; Wu et al., 2015; Cheng et al., 2016; Xie et al., 2016, 2017), and electrolyte modification. Electrolyte, which occupies 15% of the weight and about 32% of the volume of the entire battery, is a key part of a battery (Cekic-Laskovic et al., 2017). Therefore, the study of electrolyte on the development of Li metal secondary battery is of great significance. Meanwhile, compared to other modification methods, electrolyte modification is more convenient and cost-effective. Till now, electrolyte research progress more or less has been made to

address the dendrite problem. Nevertheless, the compatibility of these electrolytes with cathode has usually been overlooked. For example, some film-forming electrolyte additives, such as vinylene carbonate (VC) and fluoroethylene carbonate (FEC) are helpful to change Li dendrite formation nature (Aurbach et al., 2003; Jung et al., 2013; Webb et al., 2014; Qian et al., 2016; Pritzl et al., 2017; Xu et al., 2017), but the cell's internal resistance is greatly increased, particularly after long-term cycling, and thus limits their wide applications.

Recently, the concept of high concentrated electrolyte gets into the eyes of people. Suo et al. reported a new class of non-aqueous liquid "Solvent-in-Salt" electrolytes and applied them in Li-S batteries. It is demonstrated that the use of "Solvent-in-Salt" electrolyte inhibits the dissolution of polysulphide and protects metallic Li anodes against the formation of Li dendrites, effectively (Suo et al., 2013). A significant breakthrough has been achieved by Qian et al. (2015). They found that, with 4 M lithium bis(fluorosulfonyl)imide (LiFSI) in DME as the electrolyte, a Li/Li cell can be cycled at for more than 6,000 cycles. Meanwhile, a Cu/Li cell can be cycled for more than 1,000 cycles with an average CE of 98.4%, without dendrite growth. Nevertheless, the compatibility of the electrolyte with the cathode materials has not been investigated.

Generally, LiFSI has inherent characteristics of corrosion of aluminum (Al) foil and other metal parts in the battery (Abouimrane et al., 2009; Li et al., 2011). To solve this problem, Park et al. found that lithium borate salts are the ideal additives as corrosion inhibitors in LiFSI electrolytes. The inhibition ability of Al is revealed to be in the following order: lithium oxalyldifluoroborate (LiODFB) > lithium tetrafluoroborate ($LiBF_4$) > lithium hexafluorophosphate ($LiPF_6$) > lithium bis(oxalato)borate (LiBOB) (Park et al., 2015). Noticed that LiODFB is considered to combine the half structures of LiBOB and $LiBF_4$, and thus, it combines the advantages of LiBOB and $LiBF_4$ (Zhang, 2006). The main advantages of this salt is given by low viscosity, high ionic conductivity, good film-forming, high temperature performance, good compatibility with the positive electrode, passivation of Li foil and so on (Liu et al., 2007; Zugmann et al., 2011; Wu et al., 2012; Zhou et al., 2012).

However, it should be noted that previous studies (Zhang et al., 2010; Li et al., 2015; Zhou et al., 2016; Bian et al., 2017) only focused on the effect of LiODFB as an additive or auxiliary salt on battery performances. So far, high concentration of LiODFB single salt in ether solvent for LMBs has not been systematically reported before (Zhang et al., 2015; Poyraz et al., 2019; Yamada et al., 2019). Thus, in this work, we first employed the concentrated electrolyte based on LiODFB in LMBs. Due to its increased availability of Li^+ concentration, a highly uniform and stable solid electrolyte interface (SEI) film was formed on Li metal anode without any dendrite. Meanwhile, the compatibility of concentrated LiODFB electrolyte and $LiFePO_4$ cathode was first investigated by the electrochemical performance of Li/$LiFePO_4$ cell at room temperature and high temperature. We found that 4 M LiODFB-DME significantly improve electrochemical performance of $LiFePO_4$ cathode, compared to $LiPF_6$ electrolyte. In particular, at high temperature, the improvement is much greater. In a sense, our work shows concentrated LiODFB electrolyte may have great potential for LMBs.

EXPERIMENTAL SECTION

Electrolytes and Electrode Preparation

The $LiPF_6$ dissolved in ethylene carbonate (EC), ethyl methyl carbonate (EMC), dimethyl carbonate (DMC) with a volume ratio of 1:1:1 was formed 1.0 M $LiPF_6$ electrolyte and used as the blank electrolyte. LiODFB was purchased from Suzhou Fluolyte Co., Ltd., China. LiODFB was dissolved in dimethyl ether (DME) and formed 4 M LiODFB-DME in an Ar-filled glove box (H_2O < 0.1 ppm, O_2 < 0.1 ppm). The electrolytes were stirred to maintain homogeneity, then sealed and stored in the glove box.

The $LiFePO_4$ cathodes were prepared by mixing 80 wt.% $LiFePO_4$ (Aladdin Co., Ltd. China), 10 wt.% conductive carbon, and 10 wt.% polyvinylidene (PVDF, Solef) binder in N-methylpyrrolidone (Kelong, Chengdu). The mixed slurry was coated onto Al foil and then dried overnight at 110°C under vacuum. Disk-shaped electrodes with a diameter of 13 mm were then punched from the foil (the active material loading was 1.52 mg cm^{-2}). CR2016 coin-type cells were assembled in an Ar-filled glove box with an $LiFePO_4$ cathode working electrode, a Li foil counter electrode, and a polypropylene (Celgard 2400) separator; 45 mL of electrolyte was then injected into the cells. Finally, the assembled coin cells were sealed for further tests. Li/Li and Li/Cu cells with different electrolyte solutions and the above-mentioned separator were assembled for further tests.

Electrochemical Measurements

The assembled Li/$LiFePO_4$ coin cells were left to stand for 10 h before galvanostatic precycling for 200 cycles at 1°C (1°C = 170 mAh g^{-1}) between 2.5 and 4.2 V at 25°C using the Land battery test system (Wuhan LANHE Electronics, China). Rate-performance tests were conducted by changing the rate (0.2, 0.5, 1.0, 2.0, 5.0, and 0.2°C) every 10 cycles. Cyclic voltammetry (CV) and electrochemical impedance spectroscopy (EIS) measurements were carried out using a SI-1287 Electrochemical System (Transmission Precision Measurement Company, UK); the CV tests were performed between 2.5 and 4.2 V at a scan rate of 0.1 mV s^{-1} and the EIS tests were performed over 100 kHz to 10 mHz range with an amplitude of 10 mV before and after rate tests. Then the assembled cells were galvanostatic precycled at 65°C.

The current density for the Li metal plating/stripping was set to 1.0 mA cm^{-2} using a Land battery testing station at room temperature. And the deposition time was 1.5 h. The effective area of the Cu foil for Li deposition was 2.11 cm^2. The current density was 1.0 mA cm^{-2} from 0.01 to 1.00 V. Li/Li symmetric cells were assembled with Li metal used as the working and counter electrodes. The batteries were tested in a Tenney JR environmental chamber to ensure the stable temperature during long-term cycling process.

Morphological Characterizations

Scanning electron microscopy (SEM) (FE-SEM, LEO 1530) was employed to observe the surface topography of the $LiFePO_4$

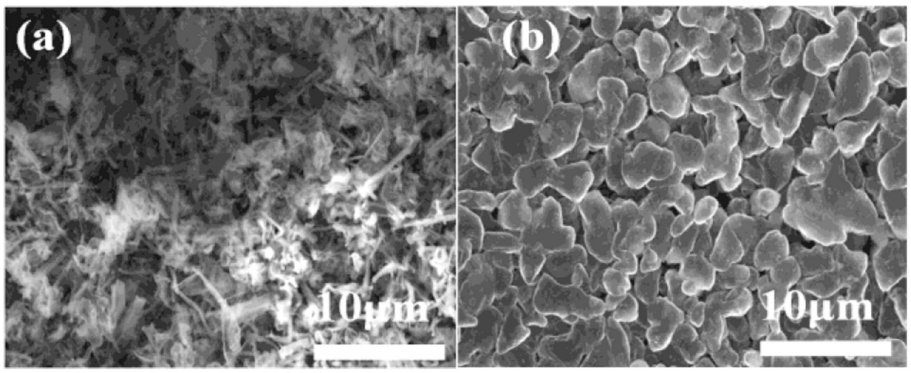

FIGURE 1 | SEM images of the morphologies of Li after plating on Cu substrates in different electrolytes. **(a)** 1 M $LiPF_6$ electrolyte; **(b)** 4 M LiODFB-DME. The current density was 1.0 mA cm^{-2} and the deposition time was 1.5 h.

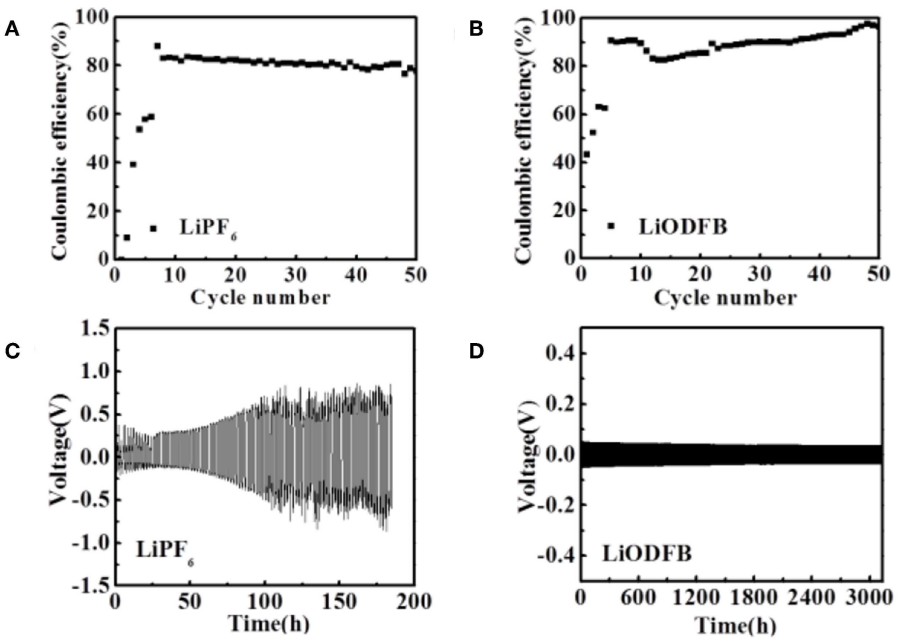

FIGURE 2 | Electrochemical performances of Li/Cu cell **(A,B)** and Li/Li cells **(C,D)** with two electrolytes at a current density of 1.0 mA cm^{-2}. **(A,C)** the 1 M $LiPF_6$ electrolyte; **(B,D)** the 4 M LiODFB-DME.

electrode and Cu foil at different cycling stages at an accelerating voltage of 5 kV. The XPS is tested to further study the composition of SEI film on the Cu foil by the Thermo Electron model K-Alpha surface analysis system. The electrodes retrieved from the cells were thoroughly rinsed in high purity dimethyl carbonate (DMC) solvent for three times and dried under vacuum before transferring to the observation chamber.

EXPERIMENTAL RESULTS

Li Metal Deposition Morphology

The morphologies of Li deposition in both electrolytes are evaluated by using coin-type Cu/Li cells. The surface morphologies of Li electrodes cycled after 1.5 h in different electrolytes is shown in **Figure 1**. In conventional carbonate based electrolyte, significant dendrite morphology can be observed (**Figure 1a**). It can easily pierce most conventional separators, causing the direct contact of the positive and negative electrodes to form a short circuit, and lead to serious security risks. On the contrary, Li deposit from the 4 M LiODFB-DME electrolyte exhibits smooth solid particle morphology (**Figure 1b**), which dramatically inhibits the growth of Li dendrite. Based on the Li metal deposition morphologies, it is reasonable to conclude that the 4 M LiODFB-DME has good negative electrode stability. The SEI film formed in the high concentration electrolyte has high ionic conductivity, which makes a uniform and stable SEI film formed. The uniform and stable SEI film can suppress the growth of Li dendrite.

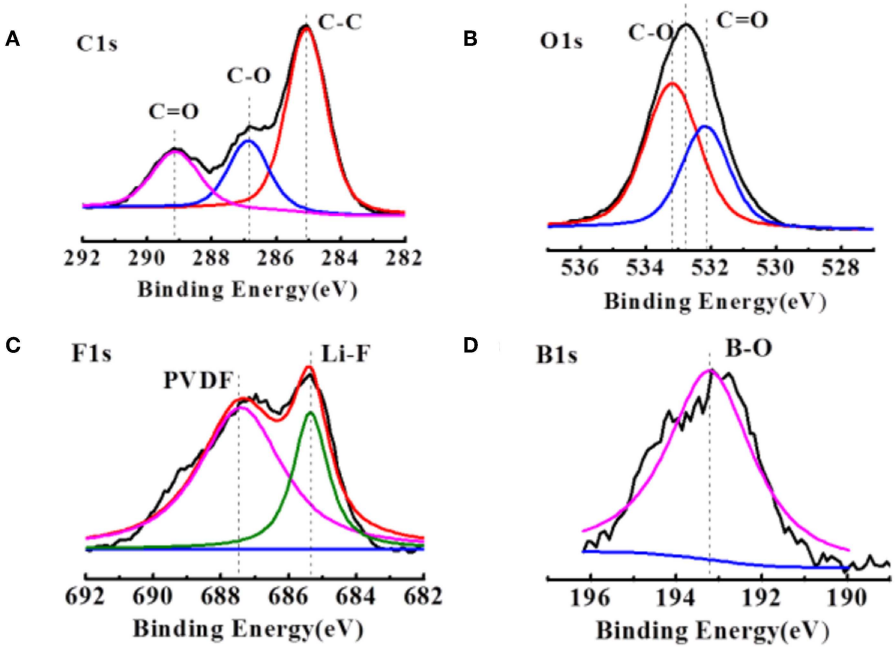

FIGURE 3 | XPS patterns of **(A,B)** the cycled Li anodes in the LiODFB electrolyte. **(C,D)** The cycled electrodes were disassembled from the Li/Li cells after 1.5 h.

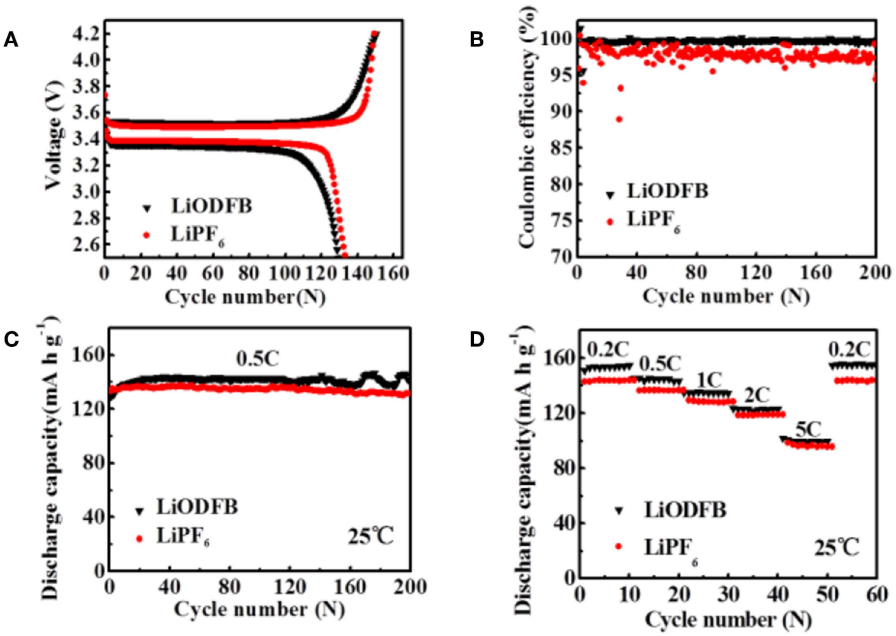

FIGURE 4 | (A) first charge/discharge profiles the Li/$LiFePO_4$ cells, **(B)** CE of Li/$LiFePO_4$ cells; **(C,D)** cycle performance of Li/$LiFePO_4$ cells at 25°C with 4 M LiODFB-DME and 1 M $LiPF_6$, **(D)** rate performances of Li/$LiFePO_4$ cells at 25°C with 4 M LiODFB-DME and 1 M $LiPF_6$.

Li Metal Plating/Stripping Cycling Stability

The impedance evolution of the coin-type Cu/Li cells after 0.5 h and 1.5 h are depicted in **Figure S1**. In the Nyquist plots, the intercept with the abscissa represents the ohmic resistance, particularly the electrolyte resistance in the cell. A significant difference in the impedance between the two electrolytes is observed. After 0.5 and 1.5 h of deposition process, the commercial electrolyte exhibits relatively higher electrode impedance **Figure S1A**. At the same time, 4 M LiODFB-DME electrolyte shows small impedance **Figure S1B**.

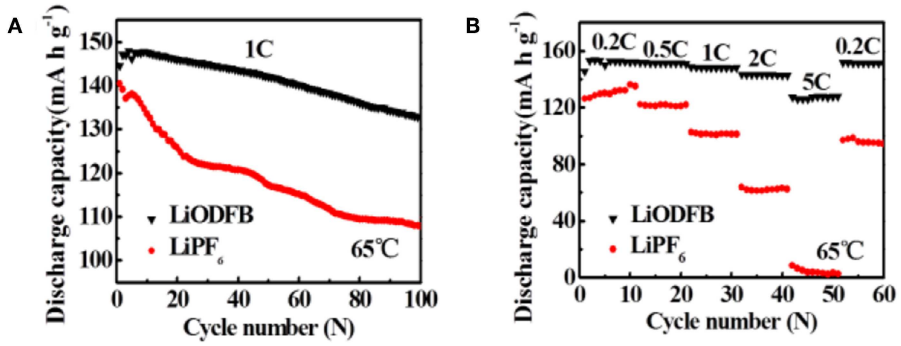

FIGURE 5 | (A) cycle performance of the Li/$LiFePO_4$ cells at 65°C with 4 M LiODFB-DME and 1 M $LiPF_6$, **(B)** rate performance of Li/$LiFePO_4$ cells at 65°C with 4 M LiODFB-DME and 1 M $LiPF_6$.

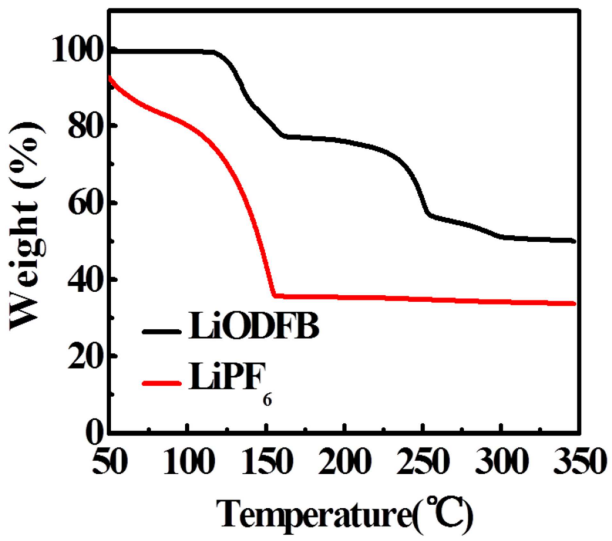

FIGURE 6 | TGA curves of the fully-charged $LiFePO_4$ electrode cycled in LiODFB and $LiPF_6$ electrolytes.

The most possible reason for the small impedance is attributed to the formation of the stable SEI film, which is consistent with the results of a dense surface morphology in **Figure 1b**. Polarization measurements of the Li/Li cells were conducted to understand the effect of different electrolytes on stabling the interface between the Li metal and electrolyte. During this experiment, a constant deposition/dissolution current density of 1.0 mA cm^{-2} was passed through the Li/Li cells for 3,000 h at room temperature. The 1 M $LiPF_6$ electrolyte shows the great over-voltage and an ascending tendency with time (**Figure 2**), which is consistent with previous report (Webb et al., 2014). Surprisingly, the 4 M LiODFB-DME electrolyte appears excellent Li deposition/dissolution performance with the stable and low over-voltage. Polarization is lower than 1 M $LiPF_6$ electrolyte. Besides, influenced by high viscosity, on the one hand, it possibly increases the pressure from the electrolyte to push back growing dendrites, resulting in a more uniform deposition on the surface of the anode. On the other hand, high viscosity limits anion convection near deposition area, which is also helpful to deposit uniformly. All of the above results confirm that the high concentration of LiODFB electrolyte in ether solvent can ensure the cycle stability in the negative.

DISCUSSION

Discussion for the Possible Function Mechanism

Figure 3A compares the C1s spectra of the delithiated graphite electrodes extracted from the cell after several cycles. The dominant peak at 284.6 eV originates mainly from the sp^2 hybridized graphite, but also includes contributions from conductive carbon added into the electrode composites. The broad feature at 286.6 eV is assigned mainly to the C atoms of the C-O-C groups in the poly(ethylene oxide), PEO, which is formed upon solvent polymerization. The formation of PEO is also confirmed by the peak at 533.6 eV in the O1s XPS spectra in **Figure 3B**. The rather broad peaks at 288.6 eV in **Figure 4A** are assigned to carbon in C=O groups in organic Li alkyl carbonates ($ROCO_2Li$) and Li carbonates (Li_2CO_3), respectively. The corresponding peak of the oxygen atoms in these groups is detected in the O1s spectra (**Figure 3C**) at 531.8 eV. **Figure 3C**, the F1s peak at 687.5 eV are assigned with PVDF, while the peak at 684.2 eV corresponding to LiF is much stronger, agreeing with the inorganic inner layer of SEI. However, there is almost no difference in contrast to the case of the commercial electrolyte in the C1s, O1s, and F1s spectra. The difference appears at F1s spectra. The B1s peaks at 193.8 eV and 192.6 eV (**Figure 3D**) indicates the presence of LiODFB and material with B–O, respectively. And no such peak in commercial electrolyte.

This result indicates that the B-O bond is involved in the formation of the film, making the SEI film is much denser (Xu et al., 2016). It is consistent with the results of a dense surface morphology in **Figure 1b**.

The Electrochemical Performances of $LiFePO_4$ Batteries

The assembled Li/$LiFePO_4$ coin cells are used to compare the cycling and rate stability using 4 M LiODFB-DME electrolyte and 1 M $LiPF_6$ electrolyte at room temperature in this part.

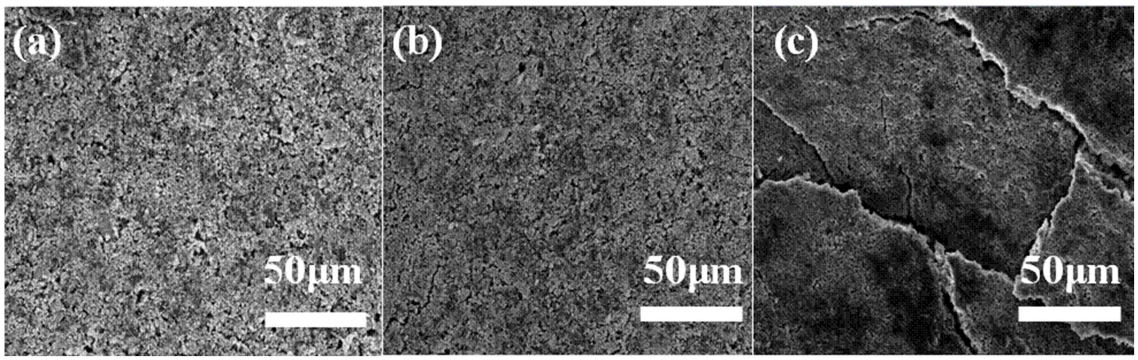

FIGURE 7 | SEM images for pristine cathode **(a)** cathodes after 100 cycles at 65°C with **(b)** the 4 M LiODFB-DME; **(c)** the 1 M $LiPF_6$.

Figure 4A shows the first charge/discharge profiles of the cells in different electrolytes at the 0.2°C current rate (1°C = 170 mAh g^{-1}). The cells are initially activated at 0.2°C for three cycles and then cycled at 0.5°C. The cells display similar voltage curves, but the cell using the 4 M LiODFB-DME electrolyte exhibits slightly smaller discharge capacities of 129 mAh g^{-1}, while the initial discharge capacity of 1 M $LiPF_6$ is 133 mAh g^{-1}. The result is directly related to the lower ionic conductivity of 4 M LiODFB-DME electrolyte compared to $LiPF_6$-based electrolyte. The long-term cycling performances of Li/$LiFePO_4$ cells are depicted in **Figure 4C**. There is no obvious difference after 200 cycles, and 4 M LiODFB-DME electrolyte shows little superiority compared to commercial $LiPF_6$-based electrolyte. However, LiODFB electrolyte shows excellent CE of 99% over 200 cycles; while the cell with the $LiPF_6$ is only 89% after 200 cycles (**Figure 4B**). It shows that LiODFB salt greatly improves the cycling stability, but the delivered capacity might have been hindered by the electrolyte's undesirable ionic conductivity. **Figure 4D** presents the rate capability of Li/$LiFePO_4$ cell in 1 M $LiPF_6$ and 4 M LiODFB-DME electrolytes. Discharge capacity of cells with 4 M LiODFB-DME are 154.8 mAh g^{-1} at 0.2°C, 143.3 mAh g^{-1} at 0.5°C, 134.4 mAh g^{-1} at 1.0°C, 123.1 mAh g^{-1} at 2.0°C, and 99.5 mAh g^{-1} at 5.0°C. As comparison, discharge capacity of cells with 1 M $LiPF_6$ are 143.9 mAh g^{-1} at 0.2°C, 136.7 mAh g^{-1} at 0.5°C, 128.3 mAh g^{-1} at 1.0°C, 118.9 mAh g^{-1} at 2.0°C, and 95.8 mAh g^{-1} at 5.0°C. Voltage profiles of both cells are also very similar **Figure S2**. It seems that discharged capacity at different cycling rates of cells with 4 M LiODFB-DME electrolyte are slightly higher than cells with 1 M $LiPF_6$ electrolyte. The outstanding thermal stability and water stability LiODFB leads to very weak side reactions and the dissolution of iron is suppressed. These are the reasons of better cycling performance of cells in 4 M LiODFB-DME electrolyte. All in all, the electrochemical performances of the two electrolytes capacity reach a considerable level at room temperature. These also can be confirmed on the impedance test results in **Figure S2**.

Furthermore, the cycling performances of Li/$LiFePO_4$ cells at 65°C are assessed in both electrolytes (**Figure 5A**). In **Figure 5A**, when the cell is working in $LiPF_6$ electrolyte, the capacity decay rapidly after cycles. We can discover it only has capacity retention of 79.3% after 100 cycles, which is consistent with the result reported by ZHANG et al. As a comparison, excellent cycle stability is observed when using 4 M LiODFB-DME electrolyte, with high capacity retention of 92.5% after 100 cycles. The rate capability of Li/$LiFePO_4$ at 65°C in different electrolytes is obtained in **Figure 5B**. Much larger discharge capacities are showed at higher rates for the 4 M LiODFB-DME. For example, the $LiPF_6$ electrolyte shows discharge capacities of 101.1 and 62.5 mAh g^{-1} at the 1.0 and 2.0°C rates, respectively, even the capacities of cell is almost close to zero at 5.0°C; While these values are increased to 148.1, 142.8, 127.7 mAh g^{-1} at the 1.0, 2.0, and 5.0°C rates for the LiODFB electrolyte. This demonstrates that LiODFB not only improve the cycling stability but also improve the rate capability in high temperature. It seems that the better thermal stability of LiODFB salts plays an important role in improving the high-temperature resilience of $LiFePO_4$ electrode.

We used TGA to study the thermal stability of fully charged electrodes in electrolytes (**Figure 6**). Evaporation of the adsorbed organic solvent appears as their weight loss before 150°C in 4 M LiODFB-DME electrolyte. As the heating progressed, a significant weight loss begins to appear at about 250°C, which originates from the decomposition of the SEI film. In contrast, the large-scale weight decay starts at 50°C in 1 M $LiPF_6$, and the mass attenuation has reached a minimum at 150°C, proving that the SEI film has completely broken before 150°C. It shows that 4 M LiODFB-DME electrolyte produces a more stable SEI film and establishes a more gentle interface between the electrode and the electrolyte. So the fully delithiated electrode is protected from directly contacting with the electrolyte. Therefore, the LiODFB electrolyte improves the thermal stability of the highly oxidized charged electrode.

SEM Micrographs of $LiFePO_4$ Electrodes

SEM analysis is performed to illustrate electrode images before and after 100 cycles in both electrolytes at 65°C. The $LiFePO_4$ electrode after long-term cycling in 4 M LiODFB-DME electrolyte (**Figure 7b**) shows a similar morphology to the pristine $LiFePO_4$ electrode (**Figure 7a**). In comparison, the electrode is severely eroded in 1 M $LiPF_6$ electrolyte after

100 cycles at 65°C in **Figure 7c**, and we can found that the $LiFePO_4$ electrode surface in 1 M $LiPF_6$ electrolyte displays some cracks among the particles. It is result from the poor thermal stability of the 1 M $LiPF_6$ electrolyte. The decomposition of $LiPF_6$ in high temperature causes serious capacity decay rapidly, resulting in very poor electrochemical performance, as shown in **Figure 5A**. The higher the current density, this effect is more serious in **Figure 5B**. These SEM observations confirm that 4 M LiODFB-DME electrolyte has excellent compatibility with $LiFePO_4$ cathodes during battery cycling at high temperature **Figure S3** shows the EDS layered image of $LiFePO_4$ electrode after 100 cycles at high magnification. The surface of the $LiFePO_4$ electrode consists of five main elements: O, P, F, and Fe. The Fe and P elements are mainly derived from $LiFePO_4$ electrode and the O, F, and B elements are derived from LiODFB lithium salt. It is proved that the B element from the LiODFB-based electrolyte participates the formation of the surface film of $LiFePO_4$ cathode. And the participation of the B elements makes the surface film of $LiFePO_4$ cathode smooth and compact. All in all, the LiODFB lithium salt protects the cathode. In addition, the SEM images of the morphologies of Al foils is shown in **Figure S4**. The surface of the Al foils had a large difference. The concentrated electrolytes suppress the Al corrosion more effectively.

CONCLUSIONS

In this work, we first developed a concentrated electrolyte based on LiODFB in ether solvents for LMBs. Based on 4 M LiODFB-DME electrolyte, Li was deposited on the copper foil and its surface showed smooth solid particle morphology without any dendrites. For the Li/$LiFePO_4$ cells, it is demonstrated that 4 M LiODFB-DME electrolyte exhibit good electrochemical performance, especially at the elevated temperature. Li/$LiFePO_4$ cells using 4 M LiODFB-DME electrolyte show a good capacity retention (92.5%) at elevated temperature (65°C), which is much higher than that of 1 M $LiPF_6$ electrolyte (79.2%). This research offers the possibility of rapid industrialization of LMBs.

DATA AVAILABILITY

The raw data supporting the conclusions of this manuscript will be made available by the authors, without undue reservation, to any qualified researcher.

AUTHOR CONTRIBUTIONS

ZF and JY conceived and designed the experiments. NG, JP, XL, and NM performed the experiments. NG, CS, and XL analyzed the data. NG and NM wrote the manuscript. KX designed the scheme. All authors reviewed the manuscript and approved the final version.

ACKNOWLEDGMENTS

We acknowledge the financial support of this work by the Project (51574191, 51304151) supported by the National Natural Science Foundation of China; Project (18JK0474) supported by Shaanxi Provincial Education Department, China; Project (2018JM5135) supported by the Natural Science Basic Research Plan in Shaanxi Province, China.

SUPPLEMENTARY MATERIAL

The Supplementary Material for this article can be found online at: https://www.frontiersin.org/articles/10.3389/fchem.2019.00494/full#supplementary-material

REFERENCES

Abouimrane, A., Ding, J., and Davidson, I. J. (2009). Liquid electrolyte based on lithium bis-fluorosulfonyl imide salt: Al corrosion studies and lithium ion battery investigations. *J. Power Sources* 189, 693–696. doi: 10.1016/j.jpowsour.2008.08.077

Aurbach, D., Gamolsky, K., Markovsky, B., Gofer, Y., Schmidt, M., Heider, U., et al. (2003). On the use of vinylene carbonate (VC) as an additive to electrolyte solutions for Li-ion batteries. *Electrochim. Acta* 47, 1423–1439. doi: 10.1016/S0013-4686(01)00858-1

Bian, X., Ge, S., Pang, Q., Zhu, K., Wei, Y., Zou, B., et al. (2017). A novel lithium difluoro(oxalate) borate and lithium hexafluoride phosphate dual-salt electrolyte for Li-excess layered cathode material. *J. Alloy. Compd.* 736, 136–142. doi: 10.1016/j.jallcom.2017.11.126

Cekic-Laskovic, I., von Aspern, N., Imholt, L., Kaymaksiz, S., Oldiges, K., Rad, B. R., et al. (2017). Synergistic effect of blended components in nonaqueous electrolytes for lithium ion batteries. *Top. Curr. Chem.* 375, 37–100. doi: 10.1007/s41061-017-0125-8

Cheng, X. B., Hou, T. Z., Zhang, R., Peng, H. J., Zhao, C. Z., Huang, J. Q., et al. (2016). Dendrite-free lithium deposition induced by uniformly distributed lithium ions for efficient lithium metal batteries. *Adv. Mater.* 28, 2888–2895. doi: 10.1002/adma.201506124

Etacheri, V., Marom, R., Elazari, R., Salitra, G., and Aurbach, D. (2011). Challenges in the development of advanced Li-ion batteries: a review. *Energy Environ. Sci.* 4, 3243–3262. doi: 10.1039/C1EE01598B

Goodenough, J. B., and Kim, Y. (2014). Challenges for rechargeable li batteries. *Chem. Mater.* 22, 587–603. doi: 10.1021/cm901452z

Jung, H., Park, S. H., Jeon, J., Choi, Y., Yoon, S., Cho, J. J., et al. (2013). Fluoropropane sultone as an SEI-forming additive that outperforms vinylene carbonate. *J. Mater. Chem.* 1, 11975–11981. doi: 10.1039/C3TA12580G

Kozen, A. C., Lin, C. F., Pearse, A. J., Schroeder, M. A., Han, X., Hu, L., et al. (2015). Next-generation lithium metal anode engineering via atomic layer deposition. *ACS Nano* 9, 5884–5892. doi: 10.1021/acsnano.5b02166

Li, F., Gong, Y., Jia, G., Wang, Q., Peng, Z., Fan, W., et al. (2015). A novel dual-salts of LiTFSI and LiODFB in $LiFePO_4$-based batteries for suppressing Al corrosion and improving cycling stability. *J. Power Sources* 295, 47–54. doi: 10.1016/j.jpowsour.2015.06.117

Li, L., Zhou, S., Han, H., Li, H., Nie, J., Armand, M., et al. (2011). Transport and electrochemical properties and spectral features of non-aqueous electrolytes containing LiFSI in linear carbonate solvents. *J. Electrochem. Soc. A* 158, 74–82. doi: 10.1149/2.jes120006

Liang, Z., Lin, D., Zhao, J., Lu, Z., Liu, Y., Liu, C., et al. (2016). Composite lithium metal anode by melt infusion of lithium into a 3D conducting scaffold with lithiophilic coating. *Proc. Natl. Acad. Sci. U.S.A.* 113, 2862–2867. doi: 10.1073/pnas.1518188113

Liang, Z., Zheng, G., Liu, C., Liu, N., Li, W., Yan, K., et al. (2015). Polymer nanofiber-guided uniform lithium deposition for battery electrodes. *Nano Lett.* 152910–2916. doi: 10.1021/nl5046318

Liu, J., Chen, Z., Busking, S., and Amine, K. (2007). Lithium difluoro(oxalato)borate as a functional additive for lithium-ion batteries. *Electrochem. Commun.* 9, 475–479. doi: 10.1016/j.elecom.2006.10.022

Park, K., Yu, S., Lee, C., and Lee, H. (2015). Comparative study on lithium borates as corrosion inhibitors of Al current collector in lithium bis(fluorosulfonyl)imide electrolytes. *J. Power Sources* 296, 197–203. doi: 10.1016/j.jpowsour.2015.07.052

Placke, T., Kloepsch, R., Dühnen, S., and Winter, M. (2017). Lithium ion, lithium metal, and alternative rechargeable battery technologies: the odyssey for high energy density. *J. Solid State Electrochem.* 21, 1939–1964. doi: 10.1007/s10008-017-3610-7

Poyraz, A. S., Laughlin, J., and Zec, Z. (2019). Improving the cycle life of cryptomelane type manganese dioxides in aqueous rechargeable zinc ion batteries: the effect of electrolyte concentration. *Electrochim. Acta* 305,423–432. doi: 10.1016/j.electacta.2019.03.093

Pritzl, D., Solchenbach, S., Wetjen, M., and Gasteiger, H. A. (2017). Analysis of vinylene carbonate (VC) as additive in graphite/$LiNi_{0.5}Mn_{1.5}O_4$ cells. *J. Electrochem. Soc. A* 164, 2625-2635. doi: 10.1149/2.1441712jes

Qian, J., Henderson, W. A., Xu, W., Bhattacharya, P., Engelhard, M., Borodin, O., et al. (2015). High rate and stable cycling of lithium metal anode. *Nat. Commun.* 6, 6362–6370. doi: 10.1038/ncomms7362

Qian, Y., Schultz, C., Niehoff, P., Schwieters, T., Nowak, S., Winter, M., et al. (2016). Investigations on the electrochemical decomposition of the electrolyte additive vinylene carbonate in Li metal half cells and lithium ion full cells. *J. Power Sources* 332, 60–71. doi: 10.1016/j.jpowsour.2016.09.100

Shi, L., Xu, A., and Zhao, T. (2017). First-principles investigations of the working mechanism of 2D h-BN as an interfacial layer for the anode of lithium metal batteries. *ACS Appl. Mater. Inter.* 9, 1987–1994. doi: 10.1021/acsami.6b14560

Suo, L., Hu, Y. S., Li, H., Armand, M., and Chen, L. (2013). A new class of Solvent-in-Salt electrolyte for high-energy rechargeable metallic lithium batteries. *Nat. Commun.* 4, 1481–1489. doi: 10.1038/ncomms2513

Thompson, R. S., Schroeder, D. J., Lopez, C. M., Neuhold, S., and Vaughey, J. T. (2011). Stabilization of lithium metal anodes using silane-based coatings. *Electrochem. Commun.* 13, 1369–1372. doi: 10.1016/j.elecom.2011.08.012

Webb, S. A., Baggetto, L., Bridges, C. A., and Veith, G. M. (2014). The electrochemical reactions of pure indium with Li and Na: anomalous electrolyte decomposition, benefits of FEC additive, phase transitions and electrode performance. *J. Power Sources* 248, 1105–1117. doi: 10.1016/j.jpowsour.2013.10.033

Wu, F., Ye, Y., Chen, R., Qian, J., Zhao, T., Li, L., et al. (2015). A systematic effect for an ultra-long cycle lithium-sulfur battery. *Nano Lett.* 15, 7431–7439. doi: 10.1021/acs.nanolett.5b02864

Wu, Q., Lu, W., Miranda, M., Honaker-Schroeder, T. K., Lakhsassi, K. Y., Dees, D., et al. (2012). Effects of lithium difluoro(oxalate)borate on the performance of Li-rich composite cathode in Li-ion battery. *Electrochem. Commun.* 24, 78–81. doi: 10.1016/j.elecom.2012.08.016

Xie, K., Wei, W., Yuan, K., Lu, W., Guo, M., Li, Z., et al. (2016). Toward dendrite-free lithium deposition via structural and interfacial synergistic effects of 3D graphene@Ni scaffold. *ACS Appl. Mater. Interfaces* 8, 26091–26097. doi: 10.1021/acsami.6b09031

Xie, K., Yuan, K., Zhang, K., Shen, C., Lv, W., Liu, X., et al. (2017). Dual functionalities of carbon nanotube films for dendrite-free and high energy-high power lithium-sulfur batteries. *ACS Appl. Mater. Interfaces* 9, 4605–4613. doi: 10.1021/acsami.6b14039

Xu, Y., Liu, J., Zhou, L., Zeng, L., and Yang, Z. (2017). FEC as the additive of 5 V electrolyte and its electrochemical performance for $LiNi_{0.5}Mn_{1.5}O_4$. *J. Electroanal. Chem.* 791, 109–116. doi: 10.1016/j.jelechem.2017.03.017

Xu, Z., Wang, J., Yang, J., Miao, X., Chen, R., Qian, J., et al. (2016). Enhanced performance of a lithium–sulfur battery using a carbonate-based electrolyte. *Angew. Chem. Int. Ed.* 55, 10372–10375. doi: 10.1002/anie.201605931

Yamada, Y., Wang, J., Ko, S., Watanabe, E., and Yamada, A. (2019). Advances and issues in developing salt-concentrated battery electrolytes. *Nat. Nanotechnol.* 14, 200–207. doi: 10.1038/s41560-019-0336-z

Yang, C. P., Yin, Y. X., Zhang, S. F., Li, N. W., and Guo, Y. G. (2015). Accommodating lithium into 3D current collectors with a submicron skeleton towards long-life lithium metal anodes. *Nat. Commun.* 6, 8058. doi: 10.1038/ncomms9058

Zhamu, A., Chen, G., Liu, C. G., Neff, D., Fang, Q., Yu, Z. N., et al. (2012). Reviving rechargeable lithium metal batteries: enabling next-generation high-energy and high-power cells. *Energy Environ. Sci.* 5, 5701–5707. doi: 10.1039/C2EE02911A

Zhang, R., Cheng, X. B., Zhao, C. Z., Peng, H. J., Shi, J. L., Huang, J. Q., et al. (2016). Conductive nanostructured scaffolds render low local current density to inhibit lithium dendrite growth. *Adv. Mater.* 28, 2155–2162. doi: 10.1002/adma.201504117

Zhang, S. S. (2006). An unique lithium salt for the improved electrolyte of Li-ion battery. *Electrochem. Commun.* 9, 1423–1428. doi: 10.1016/j.elecom.2006.06.016

Zhang, Z., Chen, X., Li, F., Lai, Y., Li, J., Liu, P., et al. (2010). $LiPF_6$ and lithium oxalyldifluoroborate blend salts electrolyte for $LiFePO_4$/artificial graphite lithium-ion cells. *J. Power Sources* 21, 7397–7402. doi: 10.1016/j.jpowsour.2010.05.056

Zhang, Z. A., Zhao, X. X., Peng, B., Lai, Y. Q., Zhang, Z. Y., Li, J., et al. (2015). Mixed salts for lithium iron phosphate-based batteries operated at wide temperature range. *Transac. Nonferr. Metal. Soc.* 25, 2260–2265. doi: 10.1016/S1003-6326(15)63839-0

Zhou, H., Liu, F., and Li, J. (2012). Preparation, thermal stability and electrochemical properties of LiODFB. *J. Mater. Sci. Technol.* 28, 723–727. doi: 10.1016/S1005-0302(12)60121-2

Zhou, H., Xiao, K., and Li, J. (2016). Lithium difluoro(oxalate)borate and $LiBF_4$ blend salts electrolyte for $LiNi_{0.5}Mn_{1.5}O_4$ cathode material. *J. Power Sources* 302, 274–282. doi: 10.1016/j.jpowsour.2015.10.073

Zugmann, S., Moosbauer, D., Amereller, M., Schreiner, C., and Wudy, F. (2011). Electrochemical characterization of electrolytes for lithium -ion batteries based on lithium difluoromono(oxalato)borate. *J. Power Sources* 196 1417–1424. doi: 10.1016/j.jpowsour.2010.08.023

Conflict of Interest Statement: The authors declare that the research was conducted in the absence of any commercial or financial relationships that could be construed as a potential conflict of interest.

frontiers in Materials

ORIGINAL RESEARCH
published: 24 July 2019
doi: 10.3389/fmats.2019.00176

Controlled Synthesis of $Ni_xCo_yS_4$/rGO Composites for Constructing High-Performance Asymmetric Supercapacitor

*Mingxia Dong, Zhixing Wang, Jiexi Wang, Huajun Guo, Xinhai Li and Guochun Yan**

School of Metallurgy and Environment, Central South University, Changsha, China

Nickel-cobalt sulfides ($Ni_xCo_yS_4$) are promising supercapacitor materials due to their high capacitance, while the sluggish kinetics in terms of charge transfer limits their energy density. To achieve both high energy and power density for the $Ni_xCo_yS_4$–based supercapacitor, sulfur-doped reduced graphene oxide (rGO) is incorporated into $Ni_xCo_yS_4$ by an *in situ* growth—ion exchange strategy to synthesize $Ni_xCo_yS_4$/rGO composites. Profited from the synergetic effect between rGO and $Ni_xCo_yS_4$, the $Ni_{1.64}Co_{2.40}S_4$/rGO electrode delivers high specific capacitance of 1,089 F g^{-1} at 1 A g^{-1}, and remains 92.6% of its original capacitance at 20 A g^{-1} (1,008 F g^{-1}). Asymmetric supercapacitors assembled with active carbon (AC) and $Ni_{1.64}Co_{2.40}S_4$/rGO ($Ni_{1.64}Co_{2.40}S_4$/rGO//AC) offer both high specific capacitance (265.5 F g^{-1} at 1 A g^{-1}) and superior rate capability at 50 A g^{-1} (recovering 63.6% of the capacitance determined at 1 A g^{-1}). In addition, the assembled device exhibits a high capacitance retention of 92.6% after 10,000 cycles at 10 A g^{-1}, which implies an excellent cyclic stability. Ragone plot reveals that the energy density of $Ni_{1.64}Co_{2.40}S_4$/rGO//AC asymmetric supercapacitor do not vanish as it delivers 30.4 Wh kg^{-1} at 10 kW kg^{-1}, demonstrating its promising application.

Keywords: nickel-cobalt sulfides, *in-situ* growth, high energy density, asymmetric supercapacitor, high cyclic stability

OPEN ACCESS

Edited by:
Shengkui Zhong,
Soochow University, China

Reviewed by:
Biao Gao,
Wuhan University of Science and Technology, China
Chaopeng Fu,
Shanghai Jiao Tong University, China

****Correspondence:***
Guochun Yan
happyygc@csu.edu.cn

Specialty section:
This article was submitted to Energy Materials, a section of the journal Frontiers in Materials

Received: *29 May 2019*
Accepted: *08 July 2019*
Published: *24 July 2019*

Citation:
Dong M, Wang Z, Wang J, Guo H, Li X and Yan G (2019) Controlled Synthesis of $Ni_xCo_yS_4$/rGO Composites for Constructing High-Performance Asymmetric Supercapacitor. Front. Mater. 6:176. doi: 10.3389/fmats.2019.00176

INTRODUCTION

With gradual consumption of fuel energy and the growing environmental problems, is the need to develop renewable energies and corresponding energy storage and conversion devices is urgent (Zhong et al., 2012; Liu et al., 2018a; Zhang Q. et al., 2018). Lithium ion battery (Li et al., 2015; Liu et al., 2016; Zhong et al., 2017; Wang J. et al., 2018), sodium-ion battery (Chen J. et al., 2018; Yan et al., 2018), Lithium-Sulfur battery (Tan et al., 2018; Wu F. et al., 2018), and supercapacitor (Gilshteyn et al., 2017; Saha et al., 2018) are representative electrochemical energy storage devices. A supercapacitor (SC) is one of the most promising energy storage devices due to their desirable characteristics, such as high power-density, super-long cycle life and high safety performance, and it plays an important role in both automobile and electronic industry (Simon et al., 2014; Eftekhari et al., 2017; Zhang L. et al., 2018). Classified by different energy storage mechanisms, electrical double layer capacitors (EDLCs), and pseudocapacitors (PCs) show differentiated advantages in the specific field. Although EDLCs deliver fast electron transfer, their

bottleneck lies in the low specific capacitance problem. On the contrary, PCs deliver satisfying specific capacitance, but poor charge transfer ability limits their application. Neither of them can be used to build a capacitor that possesses both high energy density and power density. Developing a hybrid capacitor combining with the advantages of EDLCs and PCs is an effective strategy to remedy the deficiency.

To fulfill the above design, developing advanced materials with both high capacitance and rate capability are the key factors. Normally, the composite formed with proper composition of two materials results in complementary advantages. As known to all, reduced graphene oxide (rGO) is one of the most promising electrode materials for EDLCs due to its large specific surface area, exceptionally high electronic conductivity and high theoretical specific capacitance (Booth et al., 2008; Lee et al., 2008; Ke and Wang, 2016). When rGO is introduced into the composite properly, it enhances not only the electronic conductivity of composite, but also the structural stability of the electrode (Ke and Wang, 2016; Deng et al., 2017). Therefore, taking reduced graphene oxide as a framework is an effective way to reinforce the mechanical strengths of the composites. Nickel-cobalt sulfide is one of the most promising one among various pseudocapacitor electrode materials, such as metal oxides, metal sulfides, and conductive polymers (Jinlong et al., 2017; Wen et al., 2017; Zhao et al., 2017; Liang et al., 2018). Although, there is some doubt about the definition of pseudocapacitance (Brousse, 2015; Jiang and Liu, 2019), many studies reported that transition metal sulfides were classified as one kind of pseudocapacitive materials (Xiong et al., 2015; Wang et al., 2019). However, some studies classify transition metal sulfides as battery-type electrode materials (Mohamed et al., 2018; Ma et al., 2019). Putting this controversial issue aside, it has been proven that nickel-cobalt sulfides ($Ni_xCo_yS_4$) exhibit high electronic conductivity and flexibility due to the lower optical band gap of Ni–Co and electronegativity of sulfur (Chen et al., 2013; Zhu et al., 2015). Great efforts have been devoted to the fabrication of composites, such as $NiCo_2S_4$/rGO (Annamalai et al., 2017; Nan et al., 2018; Sarkar et al., 2018; Wang Y. et al., 2018), $CoNi_2S_4$/rGO (Gao et al., 2018), NiS/rGO (Qu et al., 2018), C-$NiCo_2S_4$ (Yuan et al., 2017; Mohamed et al., 2018), CNTs-$NiCo_2S_4$ (Li D. et al., 2016), and so on. However, the influence of Ni/Co ratio of nickel-cobalt sulfide materials on the characteristics and the pseudocapacitance performances are not systematically studied.

In this work, we prepare a series of $Ni_xCo_yS_4$/rGO composites with various Ni/Co ratios in the raw materials (Ni/Co = 2.0, 1.0, 0.5, and 0.25), in which the bimetallic Ni-Co hydroxy-carbonates *in-situ* grow onto the rGO framework during the synthesis process. We demonstrate that asymmetric supercapacitor ($Ni_{1.64}Co_{2.40}S_4$/rGO//AC) assembled with $Ni_{1.64}Co_{2.40}S_4$/rGO composite (positive electrode) and active carbon (negative electrode) exhibits excellent electrochemical performance with outstanding capacitance retention of 92.6% after 10,000 cycles at high current density of 10 A g^{-1} and high energy density of 30.4 Wh kg^{-1} at the power density of 10 kW kg^{-1}. Our results offer new insights into developing advanced electrode materials for supercapacitors with high energy and power density.

EXPERIMENTAL

The graphene oxide (GO) was purchased from Suzhou Tanfeng technology co LTD, and all of other chemical reagents were provided by Sinopharm Chemical Reagent Corp in an analytical grade that were used as-received without further purification.

Synthesis of $Ni_xCo_yS_4$

In a typical synthesis of precursors, 0.025 g GO was dissolved into 100 mL deionized water to form homogeneous brown solution by ultrasonic dispersion. A certain mass of $NiCl_2{\cdot}6H_2O$, $CoCl_2{\cdot}6H_2O$ (molar ratios of Ni: Co are 2:1, 1:1; 1:2, and 1:4) and 1.6365 g urea were dissolved into the GO solution under stirring. After stirring for 30 min, the obtained suspension was transferred into a 200 mL Teflon-lined autoclave. The hydrothermal reaction was carried out at 120°C for 10 h so that the bimetallic Ni-Co hydroxy-carbonates *in-situ* grow onto the GO framework. The products were washed with deionized water and collected through filtration, and then which was lyophilized. Based on the Ni/Co ratio in the raw materials, the as-obtained precursors were labeled as NC2010, NC1515, NC1020, and NC0624, respectively.

For synthesizing the $Ni_xCo_yS_4$/rGO by sulfurizing the aforementioned precursors, the representative processes are described as followed. First, 0.2 g precursor was dispersed into 100 mL deionized water and the mixture was stirred for 30 min. Subsequently, 1.7156 g $Na_2S{\cdot}9H_2O$ was added into the suspension and stirred for 30 min. Then, the mixture was transferred into a 200 mL Teflon-lined autoclave, which was heated at 180°C for 8 h. After cooling naturally to room temperature, the black product was collected in the same way as former procedure. To further illuminate the content of Ni, Co and S in the $Ni_xCo_yS_4$/rGO composites, the Inductively Coupled Plasma-Optical Emission Spectrometry (ICP-OES) results and the C-S analysis results of $Ni_xCo_yS_4$/rGO composites are shown in **Table S1**. The as-prepared products were labeled as $Ni_{2.15}Co_{1.37}S_4$/rGO, $Ni_{1.64}Co_{2.40}S_4$/rGO, $Ni_{1.02}Co_{2.98}S_4$/rGO, $Ni_{0.60}Co_{3.60}S_4$/rGO on the basis of ICP and C-S analysis results.

Materials Characterization

Structure, morphology, and microstructure of the precursors and the corresponding $Ni_xCo_yS_4$/rGO composites were characterized by X-ray diffraction using Cu Kα (λ = 1.5406 Å) radiation (XRD, Bruker D8 AdvanceRint-2000), scanning electron microscopy (SEM, Sirion 200), and transmission electron microscopy (TEM, Tecnai G12, 200 kV). The Surface elemental valence of the sample was characterized by X-ray photoelectron spectroscopy (XPS, PHI5600, PerkineElmer).

Electrochemical Measurement

Circular Ni foams were cleaned in 1.0 mol L^{-1} KOH solution with ultrasonic cleaning for 30 min to remove impurities on the surface, and washed with deionized water three times. The preparation of electrodes was followed in the same procedure as described in previous work (Dong et al., 2018), and the diameter of Ni foam for positive and negative electrode is 12 and 16 mm, respectively.

Electrochemical tests were performed in three-electrode systems with 6 mol L^{-1} KOH as electrolyte, the working electrode was prepared by mixing $Ni_xCo_yS_4$/rGO composites, conductive additive (Super P), and binder (60 wt% PTFE emulsion) in a ratio of 8:1:1, Hg/HgO electrode as the reference electrode and Pt electrode as the counter electrode, respectively. By contrast, electrochemical tests carried out in the asymmetric supercapacitor were based on the abovementioned working electrode (positive electrode) and active carbon electrode (negative electrode), in which the active carbon electrode was prepared by mixing active carbon, conductive additive (Super P) and binder (60 wt% PTFE emulsion) in a ratio of 85:10:5. Cyclic voltammetry (CV) and electrochemical impedance spectroscopy (EIS) were tested by a CHI 660D electrochemical workstation (Chenhua Instruments, Shanghai). Galvanostatic charge-discharge (GCD) tests were carried out with the LAND electrochemical test system. Additional experimental details are described in the **Supplementary Material** of the work.

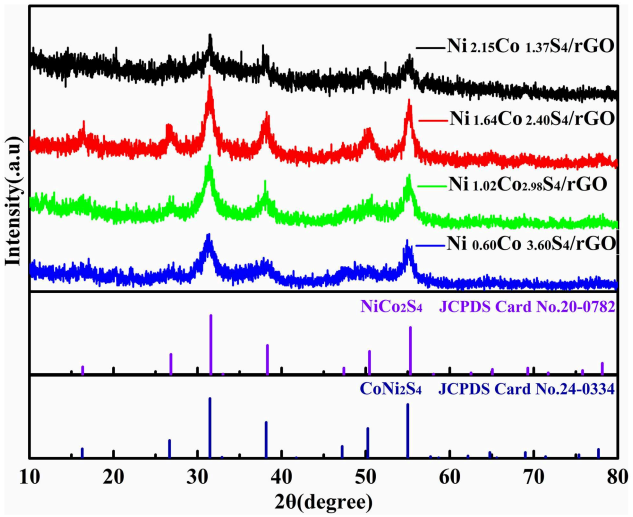

FIGURE 1 | XRD patterns of $Ni_xCo_yS_4$/rGO composites.

RESULT AND DISCUSSION

The crystallographic characteristics of the as-obtained precursors and $Ni_xCo_yS_4$/rGO composites are characterized by XRD. As shown in **Figure S2**, for all samples, most of the diffraction peaks can be indexed to $Ni_xCo_y(CO_3)_{0.5}(OH)$ ($x+y=1$) that is derived from $Co(CO_3)_{0.5}(OH)\cdot 0.11H_2O$ (JCPDS Card No.48-0083). No impurity peaks were observed, which illustrates the substitution of Co by Ni during the growth of crystals with the increasing of nickel contents in the precursors (Xiao and Yang, 2011; Wan et al., 2013). With the decrease of Ni/Co ratio, the intensities of the diffraction peaks increase gradually, suggesting that the Co element plays a role in improving the crystallinity of precursor. For the XRD patterns of $Ni_xCo_yS_4$/rGO composites (**Figure 1**), all of the XRD patterns of all $Ni_xCo_yS_4$/rGO composites show weak diffraction peaks. The diffraction peaks at the 2θ of 31.4°, 38.2°, 50.1°, and 55.1° are ascribed to (311), (400), (511), and (440) planes of the cubic $NiCo_2S_4$ (JCPDS Card No.20-0782) or $CoNi_2S_4$ (JCPDS Card No.24-0334). The $Ni_{1.64}Co_{2.40}S_4$/rGO composite owns the strongest diffraction peaks, reflecting the highest crystallinity among all samples.

SEM and TEM technique were used to characterize the morphology of the precursors and $Ni_xCo_yS_4$/rGO composites as shown in **Figures S3, S4** and **Figure 2**. **Figures S3a–d** show SEM images and EDS results of NC2010, NC1515, NC1020, and NC0624, respectively. For all precursors, a nano-needle type of Ni-Co compounds were embedded onto the surface of rGO network. With the decrease of Ni/Co ratio, the size of nano-needles gradually increases as shown in **Figure S3**. The NC0624 possess maximum microscopic size with a longitudinal length larger than 2 μm, indicating that Co plays a crucial role in the vertical growth of crystal. EDS results reveals that the ratio of Ni/Co content decrease from 1.5 to 0.2, which is in well-accordance with our experimental design. Furthermore, the TEM and high-resolution transmission electron microscope (HRTEM) images of NC1515 are carried out to further illustrate the morphology and microstructure of the precursor. As shown in **Figure S4**, the Ni-Co compounds with solid nano-needle morphology evenly distributed on the surface of rGO with transparent morphology, and the diameter of the nanoneedle is about 20 nm. The interplanar crystal spacing of 0.88 nm in the HRTEM image (**Figure S4d**) can be referred to the (100) plane of $Ni_xCo_y(CO_3)_{0.5}(OH)$.

Figures 2a–d show SEM images of $Ni_{2.15}Co_{1.37}S_4$/rGO, $Ni_{1.64}Co_{2.40}S_4$/rGO, $Ni_{1.02}Co_{2.98}S_4$/rGO, and $Ni_{0.60}Co_{3.60}S_4$/rGO composites, respectively. It is obvious that the sulfides inherit the morphological features of corresponding precursors with the $Ni_xCo_yS_4$ decorated on the surface of rGO. It is worth noting that the TEM images of $Ni_{1.64}Co_{2.40}S_4$/rGO (see **Figure S4** and **Figures 2e–h**) confirms that the solid nano-needles transfer to nano-tube during ion exchange process from the precursor to sulfides. Specifically, the hollow structures with a rough surface possess an outer diameter of about 35 nm, which is larger than the diameter of the precursor (20 nm). The TEM results of precursors and $Ni_{1.64}Co_{2.40}S_4$/rGO composite suggest that the Ni^{2+} ions and Co^{2+} ions diffused outwards from the precursor and combined with sulfur ions to form sulfides. The EDS results of $Ni_xCo_yS_4$/rGO composites in **Figure S1** reveals that Ni, Co, and S elements exist on the surface of the composites. In addition, it is worth noting that the S-doped graphene is also formed during the ion-exchange process, which is evidenced by a set of comparison experiments. Specifically, the GO was reduced in $Na_2S\cdot 9H_2O$ solution under the same condition as preparing $Ni_xCo_yS_4$/rGO composites, which can be confirmed by the C1s, and O1s XPS spectra in **Figure S5**. Moreover, the characteristic of sulfur peak in the EDS spectra (**Figure S6**) and C=S, C-S-C bonds in S2p spectra of aforementioned rGO sample confirm the existence of sulfur in rGO, which is beneficial to improve the pseudo-capacitance because of the heteroatom doping of S (Liu et al., 2017).

To further probe the formation of nickel-cobalt sulfides ($Ni_xCo_yS_4$) and the S-doped rGO in the sulfide composite, XPS

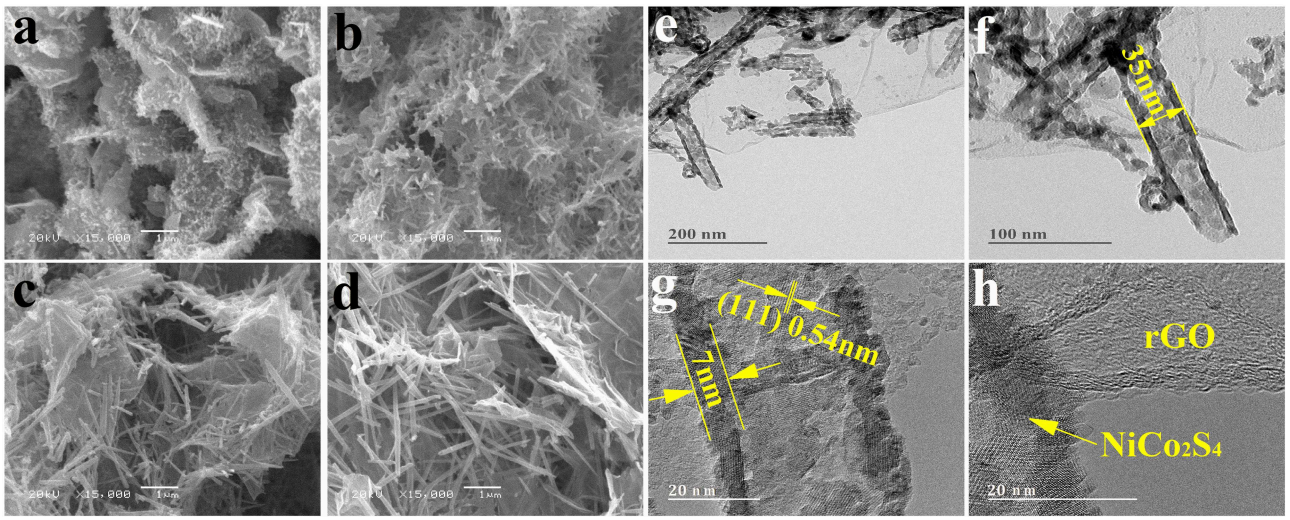

FIGURE 2 | The morphology of $Ni_xCo_yS_4$/rGO composites. **(a–d)** SEM images of $Ni_xCo_yS_4$/rGO composites; $Ni_{2.15}Co_{1.37}S_4$/rGO **(a)**, $Ni_{1.64}Co_{2.40}S_4$/rGO **(b)**, $Ni_{1.02}Co_{2.98}S_4$/rGO **(c)**, and $Ni_{0.60}Co_{3.60}S_4$/rGO **(d)**. **(e–h)** TEM and HRTEM images of $Ni_{1.64}Co_{2.40}S_4$/rGO; TEM images of $Ni_{1.64}Co_{2.40}S_4$/rGO **(e,f)**; HRTEM images of $Ni_{1.64}Co_{2.40}S_4$/rGO **(g,h)**.

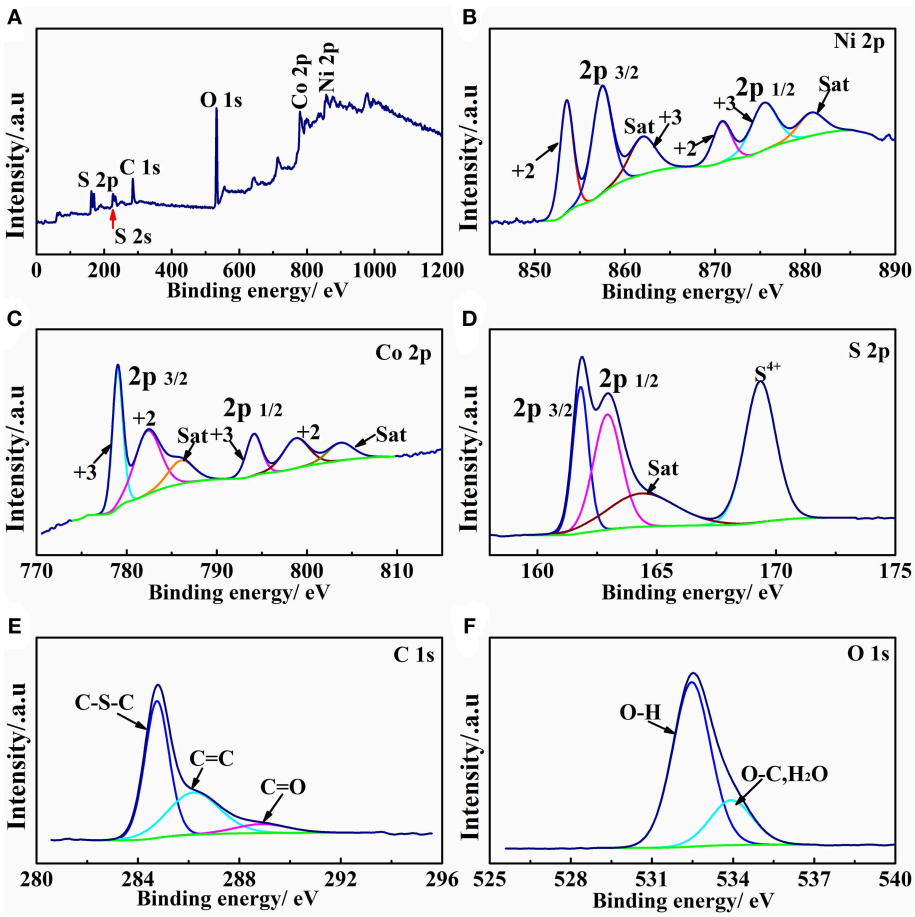

FIGURE 3 | XPS spectrum of $Ni_{1.64}Co_{2.40}S_4$/rGO composite: survey scan **(A)**, High-resolution spectra of Ni 2p **(B)**, Co 2p **(C)**, S 2p **(D)**, C 1s **(E),** and O 1s **(F)**, respectively.

(X-ray photoelectron spectroscopy) is utilized to analyze the elemental composition and valence state of the material. **Figure 3** shows survey, Ni 2p, Co 2p, S 2p, C 1s, and O 1s spectrum of the $Ni_{1.64}Co_{2.40}S_4$/rGO composite, and **Table S2** lists the peak fitting parameters of all spectrums. As shown in **Figure 3A**, it can be confirmed that Ni, Co, S, C, and O elements exist on the surface of $Ni_{1.64}Co_{2.40}S_4$/rGO composite. In high resolution spectrums of Ni 2p and Co 2p, the spectrums can be classified into 2p 3/2 and 2p 1/2 sections, and the corresponding satellite peaks are labeled as "Sat" in the plot. Specifically, the peaks at 853.5 and 870.8 eV in Ni 2p correspond to Ni^{2+}, and the peaks at 857.7 and 875.5 eV can be assigned to Ni^{3+}, confirming the coexistence of both Ni^{2+} and Ni^{3+} in the composite. Similarly, the peaks located at 779.0 eV, 794.1 eV in Co 2p corresponds to the Co^{3+}, and the peaks at 782.2 eV, 798.8 eV of Co 2p spectrums associates to the Co^{2+}, suggesting the coexistence of Co^{3+} and Co^{2+} in $Ni_{1.64}Co_{2.40}S_4$/rGO composite as well (Fan et al., 2017; Qin et al., 2017). For the S 2p spectrum, the peak located at 161.8 eV for S 2p 3/2 is attributed to S^{2-} or C-S-C bonds on the surface (Chen X. et al., 2014), while the peak at 162.9 eV for S 2p1/2 can be ascribed to S-M (metal) bonds. In addition, the peak at a high binding energy of 169.6 eV (satellite) can be attributed to the highly oxidized state sulfur species (S^{4+}) (Ma et al., 2016). The added $Na_2S{\cdot}9H_2O$ act as both of S^{2-} sources and reductant during the high temperature ion-exchange reaction, in which part of S^{2-} loses electrons and been oxidized to the higher-valence, and the GO been reduced to rGO simultaneously. Furthermore, the C 1s spectrum exhibits a major peak at 284.7 eV attributed to C-S-C bonds (Wenfang et al., 2015). Additionally, a peak located at 285.9 eV in the C 1s spectra corresponds to the C=C bond (aromatic-linked carbon), while the weak peak at 289.2 eV can be ascribed to the carboxyl groups (C=O) and sp^2 hybridized carbon from rGO, the low strength of the peak at 289.2 eV also indicates that the graphene has been reduced (Qin et al., 2017). The S 2p and C 1s XPS results reveal the existence of S-M (M=Ni or Co) and C-S-C bonds, respectively, which verifies the doping of S into rGO and the formation of transition metal sulfides in the composite material. Based on the XRD, SEM, TEM, and XPS results as analyzed in **Figures 1–3**, we proofed that the $Ni_xCo_yS_4$/rGO composites can be synthesized by such *in situ* growth—ion exchange strategy.

The electrochemical performances of $Ni_xCo_yS_4$/rGO composites are measured by cyclic voltammetry at various scan rates in a three-electrode cell as shown in **Figure 4**. For all composites, anodic and cathodic peaks with good symmetry indicate the good reversibility of the materials. The positions of anodic and cathodic peaks shift to the more positive and more negative directions with the increase of scan rates from 1 mV s^{-1} to 100 mV s^{-1}, which implies an increase of the polarization. It is known to all that the relationship between scan rate and current density is an effective method to distinguish capacitive contribution by the $i = av^b$ formula. Specifically, when the b value is 1/2, the electrode shows a total diffusion-limited behavior ($i = av^{1/2}$); and when the b value is 1, the electrode shows a capacitive process (Lim et al., 2015). **Figures 4E–H** show the b values of $Ni_{2.15}Co_{1.37}S_4$/rGO, $Ni_{1.64}Co_{2.40}S_4$/rGO, $Ni_{1.02}Co_{2.98}S_4$/rGO and $Ni_{0.60}Co_{3.60}S_4$/rGO as deduced from the slope of log (i)—log (v) curves, which are 0.55, 0.78, 0.86, and 0.89, respectively. The b values of the electrodes increase with the decrease of Ni/Co ratio, which implies that the $Ni_{2.15}Co_{1.37}S_4$/rGO composite is mainly diffusion-controlled kinetics behavior, and gradually transforms to the capacitive behavior for the $Ni_{0.60}Co_{3.60}S_4$/rGO composites. As the switch of kinetics behavior from diffusion-controlled to capacitive behavior, it will accelerate the charge transfer process so as to improve the rate capability of the $Ni_xCo_yS_4$/rGO composites.

The CV results of $Ni_{2.15}Co_{1.37}S_4$/rGO, $Ni_{1.64}Co_{2.40}S_4$/rGO, $Ni_{1.02}Co_{2.98}S_4$/rGO, and $Ni_{0.60}Co_{3.60}S_4$/rGO at 1 mV s^{-1} are presented in **Figure 5A**. Obviously, the $Ni_{2.15}Co_{1.37}S_4$/rGO material has the largest integral area, indicating the highest specific capacitance as compared to other samples. The specific capacitance of the material decreases with the decrease of Ni/Co ratio in $Ni_xCo_yS_4$/rGO composites, which is related to the microstructure transformation of the material. Specifically, $Ni_{1.64}Co_{2.40}S_4$/rGO consists of tiny one-dimensional nano-needles that convince to the sufficient contact between the active material and the electrolyte during the electrode process. In addition, the response current of the CV curves is a combination of capacitor and diffusion-controlled behavior. The respective contribution between diffusion-controlled and capacitive capacitance can be calculated by the following equation (Lim et al., 2015):

$$i(V) = k_1 v + k_2 v^{1/2} \quad (1)$$

The capacitance proportion of diffusion-controlled process and capacitor-like processes are expressed by $k_1 v$ and $k_2 v^{1/2}$, respectively. The capacitive-contribution of $Ni_{1.64}Co_{2.40}S_4$/rGO is 79.83% at 1 mV s^{-1} as shown in **Figure S7**, which confirms that the specific capacitance is mainly contributed by the capacitive-like process. Besides, the difference between the oxidation potential and reduction potential decrease obviously (the potential differences of $Ni_xCo_yS_4$/rGO composites are 0.132 V ($Ni_{2.15}Co_{1.37}S_4$/rGO), 0.104 V ($Ni_{1.64}Co_{2.40}S_4$/rGO), 0.089 V ($Ni_{1.02}Co_{2.98}S_4$/rGO), and 0.093 V ($Ni_{0.60}Co_{3.60}S_4$/rGO) respectively), indicating an gradually improved reversibility of the composites, which is beneficial to improve the rate performance of the electrodes. **Figures 5B,C** shows the rate capability of the composites as the current density range from 1 A g^{-1} to 20 A g^{-1}. It is noteworthy that the rate performance is improved distinctively with the decrease of Ni/Co molar ratio in composites. Specifically, when the current density increase to 20 A g^{-1}, the $Ni_{1.64}Co_{2.40}S_4$/rGO, $Ni_{1.02}Co_{2.98}S_4$/rGO, and $Ni_{0.60}Co_{3.60}S_4$/rGO composites can recover 92.6, 99.5, and 99.6% of their capacitance determined at 1 A g^{-1}, respectively (**Table S3**). In contrast, the $Ni_{2.15}Co_{1.37}S_4$/rGO composite can only retain 68.9% of its capacitance determined at 1 A g^{-1} under the same condition (**Table S3**). Our detailed electronic conductivity results (**Figure 5D**) evidence that higher Co content in $Ni_xCo_yS_4$/rGO composites is beneficial to improve the electronic conductivity of the composites, which is the main reason for the improvement of rate performance. Considering the merits of capacitance and rate capability of the composites, $Ni_{1.64}Co_{2.40}S_4$/rGO exhibits the best comprehensive performance in the application of supercapacitor, which delivers the capacitance of 1,089 F g^{-1} at the current density of 1 A g^{-1},

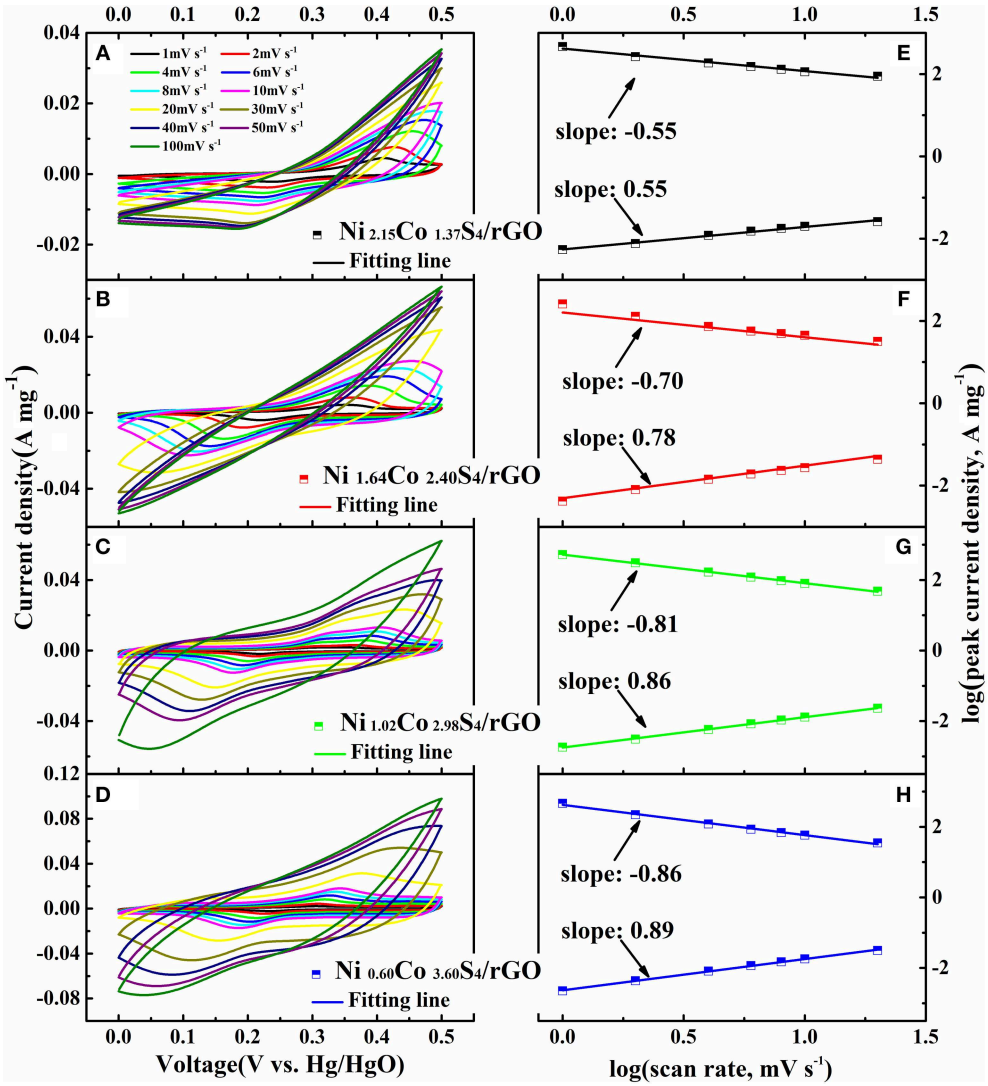

FIGURE 4 | Electrochemical properties of $Ni_xCo_yS_4$/rGO composites at three-electrode cells. CV curves of $Ni_{2.15}Co_{1.37}S_4$/rGO, $Ni_{1.64}Co_{2.40}S_4$/rGO, $Ni_{1.02}Co_{2.98}S_4$/rGO, and $Ni_{0.60}Co_{3.60}S_4$/rGO at different scan rates **(A–D)**; relationship between scan rate and current density of $Ni_{2.15}Co_{1.37}S_4$/rGO, $Ni_{1.64}Co_{2.40}S_4$/rGO, $Ni_{1.02}Co_{2.98}S_4$/rGO, and $Ni_{0.60}Co_{3.60}S_4$/rGO **(E–H)**.

and retains 1,008 F g^{-1} at the current density of 20 A g^{-1}. The GCD curves of $Ni_{2.15}Co_{1.37}S_4$/rGO, $Ni_{1.64}Co_{2.40}S_4$/rGO, $Ni_{1.02}Co_{2.98}S_4$/rGO, and $Ni_{0.60}Co_{3.60}S_4$/rGO at the current density of 1 A g^{-1} show nearly symmetric GCD curves, implying the high coulomb efficiency of the charge-discharge process (**Figure 5E** and **Figure S8**). Meanwhile, the time corresponding to the discharge platform gradually shortens with the decrease of Ni/Co ratio, indicating that the proportion of pseudocapacitance originated from Faraday reaction reduces. It is in well-accordance with the result of CV results as shown in **Figure 5A**. Moreover, the GCD curves of $Ni_{1.64}Co_{2.40}S_4$/rGO at various current densities in **Figure 5F** suggests that the electrode have excellent rate performance.

To demonstrate the practical application of $Ni_{1.64}Co_{2.40}S_4$/rGO composite for energy storage, an asymmetric supercapacitor marked as $Ni_{1.64}Co_{2.40}S_4$/rGO//AC was assembled, in which $Ni_{1.64}Co_{2.40}S_4$/rGO acts as the positive material and active carbon (AC) acts as the negative material. As shown in **Figure 6A**, the shape of the CV curve shows slight differences at various scan rate, indicating that the $Ni_{1.64}Co_{2.40}S_4$/rGO//AC asymmetric supercapacitor has good charge-discharge characteristics. The specific capacitances of $Ni_{1.64}Co_{2.40}S_4$/rGO//AC deduced from the integral area of CV curves at various current density are calculated and shown in **Figure 6B**. High capacitance (270.7 F g^{-1} at 1 mV s^{-1}) and high capacitance retention (68.5% at 100 mV s^{-1}) confirm the superior rate performance of the device, which is attributed to the proper composition and hollow structure of $Ni_{1.64}Co_{2.40}S_4$. The relationship between scan rate and current density of $Ni_{1.64}Co_{2.40}S_4$/rGO//AC during the charge-discharge process

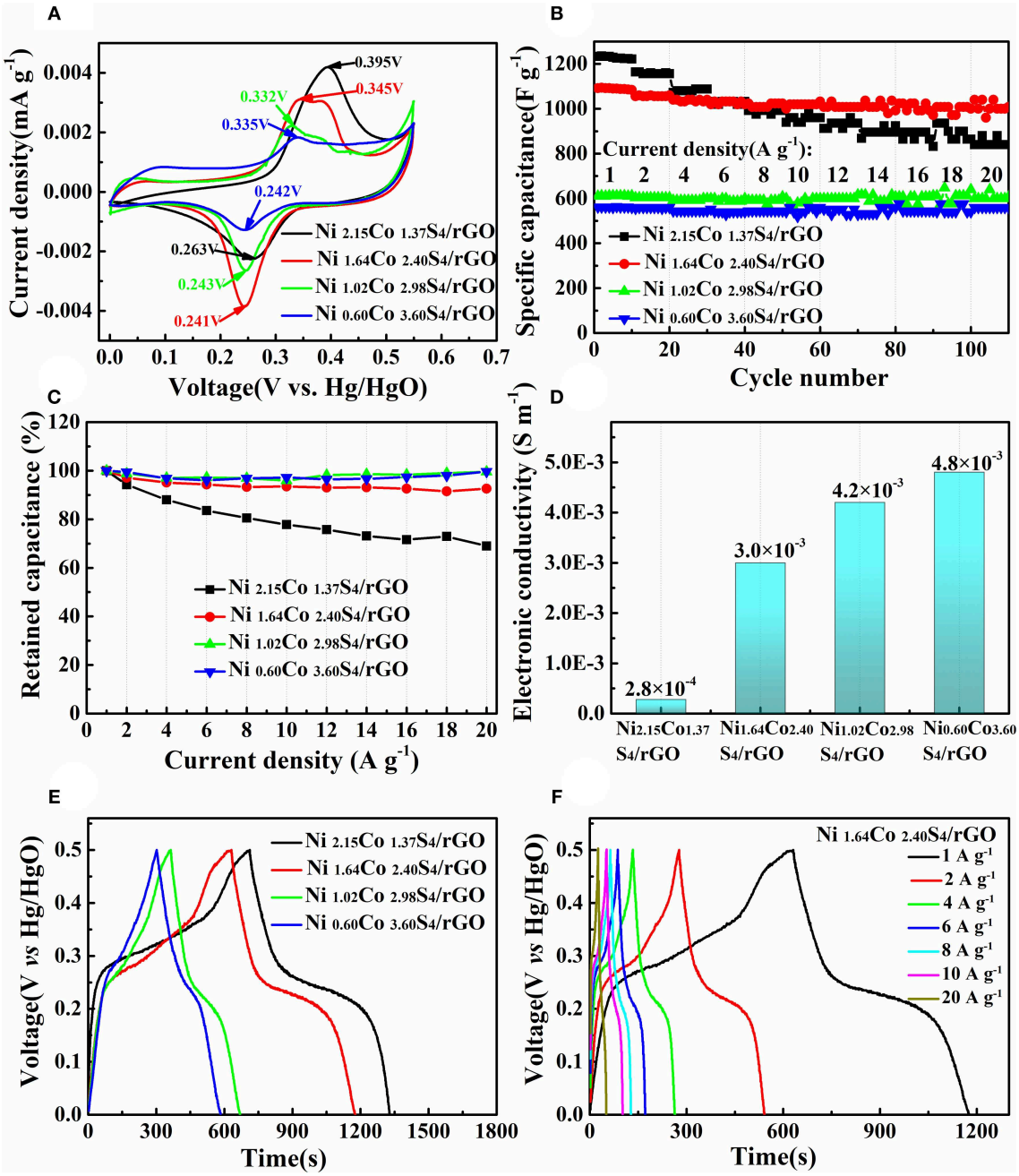

FIGURE 5 | CV curves of $Ni_xCo_yS_4$/rGO composites at the scan rate of 1 mV s^{-1} **(A)**; rate performance of $Ni_xCo_yS_4$/rGO composites at various current densities from 1 A g^{-1} to 20 A g^{-1} **(B)**; capacitance retention of $Ni_xCo_yS_4$/rGO composites with the increase of current density **(C)**; electronic conductivity of $Ni_xCo_yS_4$/rGO composites **(D)**; GCD curves of different composites at the current densities of 1 A g^{-1} **(E)**; GCD curves of $Ni_{1.64}Co_{2.40}S_4$/rGO at various current densities from 1 A g^{-1} to 20 A g^{-1} **(F)**.

is also calculated as shown in **Figure 6C**. The b value in the charge and discharge process are −0.70 and 0.77, respectively, which is quite consistent with the previous results as measured in the three-electrode cell. The specific capacitance and the corresponding GCD curves of the $Ni_{1.64}Co_{2.40}S_4$/rGO//AC asymmetric supercapacitor at various current densities are presented in **Figures 6D,E**, the specific capacitances are 265.5, 209.4, 195.6, 191.3, 180.0, and 168.8 F g^{-1} at the current density of 1, 10, 20, 30, 40, and 50 A g^{-1} respectively. The high capacitance retention of 63.6% at 50 A g^{-1} as compared to 1 A g^{-1} further verifies the excellent rate performance of the asymmetric supercapacitor. Furthermore, the long-term

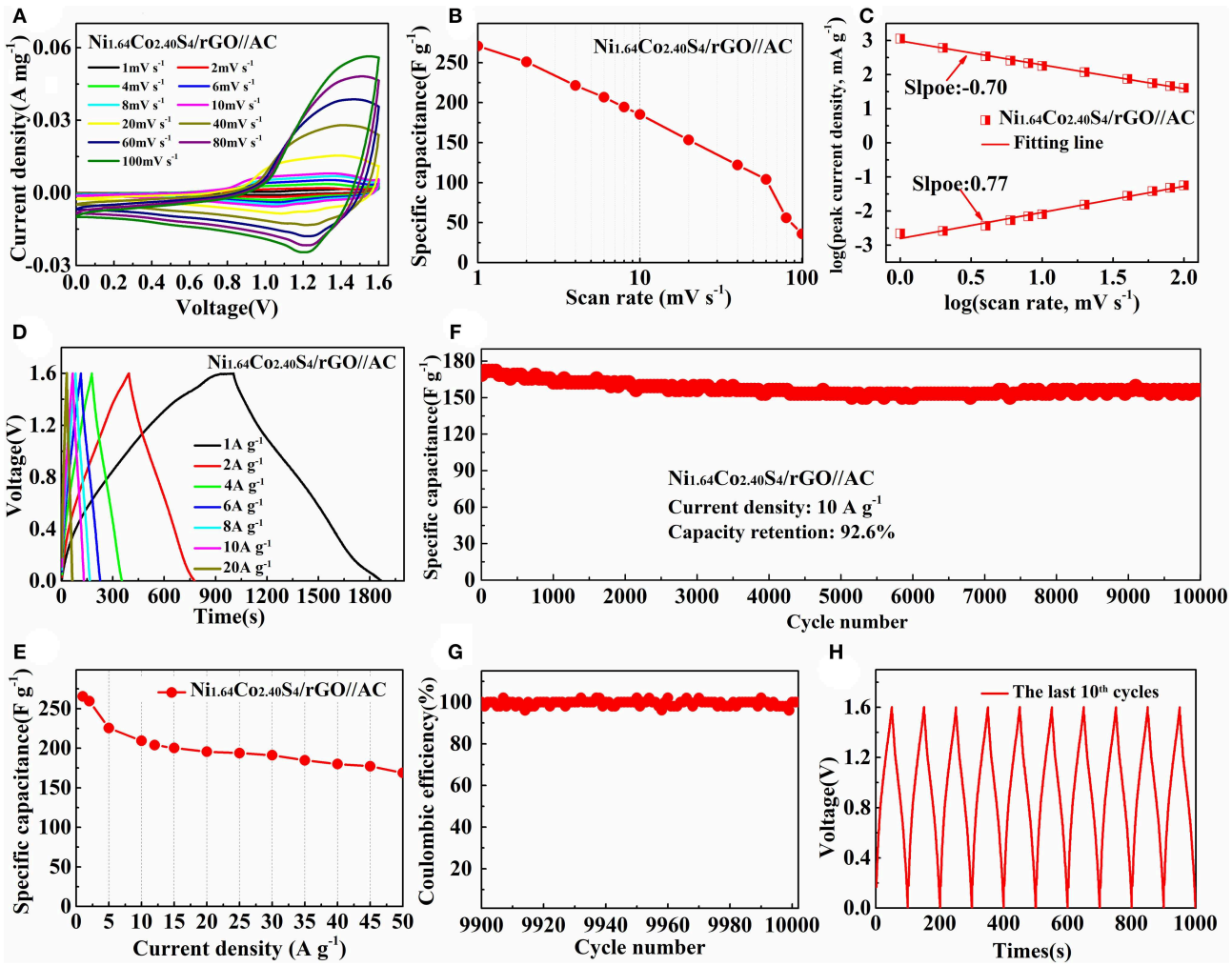

FIGURE 6 | Electrochemical properties of $Ni_{1.64}Co_{2.40}S_4$/rGO//AC asymmetric supercapacitor. CV curves of $Ni_{1.64}Co_{2.40}S_4$/rGO//AC at different scan rates **(A)**; specific capacitance of $Ni_{1.64}Co_{2.40}S_4$/rGO//AC calculated from CV curves **(B)**; relationship between scan rate and current density of $Ni_{1.64}Co_{2.40}S_4$/rGO//AC **(C)**; GCD curves of $Ni_{1.64}Co_{2.40}S_4$/rGO//AC at various current densities **(D)**; average specific capacitances in dependence of cycle number at various current densities from 1 A g^{-1} to 20 A g^{-1} **(E)**; cycle performance of $Ni_{1.64}Co_{2.40}S_4$/rGO//AC at the current density of 10 A g^{-1} **(F)**; columbic efficiency of $Ni_{1.64}Co_{2.40}S_4$/rGO//AC at the last 100 cycles **(G)**; GCD curves of $Ni_{1.64}Co_{2.40}S_4$/rGO//AC at the last 10 cycles of 10000 cycles **(H)**.

cycling measurements of the $Ni_{1.64}Co_{2.40}S_4$/rGO//AC at 10 A g^{-1} (as shown in **Figure 6F**) evidence the good cycling stability as it can retain 92.6 % of its initial capacitance after 10,000 times, demonstrating the high cyclic stability in terms of electrochemical and mechanical properties of the $Ni_{1.64}Co_{2.40}S_4$/rGO composites. Eventually, the high columbic efficiency approaching 100% and the symmetric GCD curves of the last few loops (**Figures 6G,H**) confirm the excellent electrochemical performance of the $Ni_{1.64}Co_{2.40}S_4$/rGO//AC asymmetric supercapacitor.

For positioning the level of as-obtained $Ni_{1.64}Co_{2.40}S_4$/rGO composite, we carefully investigated and compared the energy density and power density of supercapacitors using similar materials from the peer-reviewed papers. Ragone plot of these asymmetric supercapacitors derived from GCD tests are summarized and plotted in **Figure 7** and **Table S4**. Specifically, the $Ni_{1.64}Co_{2.40}S_4$/rGO//AC asymmetric supercapacitor can reach the maximum energy density of 47.2 Wh kg^{-1} at the power density of 200 W kg^{-1}, and retains an energy density of 30 Wh kg^{-1} even at high power density of 10 kW kg^{-1}. Impressively, the $Ni_{1.64}Co_{2.40}S_4$/rGO//AC asymmetric supercapacitor presented in this work is comparable or even superior to those of previous reported transition metal sulfides-based asymmetric supercapacitors and other supercapacitors (listed in **Table S5**), such as NCS/rGO/CNT-3//AC asymmetric supercapacitors (21.06 Wh kg^{-1} at the power density of 729 W kg^{-1} and 14.43 Wh kg^{-1} at the power density of 3646 W kg^{-1}) (Chiu and Chen, 2018), rGO/$CoNiS_x$/N–C//AC asymmetric supercapacitors (32.9 Wh kg^{-1} at the power density of 229.2 W kg^{-1} and 20.9 Wh kg^{-1} at the power density of 1833.3 W kg^{-1})

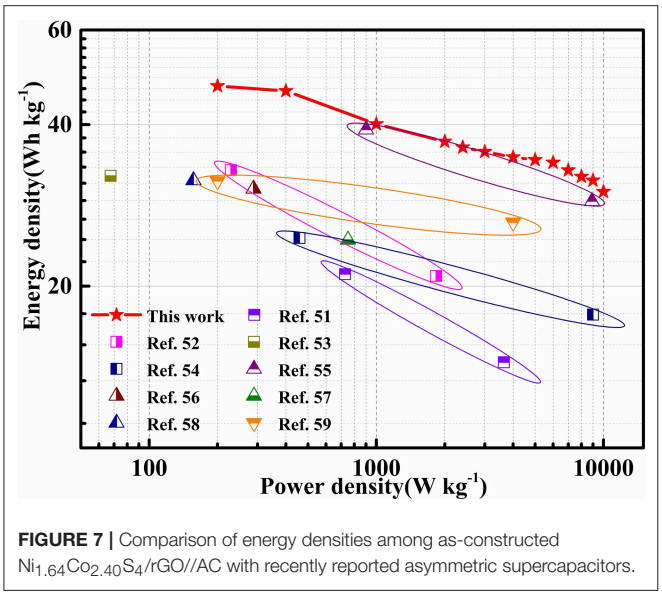

FIGURE 7 | Comparison of energy densities among as-constructed $Ni_{1.64}Co_{2.40}S_4$/rGO//AC with recently reported asymmetric supercapacitors.

(Chen Q. et al., 2018), $NiCo_2S_4$@CNFs//AC@pCNFs asymmetric supercapacitors (32.1 Wh kg^{-1} at the power density of 67.6 W kg^{-1} and 5.3 Wh kg^{-1} at the power density of 1,270 W kg^{-1}) (Liu et al., 2018b), GCM//H-GCS FASC (24.6 Wh kg^{-1} at the power density of 459.3 W kg^{-1} and 17.7 Wh kg^{-1} at the power density of 9005.3 W kg^{-1}) (Wu S. et al., 2018), NSC-900/MnO_2//NSC-900 asymmetric supercapacitors (39.15 Wh kg^{-1} at the power density of 901 W kg^{-1} and 28.8 Wh kg^{-1} at the power density of 8,907 W kg^{-1}) (Miao et al., 2018), $NiCo_2S_4$@NiO//AC (30.38 Wh kg^{-1} at the power density of 288 W kg^{-1}) (Huang et al., 2016), $NiCo_2S_4$/RGO//AC(24.4 Wh kg^{-1} at the power density of 750 W kg^{-1}) (Li Z. et al., 2016), $NiCo_2S_4$ nanotube arrays-Ni foam//RGO (31.5 Wh kg^{-1} at the power density of 156.6 W kg^{-1}) (Chen H. et al., 2014), Co_9S_8 nanoflake//AC (31.4 Wh kg^{-1} at the power density of 200 W kg^{-1} and 26.3 Wh kg^{-1} at the power density of 4,000 W kg^{-1}) (Rakhi et al., 2014).

CONCLUSION

We have reported an *in situ* growth—ion exchange method to synthesize $Ni_xCo_yS_4$/rGO composites with high energy and power density. We concluded from the composition, electronic conductivity, and electrochemical measurements that proper Ni/Co molar ratio in $Ni_xCo_yS_4$/rGO composites is vital to synthesize the material with high capacitance and rate capability. Here the as-prepared $Ni_{1.64}Co_{2.40}S_4$/rGO composite shows the best overall electrochemical performance among the obtained samples as it delivers a specific capacitance of 1,089 F g^{-1} at 1 A g^{-1}, and it maintains 1,008 F g^{-1} at high current density of 20 A g^{-1}. The derived $Ni_{1.64}Co_{2.40}S_4$/rGO//AC asymmetric supercapacitor offers high energy density of 47.2 Wh kg^{-1} (200 W kg^{-1}), together with a superior cyclic stability (maintaining 92.6 % of capacitance retention after 10,000 cycles at 10 A g^{-1}). Through this study, the synthesized and characterized $Ni_{1.64}Co_{2.40}S_4$/rGO composite provides a promising material for fabricating supercapacitors with both high energy and power density.

DATA AVAILABILITY

All datasets generated for this study are included in the manuscript/**Supplementary Files**.

AUTHOR CONTRIBUTIONS

The design and conduction of the experiment, the acquisition of data, the writing and modification of the paper are completed by MD. ZW and JW helped perfecting the experimental ideas and technical route. GY devoted many efforts to revise the manuscript. HG and XL gave advices during the discussion of the experimental results.

FUNDING

This research was supported by the National Science Foundation of China (51674295, 51804344), the Fundamental Research Funds for the Central University of Central South University (2018zzts017), the Hunan Provincial Innovation Foundation for Postgraduate (CX2018B088).

SUPPLEMENTARY MATERIAL

The Supplementary Material for this article can be found online at: https://www.frontiersin.org/articles/10.3389/fmats.2019.00176/full#supplementary-material

Supporting information for publication is available. XRD patterns, SEM images, TEM images of precursors; XPS, SEM, and EDS results of GO and rGO-$Na_2S{\cdot}9H_2O$; GCD curves of $Ni_{2.15}Co_{1.37}S_4$/rGO, $Ni_{1.02}Co_{2.98}S_4$/rGO, and $Ni_{0.60}Co_{3.60}S_4$/rGO; C-S and ICP results of $Ni_xCo_yS_4$/rGO composites.

REFERENCES

Annamalai, K. P., Liu, L., and Tao, Y. (2017). Highly exposed nickel cobalt sulfide–rGO nanoporous structures: an advanced energy-storage electrode material. *J. Mater. Chem. A* 5, 9991–9997. doi: 10.1039/C7TA01735A

Booth, T. J., Blake, P., Nair, R. R., Jiang, D., Hill, E. W., Bangert, U., et al. (2008). Macroscopic graphene membranes and their extraordinary stiffness. *Nano Lett.* 8, 2442–2446. doi: 10.1021/nl801412y

Brousse, T. (2015). To be or not to be pseudocapacitive? *J. Electrochem. Soc.* 162, A5185–A5189. doi: 10.1149/2.0201505jes

Chen, H., Jiang J., Zhang, L., Xia, D., Zhao, Y., Guo, D., et al. (2014). *In situ* growth of $NiCo_2S_4$ nanotube arrays on Ni foam for supercapacitors: maximizing utilization efficiency at high mass loading to achieve ultrahigh areal pseudocapacitance. *J. Power Sources* 254, 249–257. doi: 10.1016/j.jpowsour.2013.12.092

Chen, H., Jiang, J., Zhang, L., Wan, H., Qi, T., and Xia, D. (2013). Highly conductive $NiCo_2S_4$ urchin-like nanostructures for high-rate pseudocapacitors. *Nanoscale* 5, 8879–8883. doi: 10.1039/c3nr02958a

Chen, J., Li, L., Wu, L., Yao, Q., Yang, H., Liu, Z., et al. (2018). Enhanced cycle stability of $Na_{0.9}Ni_{0.45}Mn_{0.55}O_2$ through tailoring O_3/P_2

hybrid structures for sodium-ion batteries. *J. Power Sources* 406, 110–117. doi: 10.1016/j.jpowsour.2018.10.058

Chen, Q., Miao, J., Quan, L., Cai, D., and Zhan, H. (2018). Bimetallic $CoNiS_x$ nanocrystallites embedded in nitrogen-doped carbon anchored on reduced graphene oxide for high-performance supercapacitors. *Nanoscale* 10, 4051–4060. doi: 10.1039/C7NR08284C

Chen, X., Chen, X., Xu, X., Yang, Z., Liu, Z., Zhang, L., et al. (2014). Sulfur-doped porous reduced graphene oxide hollow nanosphere frameworks as metal-free electrocatalysts for oxygen reduction reaction and as supercapacitor electrode materials. *Nanoscale* 6, 13740–13747. doi: 10.1039/C4NR04783D

Chiu, C. T., and Chen, D. H. (2018). One-step hydrothermal synthesis of three-dimensional porous Ni-Co sulfide/reduced graphene oxide composite with optimal incorporation of carbon nanotubes for high performance supercapacitors. *Nanotechnology* 29:175602. doi: 10.1088/1361-6528/aaaff5

Deng, Y., Xu, A., Lu, W., Yu, Y., Fua, C., and Shua, T. (2017). Graphene-based ordered mesoporous carbon hybrids with large surface areas for supercapacitor. *New J. Chem.* 42, 7043–7048. doi: 10.1039/C7NJ03923A

Dong, M., Wang, Z., Li, X., Guo, H., and Wang, J. (2018). A smart architecture of nickel-cobalt sulfide nanotubes assembled nanoclusters for high-performance pseudocapacitor. *J. Alloys Compd.* 765, 505–511. doi: 10.1016/j.jallcom.2018.06.179

Eftekhari, A., Li, L., and Yang, Y. (2017). Polyaniline supercapacitors. *J. Power Sources* 347, 86–107. doi: 10.1016/j.jpowsour.2017.02.054

Fan, Y.-M., Liu, Y., Liu, X., Liu, Y., and Fan, L.-Z. (2017). Hierarchical porous $NiCo_2S_4$-rGO composites for high-performance supercapacitors. *Electrochim. Acta* 249, 1–8. doi: 10.1016/j.electacta.2017.07.175

Gao, Z., Chen, C., Chang, J., Chen, L., Wang, P., Wu, D., et al. (2018). Enhanced cycleability of faradic $CoNi_2S_4$ electrode by reduced graphene oxide coating for efficient asymmetric supercapacitor. *Electrochim. Acta* 281, 394–404. doi: 10.1016/j.electacta.2018.05.194

Gilshteyn, E. P., Amanbayev, D., Anisimov, A. S., Kallio, T., and Nasibulin, A. G. (2017). All-nanotube stretchable supercapacitor with low equivalent series resistance. *Sci. Rep.* 7:17449. doi: 10.1038/s41598-017-17801-4

Huang, Y., Shi, T., Jiang, S., Cheng, S., Tao, X., Zhong, Y., et al. (2016). Enhanced cycling stability of $NiCo_2S_4$@NiO core-shell nanowire arrays for all-solid-state asymmetric supercapacitors. *Sci. Rep.* 6:38620. doi: 10.1038/srep38620

Jiang, Y., and Liu, J. (2019). Definitions of pseudocapacitive materials: a brief review. *Energy Environ. Mater.* 2, 30–37. doi: 10.1002/eem2.12028

Jinlong, L., Tongxiang, L., Meng, Y., Ken, S., and Hideo, M. (2017). Performance comparison of $NiCo_2O_4$ and $NiCo_2S_4$ formed on Ni foam for supercapacitors. *Compos. Part B* 123, 28–33. doi: 10.1016/j.compositesb.2017.05.021

Ke, Q., and Wang, J. (2016). Graphene-based materials for supercapacitor electrodes – a review. *J. Materiom.* 2, 37–54. doi: 10.1016/j.jmat.2016.01.001

Lee, C., Wei, X., Kysar, J. W., and Hone, J. (2008). Measurement of the elastic properties and intrinsic strength of monolayer graphene. *Science* 321, 385–388. doi: 10.1126/science.1157996

Li, D., Gong, Y., and Pan, C. (2016). Facile synthesis of hybrid CNTs/$NiCo_2S_4$ composite for high performance supercapacitors. *Sci. Rep.* 6:29788. doi: 10.1038/srep29788

Li, L., Chen, Z., Zhang, Q., Xu, M., Zhou, X., Zhu, H., et al. (2015). A hydrolysis-hydrothermal route for the synthesis of ultrathin $LiAlO_2$-inlaid $LiNi_{0.5}Co_{0.2}Mn_{0.3}O_2$ as a high-performance cathode material for lithium ion batteries. *J. Mater. Chem. A* 3, 894–904. doi: 10.1039/C4TA05902F

Li, Z., Ji, X., Han, J., Hu, Y., and Guo, R. (2016). $NiCo_2S_4$ nanoparticles anchored on reduced graphene oxide sheets: *in-situ* synthesis and enhanced capacitive performance. *J. Colloid Interface Sci.* 477, 46–53. doi: 10.1016/j.jcis.2016.05.038

Liang, K., He, W., Deng, X., Ma, H., and Xu, X. (2018). Controlled synthesis of $NiCo_2S_4$ hollow spheres as high-performance electrode materials for supercapacitors. *J. Alloys Compd.* 735, 1395–1401. doi: 10.1016/j.jallcom.2017.11.153

Lim, E., Jo, C., Kim, H., Kim, M. H., Mun, Y., Chun, J., et al. (2015). Facile synthesis of Nb_2O_5@carbon core-shell nanocrystals with controlled crystalline structure for high-power anodes in hybrid supercapacitors. *ACS Nano* 9, 7497–7505. doi: 10.1021/acsnano.5b02601

Liu, S., Cai, Y., Zhao, X., Liang, Y., Zheng, M., Hu, H., et al. (2017). Sulfur-doped nanoporous carbon spheres with ultrahigh specific surface area and high electrochemical activity for supercapacitor. *J. Power Sources* 360, 373–382. doi: 10.1016/j.jpowsour.2017.06.029

Liu, Y., Fan, X., Huang, X., Liu, D., Dou, A., Su, M., et al. (2018a). Electrochemical performance of $Li_{1.2}Ni_{0.2}Mn_{0.6}O_2$ coated with a facilely synthesized $Li_{1.3}Al_{0.3}Ti_{1.7}(PO_4)_3$. *J. Power Sources* 403, 27–37. doi: 10.1016/j.jpowsour.2018.09.082

Liu, Y., Jiang, G., Sun, S., Xu, B., Zhou, J., Zhang, Y., et al. (2018b). Decoration of carbon nanofibers with $NiCo_2S_4$ nanoparticles for flexible asymmetric supercapacitors. *J. Alloys Compd.* 731, 560–568. doi: 10.1016/j.jallcom.2017.10.078

Liu, Y., Wang, Q., Zhang, Z., Dou, A., Pan, J., and Su, M. (2016). Investigation the electrochemical performance of layered cathode material $Li_{1.2}Ni_{0.2}Mn_{0.6}O_2$ coated with $Li_4Ti_5O_{12}$. *Adv. Powder Technol.* 27, 1481–1487. doi: 10.1016/j.apt.2016.05.008

Ma, L., Chen, T., Li, S., Gui, P., and Fang, G. (2019). A 3D self-supported coralline-like $CuCo_2S_4$@$NiCo_2S_4$ core-shell nanostructure composite for high-performance solid-state asymmetrical supercapacitors. *Nanotechnology* 30:255603. doi: 10.1088/1361-6528/ab08fb

Ma, L., Hu, Y., Chen, R., Zhu, G., Chen, T., Lv, H., et al. (2016). Self-assembled ultrathin $NiCo_2S_4$ nanoflakes grown on Ni foam as high-performance flexible electrodes for hydrogen evolution reaction in alkaline solution. *Nano Energy* 24, 139–147. doi: 10.1016/j.nanoen.2016.04.024

Miao, L., Zhu, D., Liu, M., Duan, H., Wang, Z., Lv, Y., et al. (2018). N, S Co-doped hierarchical porous carbon rods derived from protic salt: facile synthesis for high energy density supercapacitors. *Electrochim. Acta* 274, 378–388. doi: 10.1016/j.electacta.2018.04.100

Mohamed, S. G., Hussain, I., and Shim, J. J. (2018). One-step synthesis of hollow C-$NiCo_2S_4$ nanostructures for high-performance supercapacitor electrodes. *Nanoscale* 10, 6620–6628. doi: 10.1039/C7NR07338K

Nan, H., Han, J., Luo, Q., Yin, X., Zhou, Y., Yao, Z., et al. (2018). Economically synthesized $NiCo_2S_4$/reduced graphene oxide composite as efficient counter electrode in dye-sensitized solar cell. *Appl. Surf. Sci.* 437, 227–232. doi: 10.1016/j.apsusc.2017.12.175

Qin, H., Yang, S., Zhao, W., Yang, Z., Li, X., Li, H., et al. (2017). Synthesis of mesoporous $NiCo_2S_4$ deposited on reduced graphite oxide assistant by co-polymer Pluronic F127 for high-performance supercapacitor. *Appl. Surf. Sci.* 420, 77–82. doi: 10.1016/j.apsusc.2017.05.048

Qu, C., Zhang, L., Meng, W., Liang, Z., Zhu, B., Dang, D., et al. (2018). MOF-derived α-NiS nanorods on graphene as an electrode for high-energy-density supercapacitors. *J. Mater. Chem. A* 6, 4003–4012. doi,: 10.1039/C.7T. A.11100B.

Rakhi, R. B., Alhebshi, N. A., Anjum, D. H., and Alshareef H. N. (2014). Nanostructured cobalt sulfide-on-fiber with tunable morphology as electrodes for asymmetric hybrid supercapacitors. *J. Mater. Chem. A* 9, 16190–16198. doi: 10.1039/C4TA03341H

Saha, S., Samanta, P., Murmu, N. C., and Kuila, T. (2018). A review on the heterostructure nanomaterials for supercapacitor application. *J. Energy Storage* 17, 181–202. doi: 10.1016/j.est.2018.03.006

Sarkar, A., Bera, S., and Chakraborty, A. K. (2018). $NiCo_2S_4$ nanorod embedded rGO sheets as electrodes for supercapacitor. *AIP Conf. Proc.* 1942:140029. doi: 10.1063/1.5029160

Simon, P., Gogotsi, Y., and Dunn, B. (2014). Where do batteries end and supercapacitors begin? *Mater. Sci.* 343, 1210–1211. doi: 10.1126/science.1249625

Tan, L., Li, X., Wang, Z., Guo, H., and Wang, J. (2018). Lightweight reduced graphene oxide@MoS_2 interlayer as polysulfide barrier for high-performance lithium-sulfur batteries. *ACS Appl. Mater. Interfaces* 10, 3707–3713. doi: 10.1021/acsami.7b18645

Wan, H., Jiang, J., Yu, J., Xu, K., Ling, M., Li, Z., et al. (2013). $NiCo_2S_4$ porous nanotubes synthesis via sacrificial templates: high-performance electrode materials of supercapacitors. *CrystEngComm* 15, 7649–7651. doi: 10.1039/c3ce41243a

Wang, H., Liang, M., Ma, C., Shi, W., Duan, D., He, G., et al. (2019). Novel dealloying-fabricated $NiCo_2S_4$ nanoparticles with excellent cycling performance for supercapacitors. *Nanotechnology* 30:235402. doi: 10.1088/1361-6528/ab0605

Wang, J., Zhang, G., Liu, Z., Li, H., Liu, Y., Wang, Z., et al. (2018). $Li_3V(MoO_4)_3$ as a novel electrode material with good lithium storage properties and improved initial coulombic efficiency. *Nano Energy* 44, 272–278. doi: 10.1016/j.nanoen.2017.11.079

Wang, Y., Yang, L., Liu, Y., Zhao, Q., Ding, F., Zou, P., et al. (2018). Colorimetric determination of dopamine by exploiting the enhanced oxidase mimicking activity of hierarchical $NiCo_2S_4$-rGO composites. *Mikrochim. Acta* 185, 496. doi: 10.1007/s00604-018-3035-8

Wen, Y., Peng, S., Wang, Z., Hao, J., Qin, T., Lu, S., et al. (2017). Facile synthesis of ultrathin $NiCo_2S_4$ nano-petals inspired by blooming buds for high-performance supercapacitors. *J. Mater. Chem. A* 5, 7144–7152. doi: 10.1039/C7TA01326D

Wenfang, D., Zhang, Y., Yang, L., Tan, Y., Ma, M., and Xie, Q. (2015). Sulfur-doped porous carbon nanosheets as an advanced electrode material for supercapacitors. *RSC Adv.* 5, 13046–13051. doi: 10.1039/C4RA14820G

Wu, F., Chen, S., Srot, V., Huang, Y., Sinha, S. K., Van Aken, P. A., et al. (2018). A sulfur-limonene-based electrode for lithium-sulfur batteries: high-performance by self-protection. *Adv. Mater.* 30:e1706643. doi: 10.1002/adma.201706643

Wu, S., Hui, K. S., and Hui, K. N. (2018). Carbon nanotube@manganese oxide nanosheet core-shell structure encapsulated within reduced graphene oxide film for flexible all-solid-state asymmetric supercapacitors. *Carbon N. Y.* 132, 776–784. doi: 10.1016/j.carbon.2017.12.051

Xiao, J., and Yang, S. (2011). Sequential crystallization of sea urchin-like bimetallic (Ni, Co) carbonate hydroxide and its morphology conserved conversion to porous $NiCo_2O_4$ spinel for pseudocapacitors. *RSC Adv.* 1:588. doi: 10.1039/c1ra00342a

Xiong, X., Waller, G., Ding, D., Chen, D., Rainwater, B., Zhao, B., et al. (2015). Controlled synthesis of $NiCo_2S_4$ nanostructured arrays on carbon fiber paper for high-performance pseudocapacitors. *Nano Energy* 16, 71–80. doi: 10.1016/j.nanoen.2015.06.018

Yan, G., Dugas, R., and Tarascon, J.-M. (2018). The $Na_3V_2(PO_4)_2$ F-3/carbon na-ion battery: its performance understanding as deduced from differential voltage analysis. *J. Electrochem. Soc.* 165, A220–A227. doi: 10.1149/2.0831802jes

Yuan, D., Huang, G., Yin, D., Wang, X., Wang, C., and Wang, L. (2017). Metal-organic framework template synthesis of $NiCo_2S_4$@C encapsulated in hollow nitrogen-doped carbon cubes with enhanced electrochemical performance for lithium storage. *ACS Appl. Mater. Interfaces* 9, 18178–18186. doi: 10.1021/acsami.7b02176

Zhang, L., Hu, X., Wang, Z., Sun, F., and Dorrell, D. G. (2018). A review of supercapacitor modeling, estimation, and applications: a control/management perspective. *Renew. Sustain. Energy Rev.* 81, 1868–1878. doi: 10.1016/j.rser.2017.05.283

Zhang, Q., Chen, H., Luo, L., Zhao, B., Luo, H., Han, X., et al. (2018). Harnessing the concurrent reaction dynamics in active Si and Ge to achieve high performance lithium-ion batteries. *Energy Environ. Sci.* 11, 669–681. doi: 10.1039/C8EE00239H

Zhao, F., Huang, W., Shi, Q., Zhou, D., Zhao, L., and Zhang, H. (2017). Low temperature fabrication of hydrangea-like $NiCo_2S_4$ as electrode materials for high performance supercapacitors. *Mater. Lett.* 186, 206–209. doi: 10.1016/j.matlet.2016.09.110

Zhong, S., Hong, W., Zhang, X., Liu, J., Li, Y., Shi, Y., et al. (2017). Synthesis of $xLiVPO_4F$ center dot $yLi_3V_2(PO_4)_3$/C composite as a potential cathode material for Li-ion batteries. *Ionics (Kiel).* 23, 813–819. doi: 10.1007/s11581-016-1875-y

Zhong, S., Wu, L., Zheng, J., and Liu, J. (2012). Preparation of high tap-density $9LiFePO_4$ center dot Li3V2(PO4)(3)/C composite cathode material by spray drying and post-calcining method. *Powder Technol.* 219, 45–48. doi: 10.1016/j.powtec.2011.12.005

Zhu, Y., Wu, Z., Jing, M., Yang, X., Song, W., and Ji, X. (2015). Mesoporous $NiCo_2S_4$ nanoparticles as high-performance electrode materials for supercapacitors. *J. Power Sources* 273, 584–590. doi: 10.1016/j.jpowsour.2014.09.144

Conflict of Interest Statement: The authors declare that the research was conducted in the absence of any commercial or financial relationships that could be construed as a potential conflict of interest.

frontiers in Chemistry

ORIGINAL RESEARCH
published: 06 August 2019
doi: 10.3389/fchem.2019.00555

Flexible $Li[Li_{0.2}Ni_{0.13}Co_{0.13}Mn_{0.54}]O_2$/Carbon Nanotubes/Nanofibrillated Celluloses Composite Electrode for High-Performance Lithium-Ion Battery

*Yan Li, Han Zhang, Zhe Xiao and Renheng Wang**

International Collaborative Laboratory of 2D Materials for Optoelectronics Science and Technology of Ministry of Education, Institute of Microscale Optoelectronics, Shenzhen University, Shenzhen, China

OPEN ACCESS

Edited by:
Feixiang Wu,
Central South University, China

Reviewed by:
Xianwen Wu,
Jishou University, China
Xunhui Xiong,
South China University of Technology, China

***Correspondence:**
Renheng Wang
wangrh@szu.edu.cn

Specialty section:
This article was submitted to Electrochemistry, a section of the journal Frontiers in Chemistry

Received: *14 May 2019*
Accepted: *22 July 2019*
Published: *06 August 2019*

Citation:
Li Y, Zhang H, Xiao Z and Wang R (2019) Flexible $Li[Li_{0.2}Ni_{0.13}Co_{0.13}Mn_{0.54}]O_2$/Carbon Nanotubes/Nanofibrillated Celluloses Composite Electrode for High-Performance Lithium-Ion Battery. Front. Chem. 7:555. doi: 10.3389/fchem.2019.00555

Rapidly-growing demand for wearable and flexible devices is boosting the development of flexible lithium ion batteries (LIBs). The exploitation of flexible electrodes with high mechanical properties and superior electrochemical performances has been a key challenge for the rapid practical application of flexible LIBs. Herein, a flexible composite electrode was prepared from the mixed solutions of $Li[Li_{0.2}Ni_{0.13}Co_{0.13}Mn_{0.54}]O_2$ (LLOs), carbon nanotubes(CNTs), and nanofibrillated celluloses (NFCs) via a vacuum filtration method. The resulting LLOs/CNTs/NFCs electrode delivered an initial discharge capacity of 253 mAh g^{-1} at 0.1 C in the voltage range from 2.0 to 4.6 V, and retained a reversible capacity of 178 mAh g^{-1} with 83% capacity retention after 100 cycles at 1 C. The LLOs/CNTs/NFCs electrode exhibited excellent flexibility along with repeated bending in the bending test. The LLOs/CNTs/NFCs electrode after bending test remained a discharge capacity of 149 mAh g^{-1} after 100 cycles at 1 C, and the corresponding capacity retentions was 76%. The excellent electrochemical performance and high flexibility can be ascribed to the framework formed by CNTs with high conductivity and NFCs with good mechanical properties. The results imply that the as-fabricated electrode can be a promising candidate for the flexible LIBs.

Keywords: lithium ion battery, flexible electrode, $Li[Li_{0.2}Ni_{0.13}Co_{0.13}Mn_{0.54}]O_2$, carbon nanotubes, nanofibrillated celluloses

INTRODUCTION

Along with the rise and development of the wearable and flexible electronic products, the concept of flexible devices emerges at the right moment and engulfes the entire world (Manthiram et al., 2008; Kim and Cho, 2010; Agnès et al., 2014). One of the biggest obstacles to the application of flexible electronic products is the development of flexible electrochemical energy storage devices (Ju et al., 2014; Li et al., 2014). LIBs have unique advantages when applied to electronic devices due to its light weight, high specific power, high energy density, and

excellent electrochemical performance (Ding et al., 2011; Dunn et al., 2011; Strong et al., 2012; Yan et al., 2013; Yuan et al., 2014; Nitta et al., 2015; Li et al., 2017a,b; Yang et al., 2019). However, the separation of electrode materials and collector fluid affects the electrochemical properties when fold the traditional rigid LIBs, and even lead to short circuit and other serious safety problems (Hu and Sun, 2014; Zhou et al., 2014; He et al., 2016). Therefore, it is of great significance for the development of flexible electronics to endow LIBs with flexibility and develop flexible electrode with excellent electrochemical performance. A well-known strategy to prepare flexible electrode is adopting flexible organic substrates such as polymer and textile instead of traditional copper/aluminum foil as current collector for carrying the active materials (Wang et al., 2006, 2008; Chen et al., 2007; Gao et al., 2015; Huang et al., 2016; Zhen et al., 2016). However, these non-electroactive substrates with low conductivity will greatly affect the quick charge-discharge process of batteries. Therefore, flexible electrodes with conductive matrix such as graphite paper and carbon nanotube film have become a hot research topic, while the weak binding force between active materials and current collector will inevitably result in serious capacity fading and limit further applications (Chou et al., 2008; Xin et al., 2011; Hu et al., 2013). Recently, many researchers had proposed to build the 3D thin-film electrodes which compounding the traditional active electrode material with the conductive carbon-based material and flexible matrix. The carbon-based materials acted as the basic element of the conductive network, and the flexible matrix served on the supporting framework of the whole electrode. This method can fully combine the advantages of carbon-based materials and traditional active electrode materials (Su et al., 2010; Tai et al., 2012; Lian et al., 2014; Yu et al., 2014; Wang et al., 2017b).

Lithium-rich layered oxides (LLOs) have been extensively investigated owing to their high reversible capacity, high working voltage, high energy density, lost cost, and amity to environment (Wang et al., 2009; He et al., 2013; Hu et al., 2018). With a reversible capacity of 250 mAh g^{-1}, LLOs were attractive enough to high-energy LIBs and have demonstrated enormous potential in terms of electric vehicles and smart grid applications. As one of the most abundant renewable polymers, nanofibrillated cellulose (NFC) has several advantages such as nanoscale diameter, high homogeneity, high tensile strength and high Young modulus. The one dimension nano-structure is beneficial to bind active electrode particles in the nanometer scale, and allows for the formation of thinner films with higher space efficient (Ho et al., 2011). NFC with excellent mechanical properties can be utilized as flexible matrix and binder for composite electrodes, and has great prospects in flexible energy storage devices. For example, a flexible NFC/$LiFePO_4$/Super-P paper electrode was prepared by filtration process. NFCs acted both as electrode binder material and the separator material. The resulting thin electrode was very strong which can withstand of strength up to 5.6 Mpa. The flexible electrode delivered a reversible capacity of 146 mAh g^{-1} and an energy density of 188 mWh g^{-1} of full paper battery at 0.1 C (Leijonmarck et al., 2013). Recently, Wang et al. developed a flexible $LiFePO_4$/graphene/NFC electrode with the mechanical support of NFC, and the composite electrode shows high flexibility as well as excellent electrochemical properties (Wang et al., 2018). Carbon-based materials with high conductivity were highly desirable for high-performance LIBs. Many studies have proved that CNTs can improve the electronic conductivity of electrode and offer the buffer spaces for the volume expansion of active material during the cycling process (Chen et al., 2007; Fu et al., 2013; Kang et al., 2016). Thanks to the graphitic structure and good electrical conductivity, CNTs has the capability of forming conductive network structure and is very suitable for preparing self-supporting film electrodes (Bai et al., 2015; Wan et al., 2015). For instance, a binder-free $LiMn_2O_4$/CNT electrode with good flexibility were fabricated by *in-situ* hydrothermal growth for flexible LIBs, and the flexible electrode showed good cycling and rate performance (Jia et al., 2011).

Herein, a flexible LLOs/CNTs/NFCs composite electrode was fabricated via a facile vacuum filtration route. The resulting LLOs/CNTs/NFCs composite electrode exhibited good electrochemical performance as well as high flexibility, which

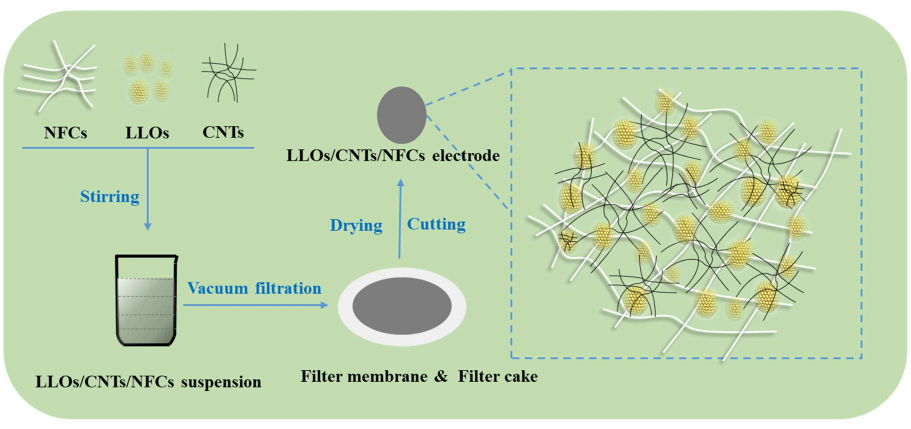

FIGURE 1 | Flow diagram of the preparation procedure of flexible LLOs/CNTs/NFCs electrode.

can be ascribed to the three-dimensional conductive framework formed by NFCs and CNTs.

EXPERIMENTAL

Synthesis and Characterization

LLOs were prepared from the $Mn_{0.54}Ni_{0.13}Co_{0.13}(CO_3)_{0.8}$ precursors (Ningbo Institute of Industrial Technology, CAS.) and lithium carbonate via solid state reaction. Commercially available CNTs (wt % > 95%, Shanghai Macklin Biochemical Co., Ltd.) and NFCs (solid content = 5%, width = 5–20 nm, length ≈ 400 μm, Ningbo Rouchuang Nanotechnology Co., Ltd.) were used without further processing. As shown in **Figure 1**, the flexible LLOs/CNTs/NFCs electrode was fabricated via a facile vacuum filtration route. Proper amount of LLOs, CNTs and NFCs with a mass ratio of 8:1:1 were dispersed in 100 ml ethanol and then stirred for 20 h, the resulting LLOs/CNTs/NFCs suspension was filtered using a PTFE membrane (0.22 lm pore size, Tianjin Jinteng Experiment Equipment Co., Ltd.). At last, the LLOs/CNTs/NFCs electrode was prepared from the filter cake after drying and cutting. The diameter of the obtained electrode was 10 mm and the weight of the active materials was about 8 mg.

For comparison, the traditional LLOs electrode with aluminum foil as current collector was also prepared according to the procedures reported earlier (Li et al., 2018).

Morphologies of the samples were investigated with scanning electron microscopy (SEM, Gemini300). The structure of the LLOs/CNTs/NFCs electrode were determined by X-ray diffraction (XRD, Bruker D8) equipped with Cu Kα radiation ranging from 10° to 80° at a scan rate of $10°\cdot min^{-1}$. Raman spectroscopy (FSRS, Renishaw in Via Reflex) was carried out to analysis of the electrode using a laser wavelength of 532 nm.

Electrochemical Measurement

The as-prepared LLOs/CNTs/NFCs electrode and the traditional LLOs electrode acted as the working electrode for the electrochemical measurements of LIBs. Li metal foil, microporous polypropylene film and the liquid organic electrolytes [1 M $LiPF_6$ in EC/DMC/EMC (1:1:1 by volume)] were used as the counter electrodes, separator and electrolyte, respectively. The charge/discharge cycling was carried out in the potential range of 2.0–4.6 V using a CR2032 coin-type cell. The LLOs/CNTs/NFCs electrodes were bended repeatedly with 5 mm curvature radius for different times. The electrochemical performances of the LLOs/CNTs/NFCs electrodes after cyclical bending were tested to investigate the application prospects for the flexible electrode. Electrochemical impedance spectroscopy (EIS) was conducted using a CHI660e electrochemical workstation in the frequency range of 10^{-2}-10^5 Hz.

RESULTS AND DISCUSSION

Figure 2A shows the XRD patterns of the flexible LLOs/CNTs/NFCs electrode. The sample was consistent with the well-crystallized LLOs which adopts a hexagonal α-$NaFeO_2$ type structure. It's worth noting that the characteristic peak (marked by the red box) can be assigned to the (002) peak of NFCs (22.5°) and CNTs (Sassi and Chanzy, 1995; Tessonnier et al., 2009). FSRS in **Figure 2B** shows two distinct Raman peaks at 1350 and 1588 cm^{-1}, which corresponded to the D-band and G-band of CNTs, respectively (Dresselhaus et al., 2007). The other evident peak centered at 1,095 cm^{-1} was assigned to the asymmetric stretching vibration mode of C–O in the NFCs (Leijonmarck et al., 2013). These results revealed that the as-prepared electrode was composed of LLOs and small amount of NFCs and CNTs, and the crystalline structure of LLOs were maintained well in the composite electrode. It can be expected that the introduction of NFCs and CNTs could enhance the overall flexibility and conductivity of the composite electrode.

SEM images of the samples and photographs of the LLOs/CNTs/NFCs electrode were presented in **Figure 3**. **Figure 3a** shows the morphology of LLOs particles, the particles have a micro-grade spherical shape with a diameter ranging from 5 to 20 μm, and the microspheres were formed by numerous primary particles. SEM image in **Figure 3c** indicates that CNTs remained a regular nanotube shape with a diameter in the range of 10–20 nm. **Figures 3c,d** shows the SEM images of the LLOs/CNTs/NFCs electrode in different magnification. The LLOs particles, CNTs and NFCs could be clearly observed in **Figure 3e**. It was evident that the micro-sized LLOs particles

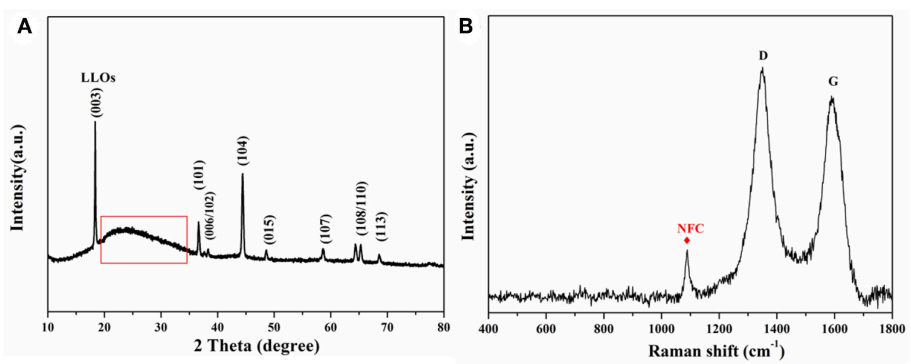

FIGURE 2 | (A) XRD patterns and **(B)** FSRS of the LLOs/CNTs/NFCs.

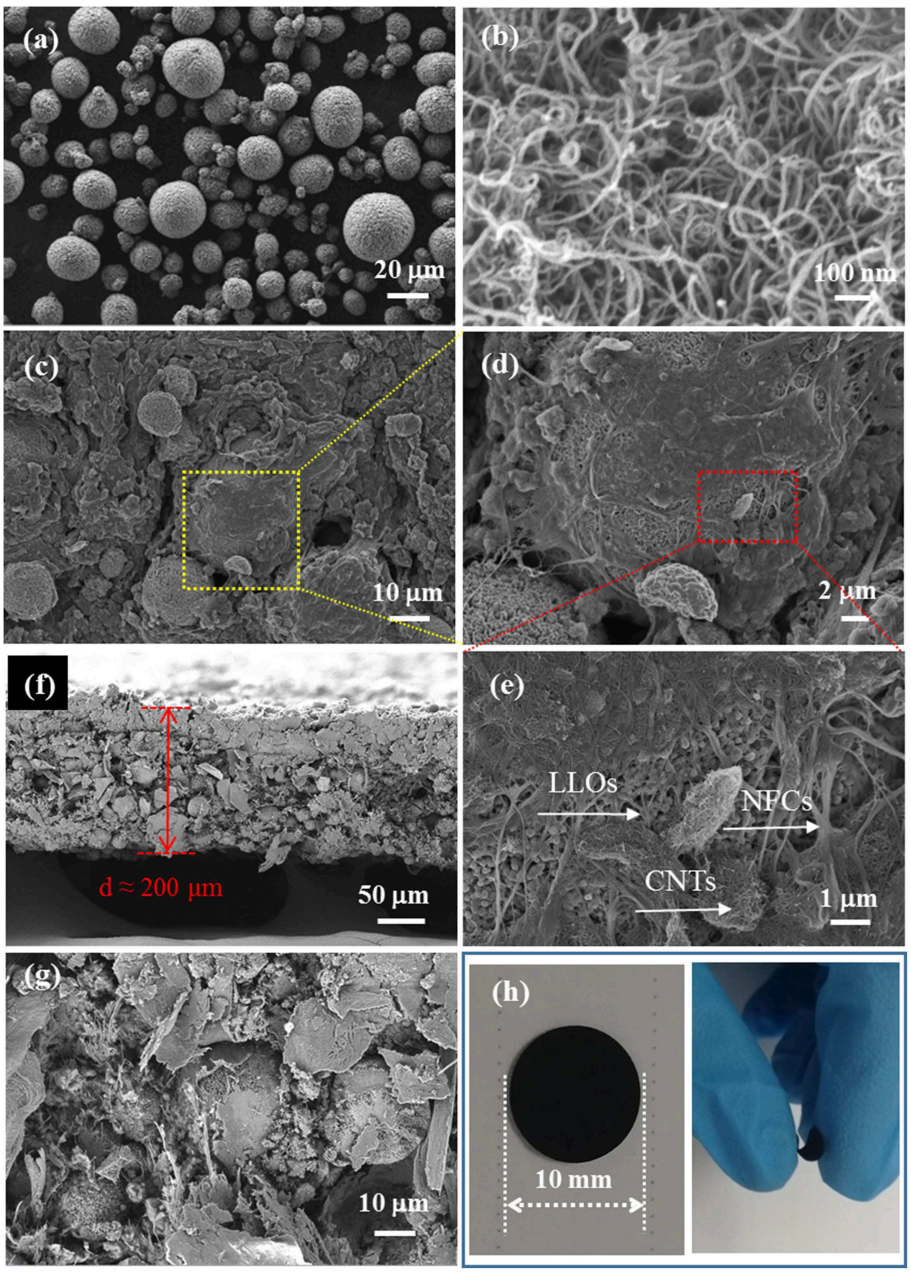

FIGURE 3 | SEM images of **(a)** LLOs, **(b)** CNTs, **(c–e)** LLOs/CNTs/NFCs electrode; **(f,g)** Cross-section images of the LLOs/CNTs/NFCs electrode; **(h)** the photos of LLOs/CNTs/NFCs electrode before and being bending.

were tightly compacted and agglutinated by the frame of NFCs and CNTs, and thus forming the flexible composite electrode. The cross-section images in **Figures 3f,g** indicate that the thickness of the flexible electrode was about 200 μm, and the LLOs particles, CNTs and NFCs were uniform mixed and distributed in the flexible electrode. The photos of the LLOs/CNTs/NFCs electrode with a diameter of 10 mm illustrate its structural integrity and high flexibility, as seen in **Figure 3h**. The surface of the LLOs/CNTs/NFCs electrode was verified to be smooth and level. The structural integrity the electrode can be attributed to the entanglement of NFCs and CNTs. The photo of the electrode being bending illustrates that the as-prepared LLOs/CNTs/NFCs electrode demonstrated good flexibility.

The electrochemical performances of the traditional LLOs electrode and LLOs/CNTs/NFCs electrode were presented in **Figure 4**. **Figure 4A** shows the first cycle curves of the two electrodes at 0.1C rate, the traditional LLOs electrode and the LLOs/CNTs/NFCs electrode exhibite discharge capacities of 253

and 259 mAh g^{-1}, respectively. They show a similar initial coulombic efficiency of about 76%. The cycle performances of the two electrodes were presented in **Figure 4B**. After 100 cycles at 1 C rate, the discharge capacities of the traditional LLOs electrode and the LLOs/CNTs/NFCs electrode remain 165 and 178 mAh g^{-1}, respectively. The corresponding capacity retentions were 77 and 83%, respectively. Also notice that both the two samples exhibite nearly 100% coulombic efficiency. As depicted in **Figure 4C**, the LLOs/CNTs/NFCs electrode shows better rate capability than that of the traditional LLOs electrode. When the current density was 2 C, the discharge capacity of the traditional LLOs electrode and the LLOs/CNTs/NFCs electrode were 157 and 168 mAh g^{-1}, respectively. The results indicate that the flexible LLOs/CNTs/NFCs electrode exhibites better reversibility and superior rate capability than the traditional LLOs electrode under the same condition. **Figure 4D** shows the EIS plots, the fitting results and the corresponding equivalent circuit of the two samples. The curves consist of a semicircle and a straight line. The semicircle in the high and medium frequency can be explained as the charge transfer resistance (R_{ct}) and double layer capacitance (C_{dl}), and the straight line in the low frequency was a representation of the Warburg impedance Z_w (Wu et al., 2019). By comparing the two curves, it was found that the traditional LLOs electrode has higher interfacial impedance compared with the LLOs/CNTs/NFCs electrode. The lower impedance of the flexible LLOs/CNTs/NFCs electrode can

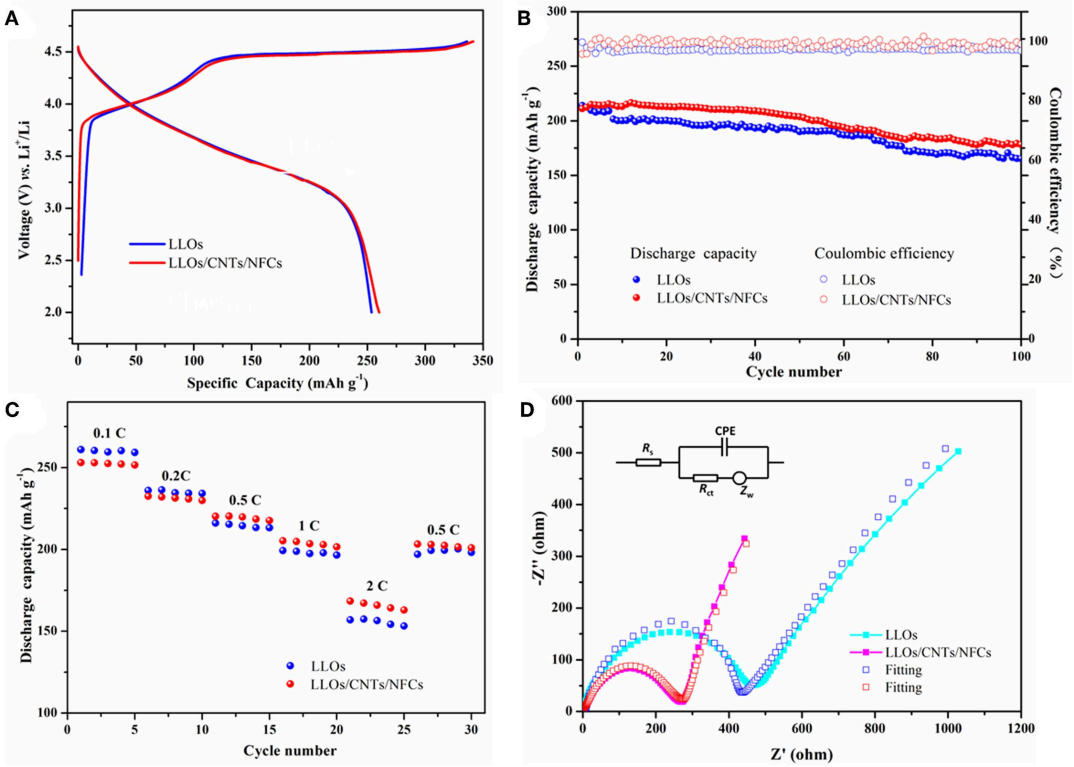

FIGURE 4 | Electrochemical performances of the traditional LLOs electrode and LLOs/CNTs/NFCs electrode: **(A)** initial charge–discharge profiles at 0.1C rate; **(B)** Cycle performances at 1 C rate and the corresponding Coulombic efficiency; **(C)** Rate performances in the rate range of 0.1–2 C; **(D)** EIS plots of two samples.

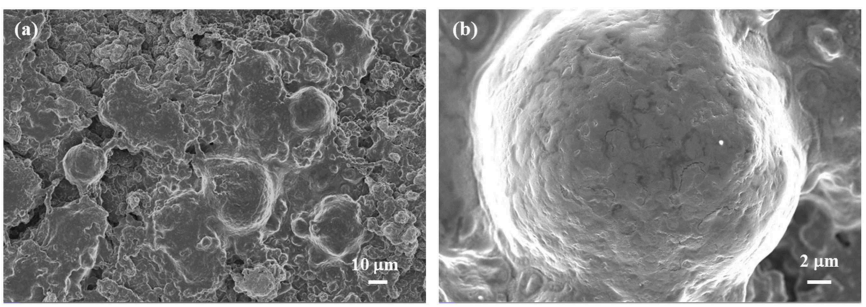

FIGURE 5 | (a) Low magnification and **(b)** high magnification SEM images of the LLOs/CNTs/NFCs electrode after 100 cycles at 1C.

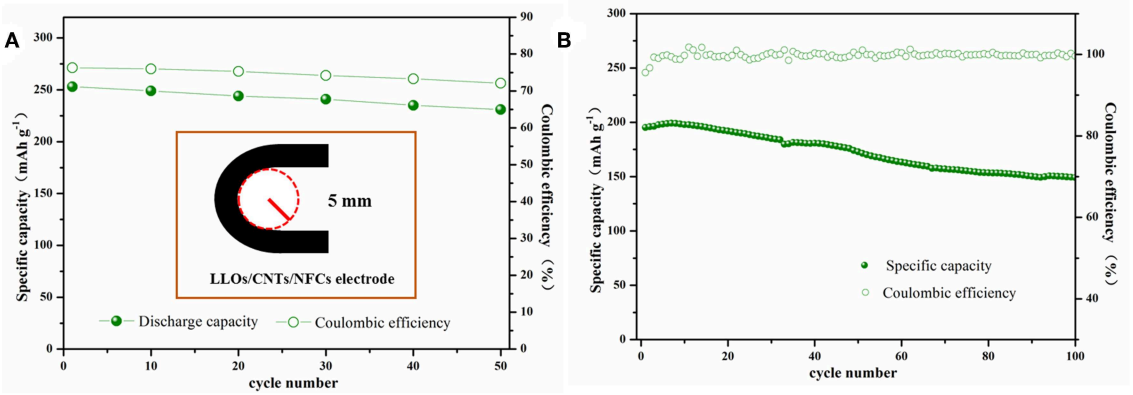

FIGURE 6 | (A) The initial discharge capacities and Coulombic efficiencies of flexible LFP/G/NFC electrode vs. bending times, and the inset represents the schematic of the bending test; **(B)** Cycle performance and Coulombic efficiencies of the LLOs/CNTs/NFCs electrode after bended repeatedly below a curvature radius of 5 mm for 50 times.

be attributed to fast charge transfer and high electrochemical activity provided by the continuous conductive network. This also demonstrates the reasons for the better cycle and rate performances of the LLOs/CNTs/NFCs electrode.

The SEM images of the LLOs/CNTs/NFCs electrode after 100 cycles at 1 C were illustrated in **Figure 5**. The low-magnification image in **Figure 5a** reveals that the integrity of the electrode was maintained well and the LLOs particles keeped the original spherical shape. It was clear from **Figure 5b** that the dense and uniform SEI film was covered to the surface of LLOs microspheres (Wang et al., 2017a). The result indicates the dominant structure stability of the LLOs/CNTs/NFCs electrode, and further proves the foregoing reasons for the good electrochemical performances of the flexible LLOs/CNTs/NFCs electrode.

In order to investigate the practical prospect of the flexible LLOs/CNTs/NFCs electrode, electrochemical performances of the flexible electrode were measured after bending. As exhibited in **Figure 6A**, the LLOs/CNTs/NFCs electrode was bent with a 5 mm curvature radius for 0–50 times. For the LLOs/CNTs/NFCs electrode, the discharge capacity and coulombic efficiency in the first cycle at 0.1 C decreased with the increase of bending times. The incipient discharge capacity of the flexible electrode after 50 times bending was 231 mAh g^{-1}, and the capacity retention rate was 91% after bending for 50 times. At the same time, the initial coulombic efficiency reduces from 76 to 72% after 50 times bending. The cycle performance and coulombic efficiency of the LLOs/CNTs/NFCs electrode after bending for 50 times was depicted in **Figure 6B**. After 100 cycles at 1 C, the LLOs/CNTs/NFCs electrode delivered a discharge capacity of 149 mAh g^{-1}, the corresponding capacity retentions was 76%, and the coulombic efficiency keeped nearly 100%. These tests manifest that the as-prepared LLOs/CNTs/NFCs electrode had high structure stability and flexibility, and the electrochemical properties declined slight after repeated bending. In the LLOs/CNTs/NFCs electrode, NFCs with extraordinary mechanical properties is beneficial to bind active electrode particles and form a flexible freestanding electrode (Nakagaito and Yano, 2004; Aulin et al., 2012). CNTs with superior mechanical properties and electrical conductivity can greatly enhance the mechanical strength and electrochemical activity of the active materials (Hu et al., 2012; Peng et al., 2014). Therefore, the improvement of mechanical and electrochemical performances of the LLOs/CNTs/NFCs electrode can be attributed to the continuous conductive network constructed by NFCs and CNT.

CONCLUSIONS

In summary, the flexible LLOs/CNTs/NFCs electrode was constructed via the vacuum filtration method. The resulting LLOs/CNTs/NFCs electrode exhibited enhanced initial discharge capacity, superior cycle stability and improved rate performance in contrast to the traditional LLOs electrode. The LLOs/CNTs/NFCs electrode exerted high flexibility during the repeated bending processes, and the electrochemical performance performance degraded less after bending. The good electrochemical performances and flexibility can be attributed to the conductive framework formed by NFCs with good mechanical properties and CNTs with high conductivity. This study provides a potential strategy to fabricated flexible electrode for LIBs with good mechanical properties and electrochemical performances.

DATA AVAILABILITY

All datasets generated for this study are included in the manuscript/supplementary files.

AUTHOR CONTRIBUTIONS

YL and RW designed and engineered the samples. YL performed the experiments. YL, HZ, ZX, and RW performed the data

analysis. YL and RW wrote the paper. All authors contributed to the theoretical analysis and the general discussion.

FUNDING

The work was supported by the National Science Foundation for Young Scientists of China (Grant No. 51804199), the Science and Technology Innovation Commission of Shenzhen (Grant No.20180123), and the National Natural Science Fund (Grant No. 61435010).

ACKNOWLEDGMENTS

Authors also acknowledge the supports from Instrumental Analysis Center of Shenzhen University (Xili Campus) and Shenzhen Institute of Information Technology.

REFERENCES

Agnès, C., Holzinger, M., Goff, A. L., Reuillard, B., Elouarzaki, K., Tingry, S., et al. (2014). Supercapacitor/biofuel cell hybrids based on wired enzymes on carbon nanotube matrices: autonomous reloading after high power pulses in neutral buffered glucose solutions. *Energ. Environ. Sci.* 7, 1884–1888. doi: 10.1039/C3EE43986K

Aulin, C., Salazar-Alvarez, G., and Lindström, T. (2012). High strength, flexible and transparent nanofibrillated cellulose–nanoclay biohybrid films with tunable oxygen and water vapor permeability. *Nanoscale* 4, 6622–6628. doi: 10.1039/c2nr31726e

Bai, S., Sun, C., Yan, H., Sun, X., Zhang, H., Luo, L., et al. (2015). Healable, Transparent, room-temperature electronic sensors based on carbon nanotube network-coated polyelectrolyte multilayers. *Small* 11, 5807–5813. doi: 10.1002/smll.201502169

Chen, J., Liu, Y., Minett, A. I., and Crean, C. (2007). Flexible, aligned carbon nanotube/conducting polymer electrodes for a lithium-ion battery. *Chem. Mater.* 19, 3595–3597. doi: 10.1021/cm070991g

Chou, S. L., Wang, J. Z., Chew, S. Y., Liu, H. K., and Dou, S. X. (2008). Electrodeposition of MnO nanowires on carbon nanotube paper as free-standing, flexible electrode for supercapacitors. *Electrochem. Commun.* 10, 1724–1727. doi: 10.1016/j.elecom.2008.08.051

Ding, S., Zhang, D., Chen, J. S., and Lou, X. W. (2011). Facile synthesis of hierarchical MoS2 microspheres composed of few-layered nanosheets and their lithium storage properties. *Nanoscale* 4, 95–98. doi: 10.1039/C1NR11552A

Dresselhaus, M. S., Dresselhaus, G., and Jorio, A. (2007). Raman spectroscopy of carbon nanotubes in 1997 and 2007. *J. Phys. Chem. C* 111, 17887–17893. doi: 10.1021/jp071378n

Dunn, B., Kamath, H., and Tarascon, J. M. (2011). Electrical energy storage for the grid: a battery of choices. *Science* 334, 928–935. doi: 10.1126/science.1212741

Fu, K., Yildiz, O., Bhanushali, H., Wang, Y., Stano, K., Xue, L., et al. (2013). Aligned carbon nanotube-silicon sheets: a novel nano-architecture for flexible lithium ion battery electrodes. *Adv. Mater.* 25, 5109–5114. doi: 10.1002/adma.201301920

Gao, Z., Song, N., Zhang, Y., and Li, X. (2015). Cotton-textile-enabled, flexible lithium-ion batteries with enhanced capacity and extended lifespan. *Nano Lett.* 15, 8194–8203. doi: 10.1021/acs.nanolett.5b03698

He, Y., Matthews, B., Wang, J., and Song, L. (2016). Innovation and challenges in materials design for flexible rechargeable batteries: from 1D to 3D. *J. Mater. Chem. A* 6, 735–753 doi: 10.1039/C7TA09301B

He, Z., Wang, Z., Guo, H., Li, X., Wu, X., Peng, Y., et al. (2013). A simple method of preparing graphene-coated $Li[Li_{0.2}Mn_{0.54}Ni_{0.13}Co_{0.13}]O_2$ for lithium-ion batteries. *Mater. Lett.* 91, 261–264. doi: 10.1016/j.matlet.2012.09.115

Ho, T. T. T., Zimmermann, T., Hauert, R., and Caseri, W. J. C. (2011). Preparation and characterization of cationic nanofibrillated cellulose from etherification and high-shear disintegration processes. *Cellulose* 18, 1391–1406. doi: 10.1007/s10570-011-9591-2

Hu, B., Li, D., Manandharm, P., Fan, Q., Kasilingam, D., and Calvert, P. (2012). CNT/conducting polymer composite conductors impart high flexibility to textile electroluminescent devices. *J. Mater. Chem.* 22, 1598–1605. doi: 10.1039/C1JM14121J

Hu, X., Guo, H., Peng, W., Wang, Z., Li, X., and Hu, Q. (2018). Effects of Nb doping on the performance of $0.5Li_2MnO_3 \cdot 0.5LiNi_{1/3}Co_{1/3}Mn_{1/3}O_2$ cathode material for lithium-ion batteries. *J. Electroanal. Chem.* 822, 57–65. doi: 10.1016/j.jelechem.2018.05.015

Hu, Y., Li, X., Geng, D., Cai, M., Li, R., and Sun, X. (2013). Influence of paper thickness on the electrochemical performances of graphene papers as an anode for lithium ion batteries. *Electrochim. Acta* 91, 227–233. doi: 10.1016/j.electacta.2012.12.106

Hu, Y., and Sun, X. (2014). Flexible rechargeable lithium ion batteries: advances and challenges in materials and process technologies. *Cheminform* 2, 10712–10738. doi: 10.1039/C4TA00716F

Huang, Z., Zhang, Z., Qi, X., Ren, X., Xu, G., Wan, P., et al. (2016). Wall-like hierarchical metal oxide nanosheet arrays grown on carbon cloth for excellent supercapacitor electrodes. *Nanoscale* 8:13273. doi: 10.1039/C6NR04020A

Jia, X., Yan, C., Chen, Z., Wang, R., Zhang, Q., Guo, L., et al. (2011). Direct growth of flexible $LiMn_2O_4$/CNT lithium-ion cathodes. *Chem. Commun.* 47, 9669–9671. doi: 10.1039/c1cc13536h

Ju, H. F., Song, W. L., and Fan, L. Z. (2014). Rational design of graphene/porous carbon aerogels for high-performance flexible all-solid-state supercapacitors. *J. Mater. Chem. A* 2, 10895–10903. doi: 10.1039/C4TA00538D

Kang, C., Cha, E., Baskaran, R., and Choi, W. (2016). Three-dimensional free-standing carbon nanotubes for a flexible lithium-ion battery anode. *Nanotechnology* 27:105402. doi: 10.1088/0957-4484/27/10/105402

Kim, M. G., and Cho, J. (2010). Reversible and high-capacity nanostructured electrode materials for Li-Ion batteries. *Adv. Funct. Mater.* 19, 1497–1514. doi: 10.1002/adfm.200801095

Leijonmarck, S., Cornell, A., Lindbergh, G., and Wågberg, L. (2013). Single-paper flexible Li-ion battery cells through a paper-making process based on nano-fibrillated cellulose. *J. Mater. Chem. A* 1, 4671–4677. doi: 10.1039/c3ta01532g

Li, L., Wu, Z., Yuan, S., and Zhang, X. B. (2014). Advances and challenges for flexible energy storage and conversion devices and systems. *Energ. Environ. Sci.* 7, 2101–2122. doi: 10.1039/c4ee00318g

Li, T., Li, X., Wang, Z., and Guo, H. (2017a). A short process for the efficient utilization of transition-metal chlorides in lithium-ion batteries: a case of $Ni_{0.8}Co_{0.1}Mn_{0.1}O_{1.1}$ and $LiNi_{0.8}Co_{0.1}Mn_{0.1}O_2$. *J. Power Sources* 342, 495–503. doi: 10.1016/j.jpowsour.2016.12.095

Li, T., Wang, J., Wang, Z., Guo, H., Li, Y., and Li, X. (2017b). A new design concept for preparing nickel-foam-supported metal oxide microspheres with superior electrochemical properties. *J. Mater. Chem. A* 5, 13469–13474. doi: 10.1039/C7TA02789C

Li, Y., Li, X., Wang, Z., Guo, H., and Wang, J. (2018). An Ostwald ripening route towards Ni-rich layered cathode material with cobalt-rich surface for lithium ion battery. *Sci. China Mater.* 61, 719–727. doi: 10.1007/s40843-017-9162-3

Lian, P., Wang, J., Cai, D., Ding, L., Jia, Q., and Wang, H. (2014). Porous SnO_2@C/graphene nanocomposite with 3D carbon conductive network as a superior anode material for lithium-ion batteries *Electrochim. Acta* 116, 103–110. doi: 10.1016/j.electacta.2013.11.007

Manthiram, A., Murugan, A. V., Sarkar, A., and Muraliganth, T. (2008). Nanostructured electrode materials for electrochemical energy storage and conversion. *Energ. Environ. Sci.* 1, 621–638. doi: 10.1039/b811802g

Nakagaito, A. N., and Yano, H. (2004). The effect of morphological changes from pulp fiber towards nano-scale fibrillated cellulose on the mechanical properties of high-strength plant fiber based composites. *Appl. Phys. A* 78, 547–552. doi: 10.1007/s00339-003-2453-5

Nitta, N., Wu, F., Lee, J. T., and Yushin, G. (2015). Li-ion battery materials: present and future. *Mater. Today* 18, 252–264. doi: 10.1016/j.mattod.2014.10.040

Peng, H. J., Huang, J.-Q., Zhao, M.-Q., Zhang, Q., Cheng, X.-B., Liu, X.-Y., et al. (2014). Nanoarchitectured Graphene/CNT@Porous Carbon with Extraordinary Electrical Conductivity and Interconnected Micro/Mesopores

for Lithium-Sulfur Batteries. *Adv. Funct. Mater.* 24, 2772–2781. doi: 10.1002/adfm.201303296

Sassi, J. F., and Chanzy, H. (1995). Ultrastructural aspects of the acetylation of cellulose. *Cellulose* 2, 111–127. doi: 10.1007/BF00816384

Strong, V., Dubin, S., Elkady, M. F., Lech, A., Wang, Y., Weiller, B. H., et al. (2012). Patterning and electronic tuning of laser scribed graphene for flexible all-carbon devices. *Acs Nano* 6, 1395–1403. doi: 10.1021/nn204200w

Su, F. Y., You, C. H., He, Y. B., Wei, L., Wei, C., Jin, F. M., et al. (2010). Flexible and planar graphene conductive additives for lithium-ion batteries. *J. Mater. Chem.* 20, 9644–9650. doi: 10.1039/c0jm01633k

Tai, Z., Yan, X., Lang, J., and Xue, Q. (2012). Enhancement of capacitance performance of flexible carbon nanofiber paper by adding graphene nanosheets. *J. Power Sources* 199, 373–378. doi: 10.1016/j.jpowsour.2011.10.009

Tessonnier, J. P., Rosenthal, D., Hansen, T. W., Hess, C., Schuster, M. E., Blume, R., et al. (2009). Analysis of the structure and chemical properties of some commercial carbon nanostructures. *Carbon* 47, 1779–1798. doi: 10.1016/j.carbon.2009.02.032

Wan, P., Wen, X., Sun, C., Chandran, B. K., Zhang, H., Sun, X., et al. (2015). Flexible transparent films based on nanocomposite networks of polyaniline and carbon nanotubes for high-performance gas sensing. *Small* 11, 5409–5415. doi: 10.1002/smll.201501772

Wang, C. Y., Ballantyne, A. M., Hall, S. B., Too, C. O., Officer, D. L., and Wallace, G. G. (2006). Functionalized polythiophene-coated textile: a new anode material for a flexible battery. *J. Power Sources* 152, 610–614. doi: 10.1016/j.jpowsour.2005.06.020

Wang, J. Z., Chou, S. L., Chen, J., Chew, S. Y., Wang, G. X., Konstantinov, K., et al. (2008). Paper-like free-standing polypyrrole and polypyrrole–LiFePO composite films for flexible and bendable rechargeable battery. *Electrochem. Commun.* 10, 1781–1784. doi: 10.1016/j.elecom.2008.09.008

Wang, Q. Y., Liu, J., Murugan, A. V., and Manthiram, A. (2009). High capacity double-layer surface modified $Li[Li_{0.2}Mn_{0.54}Ni_{0.13}Co_{0.13}]O_2$ cathode with improved rate capability. *J. Mater. Chem.* 19:4965. doi: 10.1039/b823506f

Wang, R., Li, X., Wang, Z., and Han, Z. (2017a). Electrochemical analysis graphite/electrolyte interface in lithium-ion batteries: p-Toluenesulfonyl isocyanate as electrolyte additive. *Nano Energy* 34, 131–140. doi: 10.1016/j.nanoen.2017.02.037

Wang, Y., He, Z. Y., Wang, Y. X., Fan, C., Liu, C. R., Peng, Q. L., et al. (2018). Preparation and characterization of flexible lithium iron phosphate/graphene/cellulose electrode for lithium ion batteries. *J. Colloid. Interface Sci.* 512, 398–403. doi: 10.1016/j.jcis.2017.10.042

Wang, Z., Liu, M., Wei, G., Han, P., Zhao, X., Liu, J., et al. (2017b). Hierarchical self-supported $C@TiO_2$-MoS_2 core-shell nanofiber mats as flexible anode for advanced lithium ion batteries. *Appl. Surf. Sci.* 423, 375–382. doi: 10.1016/j.apsusc.2017.06.129

Wu, X., Li, Y., Zhao, S., Zeng, F., Peng, X., Xiang, Y., et al. (2019). Fabrication of F-doped, C-coated $NiCo_2O_4$ nanocomposites and its electrochemical performances for lithium-ion batteries. *Solid State Ionics* 334, 48–55. doi: 10.1016/j.ssi.2019.01.039

Xin, Z., Hayner, C. M., Kung, M. C., and Kung, H. H. (2011). Flexible holey graphene paper electrodes with enhanced rate capability for energy storage applications. *Acs Nano* 5, 8739–8749. doi: 10.1021/nn202710s

Yan, C., Xi, W., Si, W., Deng, J., and Schmidt, O. G. (2013). Lithium-Ion batteries: highly conductive and strain-released hybrid multilayer ge/ti nanomembranes with enhanced lithium-ion-storage capability. *Adv. Mater.* 25, 644–644. doi: 10.1002/adma.201370022

Yang, S., Zhang, M., Wu, X., Wu, X., Zeng, F., Li, Y., et al. (2019). The excellent electrochemical performances of $ZnMn_2O_4/Mn_2O_3$: the composite cathode material for potential aqueous zinc ion batteries. *J. Electroanal. Chem.* 832, 69–74. doi: 10.1016/j.jelechem.2018.10.051

Yu, H., Zhu, C., Zhang, K., Chen, Y., Li, C., Gao, P., et al. (2014). Three-dimensional hierarchical MoS_2 nanoflake array/carbon cloth as high-performance flexible lithium-ion battery anodes. *J. Mater. Chem. A* 2:4551. doi: 10.1039/C3TA14744D

Yuan, C., Wu, H. B., Xie, Y., and Lou, X. W. (2014). Mixed transition-metal oxides: design, synthesis, and energy-related applications. *Angew. Chem. Int. Ed.* 53, 1488–1504. doi: 10.1002/anie.201303971

Zhen, Z., Liu, Y., Long, R., Han, Z., Huang, Z., Xiang, Q., et al. (2016). Three-dimensional-networked Ni-Co-Se nanosheet/nanowire arrays on carbon cloth: a flexible electrode for efficient hydrogen evolution. *Electrochim. Acta* 200, 142–151. doi: 10.1016/j.electacta.2016.03.186

Zhou, G. M., Li, F., and Cheng, H. M. (2014). Progress in flexible lithium batteries and future prospects. *Energ. Environ. Sci.* 7, 1307–1338. doi: 10.1039/C3EE43182G

Conflict of Interest Statement: The authors declare that the research was conducted in the absence of any commercial or financial relationships that could be construed as a potential conflict of interest.

frontiers in Chemistry

ORIGINAL RESEARCH
published: 14 August 2019
doi: 10.3389/fchem.2019.00569

Synthesis and Electrochemical Performance of ZnSe Electrospinning Nanofibers as an Anode Material for Lithium Ion and Sodium Ion Batteries

Peng Zhou[1], *Mingyu Zhang*[1]*, *Liping Wang*[2], *Qizhong Huang*[1], *Zhean Su*[1], *Liewu Li*[1], *Xiaodong Wang*[1], *Yuhao Li*[1], *Chen Zeng*[1] *and Zhenghao Guo*[1]

[1] State Key Laboratory of Powder Metallurgy, Central South University, Changsha, China, [2] Department of Biological and Environmental Engineering, Changsha University, Changsha, China

ZnSe nitrogen-doped carbon composite nanofibers (ZnSe@N-CNFs) were derived as anode materials from selenization of electrospinning nanofibers. Electron microscopy shows that ZnSe nanoparticles are distributed in electrospinning nanofibers after selenization. Electrochemistry tests were carried out and the results show the one-dimensional carbon composite nanofibers reveal a great structural stability and electrochemistry performance by the enhanced synergistic effect with ZnSe. Even at a current density of 2 A g^{-1}, the as-prepared electrodes can still reach up to 701.7 mA h g^{-1} after 600 cycles in lithium-ion batteries and 368.9 mA h g^{-1} after 200 cycles in sodium-ion batteries, respectively. ZnSe@N-CNFs with long cycle life and high capacity at high current density implies its promising future for the next generation application of energy storage.

Keywords: anode material, Li-ion and Na-ion batteries, electrospinning nanofibers, ZnSe, synthesis, electrochemical performance

OPEN ACCESS

Edited by:
Danni Lei,
Sun Yat-Sen University, China

Reviewed by:
Baihua Qu,
Xiamen University, China
Ming Zhang,
Hunan University, China

***Correspondence:**
Mingyu Zhang
zhangmingyu@csu.edu.cn

Specialty section:
This article was submitted to Electrochemistry, a section of the journal Frontiers in Chemistry

Received: *22 May 2019*
Accepted: *26 July 2019*
Published: *14 August 2019*

Citation:
Zhou P, Zhang M, Wang L, Huang Q, Su Z, Li L, Wang X, Li Y, Zeng C and Guo Z (2019) Synthesis and Electrochemical Performance of ZnSe Electrospinning Nanofibers as an Anode Material for Lithium Ion and Sodium Ion Batteries. Front. Chem. 7:569. doi: 10.3389/fchem.2019.00569

INTRODUCTION

Over the latest 20 years, lithium-ion batteries (LIBs) have experienced great development to meet the demand of portable electronic devices and hybrid electric vehicles (Mai et al., 2010; Ji et al., 2012; Li W. et al., 2016; Wu F. et al., 2017; Tian et al., 2018). However, the theoretical capacity (372 mA h g^{-1}) of the conventional graphite anode in LIBs can't meet the increasing expectations (Li L. et al., 2016; Zhang Y.-C. et al., 2016; Lee et al., 2018). At the same time, Sodium-ion batteries (SIBs), as one of the most competitive alternatives of LIBs, are drawing much attention due to the low cost and high abundance of sodium in the crust (Li et al., 2017; Zhang et al., 2017; Wu et al., 2018). Unfortunately, the larger ionic diameter of Na^+ (0.106 nm) compared with Li^+ (0.076 nm) results in the kinetic limitation and larger volume expansion of anode materials, which further leads to reduced capacity in SIBs (Xu et al., 2015; Deng et al., 2018). Therefore, it is a topmost priority to develop high-performance anode materials for LIBs and SIBs (Nitta et al., 2015; Du et al., 2018; Fan and Xie, 2019). Recently, metallic selenides ($SnSe_2$, $FeSe_2$, $CoSe_2$, etc.) have attracted much attention as anode materials thanks to their high energy density and excellent rate performance (Ko et al., 2016; Park et al., 2016; Zhang L. et al., 2016; Cui et al., 2018). Among them, ZnSe is considered as one of the most promising anode materials because of its impressive performance in both LIBs and SIBs (Cao et al., 2018). Particularly, when ZnSe was used

as anode materials in LIBs, the Zn reduction by ZnSe could react with Li^+ to form LiZn and provide additional capacity (Kwon and Park, 2014; liu et al., 2018). However, the pulverization and amorphization of ZnSe during charge and discharge result in poor cycling stability (Fu et al., 2015).

To overcome the problems mentioned above, constructing ZnSe/carbon hybrid material is considered as one of the most effective way to improve electrochemical performance of electrodes. ZnSe shows great synergistic effect with carbon, which highly improves the capacity of anode in energy storage (Zhang et al., 2015). For example, Chen et al. (2017) reported that ZnSe ND@N-PC by using zeolitic imidazolate framework (ZIF-8) and delivered an outstanding capability to LIBs of 1,134 $mA{\cdot}h{\cdot}g^{-1}$ at 0.6 $A{\cdot}g^{-1}$ after 500 cycles. Tang et al. (2018) synthesized a ZnSe microsphere/multiwalled carbon nanotube composite used as SIBs anode materials, which exhibited a high specific capacity of 382 mA h g^{-1} at 0.5 A g^{-1} after 180 cycles. Cao et al. dispersed ZnSe nanoparticles in reduced graphene oxides to synthesize ZnSe-rGO nanocomposite as an anode material for both LIBs and SIBs. The capacity of ZnSe-rGO in LIBs is 530 mA h g^{-1} at 0.5 A g^{-1} after 100 cycles and that of SIBs is 259.5 mA h g^{-1} at 0.1 A g^{-1} after 50 cycles (Cao et al., 2018). But the reported ZnSe/carbon electrodes are mainly microspheres or irregular nanoparticles (Xu Y. et al., 2016). The composite mode and microstructure of ZnSe and carbon are inefficient and then require further design. The specific capacity and stability of the ZnSe/carbon hybrid anode, especially at high current density, also need to be improved (Wang et al., 2017).

In this work, we have successfully synthesized ZnSe nitrogen-doped carbon composite nanofibers (ZnSe@N-CNFs) for both LIBs and SIBs via electrospinning and a simple selenization treatment. This unique one-dimensional (1D) nanostructure has a shorter ion diffusion path and higher electronic conductivity. In the meanwhile, the synergistic effect of encapsulated ZnSe nanoparticles in nitrogen-doped carbon nanofibers can effectively suppress the pulverization and amorphization. As a result, the as-prepared ZnSe@N-CNFs electrodes exhibit an excellent electrochemical performance as anode material for both LIBs and SIBs. The specific capacity of ZnSe@N-CNFs reach to 1,226.1 and 455.0 mA h g^{-1} in LIBs and SIBs, respectively. Meanwhile, the ZnSe@N-CNFs also shows outstanding specific capacity and stability (701.7 mA h g^{-1} after 600 cycles in LIBs and 365.6 mA h g^{-1} after 200 cycles in SIBs) at high current density of 2 A g^{-1}. It is expected that the ZnSe@N-CNFs with such great electrochemical performance have promising applications as anodes for both LIBs and SIBs, and would be a direction for design of the other anode materials.

EXPERIMENTAL SECTION

Preparation of ZnSe@N-CNFs

0.5268 g of Zinc acetate dihydrate ($C_4H_6O_4Zn{\cdot}2H_2O$, AR, Sinopharm) was dissolved in 3 ml *N*, *N*-dimethylformamide (DMF, AR, Sinopharm). 0.4534 g polyacrylonitrile (PAN, Mw 150000, Macklin) was dissolved in 3 ml DMF under magnetic stirring for 30 min at 60°C. The two solutions were mixed and stirred for another 12 h. Then the mixture was transferred into a syringe to electrospin with the distance 20 cm and voltage 13 kV, respectively. The obtained nanofibers were mixed with 1.3 g Selenium powder (99.9%, Aladdin) and calcined at 650°C for 2 h (a ramp rate of 10°C min^{-1}) in a tube furnace under vacuum to produce the ZnSe@N-CNFs.

In the meantime, carbon nanofibers (CNF) and ZnSe@N-C were prepared as comparison samples. The carbon nanofibers (CNFs) were synthesized in the same steps without adding Zinc acetate dihydrate. The ZnSe@N-C was synthesized by precursor solution directly dried at 80°C overnight and calcined at the same way with Se powder.

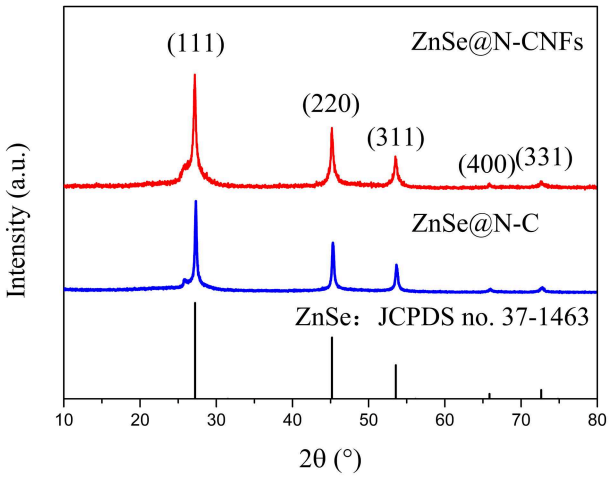

FIGURE 1 | XRD pattern of ZnSe@N-CNFs and ZnSe@N-C.

Materials Characterization

The crystal structure and the composition of the samples were investigated by X-ray diffraction (XRD, Rigaku Dmax/2550VB + 18 kW) and energy dispersive X-ray spectroscopy (EDX, FEI Nova Nano SEM230). The morphology and microstructure of samples was observed through scanning electron microscopy (SEM, FEI Nova Nano SEM230) and transmission electron microscopy (TEM, JEOL JEM-2010). The thermogravimetric analysis (TGA) was tested in air at a ramp rate of 10°C min^{-1}. The Raman spectrum test was conducted on a Renishaw in Via 2000. The specific surface areas and the pore size distribution were measured by the Brunauer-Emmett-Teller (BET) test and Barrett-Joyner-Halenda (BJH) method, respectively. The surface chemical composition of the sample was tested by the X-ray photoelectron spectroscopy (XPS, Thermo Scientific ESCALAB 250XI).

Electrochemical Characterization

A slurry made of ZnSe@N-CNFs (80 wt.%), acetylene black (10 wt.%), and carboxymethyl cellulose sodium (10 wt.%) was dissolved in deionized water and ethanol (3:2), spread onto Cu foil and dried at 80°C for 12 h to prepare the anodes. The LIBs were assembled into 2,032 coin-type cells in an Argon-filled glove box with lithium metal as the reference electrode,

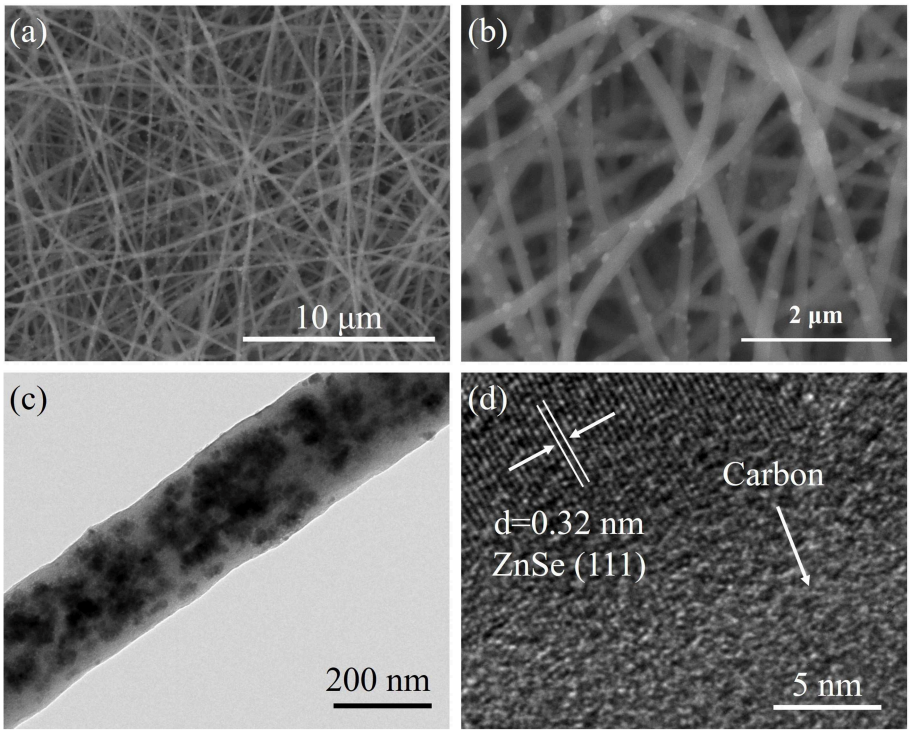

FIGURE 2 | (a,b) SEM images of ZnSe@N-CNFs at different magnification. **(c)** TEM image of ZnSe@N-CNFs. **(d)** HRTEM image of ZnSe@N-CNFs.

LiPF6 (1M) in ethylene carbonate (EC) and dimethyl carbonate (DMC) at a 1:1 volume ratio as electrolyte and polypropylene film (Celgard 2400) as separator. The SIBs were assembled with sodium metal as the reference electrode, NaCF3SO3 (1M) in diethyleneglycol dimethylether (DEGDME) used as electrolyte and glass microfiber (Whatman GF/D) as separator.

All electrochemical tests were carried out at 27°C. The cyclic voltammetry (CV) was measured with voltage window of 0.01–3.0 V by using CHI760E electrochemical workstation. The rate capability and cycle life were tested with LAND CT2001A battery test system. The electrochemical impedance spectroscopy (EIS) tests were carried out with the frequency range of 100 kHz−0.01 Hz by CHI760E electrochemical workstation.

RESULTS AND DISCUSSION

As shown in XRD pattern of **Figure 1** and **Figure S1**, all the peaks of ZnSe@N-CNFs and ZnSe@N-C can be fully indexed to ZnSe (JCPDS 37-1463), indicate the effective formation of ZnSe as we design (Tang et al., 2018). The wide peak shown at 30° of CNFs is attributed to the amorphous carbon (Lallave et al., 2007). The carbon peaks aren't obvious in the diffraction pattern of ZnSe@N-CNFs and ZnSe@N-C as the highly crystalline ZnSe reflections suppressed those of carbon.

Figures 2a,b and **Figures S2, S3** indicate the SEM image of as-synthesized samples. It can clearly reveal that the ZnSe@N-CNFs and CNFs are continuously fiber structure without aggregated particles. In contrast, ZnSe@N-C is irregular particles. To further reveal the microstructure of ZnSe@N-CNFs, TEM, and HRTEM were used and the images were shown in **Figures 2c,d**. It is clearly observed in **Figure 2c** that the morphology of ZnSe@N-CNFs is composed of composite nanofibers of about 200 nm diameter with the ZnSe particles dispersed in the fibers or deposited on their surface. The phenomenon of deposited ZnSe particles on the surface is attributed to the crystal growth during calcined (Ning et al., 2017). Clear lattice fringes can be observed from the HRTEM image in **Figure 2d** of 0.32 nm corresponding to the (111) plane of ZnSe crystal (JCPDS 37-1463). In addition, the EDX analysis is shown in **Figure S4**. The atomic ratio of Zn and Se in ZnSe@N-CNFs is about 1:1, matching the stoichiometric ratio of ZnSe compounds. The nitrogen is mainly from PAN, which would increase the conductivity and the number of active sites (Cho et al., 2016).

The TGA of ZnSe@N-CNFs was tested from room temperature to 800°C. As shown in **Figure 3A**, the huge weight loss around 300–600°C correspond to the volatilization of SeO_2 and CO_2 (Cui et al., 2017). The mass percentages of ZnSe in ZnSe@N-CNFs is calculated to be 49.45%. In addition, **Figure 3B** gives the Raman spectra of samples. The two wide peaks can be observed at around 1,340 and 1,586 cm^{-1}, which are corresponding with disordered carbon atoms (D band) and graphitic carbon atoms (G band) of carbon, respectively (Wu Q. et al., 2017). The I_D/I_G ratio of the ZnSe@N-CNFs was calculated to be 1.16. The peaks observed at around 500 cm^{-1} in ZnSe@N-CNFs and ZnSe@N-C spectra correspond to 2LO modes of ZnSe (Tang et al., 2018). To further compare

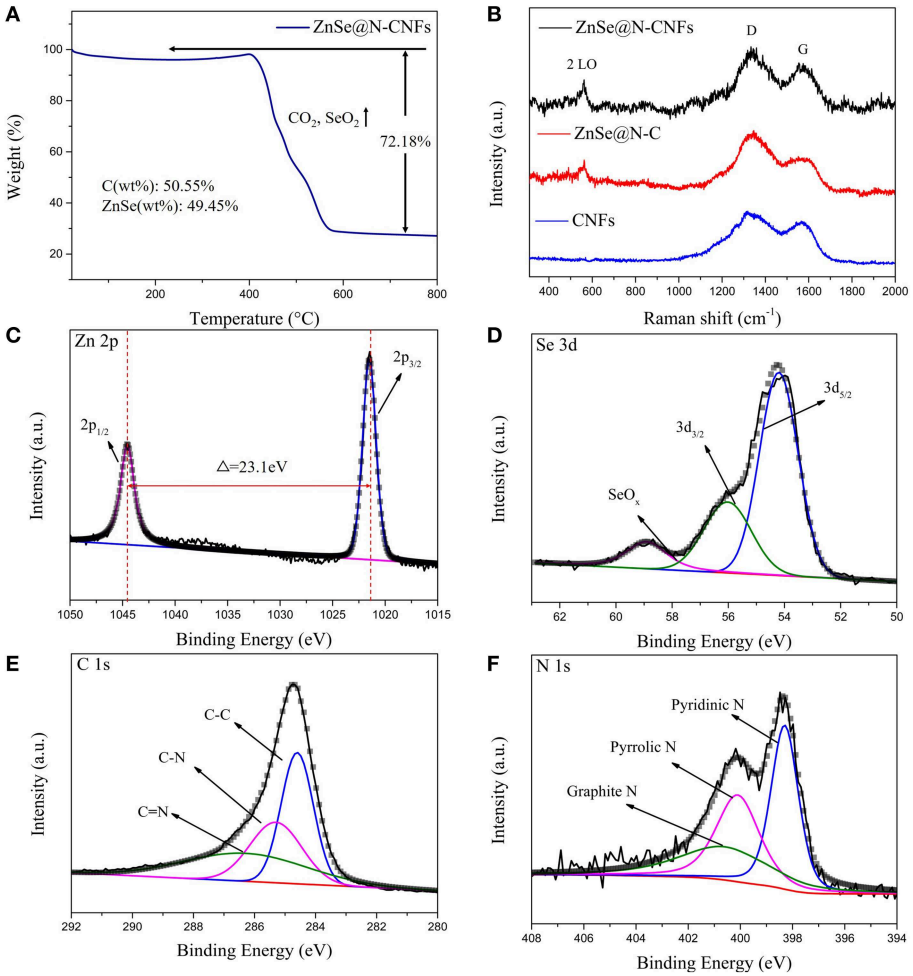

FIGURE 3 | (A) TG analysis of ZnSe@N-CNFs. **(B)** Raman spectra of ZnSe@N-CNFs, ZnSe@N-C and CNFs. **(C–F)** XPS spectra of ZnSe@N-CNFs for Zn 2p **(C)**; Se 3d **(D)**; C 1s **(E)**; N 1s **(F)**.

the pore size of ZnSe@N-CNFs and ZnSe@N-C, the specific surface was determined by nitrogen adsorption/desorption and the pore size distribution curve calculate by BJH method as shown in **Figure S5**. The specific surface area of ZnSe@N-CNFs is 30.2 m^2 g^{-1}, higher than 8.1 m^2 g^{-1} of ZnSe@N-C. The larger specific surface area is attributed to the unique 1D nanostructure. The pore diameter of ZnSe@N-CNFs and ZnSe@N-C are focused on around 3.5–3.8 nm. In addition, the number of pores in ZnSe@N-CNFs is much larger than ZnSe@N-C as shown in **Figure S5**. Although ZnSe@N-CNFs isn't designed as a porous material, it still shows an excellent specific surface area and suitable mesopore size, which can provide more ion storage active sites and reducing ion migration path (Li et al., 2019).

To investigate the surface physicochemical properties and the chemical composition of ZnSe@N-CNFs, the XPS was measured and the survey spectra of ZnSe@N-CNFs is shown in **Figure S6**. The peaks corresponding to Zn 2p, Se 3d, C 1s, and N 1s can be clearly observed, which further suggests the presence of Zn, Se, C, and N elements in ZnSe@N-CNFs. As the high resolution of Zn 2p XPS spectrum shown in **Figure 3C**, two peaks are located at 1,021.5 and 1,044.6 eV, respectively, with an energy difference of 23.1 eV between them, which confirms that the zinc exists as Zn^{2+} form (Ning et al., 2017). The fitted peaks shown in Se 3d spectrum (**Figure 3D**) at 54.2 and 56.1 eV are corresponding to the Se 3d5/2 and Se 3d3/2 spin orbit, respectively, which indicate the Se mainly exists as Se^{2-}. The peak of SeO_x locked at 59.0 eV is caused by surface oxidation (Cui et al., 2018). **Figure 3D** indicate that Se in ZnSe@N-CNFs mainly exists as ZnSe and a small amount of Se has been oxidized to SeO_x on the surface. The three fit peaks of high resolution C1s spectrum (**Figure 3E**) located at binding energy of 284.6, 285.3, and 286.5 eV are related to the C-C bonds, C-N bonds, and C = N bonds, respectively (Liao et al., 2016). Furthermore, the type of nitrogen can be obtained by analyzing the N 1s high-resolution spectrum in the **Figure 3F**. The fit peaks positioned at 398.3, 400.1, and 400.9 eV can be fit well with pyridinic N, pyrrolic peak N, and graphitic peak N, respectively (Wang et al., 2016).

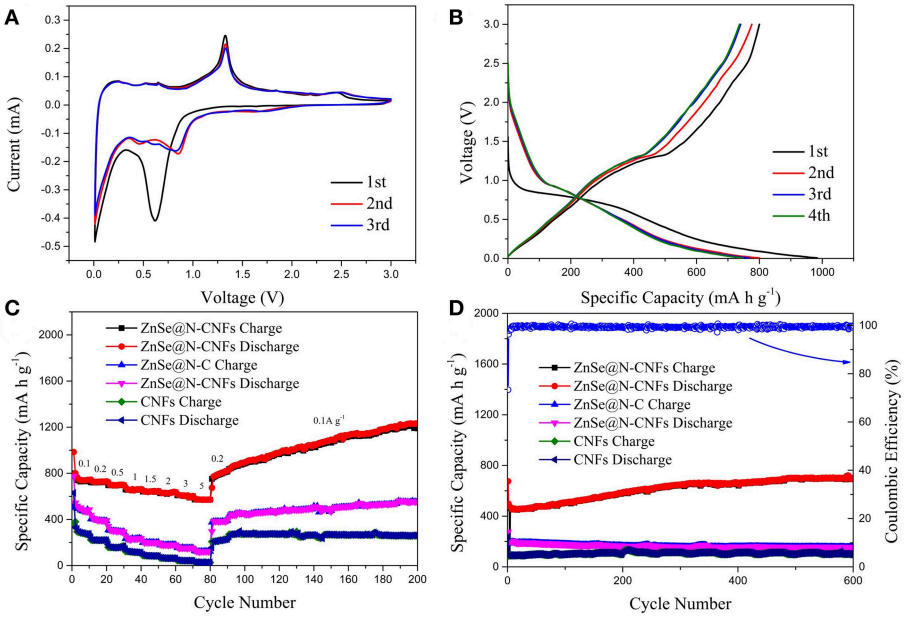

FIGURE 4 | The electrochemical performance of ZnSe@N-CNFs as anodes in LIBs: **(A)** CV curves of the ZnSe@N-CNFs at a scan rate of 0.2 mV s^{-1}; **(B)** discharge/charge voltage profiles of the ZnSe/N-CNFs at a current density of 0.1 A g^{-1}; **(C)** rate capability at various current densities between 0.1 and 5 A·g^{-1} of the ZnSe@N-CNFs; **(D)** cycling performance and corresponding coulombic efficiency of the ZnSe@N-CNFs at 2 A g^{-1}.

In view of the special compositional advantages and appealing micro-structures of continuously composite nanofibers ZnSe@N-CNFs as we design as discussed above, these properties should be beneficial for both LIBs and SIBs. The Li-storage and Na-storage properties of samples were further measured to prove the potential of ZnSe@N-CNFs as anodes material.

Figure 4 shows the electrochemical performance of ZnSe@N-CNFs as anodes in LIBs. The CV measurements were conducted at 0.2 mV s^{-1}. As shown in **Figure 4A**, the peak at 0.6 V in the initial cathodic process is attributed to the reduction from ZnSe to Zn and the formation of a solid electrolyte interface (SEI) layer (Lu et al., 2017). During the follow scan, the curves lapped well, indicating an excellent cycle reversibility. The sharp cathodic peak at around 0.8 V is ascribed to the reduction reaction of Zn^{2+} to Zn^0. After that, a series of small peaks observed at around 0.5 V are corresponding to the multi-step of forming LiZn alloy (Fu et al., 2016). In addition, the pair of small peaks at 1.6 and 2.3 V are ascribed to the formation and decomposition of Li_2Se, respectively (Xu Y. et al., 2016). The reaction of ZnSe@N-CNFs anode in LIBs could be described as the following chemical equations (Kwon and Park, 2014):

$$ZnSe + 2Li^+ + 2e^- \leftrightarrow Zn + Li_2Se \quad (1)$$

$$Zn + Li^+ + 2e^- \leftrightarrow LiZn \quad (2)$$

Figure 4B shows the discharge and charge profiles of ZnSe@N-CNFs anode at 0.1 A g^{-1} at first four cycles. The voltage window of LIBs is 0.005–3.0 V (vs. Li/Li^+). For the initial discharge curve, the extended charge plateau at around 0.8 V can be observed, which is due to the decomposition of ZnSe and the formation of the SEI layer. The initial discharge capacity and coulombic efficiency of ZnSe@N-CNFs are 984.7 mA h g^{-1} and 81.3%, respectively. For the next three cycles, the charge/discharge profiles show a similar shape, which the charge/discharge plateau is consistent with the CV curves. The coulombic efficiency improves remarkably from the second cycle, and reaching to 97.6 % for the third cycle and 99.1% for the 4th cycle.

Figure 4C depicts the rate performance of ZnSe@N-CNFs, ZnSe@N-C, and CNFs anode under various current densities from 0.1 to 5 A g^{-1}. The ZnSe@N-CNFs anode shows an excellent rate performance of 743.0, 730.3, 699.4, 662.8, 645.8, 636.2, 602.6, and 570.9 mA h g^{-1} at 0.1, 0.2, 0.5, 1, 1.5, 2, 3, 5 A g^{-1}, and recovers to 822.7 mA h g^{-1} when the current density reduced back to 0.2 A g^{-1}, respectively. In contrast, the capacity of ZnSe@N-C and CNFs anode only has got the values of 43.0 and 26.4 mA h g^{-1} at 5 A g^{-1}, and recovers to 379.8 and 228.9 mA h g^{-1} when the current density back to 0.2 A g^{-1}. Because of the simple carbonization and without any additional processing, the CNFs exhibits worse Li^+ storage performance especially at high current density. Furthermore, when the current density is changed to 0.1A g^{-1}, the capacity of ZnSe@N-CNFs gradually increases to 1,226.1 mA h g^{-1} after 200 cycles, much higher than ZnSe@N-C and CNFs. The high capacities of ZnSe@N-CNFs is attributed to the special 1D structure. The carbon can effectively prevent the agglomeration of ZnSe particles and lead to more interface of ZnSe and carbon which can provide additional pseudocapacitive capacities In addition, the gradual amorphization process of metallic selenides

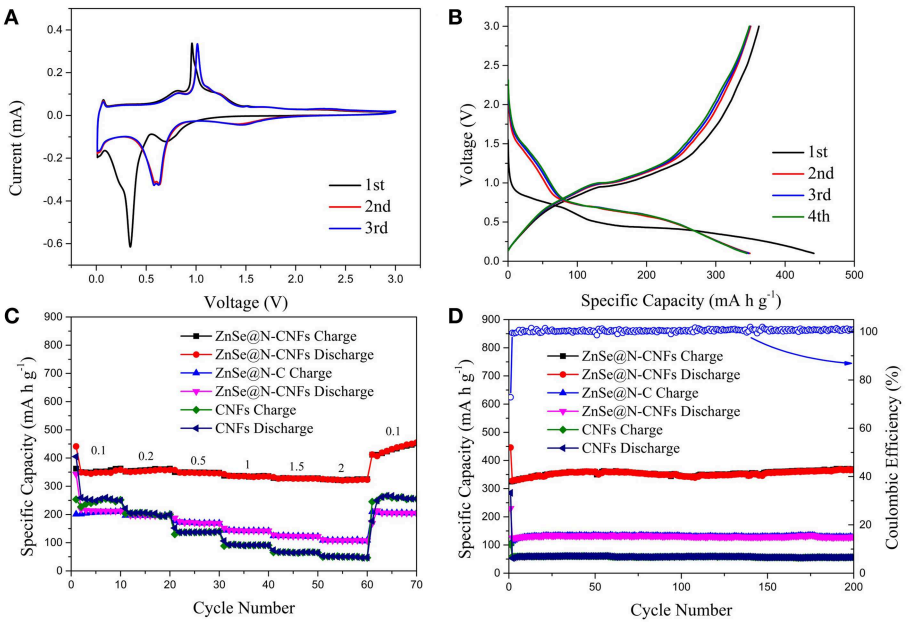

FIGURE 5 | The electrochemical performance of ZnSe@N-CNFs as anodes in SIBs: **(A)** CV curves of the ZnSe@N-CNFs at a scan rate of 0.2 mV s^{-1}; **(B)** discharge/charge voltage profiles of the ZnSe/N-CNFs at a current density of 0.1 A g^{-1}; **(C)** rate capability at various current densities between 0.1 and 2 A·g^{-1} of the ZnSe@N-CNFs; **(D)** cycling performance and corresponding coulombic efficiency of the ZnSe@N-CNFs at 2 A g^{-1}.

electrodes during the reversible reactions of anode can provide more interface of ZnSe particle and carbon, which enhance the pseudocapacitive capacities (Gu et al., 2015). More importantly, as shown in **Figure 4D**, the ZnSe@N-CNFs electrode exhibits excellent discharge capacity of 701.7 mA h g^{-1} after 600 cycles at 2 A g^{-1}, and the coulombic efficiency retained over 96% after the first cycle. However, the ZnSe@N-C and CNFs only achieved 155.5 and 99.4 mA h g^{-1} at the same current density after 600 cycles.

Figure 5 displays the electrochemical performance of ZnSe@N-CNFs, ZnSe@N-C, and CNFs as anodes in SIBs. The CV curves of ZnSe@N-CNFs anode in SIBs are shown in **Figure 5A** at 0.2 mV s^{-1}. The obvious peak observed at around 0.4 V in the initial cathodic process is associated with the formation of the SEI layer and insertion of sodium-ion, which is similar to lithium storage (Ge et al., 2015). After that, the following CV curves are well-overlapped, which means the wonderful cycle reversibility of ZnSe@N-CNFs electrodes. The pair of peaks at 0.7 and 1.1 V relate to the transformation of Zn^{2+} and Zn^0. And the pair of peaks at 1.5 and 2.5 V relates to synthesis and decomposition of Na_2Se, respectively (Tang et al., 2018). In summary, the reaction of ZnSe@N-CNFs anode in SIBs could be described as following chemical equations (Cao et al., 2018):

$$ZnSe + 2Na^+ + 2e^- \leftrightarrow Zn + Na_2Se \quad (3)$$

The cycling performances of ZnSe@N-CNFs at 2 Ag^{-1} with voltage window of 0.005–3 V (vs. Na/Na^+) were shown in **Figure S7**. The reversible capacity declined rapidly after 30 cycles. According to previous reports, by increasing the cut-off voltage can reduce the irreversible reactions with carbon and decomposition of electrolytes (Cui et al., 2018). Besides, as **Figure 5A** shows, there is no obvious reaction peak at low voltage. Therefore, 0.1–3 V (vs. Na/Na^+) was chosen as the voltage window during discharge and charge test for SIBs. The voltage profiles of ZnSe@N-CNFs with 0.1 Ag^{-1} for the first four cycles are shown in **Figure 5B**. The first discharge and charge capacities are 441.5 and 362.3 mA h g^{-1}, respectively, resulting in a coulombic efficiency of 82.1%. The huge capacity loss is attributed to SEI layers (Park and Kang, 2016). The coulombic efficiency increases rapidly to 100.3% for the second cycle. After the first cycle, the curves coincide well, indicate that the formed SEI layers is very stable and the great cycle reversibility of ZnSe@N-CNFs electrodes in SIBs (Liu et al., 2018).

The rate capability of as-synthesized samples was evaluated at various currents in the range of 0.1–2 A g^{-1}, and the results are given in **Figure 5C**. The capacity of ZnSe@N-CNFs is retained as 358.2, 357.9, 346.1, 334.8, 326.7, and 323.3 mA h g^{-1} at current densities of 0.1, 0.2, 0.5, 1, 1.5, 2 A g^{-1}, respectively. After the current densities back to 0.1 A g^{-1}, the capacity is raised to 455.0 mA h g^{-1}. Moreover, as shown in **Figure 5D**, the ZnSe@N-CNFs deliver an initial discharge capacity of 446.2 mA h g^{-1} with initial columbic efficiency of 72.9% at 2 A g^{-1}. And thereafter from the second cycle on, the columbic efficiency is over 99% and the reversible capacity is 365.6 mA h g^{-1} after 200 cycles. Both the rate capability and cycle performance are much better than ZnSe@N-C and CNFs. Both high capacity and increasing capacity can be attributed to the pseudocapacitive effect and its growth during cycling, the same as LIBs.

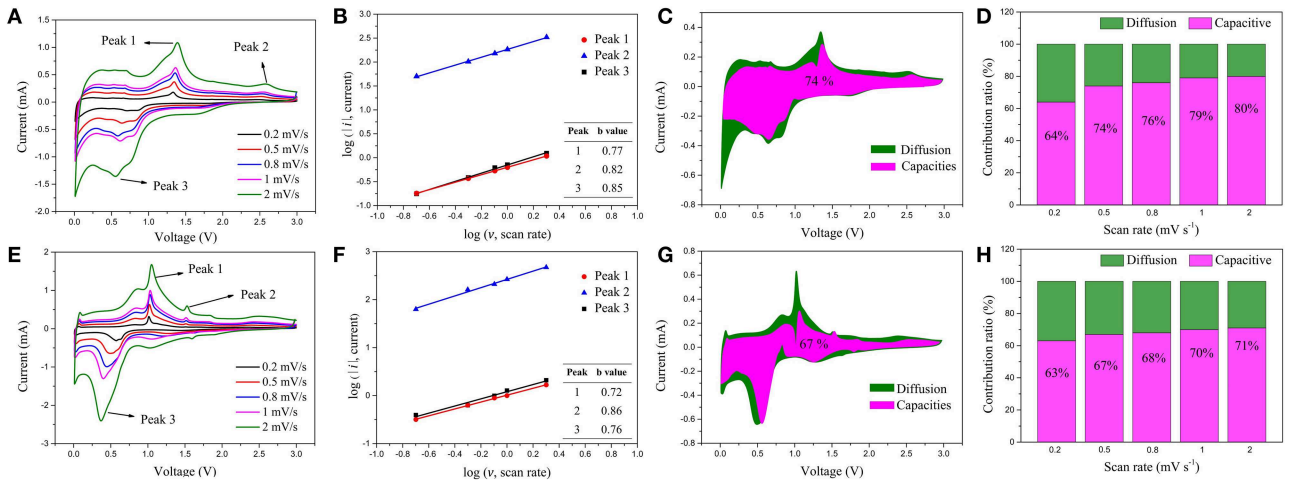

FIGURE 6 | (A) CV curves of the ZnSe@N-CNFs electrode for LIBs at different scan rates; **(B)** corresponding log(i) vs. log(v) plots for LIBs at each redox peak (peak current: i, scan rate: v) of the ZnSe@N-CNFs electrode; **(C)** capacitive and diffusion controlled contributions to charge storage of ZnSe@N-CNFs electrode for LIBs at 0.5 mV·s^{-1}; **(D)** normalized contribution ratio of capacitive and diffusion-controlled capacities of ZnSe@N-CNFs electrode for LIBs at different scan rates; **(E)** CV curves of the ZnSe@N-CNFs electrode for SIBs at different scan rates; **(F)** corresponding log(i) vs. log(v) plots for SIBs at each redox peak (peak current: i, scan rate: v) of the ZnSe@N-CNFs electrode; **(G)** capacitive and diffusion controlled contributions to charge storage of ZnSe@N-CNFs electrode for SIBs at 0.5 mV·s^{-1}; **(H)** normalized contribution ratio of capacitive and diffusion-controlled capacities of ZnSe@N-CNFs electrode for SIBs at different scan rates.

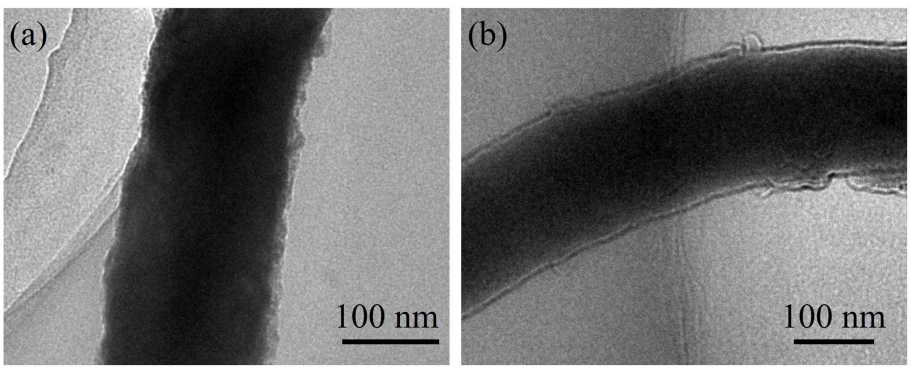

FIGURE 7 | TEM images of ZnSe@N-CNFs composites after 600 cycles at 2 A g^{-1} in LIBs **(a)**; after 200 cycles at 2 A g^{-1} in SIBs **(b)**.

No matter in LIBs or SIBs, the ZnSe@N-CNFs all shows satisfactory performance with high capacity and strong cycling stability. To further investigate the reason for the outstanding performance and evaluate the pseudocapacitive behavior of ZnSe@N-CNFs composite electrodes, the CV tests at different scan rates of 0.2–2 mV s^{-1} in LIBs and SIBs were conducted, as shown in **Figures 6A,E**. The relation between peak current (i) and scan rate (v) can describe by following two equations (Xu Y. et al., 2016):

$$i = av^b \quad (4)$$

$$\log(i) = b\log(v) + \log a \quad (5)$$

When the value of the slope b is 0.5, the ion storage process can be considered as diffusion controlled. When the value of slope b is 1, the ion storage process can be considered as capacitive controlled (Tang et al., 2018). The value of b of ZnSe@N-CNFs anode in LIBs and SIBs is calculated and showing in **Figure 6B,F**, respectively. The value of b in each peak is between 0.5 to 1, which can be considered that the ion storage process of ZnSe@N-CNFs anode is controlled by both capacitive and diffusion (Zhou et al., 2019).

According to the relational equation of $i = av$ for capacitive processes and $i = av^{1/2}$ for diffusion processes, by introducing the adjustable constant parameters as $k_1$and k_2, the current $i(v)$ response at fix voltage can be separated to two parts of capacitive and diffusion currents by following equation (Xu D. et al., 2016):

$$i_{(v)} = k_1 v + k_2 v^{1/2} \quad (6)$$

As **Figures 6C,G** shows, the contribution from capacitive capacity of ZnSe@N-CNFs anode in LIBs and SIBs at 0.5 $mV{\cdot}s^{-1}$ are calculated to ∼74 and 67%, respectively. With the scan rate increase, the contribution of capacitive gradually increases. As the **Figure 6D** shows, when the scan rate increased to 2 $mV{\cdot}s^{-1}$, the capacitive contributions of ZnSe@N-CNFs anode in LIBs reach to as high as 80%. And as for SIBs shown in **Figure 6H**, the capacitive contribution of ZnSe@N-CNFs anode also reaches to as high as 71% at 2 $mV{\cdot}s^{-1}$.The capacitive contribution for SIBs is lower than that in LIBs, which is attributed to the larger diameter of Na^+. The large capacitive contribution of ZnSe@N-CNFs indicates that the unique 1D structure can effectively provide the additional capacity, which explains the high capacity in both LIBs and SIBs (Chen et al., 2016). Moreover, as shown in **Figure S8**, the capacitive contribution increased in both LIBs and SIBs, which proved that the capacity increases along with the cyclic test mainly caused by the capacitive contribution.

The morphology of ZnSe@N-CNFs anodes after cycles have been observed and shown in **Figure 7**. Even after long cycles at large current densities, the ZnSe@N-CNFs in both LIBs and SIBs still remain it's 1D structure without additional agglomeration, while the excellent microstructural stability may explain the great cycles stability of ZnSe@N-CNFs. The ZnSe particles disappeared in **Figure 7** comparing with **Figure 2c** after the long cycles is due to the transformation to amorphous phase and, which can provide more interface for the capacitive behavior.

In addition, the EIS analysis was carried out for LIBs and SIBs of ZnSe@N-CNFs to evaluate the conductivity of anode. **Figures S9, S10** show the Nyquist plots and fitting curve of ZnSe@N-CNFs anode in LIBs and SIBs, respectively (Cui et al., 2018). The R_e is the electrolyte resistance, the R_f is the SEI layer resistance and R_{ct} corresponds to the charge transfer resistance. As the fitting results are shown in **Table S1**, the R_e, R_f and R_{ct} of the ZnSe@N-CNFs anode in LIBs is 4.74, 1.86, and 8.82 Ω, respectively. It also can be observed that the ZnSe@N-CNFs anode shows great performance of R_e (9.55 Ω), R_f (1.95 Ω), and R_{ct} (10.37 Ω) in SIBs. The impedance parameters in SIBs is slightly larger than in LIBs, indicating the higher kinetic resistance of SIBs. The satisfactory conductivity performance of ZnSe@N-CNFs anode suggests that ZnSe@N-CNFs can provide a short way for electrons and ions transfer, leading to an outstanding electrochemical performance (Miao et al., 2015; Zhao et al., 2017).

CONCLUSION

In summary, the ZnSe@N-CNFs anode was successfully fabricated from 1D electrospinning nanofibers with excellent electrochemical performance in both LIBs and SIBs even at higher current density. The ZnSe@N-CNFs anode delivered a high-capacity of 1,214.0 mA h g^{-1} and 447.5 mA h g^{-1} in LIBs and SIBs, respectively. Furthermore, even the current density was set to 2 A g^{-1}, the ZnSe@N-CNFs electrode delivered still maintained at 701.7 mA h g^{-1} after 600 cycles in LIBs and 368.9 mA h g^{-1} after 200 cycles in SIBs, respectively. The remarkable performance is attributed to the high capacitive contribution and stable conductive structure, so that the design scope of the metal selenide electrodes could be further expanded.

DATA AVAILABILITY

All datasets generated for this study are included in the manuscript/**Supplementary Files**.

AUTHOR CONTRIBUTIONS

MZ supervised the materials synthesis, tests, and manuscript preparation of PZ. All other authors attended part of the work and provided some beneficial advises and discussions on this work.

FUNDING

The authors gratefully acknowledge support from the Natural Science Foundation of Hunan Province, China (Grant No. 2018JJ2513), and the Key Project of Research Foundation of Education Bureau of Hunan Province, China (Grant No. 18A378).

ACKNOWLEDGMENTS

The authors also gratefully thank Professor Kejian He for his linguistic assistance during the preparation of this manuscript.

SUPPLEMENTARY MATERIAL

The Supplementary Material for this article can be found online at: https://www.frontiersin.org/articles/10.3389/fchem.2019.00569/full#supplementary-material

REFERENCES

Cao, X., Li, A., Yang, Y., and Chen, J. (2018). ZnSe nanoparticles dispersed in reduced graphene oxides with enhanced electrochemical properties in lithium/sodium ion batteries. *RSC Adv.* 8, 25734–25744. doi: 10.1039/c8ra03479f

Chen, C., Dong, Y., Li, S., Jiang, Z., Wang, Y., Jiao, L., et al. (2016). Rapid synthesis of three-dimensional network structure CuO as binder-free anode for high-rate sodium ion battery. *J. Power Sourc.* 320, 20–27. doi: 10.1016/j.jpowsour.2016.04.063

Chen, Z., Wu, R., Wang, H., Zhang, K. H. L., Song, Y., Wu, F., et al. (2017). Embedding ZnSe nanodots in nitrogen-doped hollow carbon architectures for superior lithium storage. *Nano Res.* 11, 966–978. doi: 10.1007/s12274-017-1709-x

Cho, J. S., Lee, S. Y., and Kang, Y. C. (2016). First introduction of $NiSe_2$ to anode material for sodium-ion batteries: a hybrid of graphene-wrapped $NiSe_2$/C porous nanofiber. *Sci. Rep.* 6:23338. doi: 10.1038/srep23338

Cui, C., Wei, Z., Zhou, G., Wei, W., Ma, J., Chen, L., et al. (2018). Quasi-reversible conversion reaction of $CoSe_2$/nitrogen-doped carbon nanofibers

towards long-lifetime anode materials for sodium-ion batteries. *J. Mater. Chem. A* 6, 7088–7098. doi: 10.1039/c8ta01168k

Cui, C., Zhou, G., Wei, W., Chen, L., Li, C., and Yue, J. (2017). Boosting sodium-ion storage performance of $MoSe_2$@C electrospinning nanofibers by embedding graphene nanosheets. *J. Alloys Compounds* 727, 1280–1287. doi: 10.1016/j.jallcom.2017.08.258

Deng, P., Yang, J., He, W., Li, S., Zhou, W., Tang, D., et al. (2018). Tin-assisted Sb2S3 nanoparticles uniformly grafted on graphene effectively improves sodium-ion storage performance. *ChemElectroChem* 5, 811–816. doi: 10.1002/celc.201800016

Du, C. F., Liang, Q., Zheng, Y., Luo, Y., Mao, H., and Yan, Q. (2018). Porous MXene frameworks support pyrite nanodots toward high-rate pseudocapacitive Li/Na-ion storage. *ACS Appl. Mater. Interfaces* 10, 33779–33784. doi: 10.1021/acsami.8b13750

Fan, T.-E., and Xie, H.-F. (2019). Sb2S3-rGO for high-performance sodium-ion battery anodes on Al and Cu foil current collector. *J. Alloys Compounds* 775, 549–553. doi: 10.1016/j.jallcom.2018.10.103

Fu, Y., Zhang, Z., Du, K., Qu, Y., Li, Q., and Yang, X. (2015). Spherical-like ZnSe with facile synthesis as a potential electrode material for lithium ion batteries. *Mater. Lett.* 146, 96–98. doi: 10.1016/j.matlet.2015.02.019

Fu, Y., Zhong, B., Chen, Y., Song, Y., Zhou, R., Song, Y., et al. (2016). Porous ZnO@C core–shell nanocomposites as high performance electrode materials for rechargeable lithium-ion batteries. *J. Porous Mater.* 24, 613–620. doi: 10.1007/s10934-016-0297-6

Ge, X., Li, Z., Wang, C., and Yin, L. (2015). Metal-organic frameworks derived porous core/shell structured ZnO/$ZnCo_2O_4$/C hybrids as anodes for high-performance lithium-ion battery. *ACS Appl. Mater. Interfaces* 7, 26633–26642. doi: 10.1021/acsami.5b08195

Gu, X., Yue, J., Chen, L., Liu, S., Xu, H., Yang, J., et al. (2015). Coaxial MnO/N-doped carbon nanorods for advanced lithium-ion battery anodes. *J. Mater. Chem. A* 3, 1037–1041. doi: 10.1039/c4ta05622a

Ji, L., Zheng, H., Ismach, A., Tan, Z., Xun, S., Lin, E., et al. (2012). Graphene/Si multilayer structure anodes for advanced half and full lithium-ion cells. *Nano Energy* 1, 164–171. doi: 10.1016/j.nanoen.2011.08.003

Ko, Y. N., Choi, S. H., and Kang, Y. C. (2016). Hollow cobalt selenide microspheres: synthesis and application as anode materials for Na-ion batteries. *ACS Appl. Mater. Interfaces* 8, 6449–6456. doi: 10.1021/acsami.5b11963

Kwon, H.-T., and Park, C.-M. (2014). Electrochemical characteristics of ZnSe and its nanostructured composite for rechargeable Li-ion batteries. *J. Power Sourc.* 251, 319–324. doi: 10.1016/j.jpowsour.2013.11.033

Lallave, M., Bedia, J., Ruiz-Rosas, R., Rodríguez-Mirasol, J., Cordero, T., Otero, J. C., et al. (2007). Filled and hollow carbon nanofibers by coaxial electrospinning of alcell lignin without binder polymers. *Adv. Mater.* 19, 4292–4296. doi: 10.1002/adma.200700963

Lee, J., Kitchaev, D. A., Kwon, D. H., Lee, C. W., Papp, J. K., Liu, Y. S., et al. (2018). Reversible Mn(2+)/Mn(4+) double redox in lithium-excess cathode materials. *Nature* 556, 185–190. doi: 10.1038/s41586-018-0015-4

Li, L., Wang, L., Zhang, M., Huang, Q., Chen, L., and Wu, F. (2019). High-performance lithium-ion battery anodes based on Mn3O4/nitrogen-doped porous carbon hybrid structures. *J. Alloys Compounds* 775, 51–58. doi: 10.1016/j.jallcom.2018.10.106

Li, L., Zhou, G., Yin, L., Koratkar, N., Li, F., and Cheng, H.-M. (2016). Stabilizing sulfur cathodes using nitrogen-doped graphene as a chemical immobilizer for Li S batteries. *Carbon* 108, 120–126. doi: 10.1016/j.carbon.2016.07.008

Li, S., Qu, B., Huang, H., Deng, P., Xu, C., Li, Q., et al. (2017). Controlled synthesis of iron sulfide coated by carbon layer to improve lithium and sodium storage. *Electrochim. Acta* 247, 1080–1087. doi: 10.1016/j.electacta.2017.07.106

Li, W., Zeng, L., Wu, Y., and Yu, Y. (2016). Nanostructured electrode materials for lithium-ion and sodium-ion batteries via electrospinning. *Sci. China Mater.* 59, 287–321. doi: 10.1007/s40843-016-5039-6

Liao, S. H., Lu, S. Y., Bao, S. J., Yu, Y. N., and Wang, M. Q. (2016). $NiMoO_4$ nanofibres designed by electrospining technique for glucose electrocatalytic oxidation. *Anal. Chim. Acta* 905, 72–78. doi: 10.1016/j.aca.2015.12.017

Liu, D.-H., Li, W.-H., Liang, H.-J., L.ü H.-Y., Guo, J.-Z., Wang J, et al. (2018). Coaxial α-MnSe@N-doped carbon double nanotubes as superior anode materials in Li/Na-ion half/full batteries. *J. Mater. Chem. A* 6, 15797–15806. doi: 10.1039/c8ta03967d

liu, H., Shi, L., Li, D., Yu, J., Zhang, H.-M., and Ullah, S., et al. (2018). Rational design of hierarchical ZnO@Carbon nanoflower for high performance lithium ion battery anodes. *J. Power Sourc.* 387, 64–71. doi: 10.1016/j.jpowsour.2018.03.047

Lu, B., Liu, J., Hu, R., Wang, H., Liu, J., and Zhu, M. (2017). Facile synthesis of self-supported Mn_3O_4@C nanotube arrays constituting an ultrastable and high-rate anode for flexible Li-ion batteries. *J. Mater. Chem. A* 5, 8555–8565. doi: 10.1039/c7ta01698k

Mai, L., Xu, L., Han, C., Xu, X., Luo, Y., Zhao, S., et al. (2010). Electrospun ultralong hierarchical vanadium oxide nanowires with high performance for lithium ion batteries. *Nano Lett.* 10, 4750–4755. doi: 10.1021/nl103343w

Miao, Y. E., Huang, Y., Zhang, L., Fan, W., Lai, F., and Liu, T. (2015). Electrospun porous carbon nanofiber@MoS_2 core/sheath fiber membranes as highly flexible and binder-free anodes for lithium-ion batteries. *Nanoscale* 7, 11093–11101. doi: 10.1039/c5nr02711j

Ning, H., Xie, H., Zhao, Q., Liu, J., Tian, W., Wang, Y., et al. (2017). Electrospinning ZnO/carbon nanofiber as binder-free and self-supported anode for Li-ion batteries. *J. Alloys Compounds* 722, 716–720. doi: 10.1016/j.jallcom.2017.06.099

Nitta, N., Wu, F., Lee, J. T., and Yushin, G. (2015). Li-ion battery materials: present and future. *Mater. Today* 18, 252–264. doi: 10.1016/j.mattod.2014.10.040

Park, G. D., and Kang, Y. C. (2016). One-pot synthesis of CoSex -rGO composite powders by spray pyrolysis and their application as anode material for sodium-ion batteries. *Chemistry* 22, 4140–4146. doi: 10.1002/chem.201504398

Park, G. D., Kim, J. H., and Kang, Y. C. (2016). Large-scale production of spherical $FeSe_2$-amorphous carbon composite powders as anode materials for sodium-ion batteries. *Mater. Charact.* 120, 349–356. doi: 10.1016/j.matchar.2016.09.019

Tang, C., Wei, X., Cai, X., An, Q., Hu, P., Sheng, J., et al. (2018). ZnSe microsphere/multiwalled carbon nanotube composites as high-rate and long-life anodes for sodium-ion batteries. *ACS Appl. Mater. Interfaces* 10, 19626–19632. doi: 10.1021/acsami.8b02819

Tian, S., Zhu, G., Tang, Y., Xie, X., Wang, Q., Ma, Y., et al. (2018). Three-dimensional cross-linking composite of graphene, carbon nanotubes and Si nanoparticles for lithium ion battery anode. *Nanotechnology* 29:125603. doi: 10.1088/1361-6528/aaa84e

Wang, L., Yang, C., Dou, S., Wang, S., Zhang, J., Gao, X., et al. (2016). Nitrogen-doped hierarchically porous carbon networks: synthesis and applications in lithium-ion battery, sodium-ion battery and zinc-air battery. *Electrochim. Acta* 219, 592–603. doi: 10.1016/j.electacta.2016.10.050

Wang, Z., Cao, X., Ge, P., Zhu, L., Xie, L., Hou, H., et al. (2017). Hollow-sphere ZnSe wrapped around carbon particles as a cycle-stable and high-rate anode material for reversible Li-ion batteries. *N. J. Chem.* 41, 6693–6699. doi: 10.1039/c7nj01230f

Wu, F., Borodin, O., and Yushin, G. (2017). *In situ* surface protection for enhancing stability and performance of conversion-type cathodes. *MRS Energy Sustainability* 4:E9. doi: 10.1557/mre.2017.11

Wu, F., Zhao, C., Chen, S., Lu, Y., Hou, Y., Hu, Y.-S., et al. (2018). Multi-electron reaction materials for sodium-based batteries. *Mater. Today* 21, 960–973. doi: 10.1016/j.mattod.2018.03.004

Wu, Q., Liu, J., Yuan, C., Li, Q., and Wang, H.-G. (2017). Nitrogen-doped 3D flower-like carbon materials derived from polyimide as high-performance anode materials for lithium-ion batteries. *Appl. Surf. Sci.* 425, 1082–1088. doi: 10.1016/j.apsusc.2017.07.118

Xu, D., Chen, C., Xie, J., Zhang, B., Miao, L., Cai, J., et al. (2016). A hierarchical N/S-codoped carbon anode fabricated facilely from cellulose/polyaniline microspheres for high-performance sodium-ion batteries. *Adv. Energy Mater.* 6:1501929. doi: 10.1002/aenm.201501929

Xu, X., Ji, S., Gu, M., and Liu, J. (2015). *In situ* synthesis of MnS hollow microspheres on reduced graphene oxide sheets as high-capacity and long-life anodes for Li- and Na-ion batteries. *ACS Appl. Mater. Interfaces* 7, 20957–20964. doi: 10.1021/acsami.5b06590

Xu, Y., Liang, J., Zhang, K., Zhu, Y., Wei, D., and Qian, Y. (2016). Origin of additional capacities in selenium-based ZnSe@C nanocomposite Li-ion battery electrodes. *Electrochem. Commun.* 65, 44–47. doi: 10.1016/j.elecom.2016.02.009

Zhang, L., Lu, L., Zhang, D., Hu, W., Wang, N., Xu, B., et al. (2016). Dual-buffered SnSe@CNFs as negative electrode with outstanding lithium storage performance. *Electrochim. Acta* 209, 423–429. doi: 10.1016/j.electacta.2016.05.106

Zhang, Y., Pan, A., Ding, L., Zhou, Z., Wang, Y., Niu, S., et al. (2017). Nitrogen-doped yolk-shell-structured CoSe/C dodecahedra for high-performance sodium ion batteries. *ACS Appl. Mater. Interfaces* 9, 3624–3633. doi: 10.1021/acsami.6b13153

Zhang, Y.-C., You, Y., Xin, S., Yin, Y.-X., Zhang, J., Wang, P., et al. (2016). Rice husk-derived hierarchical silicon/nitrogen-doped carbon/carbon nanotube spheres as low-cost and high-capacity anodes for lithium-ion batteries. *Nano Energy* 25, 120–127. doi: 10.1016/j.nanoen.2016.04.043

Zhang, Z., Fu, Y., Yang, X., Qu, Y., and Li, Q. (2015). Nanostructured ZnSe anchored on graphene nanosheets with superior electrochemical properties for lithium ion batteries. *Electrochim. Acta* 168, 285–291. doi: 10.1016/j.electacta.2015.04.025

Zhao, X., Wang, H.-E., Cao, J., Cai, W., and Sui, J. (2017). Amorphous/crystalline hybrid MoO_2 nanosheets for high-energy lithium-ion capacitors. *Chem. Commun.* 53, 10723–10726. doi: 10.1039/c7cc06851d

Zhou, P., Chen, L., Zhang, M., Huang, Q., Cui, C., X., et al. (2019). Embedding α-MnSe nanodots in nitrogen-doped electrospinning carbon nanofibers to enhanced storage properties of lithium-ion batteries. *J. Alloys Compounds* 797, 826–833. doi: 10.1016/j.jallcom.2019.05.107

Conflict of Interest Statement: The authors declare that the research was conducted in the absence of any commercial or financial relationships that could be construed as a potential conflict of interest.

frontiers in Chemistry

ORIGINAL RESEARCH
published: 20 August 2019
doi: 10.3389/fchem.2019.00572

Toward High-Performance Li Metal Anode via Difunctional Protecting Layer

Jinlei Gu[1], Chao Shen[1], Zhao Fang[2], Juan Yu[2], Yong Zheng[3], Zhanyuan Tian[3], Le Shao[3], Xin Li[1]* and Keyu Xie[1]**

[1] State Key Laboratory of Solidification Processing, Center for Nano Energy Materials, School of Materials Science and Engineering, Northwestern Polytechnical University and Shaanxi Joint Laboratory of Graphene (NPU), Xi'an, China, [2] School of Metallurgical Engineering, Xi'an University of Architecture and Technology, Xi'an, China, [3] Shaanxi Coal and Chemical Technology Institute Co., Ltd, Xi'an, China

Li-metal batteries are the preferred candidates for the next-generation energy storage, due to the lowest electrode potential and high capacity of Li anode. However, the dangerous Li dendrites and serious interface reaction hinder its practical application. In this work, we construct a difunctional protecting layer on the surface of the Li anode (the $AgNO_3$-modified Li anode, AMLA) for Li-S batteries. This stable protecting layer can hinder the corrosion reaction with intermediate polysulfides (Li_2S_x, $4 \leq x \leq 8$) and suppress the Li dendrites by regulating Li metal nucleation and depositing Li under the layer uniformly. The AMLA can cycle more than 50 h at 5 mA cm^{-2} with the steady overpotential of lower than 0.2 V and show high capacity of 666.7 mAh g^{-1} even after 500 cycles at 0.8375 mA cm^{-2} in Li-S cell. This work makes great contribution to the protection of the Li anode and further promotes the practical application.

Keywords: $AgNO_3$, difunctional protecting layer, Li anode, Li-S battery, Li dendrites

OPEN ACCESS

Edited by:
Feixiang Wu,
Central South University, China

Reviewed by:
Xunhui Xiong,
South China University of Technology, China
Jia Feng Zhang,
Central South University, China
Xianwen Wu,
Jishou University, China

***Correspondence:**
Chao Shen
shenchao@nwpu.edu.cn
Xin Li
1814938717@qq.com
Keyu Xie
kyxie@nwpu.edu.cn

Specialty section:
This article was submitted to Electrochemistry, a section of the journal Frontiers in Chemistry

Received: *12 June 2019*
Accepted: *29 July 2019*
Published: *20 August 2019*

Citation:
Gu J, Shen C, Fang Z, Yu J, Zheng Y, Tian Z, Shao L, Li X and Xie K (2019) Toward High-Performance Li Metal Anode via Difunctional Protecting Layer. Front. Chem. 7:572. doi: 10.3389/fchem.2019.00572

INTRODUCTION

Li metal is the most promising anode material for the next-generation batteries (Li-metal batteries), such as Li-S batteries (Su et al., 2018) and Li-air batteries (Cao et al., 2019), due to the lowest electrode potential (−3.04 V, compare to the hydrogen electrode) and the high capacity (3,860 mAh g^{-1}, which is 10 times than the commercial graphite) (Liu et al., 2016; Yan K. et al., 2016; Liang et al., 2017; Zhang K. et al., 2017; Bai et al., 2018; Cheng et al., 2018, 2019; Li et al., 2018; Terlicka et al., 2019). However, the intense chemical activity of Li metal leads to sever interface reactions between Li and electrolyte, which results in low Coulomb efficiency and increasing interface impedance (Zheng et al., 2014; Shen et al., 2018). Besides, the inhomogeneous Li deposition leads to forming the dangerous Li dendrites on the Li anode (Tao et al., 2017). During the battery cycling, the Solid Electrolyte Interface (the SEI film) to rupture and re-repair continuously since the uncontrollable Li dendrites. It will trigger the serious side reaction to consume the electrolyte and Li (Hou et al., 2019). More severely, the Li dendrites will pierce through the separator, and cause serious safety hazard (the battery short-circuited, producing a large amount of joule heat and triggering an explosion; Peng et al., 2016; Yang et al., 2017; Zhang et al., 2018; Hou et al., 2019). Thus, the Li anode cannot be commercialized without addressing the above problems (Cheng et al., 2018).

Recently, a variety of approaches are employed to hinder the interface reaction and suppress the Li dendrites to promote the practicality of the Li anode. Firstly, the electrolyte additives are added into electrolyte to increase the stability and dense of the SEI film to suppress the serious interface

reaction (Zhang, 2012; Jing et al., 2015; Xie et al., 2016; Shiga et al., 2017; An et al., 2019; Chen et al., 2019; Wang et al., in press). However, the SEI film still has limited structure strength, the growth of Li dendrites will destroy it during the cycles. In addition, researchers suppress the Li dendrites through controlling nucleation sites of Li (Zhang et al., 2016, 2018; Jin et al., 2017; Pei et al., 2017; Zhang R. et al., 2017; Hou et al., 2019; Li et al., 2019) and forming a protective layer (Hiratani et al., 1988; Choi et al., 2004; Kozen et al., 2015; Liu et al., 2016, 2018; Peng et al., 2016; Liang et al., 2017; Xie et al., 2017; Bai et al., 2018; Li et al., 2018; Wang et al., 2019) on the Li anode. For example, Liang et al. form a Li-rich composite alloy/LiCl layer on the Li anode (Liang et al., 2017). The Li^+ goes through the protecting layer fast to let Li be deposited under it to suppress the Li dendrites because of the high ionic conduction of the alloy layer. Nevertheless, the uneven deposition of Li is not improved, which means that Li dendrites still are formed. Moreover, Yang et al. struct a 3D host material with ubiquitous and uniform nanoseeds (the ultrafine Ag nanoparticles) to regulate the Li nucleation and deposition homogeneously (Yang et al., 2017). However, this method increases the interface area between electrolyte and Li anode to aggravate the interface reaction and cannot protect the SEI film as the large volume change during the deposition and dissolution process of the Li. Thurs, single method cannot protect the Li anode in the Li-metal batteries well. It is very important to form a protecting layer on the Li anode, which can lead the homogeneous deposition of Li under it and remain the stable SEI film to hinder the interface reaction.

Herein, we form such difunctional protecting layer on the Li anode as the $AgNO_3$-modified Li anode (AMLA) through a simple way, dropping the solution of $AgNO_3$ on the Li anode. In order to study the effect of this layer, we apply it to the Li-S batteries. This difunctional protecting layer is consisted of the LiAg alloy and the modified SEI film by $LiNO_3$. On the one hand, the layer can suppress the Li dendrites to keep the integrity of the SEI film. The LiAg alloy can regulate Li nucleation and let Li depositing under the protecting layer uniformly to suppress the Li dendrites. On the other hand, the modified SEI film by $LiNO_3$ can protect the Li anode from the electrolyte to suppress the corrosive reaction between Li and intermediate polysulfides (Jing et al., 2015; Li et al., 2015; Yan C. et al., 2016). The difunctional protecting layer can improve the Li anode through suppressing the Li dendrites and hindering the corrosion reaction in the Li-S batteries.

MATERIALS AND METHODS

Synthesis of the Protecting Layer on the Li Anode

The $AgNO_3$ solution used polar solvent tetrahydrofuran (THF) as the solvent to disperse the $AgNO_3$. Put 50 mg $AgNO_3$ (AR, ≥99.8%) in 10 ml THF (≥99.8%, HPLC) solvent in the glove box filled with argon (H_2O < 0.1 ppm, O < 0.1 ppm). After heating and stirring for 24 h, the solution was ultrasonic disperse until uniform clarification solution is obtained. The template for making the solution is 30°C and the speed of stirring is 500 rpm min^{-1}. Drop 20 μL of prepared solution onto the Li anode through using the pipette. Heat for 3 min to ensure no THF solvent residual with the template of 40°C.

Characterizations

X-ray diffraction (XRD) was characterized by STOE PANalytical Empyrean. The experimental conditions are as follows: the radiation is the CuKα radiation and the λ is 1.5406 Å, the scanning Angle is 20–90°, the current and voltage are 40 mA and 40 kV, the scanning time is 8 min (the scanning step length is 3°, the dwell time is 20 s). X-ray photoelectron spectroscopy (XPS) characterizations were characterized by an ESCALAB250xi XPS system. Energy Dispersion Spectrum (EDS) and Scanning electron microscope (SEM) studies were carried out with FESEM, FEI Tecnai G2 F30. All of the samples were washed by the 1,2-dimethoxyethane (DME) for three times and tested after the DME evaporated.

Electrochemical Measurements

The CR2016-type coin cells were used to study the electrochemical performance, which assembled with one 0.5 mm metallic gasket in the glove box. Celgard type 2400 polypropylene film was used as separator. The electrolyte in the experiments was that 1 M Li bis(trifluoromethane sulfonyl)imide (LiTFSI) is dissolved in the solvent consisting of 1,2-dimethoxyethane (DME) and 1,3-dioxolane (DOL), where the ratio was 1:1 by volume. There were two kinds of cells (the symmetrical cell and Li-S cell) used to study the electrochemical performance of the protecting layer. The symmetric cells used the Li anode or the AMLA on each side, as shown in the **Figure 4a**. The electrochemical performance of symmetrical cells was measured by symmetrical cycle test and electrochemical impedance spectroscopy (EIS) test. As the symmetrical cycle test, the symmetrical cells were cycled with the Li deposit amount of 0.5 mAh cm^{-2} at 1, 2, and 5 mA cm^{-2} to make the change of voltage—time curve on a LAND battery system. The frequency range of the EIS test was from 0.01 to 1,000,000 Hz and the amplitude was 10 mV, which was carried out on Solartron electrochemical workstation (1260 + 1287, England).

For the Li-S cell, the S cathode was formation: firstly, forming the slurry through mixing the S, binder (polyvinylidene fluoride, PVDF) and conductive carbon black (super-P acetylene black), at a weight ratio of 8:1:1, in the solution of N-methyl-2-pyrrolidone (NMP); then, casting the slurry on carbon-coated aluminum foil at 200 μm with the doctor blade as S cathodes; in the last, vacuum drying the cathode at 60°C for 10 h and rushing into 12 mm diameter wafer, the plate load per unit area is about 1.0 mg cm^{-2}. The Li-S cell was composed of the S cathode and Li anode or the AMLA.

Galvanostatic charge-discharge tests were carried to study the electrochemical performance of the cell, and the current density was 0.5 C (1 C = 1,675 mA g^{-1}) with the voltage windows of 1.7–2.8 V.

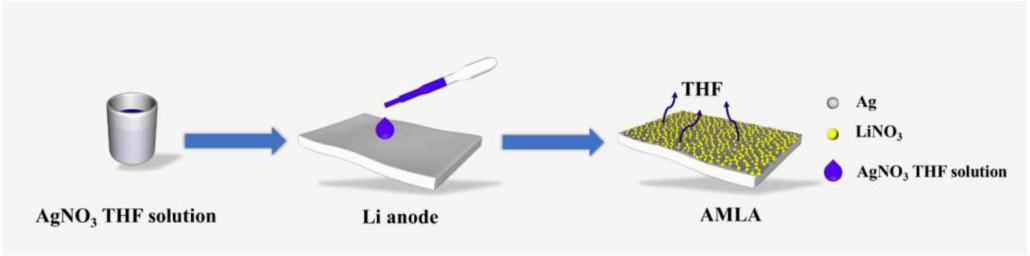

FIGURE 1 | The illustration of the synthesis of the AMLA.

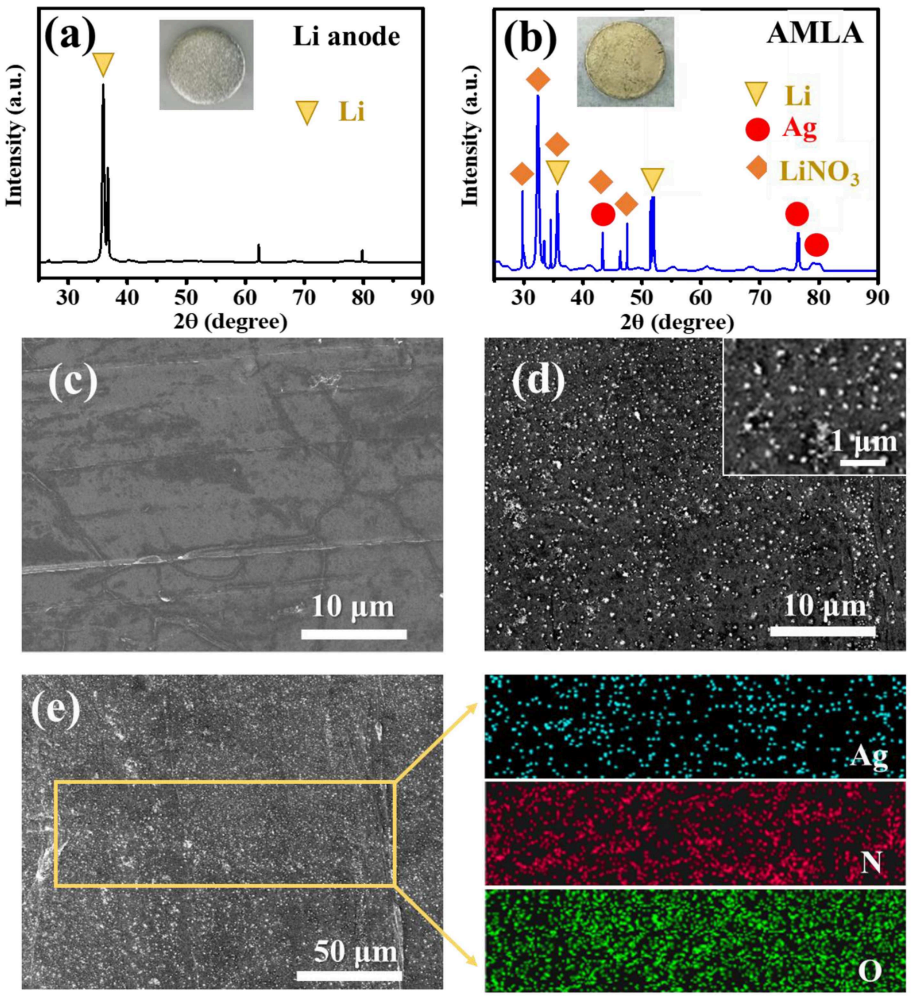

FIGURE 2 | The XRD curves of Li anode **(a)** and AMLA **(b)**, and the circle sheets in the figures represent the Li anode in different states. **(c)** The SEM image of Li anode. **(d)** The SEM image of AMLA. **(e)** The EDS images of ALMA, and the blue spots represent the element Ag, the red ones represent the element N, and the green ones represent the element O.

RESULTS AND DISCUSSION

The AMLA is formed by a very simple way, dropping the THF solution of $AgNO_3$ on the Li anode, as illustrated in **Figure 1**. After the redundant THF evaporates, a thin mixing layer of $LiNO_3$ and Ag is formed on the Li anode and we can see the color of the Li metal changes to yellow. The mixing layer is made *in situ* spontaneous reduction of $AgNO_3$ by Li, due to that the redox potential of Ag/Ag^+ couples (0.8 V, compare to the hydrogen electrode) is much higher than the Li/Li^+. And this reaction can

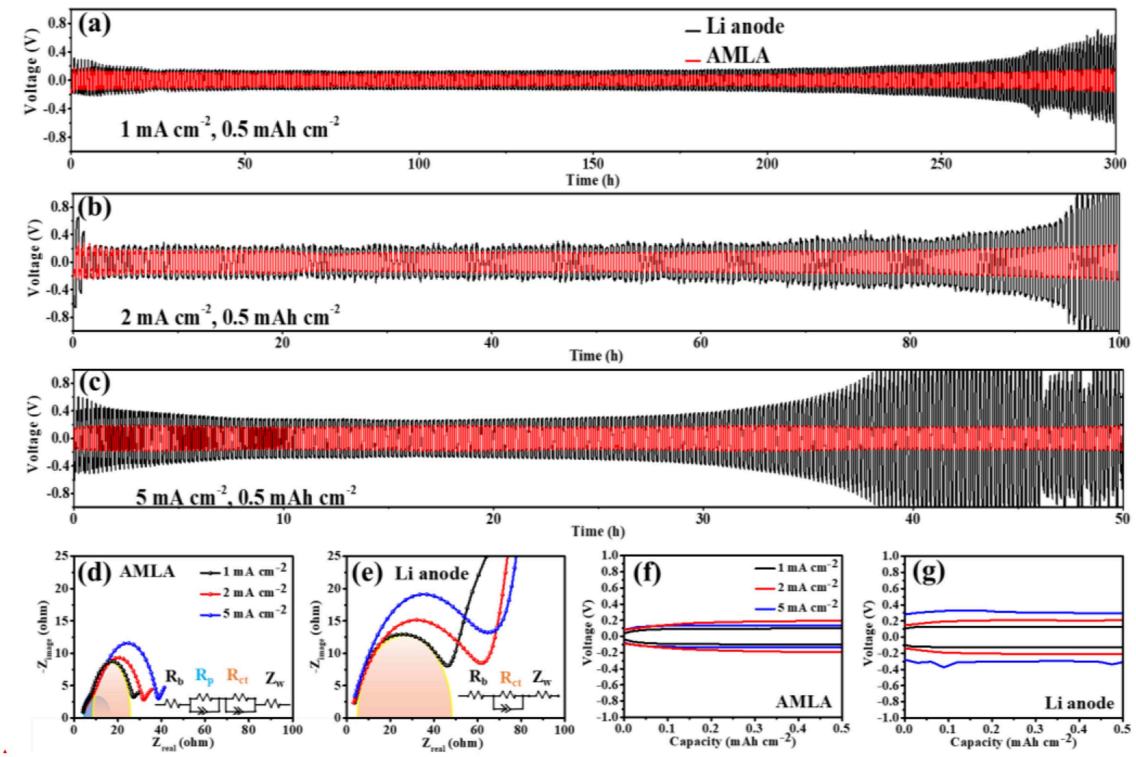

FIGURE 3 | The electrochemical performances of symmetrical cells. **(a–c)** The voltage-time curves of Li anode (back) and AMLA (red) electrodes under 1, 2, and 5 mA cm^{-2}current density, the deposit amount of Li^{+} is 0.5 mAh cm^{-2} for all the battery. The EIS figures of AMLA **(d)** and Li anode **(e)** after 30 times' cycles under 1 mA cm^{-2} (black), 2 mA cm^{-2} (red), and 5 mA cm^{-2} (blue) current density. The polarization voltage figures of AMLA **(f)** and Li anode **(g)** after 30 times' cycles, under 1 mA cm^{-2} (black), 2 mA cm^{-2} (red), and 5 mA cm^{-2} (blue) current density.

be represented by the following equation:

$$AgNO_3 + Li \rightarrow LiNO_3 + Ag \quad (1)$$

The formation of $LiNO_3$ and Ag can be confirmed through employing the XRD. The characteristic diffraction peaks of Ag (PDF#01-1167) at 44.50°, 77.63°, and 81.57° corresponding to the (200), (311), and (222) facets appear on the AMLA (**Figure 2b**), comparing the only characteristic diffraction peaks of Li in the **Figure 2a** (Taillades and Sarradin, 2004; Offor et al., 2015). In addition, there are another four characteristic diffraction peaks of $LiNO_3$, which is at 24.82°, 32.10°, 35.28°, and 42.45° (**Figure 2b**), corresponding to the (012), (104), (006), and (113) facets in the PDF#01-1225. In addition, the morphologies of the Li anode (**Figure 2c**) and AMLA (**Figure 2d**) are characterized by the SEM. The surface of the Li anode is very smooth, while the AMLA is rough with a lot of Ag nanoparticles. The size of these nanoparticles is smaller than 100 nm and they are homogeneous distribution as confirmed by the EDS of the AMLA (**Figure 2e**). All of these results confirm that we form the mixing uniform layer of $LiNO_3$ and Ag on the Li anode as the Equation (1).

The electrochemical performances of the cells with the AMLA show much better due to the mixing layer of $LiNO_3$ and Ag, comparing to the symmetrical cells with the Li anode (**Figure 3**). First of all, the symmetrical cells with the AMLA own more stable cycle performance and longer lifetime. The symmetrical cells are cycled at 1, 2, and 5 mA cm^{-2} with the Li deposit amount of 0.5 mAh cm^{-2}. The voltage-time curves of the Li anode (back) and AMLA (red) are showed in the **Figures 3a–c**. The symmetrical cell with the Li anode is only stably cycled for 200 h with overpotential of 0.1 V, when the current density is 1 mA cm^{-2}. Subsequently, the overpotential raise up with the decomposition of the electrolyte and the thicker SEI film during the cycling (Yang et al., 2017). After cycling for 300 h, the overpotential of the cell becomes higher than 0.5 V. In addition, the cell with the Li anode appears violent voltage fluctuation after 76 h at low current density of 2 mA cm^{-2} and 35 h at high current density of 5 mA cm^{-2} (**Figures 3b,c**), which is caused by the reaction between Li and electrolyte (Liu et al., 2018). And there is a performance that as the voltage first decreases and then increases just like a neck shape in the voltage-time curve of the symmetrical cell with the Li anode at 5 mA cm^{-2}. This special curve results from the generation and growth of dendrites (Liu et al., 2016). However, the symmetrical cell with the AMLA shows much more stable cycling at different current density. As we can see, the cell with the AMLA can be cycled more than 50 h with steady overpotential, even at 5 mA cm^{-2}, which is lower than 0.2 V (**Figure 3c**). Furthermore, the cell with the AMLA shows the lower resistance after 30 times' cycles (**Figures 3d,e**). The resistance is consisted of

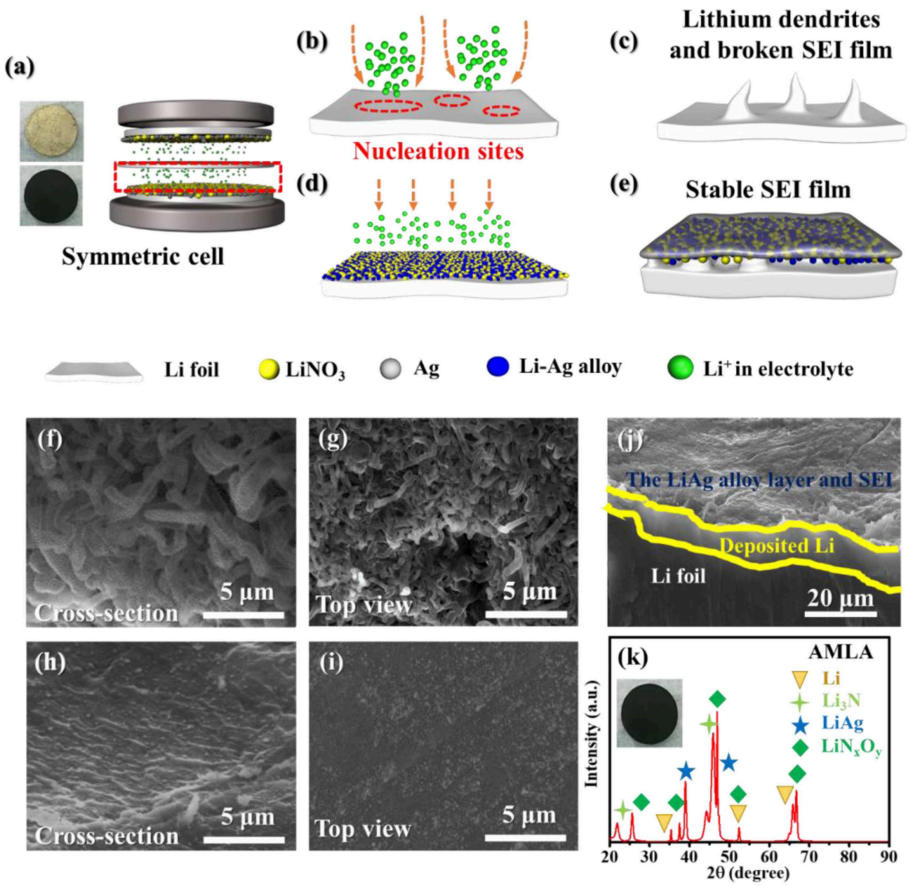

FIGURE 4 | The change of anode when during charge/discharge progress and the morphology of Li anode and AMLA. **(a)** The schematic of symmetric cell. **(b,c)** The schematic of change on Li anode during charge/discharge progress. **(d,e)** The schematic of change on AMLA during charge/discharge progress. **(f,g)** SEM images of cross-section and top-view of Li anode after cycles. **(h,i)** SEM images of cross-section **(h)** and top-view **(i)** of AMLA after cycles. **(j)** SEM images of cross-section AMLA with the deposit amount of 1 mAh cm^{-2} as the current density of 1 mA cm^{-2}. The XRD curves of AMLA **(k)**.

the ohmic resistance (R_b), interfacial resistance of the electrode (R_i), and diffusion impedance of lithium ions in solids (Z_w) (Wu et al., 2019; Zhou et al., 2019). In the symmetrical cells, the most important resistance is the Ri, because the R_b (4 Ω) and the Z_w (the slop of the sloping line at the low frequency region are the same) are the same in different electrodes. As for the AMLA, there are two semicircles in the high frequency region of the EIS curve, due to the mixing layer of $LiNO_3$ and Ag: the first one represents the lithium ion transfer impedance (R_p) and the second one represents the charge transfer impedance (R_{ct}) (Wu et al., 2019). Therefore, the R_i of the AMLA is consisted of R_p and R_{ct}. However, there is only one semicircle for the Li anode, because of the two synchronous processes of lithium ion transfer and charge transfer. So, the R_i is the same as the R_{ct} in the Li anode. The R_i of the AMLA is negatively changed at different current density as 23 Ω at 1 mA cm^{-2}, 26 Ω at 2 mA cm^{-2}, and 34 Ω at 5 mA cm^{-2} (**Figure 3d**). Whereas, the R_i (R_{ct}) of the Li anode is twice higher than the AMLA and increased with the higher current density (45 Ω at 1 mA cm^{-2}, 60 Ω at 2 mA cm^{-2}, and 70 Ω at 5 mA cm^{-2}, **Figure 3e**). The hysteresis in the voltage profile is even lower than 0.2 V for the AMLA at current density of 5 mA cm^{-2}, while it increased higher than 0.35 V for the Li anode (**Figures 3f,g**). The mixing uniform layer of $LiNO_3$ and Ag can improve the electrochemistry performance in the symmetrical cells, which is formed in the AMLA before cycling.

Except for the electrochemistry performance, the mixing uniform layer of $LiNO_3$ and Ag changes the surface of the Li anode after cycling (**Figures 4f–i**). For the Li anode, there are a lot of drastic Li dendrites on the surface in the cross-section and top view SEM images (**Figures 4f,g**). These Li dendrites are wire shape with length of 5–10 μm and diameter of 1–2 μm. It is indicating that the nucleation and deposition of Li are inhomogeneous (**Figures 4b,c**). These Li dendrites will increase the interface of the Li anode contacting with electrolyte to accelerate the side reaction as violent voltage fluctuation during the cycling (**Figures 3a–c**). And, it will consume large amounts of electrolyte and deteriorate the cycle performance. Furthermore, these Li dendrites will pierce the separator and cause safety hazard. In contrast, the morphologies of the Li anode are much smooth without any Li dendrites (**Figures 4d,e**).

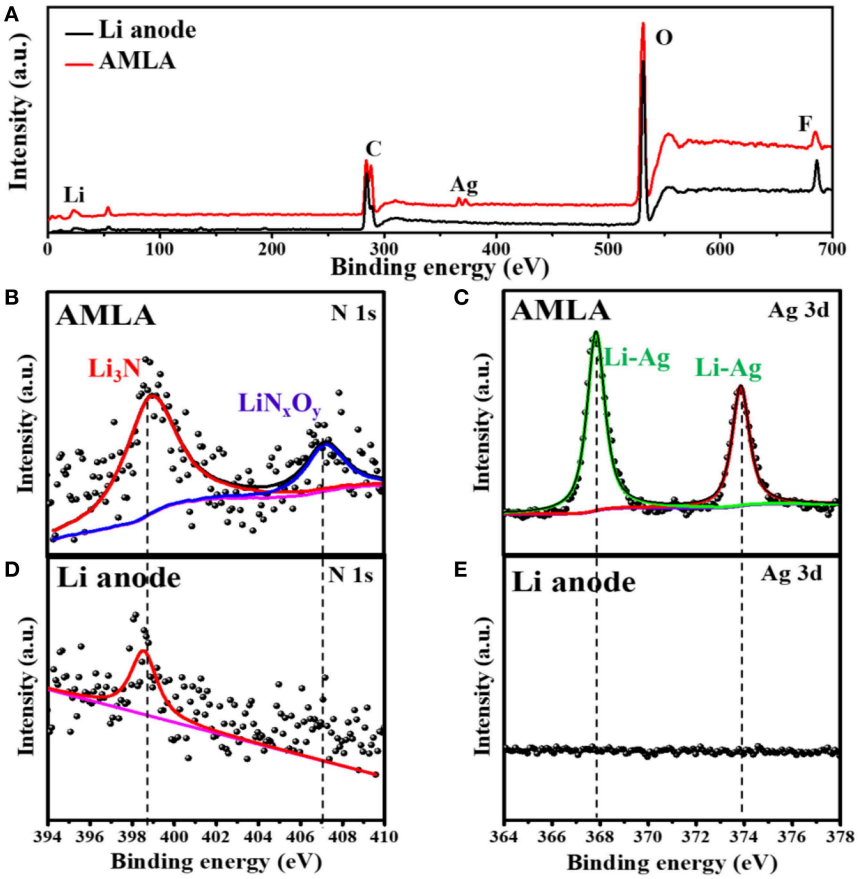

FIGURE 5 | The XPS spectra of Li anode and AMLA after cycles. The full XPS spectra **(A)** of Li anode (back) and AMLA (red) electrodes after cycles. XPS spectra of different element of AMLA: **(B)** N 1s and **(C)** Ag 3d. XPS spectra of different element of Li anode: **(D)** N 1s and **(E)** Ag 3d.

In order to understand the mechanism of performance of the AMLA, we use the XRD to study the surface of the Li anode and AMLA anode after the cycling (**Figure 4k**). Once disassembling the symmetrical cell, the first thing we find that the color of the AMLA anode becomes black from yellow. It means that there are somethings formed on the anode during the cycling. In the XRD spectrum of it, there are some characteristic diffraction peaks of another three main composites except Li, corresponding to the LiAg alloy, Li_3N, and LiN_xO_y, which can be represented:

$$Ag + Li^+ + e^- \rightarrow LiAg \quad (2)$$

$$NO_3^- + Li^+ + e^- \rightarrow LiN_xO_y + Li_3N \quad (3)$$

Equation (2) is the reaction between Li and Ag to form the LiAg alloy on the electrode during cycling. Equation (3) is the decomposition of $LiNO_3$ (Jing et al., 2015), which forms beyond the anode in the electrolyte. Apart from the XRD, we also use the XPS to study the surface of the Li anode and AMLA anode (**Figure 5**). The full XPS spectra (**Figure 5A**) shows: (i) the ration of Li element in the Li anode (2.6%) is lower than in the AMLA anode (10.5%); (ii) the ration of F element in the Li anode (46.0%) is higher than in the AMLA (40.8%); (iii) the peaks of Ag element come on in the AMLA anode. Without $AgNO_3$, the severe interface reaction between the Li anode and electrolyte forms much by-products with F, C, O, and so on, as the higher ratio of F on the surface. In addition, these by-products thicker the SEI film, which will make less Li be detected, as the lower ratio of Li. Moreover, Ag 3d spectrum shows two peaks at binding energy of 367.84 eV for Ag $3d_{5/2}$ and 373.86 eV for Ag $3d_{3/2}$, which means the LiAg alloy is formed (Zhang et al., 2018), shown in the **Figure 5C**. N 1 s (**Figure 5B**) can be assigned to Li_3N (398.94 eV) and LiN_xO_y (407.11 eV), while no LiN_xO_y can be detected in the Li anode (**Figure 5D**) (Yan C. et al., 2016; Zhang et al., 2018). These results are the same as the XRD result in **Figure 4k**, which also further confirm the reaction as the Equations (2) and (3). Due to adding $AgNO_3$ on the surface of the Li anode, we construct outstanding protecting layers with LiAg, LiN_3, and LiN_xO_y. According to the result of the XRD and XPS spectrum, we propose that there is a difunctional protecting layer on the surface of the Li anode to suppress Li dendrites and protect it from being decomposed by electrolyte. This difunctional protecting layer contains the LiAg alloy and the modified SEI by $LiNO_3$. And, it can be explained as the schematic of change on the AMLA anode during charge/discharge progress

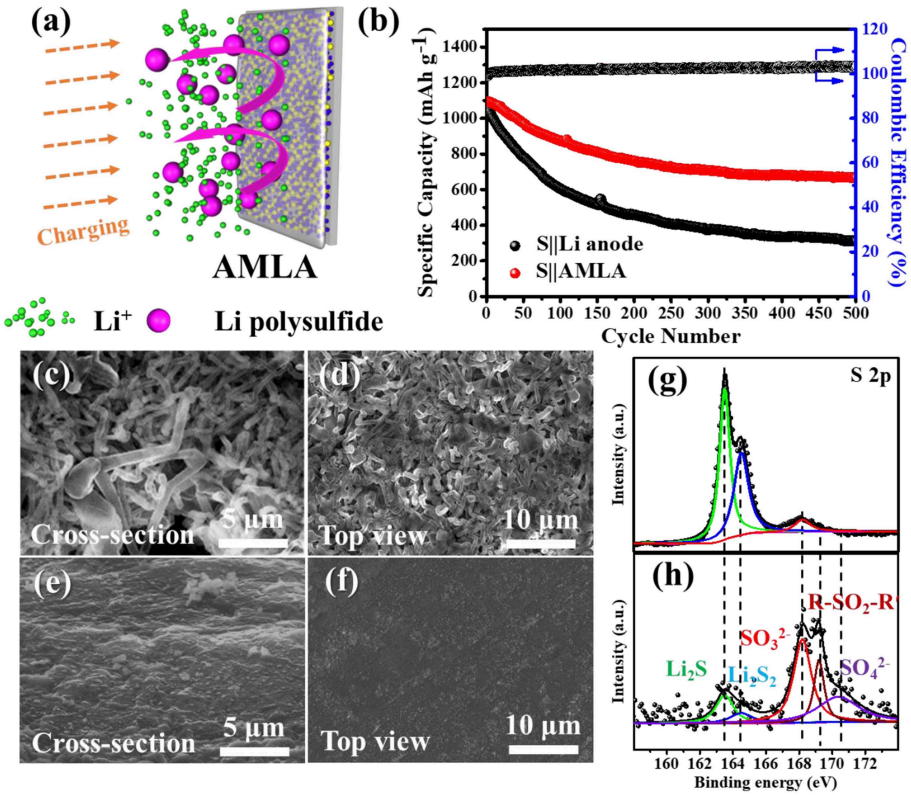

FIGURE 6 | The electrochemical performances of the Li-S cells. **(a)** The schematic of great effect of AMLA in the full cell. **(b)** The cycle performances of S||AMLA and S||Li anode cells under galvanostatic test with the current density 0.5 C (1 C = 1,675 mA g^{-1}). **(c,d)** SEM images of cross-section and top-view of Li anode after cycles. **(e,f)** SEM images of cross-section and top-view of AMLA after cycles. The XPS spectra of S 2p elemental: AMLA **(h)** and Li anode **(g)** electrodes after cycles.

(**Figures 4d,e**). First of all, the LiAg alloy can suppress Li dendrites and maintain the integrity of the SEI film. The metal Ag has a great solubility in Li (9 at.% @ 145.5°C), which means that the metal Ag is lithiophilia. Moreover, the LiAg alloy is formed before the pure Li phase (Yan K. et al., 2016). Thus, the LiAg alloy particles are great nucleation sites of Li, because of the extreme lithiophilia. In addition, the metal Ag has the best conductivity in all of metal as the resistivity of 1.586×10^{-8} Ω·m at 25°C, which makes the LiAg alloy particles have better conduction than the pure Li (Zhang et al., 2018). To sum up, the distribution of the current and the nucleation of Li are uniform as the homogeneously distribution of LiAg nanoparticles. They result in even Li deposition. In addition, the Li diffusion in the phase LiAg alloy ($>10^{-8}$ cm^2 s^{-1}; Ma et al., 2014) is far higher than in the metal Li ($<10^{-10}$ cm^2 s^{-1}; Hiratani et al., 1988), which makes the Li deposit under the LiAg alloy. In a conclusion, the LiAg alloy will form firstly, and then the Li will deposit uniformly under the LiAg alloy (Yan K. et al., 2016), as shown in the **Figure 4j**. The thickness of deposited Li is about 5–10 μm. Hence, the LiAg alloy can suppress the Li dendrites and protect the integrity of SEI with the low expansion volumetric, which makes no violent voltage fluctuation during the cycles of the cell (Terlicka et al., 2019). Secondly, the modified SEI by $LiNO_3$ can protect the Li from electrolyte. The $LiNO_3$ made in the AMLA anode will react with electrolyte to form the Li_3N and LiN_xO_y (Shi et al., 2018). In addition, the great ionic conductivity of Li_3N will make the Li^+ diffuse through the SEI easily (Ma et al., 2014). Above, these two reacted productions will form dense and stable SEI with great ionic conductivity (Shen et al., 2018). Therefore, this SEI protects the Li from the electrolyte, which will prevent the reaction between the electrolyte and Li, thereby reducing electrolyte consumption (Shi et al., 2018). It also hinders the side reaction between the intermediate Li polysulfides (Li_2S_x, $4 \leq x \leq 8$) and the Li anode to decrease the loss of active materials, when the AMLA anode is used in the Li-S battery (**Figure 6a**; Yan C. et al., 2016; Zhang K. et al., 2017).

The electrochemical performances of the Li-S cells are showed in the **Figure 6b**. These cells with different electrodes (the Li anode and AMLA) are tested by galvanostatic at 0.8375 mA cm^{-2} (0.5 C, 1 C = 1,675 mA g^{-1}). As shown, the discharge capacity of Li-S cell with the AMLA anode remains as high as 666.7 mAh g^{-1} and the capacity retention after 500 cycles is 60.8%. However, the cell with the Li anode shows a capacity of 310.8 mAh g^{-1} with a capacity retention of only 29.1%, which is just half of the AMLA. What's more, the morphologies of the AMLA are still smooth without any Li dendrites the same as it in symmetric cells (**Figures 6c–f**). In a conclusion, the protecting layer formed by the $AgNO_3$ can protect the Li electrode by

suppressing the Li dendrites and prolong the cycle lifetime by hindering the corrosion reaction in the Li-S cell. This effect can be furtherly studied by the XPS in the **Figures 6g,h**. S 2p spectrum of the Li anode shows two main peaks at binding energy of 163.49 eV for Li_2S and 164.48 eV for Li_2S_2, which are the reaction products of Li with intermediate Li polysulfides (**Figure 6h**). These two composites decrease the active materials in the S cathode. However, the rations of Li_2S_2 and Li_2S are much lower than SO_3^{2-} (168.11 eV), R-SO_2-R′ (169.12 eV), and SO_4^{2-} (170.37 eV), which are the compositions of the SEI film in the S 2p spectrum of the AMLA (**Figure 6g**). It means that there are negative Li_2S_2 and Li_2S and the corrosion reaction is suppressed. The difunctional protecting layer formed in the AMLA is favorable to suppress the Li dendrites, and protect the Li from the corrosion reaction by the intermediate Li polysulfides at the same time.

CONCLUSIONS

In general, we introduce an effective and simple strategy to improve the Li anode by forming the difunctional protecting layer on the Li anode. The difunctional protecting layer is manufactured through dropping the solution of $AgNO_3$ on the Li anode directly. They suppress the Li dendrites by depositing Li^+ under them uniformly and hinder the Li anode from the electrolyte to suppress the corrosion reaction. Comparing to the Li anode, the AMLA shows superior electrochemical performance with stable overpotential in the symmetric cell and longer cycling lifetime in Li-S battery. The cell with the AMLA can be cycled more than 50 h at 5 mA cm^{-2} with the steady overpotential of lower than 0.2 V. In the Li-S battery, after 500 cycles, the AMLA can still remain the high discharge specific capacity of 666.7 mAh g^{-1} as capacity retention rate of 60.8 % at 0.8375 mA cm^{-2} (0.5 C, 1 C = 1,675 mA g^{-1}). We believe this simple approach can improve the Li anode to offer great guidance for further application of next-generation batteries, such as Li-S batteries.

DATA AVAILABILITY

All datasets generated for this study are included in the manuscript and/or the supplementary material.

AUTHOR CONTRIBUTIONS

CS developed the concept. XL designed the experiments. JG conducted the experiments. ZF and JY built the cells. YZ, ZT, and LS carried out the performance characterizations. CS and KX co-supervised the research. JG and ZF co-wrote the manuscript. All authors discussed the results and commented on the manuscript.

FUNDING

This work was supported by the National Key R&D Program of China (2018YFB0104200).

REFERENCES

An, W., Gao, B., Mei, S., Xiang, B., Fu, J., Wang, L., et al. (2019). Scalable synthesis of ant-nest-like bulk porous silicon for high-performance lithium-ion battery anodes. *Nat. Commun.* 10:1447. doi: 10.1038/s41467-019-09510-5

Bai, M., Xie, K., Yuan, K., Zhang, K., Li, N., Shen, C., et al. (2018). A scalable approach to dendrite-free lithium anodes via spontaneous reduction of spray-coated graphene oxide layers. *Adv. Mater.* 30:e1801213. doi: 10.1002/adma.201801213

Cao, Y., Lu, H., Hong, Q., Xu, B., Wang, J., Deng, Y., et al. (2019). Synthesis of Ag/Co@CoO NPs anchored within N-doped hierarchical porous hollow carbon nanofibers as a superior free-standing cathode for LiO_2 batteries. *Carbon* 144, 280–288. doi: 10.1016/j.carbon.2018.12.048

Chen, L., Li, W., Fan, L. Z., Nan, C. W., and Zhang, Q. (2019). Intercalated electrolyte with high transference number for dendrite-free solid-state lithium batteries. *Adv. Funct. Mater.* 29:1901047. doi: 10.1002/adfm.201901047

Cheng, X. B., Yan, C., Zhang, X. Q., Liu, H., and Zhang, Q. (2018). Electronic and ionic channels in working interfaces of lithium metal anodes. *ACS Energy Lett.* 3, 1564–1570. doi: 10.1021/acsenergylett.8b00526

Cheng, X. B., Zhao, C. Z., Yao, Y. X., Liu, H., and Zhang, Q. (2019). Recent advances in energy chemistry between solid-state electrolyte and safe lithium-metal anodes. *Chem* 5, 74–96. doi: 10.1016/j.chempr.2018.12.002

Choi, N.-S., Lee, Y. M., Cho, K. Y., Ko, D.-H., and Park, J.-K. (2004). Protective layer with oligo(ethylene glycol) borate anion receptor for lithium metal electrode stabilization. *Electrochem. Commun.* 6, 1238–1242. doi: 10.1016/j.elecom.2004.09.023

Hiratani, M., Miyauchi, K., and Kudo, T. (1988). Effect of a lithium alloy layer inserted between a lithium anode and a solid electrolyte. *Solid State Ionics* 28, 1406–1410. doi: 10.1016/0167-2738(88)90394-3

Hou, Z., Yu, Y., Wang, W., Zhao, X., Di, Q., Chen, Q., et al. (2019). Lithiophilic Ag nanoparticle layer on Cu current collector toward stable Li metal anode. *ACS Appl. Mater. Inter.* 11, 8148–8154. doi: 10.1021/acsami.9b01521

Jin, C. B., Sheng, O. W., Luo, J. M., Yuan, H. D., Fang, C., Zhang, W., et al. (2017). 3D lithium metal embedded within lithiophilic porous matrix for stable lithium metal batteries. *Nano Energy* 37, 177–186. doi: 10.1016/j.nanoen.2017.05.015

Jing, G., Wen, Z., Wu, M., Jin, J., and Yu, L. (2015). Vinylene carbonate–$LiNO_3$: a hybrid additive in carbonic ester electrolytes for SEI modification on Li metal anode. *Electrochem. Commun.* 51, 59–63. doi: 10.1016/j.elecom.2014.12.008

Kozen, A. C., Chuan-Fu, L., Pearse, A. J., Schroeder, M. A., Xiaogang, H., Liangbing, H., et al. (2015). Next-generation lithium metal anode engineering via atomic layer deposition. *ACS Nano* 9:5884. doi: 10.1021/acsnano.5b02166

Li, J., Li, Z., Huang, W., Chen, L., Lv, F., Zou, M., et al. (2019). A facile strategy to construct silver-modified, ZnO-incorporated and carbon-coated silicon/porous-carbon nanofibers with enhanced lithium storage. *Small* 15:e1900436. doi: 10.1002/smll.201900436

Li, N., Wei, W., Xie, K., Tan, J., Zhang, L., Luo, X., et al. (2018). Suppressing dendritic lithium formation using porous media in lithium metal-based batteries. *Nano Lett.* 18, 2067–2073. doi: 10.1021/acs.nanolett.8b00183

Li, W., Yao, H., Yan, K., Zheng, G., Liang, Z., Chiang, Y. M., et al. (2015). The synergetic effect of lithium polysulfide and lithium nitrate to prevent lithium dendrite growth. *Nat. Commun.* 6:7436. doi: 10.1038/ncomms8436

Liang, X., Pang, Q., Kochetkov, I. R., Sempere, M. S., Huang, H., Sun, X., et al. (2017). A facile surface chemistry route to a stabilized lithium metal anode. *Nat. Energy* 2:17119. doi: 10.1038/nenergy.2017.119

Liu, F., Xiao, Q., Wu, H. B., Shen, L., Xu, D., Cai, M., et al. (2018). Fabrication of hybrid silicate coatings by a simple vapor deposition method for lithium metal anodes. *Adv. Energy Mater.* 8:1701744. doi: 10.1002/aenm.201701744

Liu, Y., Lin, D., Liang, Z., Zhao, J., Yan, K., and Cui, Y. (2016). Lithium-coated polymeric matrix as a minimum volume-change and dendrite-free lithium metal anode. *Nat. Commun.* 7:10992. doi: 10.1038/ncomms10992

Ma, G., Wen, Z., Wu, M., Shen, C., Wang, Q., Jin, J., et al. (2014). A lithium anode protection guided highly-stable lithium-sulfur battery. *Chem. Commun.* 50, 14209–14212. doi: 10.1039/C4CC05535G

Offor, P. O., Okorie, B. A., Ezema, F. I., Aigbodion, V. S., Daniel-Mkpume, C. C., and Omah, A. D. (2015). Synthesis and characterization of nanocrystalline zinc sulphide thin films by chemical spray pyrolysis. *J. Alloys Compd.* 650, 381–385. doi: 10.1016/j.jallcom.2015.07.169

Pei, A., Zheng, G., Shi, F., Li, Y., and Cui, Y. (2017). Nanoscale nucleation and growth of electrodeposited lithium metal. *Nano Lett.* 17, 1132–1139. doi: 10.1021/acs.nanolett.6b04755

Peng, Z., Wang, S., Zhou, J., Jin, Y., Liu, Y., Qin, Y., et al. (2016). Volumetric variation confinement: surface protective structure for high cyclic stability of lithium metal electrodes. *J. Mater. Chem. A* 4, 2427–2432. doi: 10.1039/C5TA10050J

Shen, C., Yan, H., Gu, J., Gao, Y., Yang, J., and Xie, K. (2018). Li_2O-reinforced solid electrolyte interphase on three-dimensional sponges for dendrite-free lithium deposition. *Front. Chem.* 6:517. doi: 10.3389/fchem.2018.00517

Shi, Q., Zhong, Y., Wu, M., Wang, H., and Wang, H. (2018). High-capacity rechargeable batteries based on deeply cyclable lithium metal anodes. *Proc. Natl. Acad. Sci. U.S.A.* 115, 5676–5680. doi: 10.1073/pnas.1803634115

Shiga, T., Kato, Y., Kondo, H., and Okuda, C. A. (2017). Self-extinguishing electrolytes using fluorinated alkyl phosphates for lithium batteries. *J. Mater. Chem. A* 5, 5156–5162. doi: 10.1039/C6TA09915G

Su, D., Zhou, D., Wang, C., and Wang, G. (2018). Toward high performance lithium-sulfur batteries based on Li_2S cathodes and beyond: status, challenges, and perspectives. *Adv. Funct. Mater.* 28:1800154. doi: 10.1002/adfm.201800154

Taillades, G., and Sarradin, J. (2004). Silver: high performance anode for thin film lithium ion batteries. *J. Power Sources* 125, 199–205. doi: 10.1016/j.jpowsour.2003.07.004

Tao, R., Bi, X., Li, S., Yao, Y., Wu, F., Wang, Q., et al. (2017). Kinetics tuning the electrochemistry of lithium dendrites formation in lithium batteries through electrolytes. *ACS Appl. Mater. Inter.* 9, 7003–7008. doi: 10.1021/acsami.6b13859

Terlicka, S., Debski, A., Budziak, A., Zabrocki, M., and Gasior, W. (2019). Structural and physical studies of the Ag-rich alloys from Ag-Li system. *Thermochim. Acta* 673, 185–191. doi: 10.1016/j.tca.2019.01.016

Wang, G., Xiong, X., Xie, D., Fu, X., Lin, Z., Yang, C., et al. (2019). A scalable approach for dendrite-free alkali metal anodes via room-temperature facile surface fluorination. *ACS Appl. Mater. Inter.* 11, 4962–4968. doi: 10.1021/acsami.8b18101

Wang, G., Xiong, X., Xie, D., Fu, X., Ma, X., Li, Y., et al. (in press). Suppressing dendrite growth by a functional electrolyte additive for robust Li metal anodes. *Energy Storage Mater*. doi: 10.1016/j.ensm.2019.02.026

Wu, X., Li, Y., Zhao, S., Zeng, F., Peng, X., Xiang, Y., et al. (2019). Fabrication of F-doped, C-coated $NiCo_2O_4$ nanocomposites and its electrochemical performances for lithium-ion batteries. *Solid State Ionics* 334, 48–55. doi: 10.1016/j.ssi.2019.01.039

Xie, K., Wei, W., Yuan, K., Lu, W., Guo, M., Li, Z., et al. (2016). Toward dendrite-free lithium deposition via structural and interfacial synergistic effects of 3D graphene@Ni scaffold. *ACS Appl. Mater. Inter.* 8, 26091–26097. doi: 10.1021/acsami.6b09031

Xie, K., Yuan, K., Zhang, K., Shen, C., Lv, W., Liu, X., et al. (2017). Dual functionalities of carbon nanotube films for dendrite-free and high energy-high power lithium-sulfur batteries. *ACS Appl. Mater. Inter.* 9, 4605–4613. doi: 10.1021/acsami.6b14039

Yan, C., Cheng, X. B., Zhao, C. Z., Huang, J. Q., Yang, S. T., and Zhang, Q. (2016). Lithium metal protection through in-situ formed solid electrolyte interphase in lithium-sulfur batteries: The role of polysulfides on lithium anode. *J. Power Sources* 327, 212–220. doi: 10.1016/j.jpowsour.2016.07.056

Yan, K., Lu, Z., Lee, H. W., Xiong, F., Hsu, P. C., Li, Y., et al. (2016). Selective deposition and stable encapsulation of lithium through heterogeneous seeded growth. *Nat. Energy* 1:16010. doi: 10.1038/nenergy.2016.10

Yang, C., Yao, Y., He, S., Xie, H., Hitz, E., and Hu, L. (2017). Ultrafine silver nanoparticles for seeded lithium deposition toward stable lithium metal anode. *Adv. Mater.* 29:1702714. doi: 10.1002/adma.201702714

Zhang, K., Xie, K., Yuan, K., Lu, W., Hu, S., Wei, W., et al. (2017). Enabling effective polysulfide trapping and high sulfur loading via a pyrrole modified graphene foam host for advanced lithium–sulfur batteries. *J. Mater. Chem. A* 5, 7309–7315. doi: 10.1039/C7TA00445A

Zhang, R., Chen, X., Shen, X., Zhang, X. Q., Chen, X. R., Cheng, X. B., et al. (2018). Coralloid carbon fiber-based composite lithium anode for robust lithium metal batteries. *Joule* 2, 764–777. doi: 10.1016/j.joule.2018.02.001

Zhang, R., Chen, X. R., Chen, X., Cheng, X. B., Zhang, X. Q., Yan, C., et al. (2017). Lithiophilic sites in doped graphene guide uniform lithium nucleation for dendrite-free lithium metal anodes. *Angew. Chem. Int. Ed. Engl.* 56, 7764–7768. doi: 10.1002/anie.201702099

Zhang, R., Cheng, X. B., Zhao, C. Z., Peng, H. J., Shi, J. L., Huang, J. Q., et al. (2016). Conductive nanostructured scaffolds render low local current density to inhibit lithium dendrite growth. *Adv. Mater.* 28, 2155–2162. doi: 10.1002/adma.201504117

Zhang, S. S. (2012). Role of $LiNO_3$ in rechargeable lithium/sulfur battery. *Electrochim. Acta* 70, 344–348. doi: 10.1016/j.electacta.2012.03.081

Zheng, G., Lee, S. W., Liang, Z., Lee, H. W., Yan, K., Yao, H., et al. (2014). Interconnected hollow carbon nanospheres for stable lithium metal anodes. *Nat. Nanotechnol.* 9, 618–623. doi: 10.1038/nnano.2014.152

Zhou, C. X., Wang, P. B., Zhang, B., Tang, L. B., Tong, H., He, Z. J., et al. (2019). Formation and effect of residual lithium compounds on Li-rich cathode material $Li_{1.35}[Ni_{0.35}Mn_{0.65}]O_2$. *ACS Appl. Mater. Inter.* 11, 11518–11526. doi: 10.1021/acsami.9b01806

Conflict of Interest Statement: YZ, ZT, and LS were employed by company Shaanxi Coal and Chemical Technology Institute Co., Ltd.

The remaining authors declare that the research was conducted in the absence of any commercial or financial relationships that could be construed as a potential conflict of interest.

frontiers in Chemistry

ORIGINAL RESEARCH
published: 27 August 2019
doi: 10.3389/fchem.2019.00591

Electrochemical Analysis for Enhancing Interface Layer of Spinel $LiNi_{0.5}Mn_{1.5}O_4$ Using p-Toluenesulfonyl Isocyanate as Electrolyte Additive

Zhe Xiao†, Renheng Wang†, Yan Li, Yiling Sun, Shuting Fan, Keyu Xiong, Han Zhang and Zhengfang Qian**

College of Physics and Optoelectronic Engineering, Shenzhen University, Shenzhen, China

OPEN ACCESS

Edited by:
Junchao Zheng,
Central South University, China

Reviewed by:
Zhiqiang Zhu,
Nanyang Technological University, Singapore
Bin Huang,
Guilin University of Technology, China
Zhenjiang He,
Central South University, China

***Correspondence:**
Renheng Wang
wangrh@szu.edu.cn
Zhengfang Qian
zqian2013@qq.com

†*These authors have contributed equally to this work*

Specialty section:
This article was submitted to Electrochemistry, a section of the journal Frontiers in Chemistry

Received: *13 June 2019*
Accepted: *09 August 2019*
Published: *27 August 2019*

Citation:
Xiao Z, Wang R, Li Y, Sun Y, Fan S, Xiong K, Zhang H and Qian Z (2019) Electrochemical Analysis for Enhancing Interface Layer of Spinel $LiNi_{0.5}Mn_{1.5}O_4$ Using p-Toluenesulfonyl Isocyanate as Electrolyte Additive. Front. Chem. 7:591. doi: 10.3389/fchem.2019.00591

$LiNi_{0.}5Mn_{1.5}O_4$ (LNMO) is a potential cathode material for lithium-ion batteries with outstanding energy density and high voltage plateau (>4.7 V). However, the interfacial side reaction between LNMO and the liquid electrolyte seriously causes capacity fading during cycling at the high voltage. Here, p-toluenesulfonyl isocyanate (PTSI) is used as the electrolyte additive to overcome the above problem of LNMO. The results show that the specific capacity of LNMO/Li cell with 0.5 wt.% PTSI at the first cycle is effectively enhanced by 36.0 mAh/g and has better cycling performance than that without PTSI at 4.98 V. Also, a stable solid electrolyte interface (SEI) film derived from PTSI is generated on the electrode surface, which could alleviate the strike of hydrofluoric acid (HF) caused by electrolyte decomposition. These results are explained by the molecular structure of PTSI, which contains SO_3. The S=O groups can delocalize the nitrogen nucleus to block the reactivity of PF_5.

Keywords: lithium ion battery, $LiNi_{0.5}Mn_{1.5}O_4$, p-toluenesulfonyl isocyanate, solid electrolyte interface, electrolyte additive

INTRODUCTION

Over the past few years, the high energy and power density capability of lithium-ion batteries (LIBs) have been interested extremely, due to potential applications in electric vehicles (EVs), hybrid electric vehicles (HEVs), and plug-in hybrid electric vehicles (PHEVs) (Taracson and Armand, 2001; Armand and Tarascon, 2008; Ji et al., 2011; Kim et al., 2012). In order to improve the energy density and power density of batteries, a large number of Li compounds (e.g., olivine-type materials, silicates, Mn-rich, and Ni-rich layered materials) have been studied by researchers all over the world (Chen et al., 2014; Zhang et al., 2014; He et al., 2015a,b; Panchal et al., 2017; Chan et al., 2018; Li et al., 2018; Qiu et al., 2018). Spinel $LiNi_{0.5}Mn_{1.5}O_4$ (LNMO) is a promising material to replace layered $LiCoO_2$ as a cathode for high power density LIBs (Carlier et al., 2003; Su et al., 2017; Sun et al., 2018). LNMO has an high charge-discharge platform (>4.7 V) and outstanding cycling stability (Wang F. et al., 2017). Unfortunately, the high charging voltage (~4.7 V) is higher than the stable voltage of $LiPF_6$-based electrolyte, resulting in rapid oxidation decomposition of the electrolyte and unnecessary secondary reactions at the LNMO/electrolyte interface (Li et al., 2013; Deng et al., 2017; Ma et al., 2019). Furthermore, hydrofluoric acid (HF) derives from hydrolysis

of $LiPF_6$-based electrolyte, which can dissolve Mn^{3+} from LNMO (Xiao et al., 2017). The Mn^{3+} dissolution into the electrolyte causes a cracking solid electrolyte interface (SEI) and reduces rapidly specific capacity, so the LNMO cell exhibits poor cycling peculiarity (Liu et al., 2017; Mou et al., 2018).

One way is to make electrolyte additives form a stable SEI film on the cathode, which inhibits LNMO electrode interface erosion and electrolyte decomposition, scavenging type to capture HF (Haregewoin et al., 2016; Wang et al., in press). As the strong acid produced from $LiPF_6$ is considered the initiator which induces the cleavage and polymerization of cyclic carbonate under high voltage conditions, many researchers are trying to add some oxidation-resistant solvents, for example, sulfones (Hilbig et al., 2017; Su et al., 2017), nitriles (Abu-Lebdeh and Davidson, 2009) and fluoro solvents (Kim et al., 2017). However, when adding the oxidation-resistant solvents there are new problems, including a decrease of conductivity, an increase of viscosity and poor compatibility. Hence, a number of suitable functional additives, such as (pentafluorophenyl) diphenylphosphine (PFPDPP) (Bolloju et al., 2019), dimethyl phenylphosphonite (DMPP) (Mai et al., 2015), tris (trimethylsilyl) phosphite (TMSP) (Wang et al., 2016), triethyl borate (TEB) (Chen et al., 2017), lithium bisoxalatodifluorophosphate (LiBODFP) (Yang et al., 2019), and so on, have been developed to perform better of LIBs under high voltage. As previously reported (Wang R. H. et al., 2015), p-toluenesulfonyl isocyanate (PTSI) has excellent physical and chemical properties because of SO_3 and S=O groups. What's more, the lowest unoccupied molecular orbital (LUMO) (−0.2469 Ha) occupied by PTSI is lower than that by vinylene carbonate (VC, LUMO = −0.2274 Ha) (Xu, 2004; Wu et al., 2012).

In this work, PTSI will be used as an additive for $LiPF_6$-based electrolyte. The main direction of the experiment is to study the SEI film generated between electrolyte and LNMO electrode surface. We hope the PTSI can form a stable SEI film, suppress the corrosion of LNMO electrode by HF, reduce the formation of other products, and improve the circulation ability of LNMO battery at high voltage.

EXPERIMENTAL

Preparation of the Electrolyte

The basic electrolyte (Jiangxi Youli New Materials Co., Ltd., China) was a 1 M (M = mol/L) ethylene carbonate (EC)/ethyl carbonate (EMC)/diethyl carbonate (DEC) $LiPF_6$-based electrolyte in 1:1:1 configuration. The desired concentration 0.5 wt.% of PTSI additive was achieved by dissolving the corresponding amount of PTSI in the base electrolyte and stirring for 5 min in an argon-filled glovebox, and the oxygen and water content were <1 ppm. The supernatant was measured using a Karl Fischer 831 Coulometer (Metrohm) for H_2O and Karl Fischer 798 GPT Titrino (Metrohm) for HF, respectively.

Electrochemical Characterization

LNMO electrodes were prepared from 80 wt.% LNMO powder, 10 wt.% carbon black, and 10 wt.% poly vinylidene fluoride (PVDF). N-methyl pyrrolidinone (NMP) was then added and ground evenly. Next, spread the mixture slurry evenly on the thin aluminum foil and vacuum dry at 120°C for 12 h. The 10 mm diameter electrode disc was then perforated from the coated foil. The LNMO/Li of 2,032 coins were assembled in argon filled ball cases with 2,400 Celgard dividers.

Electrochemical impedance spectroscopies (EIS) of LNMO/Li cells after 1 cycle, 2 cycles, and 3 cycles at 4.98 V were recorded by an electrochemical workstation (CHI660E, Chenhua, Shanghai), and the open-circuit voltages of the cells were set as the initial potential. The frequency range of LNMO/Li cells was 10,000∼0.01 Hz. Cyclic voltammetry (CV) was detected by an electrochemical workstation with five cycles at a sweep rate of 0.1 mV s^{-1}.

Surface Detections of the LNMO Electrode

LNMO/Li cells after cycles were disassembled. First, the LNMO electrode was washed three times with high-purity DMC, and then transferred to a vacuum drying box at 45°C and placed in it for 4 h. The microstructure and morphology of LNMO electrode were recorded by scanning electron microscope (SEM). The surface morphology of LNMO electrode was detected though the transmission electron microscopy (TEM). X-ray photoelectron spectroscopy (XPS) was used to analyze the composition of chemical elements on the surface of LNMO electrode.

RESULTS AND DISCUSSION

Cycling Performance Analyses

It can be clearly seen that the discharge specific capacity of LNMO/Li cell with 0.5 wt.% PTSI was higher than that without additives at the first cycle from in **Figure 1**. From in **Figures 1A,B**, the discharge specific capacity of LNMO/Li cell with additional PTSI reached 143.8 mAh/g, while the discharge specific capacity of the cell without additive is only 107.6 mAh/g. It can be concluded that PTSI additive could improve the initial discharge specific capacity of LNMO/Li cell. What's more, the specific capacity of LNMO/Li cell with 0.5 wt.% PTSI added after 40 cycles was much higher than that of LNMO/Li cell without additive. This also reflected that PTSI can indeed improve the specific capacity of LNMO/Li cell and provide a new scheme for improving the energy density of LIBs. In addition, the coulomb efficiency of the battery was constantly improved maintained a high level, as shown in **Figure 1C**. The coulomb efficiency of LNMO/Li cell without additives is 96% at the 40th cycle, while LNMO/Li cell with 0.5 wt.% PTSI added reached 99%. This indicated that the PISI additive can improve the coulomb efficiency during the charging/discharging cycle of LNMO/Li cell.

Impedance Analysis

In order to explore the interface impedance of SEI film between electrolyte and LNMO electrode, EIS of LNMO/Li cells with 0.5 wt.% PTSI and with no additive were recorded, as shown in **Figure 2**. In impedance spectroscopy, the semicircular high frequency region represents the migration of lithium ions through the interface at the surface of the LNMO electrode, and the center frequency range of the semicircle corresponds to the charge transfer process (Zhao et al., 2018). The results

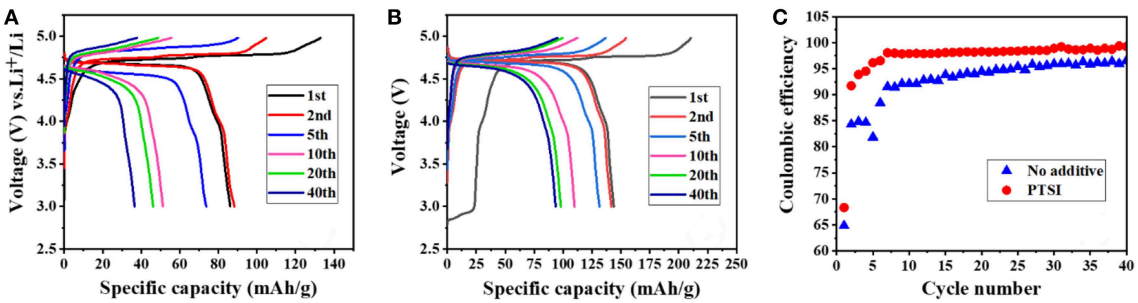

FIGURE 1 | (A,B) Cycling performance of LNMO/Li cells at different cycles with no additive and with 0.5 wt.% PTSI additive in a voltage range of 3.0–4.98 V; **(C)** Coulombic efficiency of LNMO/Li cells with no additive and with 0.5 wt.% PTSI.

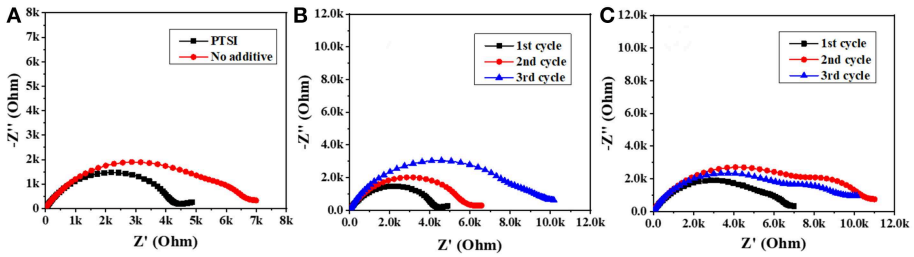

FIGURE 2 | Impedance spectrum of LNMO/Li cells: **(A)** after 1 cycle; **(B)** the first three cycles with 0.5 wt.% PTSI; **(C)** the first three cycles with no additive.

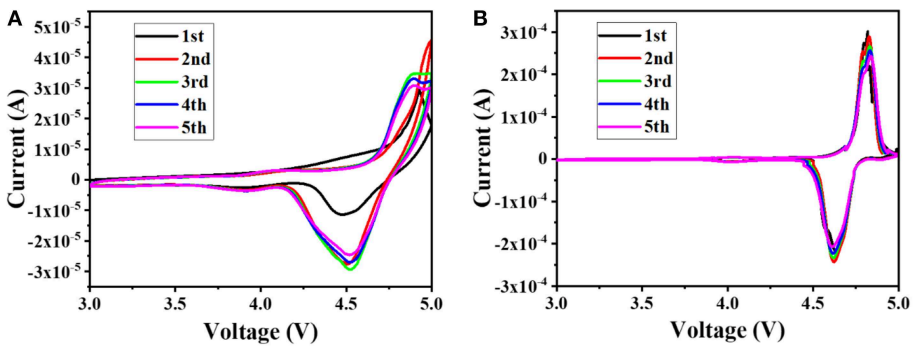

FIGURE 3 | CVs of Li/LNMO cell with no additive **(A)** and with 0.5 wt.% PTSI **(B)**, at a sweep rate of 0.1 mV s^{-1}.

show that the interfacial impedance of LNMO electrode with 0.5 wt.% PTSI additive is significantly lower than that of LNMO electrode with no additive, suggesting that the surface of the LNMO electrode with 0.5 wt.% PTSI is improved. What is more, the two semicircles in the impedance spectra with 0.5 wt.% PTSI are significantly reduced compared with those with no additive. As the number of cycles increases, the impedance change of LNMO electrode with the addition of PTSI is much smaller than that of the LNMO electrode with no additive. In the lithiation/delithiation process, the surface layer impedance reduction and charge transfer will reduce ohmic polarization and activation polarization, which also confirms the above superior cyclic performance of the LNMO/Li cells with 0.5 wt.% PTSI.

CV Measurements

In order to better understand the effect of the additive PTSI on the LNMO cell, the battery was subjected to the CV measurements at a sweep rate of 0.1 mV s^{-1} at 25°C, and the results are shown in **Figure 3**. It can be seen from the figure that there is a major redox peak at around 4.7 V, which corresponds to the redox process of Ni^{2+} and Ni^{4+}(Talyosef et al., 2005). According to the comparison of **Figures 3A,B**, the peak current of the Li/LNMO cell to which 0.5 wt.% of PTSI was added is significantly larger than the peak current of the Li/LNMO cell without additives. In addition, the potential difference between the two peaks in the CV diagram of the LNMO cell to which PTSI was added is small, and as the number of cycles increases,

the coincidence degree of the CV measurements pattern of the LNMO cells to which the PTSI was added is higher, indicating that the addition of PTSI makes the circulation of the LNMO cell more stable.

SEM and TEM Analyses

To further study the effect of additive PTSI on the performance of LNMO electrode, SEM tests were carried out on the fresh electrode and the cycled LNMO electrode, as shown in **Figure 4**. The surface of the fresh electrode is very smooth and clean, without sediments, while the cycled LNMO electrodes show very different surface morphology. Compared to the fresh LNMO electrode, the surface of LNMO electrode with no additive is not smooth, which is coated with thick materials. Therefore, it increases the surface area, leading to an interface reaction that affects the transport of Li^+ through the electrode. In contrast, the surface of the cycled LNMO electrode with 0.5 wt.% PTSI shows smooth and flat, forming thin materials on the surface. The relatively low viscosity of the additive PTSI improves permeability of electrolytes to LNMO electrode (Wang R. et al., 2015). Meanwhile, the reduction potential of PTSI was higher than carbonate solvents, which hinders the solvent decomposition in $LiPF_6$-based electrolyte.

In addition, in order to better describe the effect of additive PTSI on LNMO electrode, the corresponding TEM images of LNMO electrode after 40 cycles were obtained in **Figure 5**. It can be clearly seen that the LNMO electrode with 0.5 wt.% PTSI has a relatively clear layer boundary, which is the SEI film (∼3 nm) generated on the surface of the electrode. The film is dense and uniform, which can effectively protect the LNMO electrode. However, a very uneven and thick SEI film (∼12 nm) is generated on the LNMO electrode with no additive, which will slow down the transfer of Li^+ between electrolyte and electrode. It markedly indicates that the decomposition of electrolyte, as well as the electrode erosion from the electrolyte with no additive, is more serious.

XPS Analysis

In order to verify the specific elements of surface layer about fresh electrode, non-additive electrode and the electrode with 0.5 wt.% PTSI after 40 cycles were detected by XPS in **Figure 6**. The C 1s spectra have four main peaks: C-C bond from the carbon black (284.1 eV), C-H bond roots in lithium alkyl carbonates (R-CH_2OCO_2-Li) and PVDF (286.0 eV), C=O bond belongs to lithium alkyl carbonates (R-CH_2OCO_2-Li) and polycarbonates (287.6 eV), and Li_2CO_3 (290.1 eV) (Funabiki et al., 1997; Levi et al., 2000; Dedryvere et al., 2010; An et al., 2016; Wang R. H. et al., 2015). It can be seen that the strength of Li_2CO_3 on the surface of LNMO electrode with 0.5 wt.% PTSI is significantly weaker than that on the surface of LNMO electrode with no additive, indicating the inhibitory effect of PTSI on electrolyte decomposition.

The O 1s spectrum displays five different peaks, including C-O peak (532.8 eV), Mn-O bond (529.7 eV), Li_2CO_3 (531.8 eV), C=O bond (532.4 eV), and C-O-C bond in lithium alkyl carbonates (R-CH_2OCO_2-Li) (533.8 eV) (Dedryvère et al., 2005; Bae et al., 2014; Wang et al., 2016). After PTSI was added, the C=O bond energy intensity increased, indicating that the polarization of EC and DEC solvents is effectively inhibited. In addition, Li_2CO_3 peak with no additive is stronger. That is, there are many inorganic decomposition products on the surface of the LNMO electrode with no additive.

In the F 1s spectrum, there is a significant difference between the two electrodes after cycling in different electrolytes. The

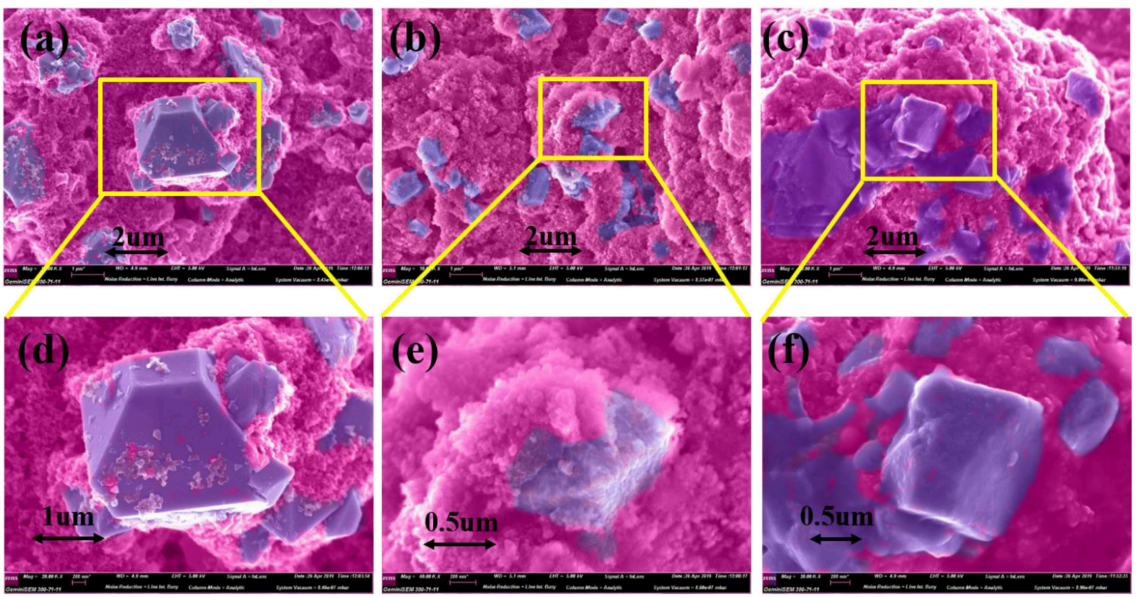

FIGURE 4 | SEM images of LNMO electrodes with different electrolytes after 40 cycles: **(a,d)** fresh, **(b,e)** with no additive, and **(c,f)** with 0.5 wt.% PTSI.

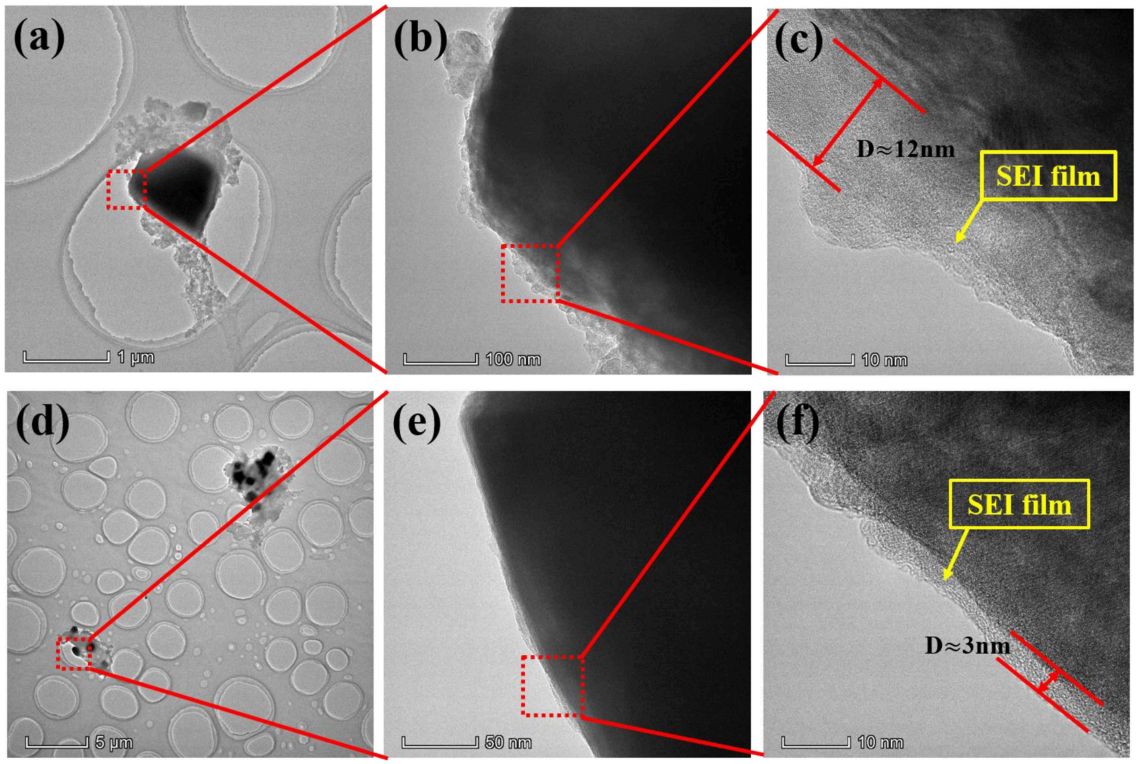

FIGURE 5 | TEM images of LNMO electrodes after 40 cycles: **(a–c)** no additive and **(d–f)** with 0.5 wt.% PTSI.

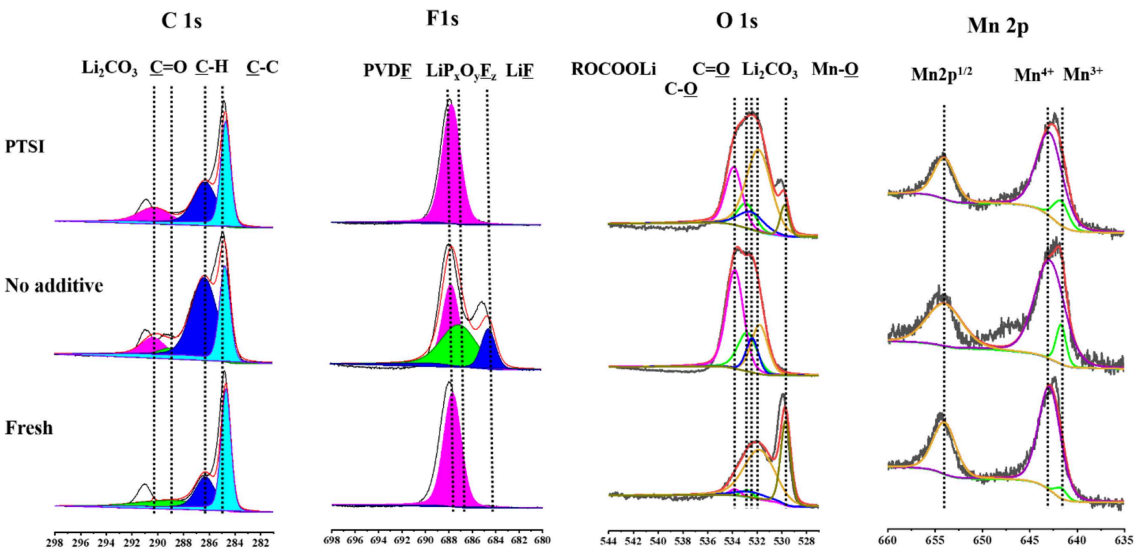

FIGURE 6 | XPS survey spectra of LNMO electrode with 0.5 wt.% PTSI and with no additive after 40 cycles.

peak strength of LiF (684.5 eV) and PVDF (687.7 eV) with 0.5 wt.% PTSI was significantly lower than that with no additive (Park et al., 2010; Zhou et al., 2011), indicating that there are few inorganic products on the electrode surface. When LiF content in the SEI film increasing, it will cause erosion to the electrode and inhibit the transport of Li ions. Hence, the impedance of LNMO electrode surface will increase accordingly. So, the SEI film generated by PTSI enhances the electrical charge transfer channel between LNMO electrode and electrolyte.

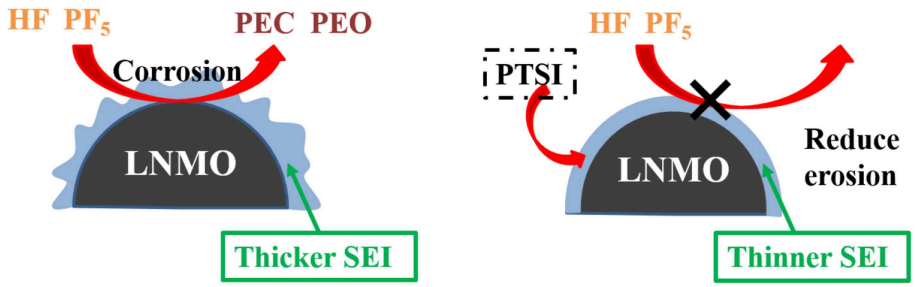

FIGURE 7 | Schematic illustration of the effect of the electrolyte without and with PTSI additives on the LNMO cathode surface.

In the Mn 2p spectrum, there are three main characteristic peaks, which belong to Mn^{3+} (641.7 eV), Mn^{4+} (642.9 eV), and Mn $2p^{1/2}$ (653.6 eV) (Treuil et al., 1999). It is found that the Mn^{3+} peak strength of no additive electrolyte is lower than that of PTSI additive electrolyte, suggesting that HF causes the erosion of LNMO electrode surface.

In conclusion, SEM, TEM, and XPS indicate that the SEI film of LNMO electrode with 0.5 wt.% PTSI is thinner than that of LNMO electrode with no additive. The optimization of SEI film can greatly promote the transport of Li^+ to a large extent and inhibit the oxidation decomposition of electrolyte, which can prevent the product from damaging the electrode.

The Proposed Mechanism for LNMO/Electrolyte Interface Film

According to the above analysis, a schematic diagram of SEI film formation on the surface of LNMO electrode is obtained, as shown in **Figure 7**. Compared with the alkyl carbonic (Li_2CO_3 and $ROCO_2Li$) generated by EC, the decomposition products (Li_2SO_3, Li_2S, and $ROSO_2Li$) formed by the additive PTSI are relatively more stable, which inhibits HF to corrode the surface of LNMO electrode and reduces interface impedance (Wang R. et al., 2017). Therefore, the diffusion of Li^+ across the surface of LNMO was enhanced.

PF_5 acted as a catalyst for the oxidation and corrosion of electrolyte, and could guide the reaction path of electrolyte to HF and H_2O (Sloop et al., 2003). What's more, PF_5 decomposed into EC and DEC. The open-loop reaction of EC was catalyzed by PF_5, which leads to the polymerization of the reaction to produce polyethylene carbonate (PEC) and polyethylene oxide (PEO) similar products. As PF_5 lack electrons, PTSI contains many electrons, including the S=O group, which caused the nitrogen nucleus to be delocalized and the weak base to be sited as inhibiting PF_5 reactivity (Wu et al., 2012; Wang R. H. et al., 2015). The HF generated and LiF formed from $LiPF_6$ will be inhibited. The SEI film formed on the surface of the LNMO electrode can reduce the interfacial resistance between LNMO and electrolyte.

What's more, PTSI played an important role in the development of SEI film, which successfully prevented HF from passing through the modified film to corrode the LNMO electrode. By reducing the reaction between PF_5 and electrolyte, the content of LiF in the SEI film was reduced and the formation of HF was inhibited. The results show that PTSI can significantly inhibit the degree of oxidative decomposition of carbonate solvent during LNMO/Li cell cycle. It is concluded that PTSI is used as electrolyte additive for LNMO electrode at a high range voltage of 3.0–4.98 V.

CONCLUSIONS

In this work, we report a electrolyte based on 1 M $LiPF_6$ EC/EMC/DEC (1:1 by wt.%) with 0.5 wt.% PTSI for LNMO/Li. Electrochemical tests, EIS, CV, SEM, TEM, and XPS display that the decomposition of carbonate solvent has been inhibited and a dense SEI film on the electrode surface is formed. The electrolyte using PTSI as a non-aqueous electrolyte additive has good electrochemical stability at high voltages 4.98 V. The SEI film generated from PTSI is a stable protective layer, which inhibits HF erosion and reduces the interface resistance. As a result, LNMO/Li cells show excellent cycling performance.

DATA AVAILABILITY

All datasets generated for this study are included in the manuscript/supplementary files.

AUTHOR CONTRIBUTIONS

ZX, RW, and ZQ designed and engineered the samples. ZX and RW performed the experiments. ZX, RW, YL, YS, SF, KX, HZ, and ZQ performed the data analysis. ZX, RW, and ZQ wrote the paper. All authors contributed to the theoretical analysis and the general discussion.

FUNDING

The work was supported by the National Science Foundation for Young Scientists of China (Grant No. 51804199), the Science and Technology Innovation Commission of Shenzhen (Grant No. 20180123), and the National Natural Science Fund (Grant No. 61435010).

ACKNOWLEDGMENTS

Authors acknowledge the supports from Instrumental Analysis Center of Shenzhen University (Xili Campus) and Shenzhen Institute of Information Technology. The authors also wish to acknowledge the assistance on SEM and TEM observations received from the Electron Microscope Center of the Shenzhen University.

REFERENCES

Abu-Lebdeh, Y., and Davidson, I. (2009). High-voltage electrolytes based on adiponitrile for Li-ion batteries. *J. Electrochem. Soc.* 156, A60–A65. doi: 10.1149/1.3023084

An, S. J., Li, J., Sheng, Y., Daniel, C., and Wood, D. L. (2016). Long-term lithium-ion battery performance improvement via ultraviolet light treatment of the graphite anode. *J. Electrochem. Soc.* 163, A2866–A2875. doi: 10.1149/2.0171614jes

Armand, M., and Tarascon, J. M. (2008). Building better batteries. *Nature* 451:652. doi: 10.1038/451652a

Bae, S. Y., Shin, W. K., and Kim, D. W. (2014). Protective organic additives for high voltage $LiNi_{0.5}Mn_{1.5}O_4$ cathode materials. *Electrochim. Acta* 125, 497–502. doi: 10.1016/j.electacta.2014.01.124

Bolloju, S., Chiou, C. Y., Vikramaditya, T., and Lee, J. T. (2019). (Pentafluorophenyl) diphenylphosphine as a dual-functional electrolyte additive for $LiNi_{0.5}Mn_{1.5}O_4$ cathodes in high-voltage lithium-ion batteries. *Electrochim. Acta* 299, 663–671. doi: 10.1016/j.electacta.2019.01.037

Carlier, D., Van der Ven, A., Delmas, C., and Ceder, G. (2003). First-principles investigation of phase stability in the O_2-$LiCoO_2$ system. *Chem. Mater.* 15, 2651–2660. doi: 10.1021/cm030002t

Chan, Z. M., Kitchaev, D. A., Weker, J. N., Schnedermann, C., Lim, K., Ceder, G., et al. (2018). Electrochemical trapping of metastable Mn3+ ions for activation of MnO2 oxygen evolution catalysts. *Proc. Natl. Acad. Sci. U.S.A.* 115, E5261–E5268. doi: 10.1073/pnas.1722235115

Chen, Y., Chen, Z., and Xie, K. (2014). Effect of annealing on the first-cycle performance and reversible capabilities of lithium-rich layered oxide cathodes. *J. Phys. Chem. C* 118, 11505–11511. doi: 10.1021/jp500138s

Chen, Z., Wang, C., Xing, L., Wang, X., Tu, W., Zhu, Y., et al. (2017). Borate electrolyte additives for high voltage lithium nickel manganese oxide electrode: a comparative study. *Electrochim. Acta* 249, 353–359. doi: 10.1016/j.electacta.2017.08.027

Dedryvere, R., Foix, D., Franger, S., Patoux, S., Daniel, L., and Gonbeau, D. (2010). Electrode/electrolyte interface reactivity in high-voltage spinel $LiMn_{1.6}Ni_{0.4}O_4$/$Li_4Ti_5O_{12}$ lithium-ion battery. *J. Phys. Chem. C* 114, 10999–11008. doi: 10.1021/jp1026509

Dedryvère, R., Gireaud, L., Grugeon, S., Laruelle, S., Tarascon, J. M., and Gonbeau, D. (2005). Characterization of lithium alkyl carbonates by X-ray photoelectron spectroscopy: experimental and theoretical study. *J. Phys. Chem. B* 109, 15868–15875. doi: 10.1021/jp051626k

Deng, S., Xiao, B., Wang, B., Li, X., Kaliyappan, K., Zhao, Y., et al. (2017). New insight into atomic-scale engineering of electrode surface for long-life and safe high voltage Lithium ion cathodes. *Nano Energy* 38, 19–27. doi: 10.1016/j.nanoen.2017.05.007

Funabiki, A., Inaba, M., and Ogumi, Z. (1997). Ac impedance analysis of electrochemical lithium intercalation into highly oriented pyrolytic graphite. *J. Power Sources* 68, 227–231. doi: 10.1016/S0378-7753(96)02556-6

Haregewoin, A. M., Wotango, A. S., and Hwang, B. J. (2016). Electrolyte additives for lithium ion battery electrodes: progress and perspectives. *Energy Environ. Sci.* 9, 1955–1988. doi: 10.1039/C6EE00123H

He, Z., Wang, Z., Chen, H., Huang, Z., Li, X., and Guo, H., et al. (2015a). Electrochemical performance of zirconium doped lithium rich layered $li_{1.2}Mn_{0.54}Ni_{0.13}Co_{0.13}O_2$ oxide with porous hollow structure. *J. Power Sources* 299, 334–341. doi: 10.1016/j.jpowsour.2015.09.025

He, Z., Wang, Z., Huang, Z., Hao, C., Li, X., and Guo, H. (2015b). A novel architecture designed for lithium rich layered $Li[Li_{0.2}Mn_{0.54}Ni_{0.13}Co_{0.13}]O_2$ oxides for lithium-ion batteries. *J. Mater. Chem. A* 3, 16817–16823. doi: 10.1039/C5TA04424C

Hilbig, P., Ibing, L., Wagner, R., Winter, M., and Cekic-Laskovic, I. (2017). Ethyl methyl sulfone-based electrolytes for lithium ion battery applications. *Energies* 10:1312. doi: 10.3390/en10091312

Ji, L., Lin, Z., Alcoutlabi, M., and Zhang, X. (2011). Recent developments in nanostructured anode materials for rechargeable lithium-ion batteries. *Energy Environ. Sci.* 4, 2682–2699. doi: 10.1039/c0ee00699h

Kim, J., Go, N., Kang, H., Tron, A., and Mun, J. (2017). Effect of fluoroethylene carbonate in the electrolyte for $LiNi_{0.5}Mn_{1.5}O_4$ cathode in lithium-ion batteries. *J. Electrochem. Sci. Technol.* 8, 53–60. doi: 10.5229/JECST.2017.8.1.53

Kim, T. H., Park, J. S., Chang, S. K., Choi, S., Ryu, J. H., and Song, H. K. (2012). The current move of lithium ion batteries towards the next phase. *Adv. Energy Mater.* 2, 860–872. doi: 10.1002/aenm.201200028

Levi, M. D., Gamolsky, K., Aurbach, D., Heider, U., and Oesten, R. (2000). On electrochemical impedance measurements of $LixCo_{0.2}Ni_{0.8}O_2$ and $LixNiO_2$ intercalation electrodes. *Electrochim. Acta* 45, 1781–1789. doi: 10.1016/S0013-4686(99)00402-8

Li, J., Baggetto, L., Martha, S. K., Veith, G. M., Nanda, J., Liang, C., et al. (2013). An artificial solid electrolyte interphase enables the use of a $LiNi_{0.5}$ $Mn_{1.5}$ O_4 5V cathode with conventional electrolytes. *Adv. Energy Mater.* 3, 1275–1278. doi: 10.1002/aenm201300378

Li, Z., Zhao, H., Lv, P., Zhang, Z., Zhang, Y., Du, Z., et al. (2018). Watermelon-like structured SiO_x-TiO_2@C nanocomposite as a high-performance lithium-ion battery anode. *Adv. Funct. Mater.* 28:1605711. doi: 10.1002/adfm.201605711

Liu, W., Shi, Q., Qu, Q., Gao, T., Zhu, G., Shao, J., et al. (2017). Improved Li-ion diffusion and stability of a $LiNi_{0.5}Mn_{1.5}O_4$ cathode through *in situ* co-doping with dual-metal cations and incorporation of a superionic conductor. *J. Mater. Chem. A* 5, 145–154. doi: 10.1039/C6TA08891K

Ma, Y., Chen, K., Ma, J., Xu, G., Dong, S., Chen, B., et al. (2019). A biomass based free radical scavenger binder endowing a compatible cathode interface for 5V lithium-ion batteries. *Energy Environ. Sci.* 12, 273–280. doi: 10.1039/C8EE02555J

Mai, S., Xu, M., Liao, X., Xing, L., and Li, W. (2015). Improving cyclic stability of lithium nickel manganese oxide cathode at elevated temperature by using dimethyl phenylphosphonite as electrolyte additive. *J. Power Sources* 273, 816–822. doi: 10.1016/j.jpowsour.2014.09.171

Mou, J., Deng, Y., Song, Z., Zheng, Q., Lam, K. H., and Lin, D. (2018). Excellent rate capability and cycling stability in Li^+-conductive Li_2SnO_3-coated $LiNi_{0.5}Mn_{1.5}O_4$ cathode materials for lithium-ion batteries. *Dalton Transac.* 47, 7020–7028. doi: 10.1039/C8DT00014J

Panchal, S., Mcgrory, J., Kong, J., Fraser, R., Fowler, M., Dincer, I., et al. (2017). Cycling degradation testing and analysis of a $LiFePO_4$ battery at actual conditions. *Int. J. Energy Res.* 41, 2565–2575. doi: 10.1002/er.3837

Park, J. H., Kim, J. S., Shim, E. G., Park, K. W., Hong, Y. T., Lee, Y. S., et al. (2010). Polyimide gel polymer electrolyte-nanoencapsulated $LiCoO_2$ cathode materials for high-voltage Li-ion batteries. *Electrochem. Commun.* 12, 1099–1102. doi: 10.1016/j.elecom.2010.05.038

Qiu, H., Wang, Y., and Ye, S. (2018). Rationally-directed synthesis and characterization of nickel-rich cathode material for lithium ion battery. *Energy Technol.* 6, 2419–2428. doi: 10.1002/ente.201800415

Sloop, S. E., Kerr, J. B., and Kinoshita, K. (2003). The role of li-ion battery electrolyte reactivity in performance decline and self-discharge. *J. Power Sources* 119–121, 330–337. doi: 10.1016/S0378-7753(03)00149-6

Su, C. C., He, M., Redfern, P. C., Curtiss, L. A., Shkrob, I. A., and Zhang, Z. (2017). Oxidatively stable fluorinated sulfone electrolytes for high voltage high energy lithium-ion batteries. *Energy Environ. Sci.* 10, 900–904. doi: 10.1039/C7EE00035A

Sun, W., Li, Y., Liu, Y., Guo, Q., Luo, S., Yang, J., et al. (2018). Hierarchical waxberry-like $LiNi_{0.5}Mn_{1.5}O_4$ as an advanced cathode material for lithium-ion batteries with a superior rate capability and long-term cyclability. *J. Mater. Chem. A* 6, 14155–14161. doi: 10.1039/C8TA04572K

Talyosef, Y., Markovsky, B., Salitra, G., Aurbach, D., Kim, H. J., and Choi, S. (2005). The study of $LiNi_{0.5}Mn_{1.5}O_4$ 5V cathodes for Li-ion batteries. *J. Power Sources* 146, 664–669. doi: 10.1016/j.jpowsour.2005.03.064

Taracson, J. M., and Armand, M. (2001). Issues and challenges facing lithium ion batteries. *Nature* 414, 359–367. doi: 10.1038/35104644

Treuil, N., Labrugère, C., Menetrier, M., Portier, J., Campet, G., Deshayes, A., et al. (1999). Relationship between chemical bonding nature and electrochemical property of $LiMn_2O_4$ spinel oxides with various particle sizes:"electrochemical grafting" concept. *J. Phys. Chem. B* 103, 2100–2106. doi: 10.1021/jp984316t

Wang, F., Suo, L., Liang, Y., Yang, C., Han, F., Gao, T., et al. (2017). Spinel $LiNi_{0.5}Mn_{1.5}O_4$ cathode for high-energy aqueous lithium-ion batteries. *Adv. Energy Mater.* 7:1600922. doi: 10.1002/aenm.201600922

Wang, G., Xiong, X., Xie, D., Fu, X., Ma, X., Li, Y., et al. (in press). Suppressing dendrite growth by a functional electrolyte additive for robust Li metal anodes. *Energy Storage Mater.* doi: 10.1016/j.ensm.2019.02.026

Wang, R., Li, X., Wang, Z., Guo, H., and Wang, J. (2015). Electrochemical analysis for cycle performance and capacity fading of lithium manganese oxide spinel cathode at elevated temperature using p-toluenesulfonyl isocyanate as electrolyte additive. *Electrochim. Acta* 180, 815–823. doi: 10.1016/j.electacta.2015.09.019

Wang, R., Li, X., Wang, Z., and Zhang, H. (2017). Electrochemical analysis graphite/electrolyte interface in lithium-ion batteries: p-Toluenesulfonyl isocyanate as electrolyte additive. *Nano Energy* 34, 131–140. doi: 10.1016/j.nanoen.2017.02.037

Wang, R. H., Li, X. H., Wang, Z. X., Guo, H. J., and He, Z. J. (2015). Electrochemical analysis for enhancing interface layer of spinel $Li_4Ti_5O_{12}$: p-toluenesulfonyl isocyanate as electrolyte additive. *ACS Appl. Mater. Interfaces* 7, 23605–23614. doi: 10.1021/acsami.5b07047

Wang, Z., Xing, L., Li, J., Xu, M., and Li, W. (2016). Triethylborate as an electrolyte additive for high voltage layered lithium nickel cobalt manganese oxide cathode of lithium ion battery. *J. Power Sources* 307, 587–592. doi: 10.1016/j.jpowsour.2015.11.091

Wu, F., Xiang, J., Li, L., Chen, J., Tan, G., and Chen, R. (2012). Study of the electrochemical characteristics of sulfonyl isocyanate/sulfone binary electrolytes for use in lithium-ion batteries. *J. Power Sources* 202, 322–331. doi: 10.1016/j.jpowsour.2011.11.065

Xiao, B., Liu, H., Liu, J., Sun, Q., Wang, B., Kaliyappan, K., et al. (2017). Nanoscale manipulation of spinel lithium nickel manganese oxide surface by multisite Ti occupation as high-performance cathode. *Adv. Mater.* 29:1703764. doi: 10.1002/adma.201703764

Xu, K. (2004). Nonaqueous liquid electrolytes for lithium-based rechargeable batteries. *Chem. Rev.* 104, 4303–4418. doi: 10.1021/cr03 0203g

Yang, T., Zeng, H., Wang, W., Zhao, X., Fan, W., Wang, C., et al. (2019). Lithium bisoxalatodifluorophosphate (LiBODFP) as a multifunctional electrolyte additive for 5 V $LiNi_{0.5}Mn_{1.5}O_4$-based lithium-ion batteries with enhanced electrochemical performance. *J. Mater. Chem. A* 7, 8292–8301. doi: 10.1039/C9TA01293A

Zhang, H. Z., Qiao, Q. Q., Li, G. R., and Gao, X. P. (2014). PO_4 3–polyanion-doping for stabilizing Li-rich layered oxides as cathode materials for advanced lithium-ion batteries. *J. Mater. Chem. A* 2, 7454–7460. doi: 10.1039/C4TA00699B

Zhao, D., Wang, P., Zhao, Q., Li, S., and Zhou, Z. (2018). Improvement of interfacial stability for $LiNi_{0.5}Mn_{1.5}O_4$ cathode: insight into the effect and mechanism of additive with special structure. *Energy Technol.* 6, 2450–2460. doi: 10.1002/ente.201800339

Zhou, L., Dalavi, S., Xu, M., and Lucht, B. L. (2011). Effects of different electrode materials on the performance of lithium tetrafluorooxalatophosphate (LiFOP) electrolyte. *J. Power Sources* 196, 8073–8084. doi: 10.1016/j.jpowsour.2011.04.061

Conflict of Interest Statement: The authors declare that the research was conducted in the absence of any commercial or financial relationships that could be construed as a potential conflict of interest.

frontiers in Chemistry

ORIGINAL RESEARCH
published: 18 October 2019
doi: 10.3389/fchem.2019.00689

Facile One-Step Hydrothermal Synthesis of $Na_3V_2(PO_4)_2F_3$@C/CNTs Tetragonal Micro-Particles as High Performance Cathode Material for Na-Ion Batteries

Hao Guo[1,2], *Yong Hu*[1], *Xiaoping Zhang*[1], *Rongliang Zhang*[2], *Dong Hou*[1]*, *Yulei Sui*[1] and *Ling Wu*[1]*

[1] School of Iron and Steel, Soochow University, Suzhou, China, [2] Zhangjiagang Campus School of Metallurgical and Material Engineering, Jiangsu University of Science and Technology, Zhenjiang, China

OPEN ACCESS

Edited by:
Junchao Zheng,
Central South University, China

Reviewed by:
Yunjian Liu,
Jiangsu University, China
Qiaobao Zhang,
Xiamen University, China
Lingjun Li,
Changsha University of Science and Technology, China

***Correspondence:**
Dong Hou
houdong0702@suda.edu.cn
Ling Wu
lwu@suda.edu.cn

Specialty section:
This article was submitted to Electrochemistry, a section of the journal Frontiers in Chemistry

Received: 04 August 2019
Accepted: 07 October 2019
Published: 18 October 2019

Citation:
Guo H, Hu Y, Zhang X, Zhang R, Hou D, Sui Y and Wu L (2019) Facile One-Step Hydrothermal Synthesis of $Na_3V_2(PO_4)_2F_3$@C/CNTs Tetragonal Micro-Particles as High Performance Cathode Material for Na-Ion Batteries. Front. Chem. 7:689. doi: 10.3389/fchem.2019.00689

In this paper, we report a facile one-step hydrothermal method to synthesize tetragonal $Na_3V_2(PO_4)_2F_3$@C particles which are connected by carbon nanotubes (CNTs) networks, using water as hydrothermal solvents. In this strategy, the reduction and crystallization of materials are carried out in the hydrothermal process (180°C, 12 h), no additional heat treatment is required. The well-crystallized $Na_3V_2(PO_4)_2F_3$ tetragonal grains (5–10 μm) are coated with amorphous nano-carbon and connected by highly conductive CNTs. The addition of CNTs can not only improve the conductivity of materials but also effectively inhibit the $Na_3V_2(PO_4)_2F_3$ grains over growth. The $Na_3V_2(PO_4)_2F_3$@C/CNTs composite possesses very flat charge/discharge platforms of 3.6 and 4.1 V. The sample exhibits an initial discharge specific capacity of 120.2 and 74.3 mAh g^{-1} at 0.1 and 10 C rate, respectively, and shows excellent cyclical stability. The composite owns excellent electrochemical performances owing to the three-dimensional highly conductive network which is co-constructed by the CNTs and nano-carbon coating layer.

Keywords: Na-ion batteries, cathode materials, $Na_3V_2(PO_4)_2F_3$, carbon nanotubes, hydrothermal

INTRODUCTION

Recently years, sodium-ion batteries (SIBs) have been receiving great attention due to the low cost and abundant sodium resource. At present, the cathode materials of SIBs mainly include the transition metal oxides (Na_xMeO_2, Me = Fe, Mn, Co, Ni, and V, etc.) (Delmas et al., 1981; Doeff et al., 1994; Guignard et al., 2013; Vassilaras et al., 2013; Chen et al., 2017, 2018), polyanionic compounds ($Na_3V_2(PO_4)_3$, $Na_3V_2(PO_4)_2F_3$, and Na_2MnPO_4F, etc.) (Xie et al., 2017; Wu et al., 2018a,b; Zheng et al., 2018; Ge et al., 2019; Leng et al., 2019) and Prussian blue compounds ($A_xM_A[M_B(CN)_6]\cdot yH_2O$) (Qian et al., 2012; Lee et al., 2013; Wang et al., 2013; Yue et al., 2014). Among these materials, $Na_3V_2(PO_4)_2F_3$ (NVPF) is widely concerned owing to its NASICON structure (Na superionic conductor) and excellent electrochemical performances. Based on the strong induction effect of PO_4^{3-} and the strong electronegativity of F^-, NVPF shows high operating voltages (3.6 and 4.1 V), high energy density (~507 Wh kg^{-1}) and excellent thermal stability (Bianchini et al., 2015; Song et al., 2015). Most importantly, the particular NASICON

structure can provide three-dimensional (3D) channels for the fast transmission of Na^+, making NVPF exhibit relatively higher ionic conductivity than many other SIBs cathode materials.

Generally, NVPF materials are mainly synthesized by solid-state reaction method (Gover et al., 2006; Shakoor et al., 2012; Park et al., 2014), spray-drying method (Eshraghi et al., 2017; Shen et al., 2018), sol-gel method (Jiang et al., 2009; Pineda-Aguilar et al., 2017), and hydrothermal method (Serras et al., 2014; Cai et al., 2018; Guo et al., 2018), etc. In order to obtain a well-crystallized NVPF, most of the above mentioned methods usually require high temperature calcination processes (480–850°C). Nevertheless, high temperature will result in that the NVPF particles become irregular, inhomogeneous or even agglomerate together to form larger clusters, which is unfavorable for the Na-ions transmission. Also, the F element may be lost during the calcination process, introducing some impurity phases such as $Na_3V_2(PO_4)_3$ (Eshraghi et al., 2017). Furthermore, the excess calcination process will greatly increase the energy consumption. Although several solvothermal routes (Xu et al., 2014; Qi et al., 2015; Zhao et al., 2015; Zhu et al., 2017) have been reported to synthesize NVPF without heat treatment, the required organic solvents [ethanol, acetone, DMF, and acid-base coupling extractant (PN) etc.] have high vapor pressures which are very dangerous. Thus, the vessel used for the solvothermal process must withstand great high pressures, leading to an extra production cost. And the organic raw materials [such as Vanadium (III) acetylacetonate] used in the solvothermal process are also very expensive. In addition, the organic solvents are usually toxic and harmful to the environment. Thus, the solvothermal method is difficult for the practical application.

Therefore, a green and cheap synthetic route for NVPF without additional calcination process should be developed urgently. Here, we propose a water based hydrothermal route to prepare well-crystallized NVPF, without any extra heat treatment process. In this route, all the raw materials (H_3PO_4, NH_4VO_3, NaF, and oxalic acid) are common and cheap, and NVPF@C tetragons can be one-step synthesized at 180°C with deionized water as solvent. Particularly, here oxalic acid is used as a chelating agent, reducing agent, and carbon source at the same time. In addition, we further add CNTs in the process to obtain NVPF@C/CNTs composite material. The addition of CNTs can not only enhance the conductivity of materials but also restrict the grains over growth. Most importantly, the embedded and wrapped CNTs combined with a uniform nano-carbon layer for NVPF construct a highly conductive 3D network for the transmission of electron and Na^+. As a result, the micron scale (5–10 μm) NVPF@C/CNTs composite synthesized in this study shows excellent rate capability and cycling performance, which can compete with the nanoscale NVPF materials reported in many other reports (Li et al., 2018a,b). It is well-known that the micron-sized cathode materials are preferred rather than nanosized ones for the commercial batteries (such as $LiCoO_2$ and $LiNi_xCo_yMn_zO_2$), as the bigger particles need less binder, solvent and conductive additive to prepare an efficient electrode (Choi and Aurbach, 2016). The micron-sized particles also show higher tap density than the nanosized ones. In a word, this is a green, low cost and efficient water based hydrothermal method for the preparation of NVPF cathode material, and the micron sized NVPF@C/CNTs composite produced by this method is a promising cathode material for SIBs.

EXPERIMENTAL

Materials Synthesis

The synthesis route of $Na_3V_2(PO_4)_2F_3$@C/CNTs cathode material is shown in **Figure 1**. Firstly, 0.01 mol H_3PO_4 (A.R., Aladdin) and 0.05 g CNTs (commercially available carbon nanotubes) were added into 30 ml deionized water, followed by sonication for 15 min. Then, 0.015 mol $C_2H_2O_4$ (A.R., Aladdin), 0.01 mol NH_4VO_3 (A.R., Aladdin) and 0.015 mol NaF (A.R., Aladdin) were sequentially added, and continuously stirred for 30 min. Thereafter, the mixture was transferred to a Teflon cup of 50 mL inner volume, placed in a stainless steel autoclave and kept in an oven at 180°C for 12 h. After cooling to room temperature, the sample in the kettle was taken out, centrifuged and dried to get $Na_3V_2(PO_4)_2F_3$@C/CNTs composite material (denoted as NVPF@C/CNTs). The $Na_3V_2(PO_4)_2F_3$@C (denoted

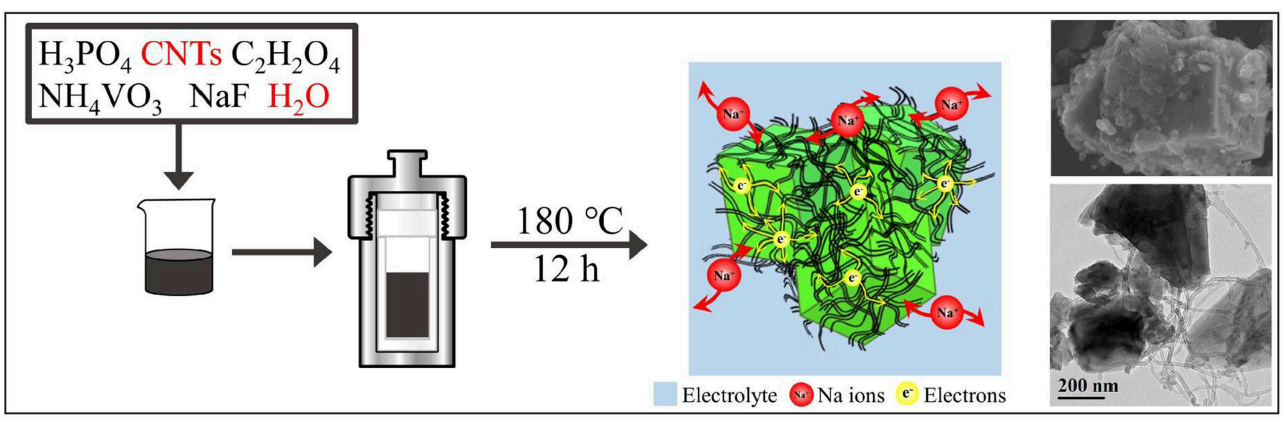

FIGURE 1 | Schematic diagram of synthetic NVPF@C/CNTs cathode material.

as NVPF@C) cathode material was prepared without the addition of CNTs by using the same synthesis route.

Characterization

XRD was carried out on a Rigaku Ultima IV diffractometer using Cu Kα radiation (40 kV); step scan 0.02, 2θ range 10–90°, step time of 2° min^{-1}. IR spectrum was tested on a VERTEX70 spectrometer with a transmission mode in the range of 600–2,000 cm^{-1}. XPS was performed using a Kratos X-ray photoelectron spectrometer (Axis Ultra-DLD) with Mg Kα radiation ($h\nu$ = 1283.3 eV), and all the spectra were calibrated with the C 1s peak at 284.8 eV. The carbon content was measured by C–S analysis (Eltar, Germany). SEM (Hitachi SU-5000) was performed to study the morphology of materials. HRTEM and EDX analyses were carried out with a FEI Tecnai G2 F20 microscope at 200 kV.

Battery Fabrication and Electrochemical Tests

The positive electrode was prepared with the $Na_3V_2(PO_4)_2F_3$ samples, acetylene black and PVDF in the weight ratio of 8:1:1. The N-methylpyrrolidone and Al-foil were used as solvent and current collector, respectively. The metallic sodium-foil and glass fiber membrane (Whatman GF/A) were used as the negative electrode and separator, respectively. The $NaClO_4$ (1 M) solution in propylene carbonate (PC) and fluoroethylene carbonate (FEC) (95% PC and 5% FEC in volume) was used as the electrolyte. The CR2025 cells were assembled in an Ar-filled dry glove box (H_2O and O_2 < 0.1 ppm). The cells were tested at different C-rates (0.1–10 C, 1C = 120 mA g^{-1}) between 2.5 and 4.3 V at ambient temperature. The cyclic voltammetry (CV) was carried out with a CHI-660D electrochemical workstation; potential range 2.5–4.3 V (vs. Na^+/Na), scan rate 0.1 mV s^{-1}.

RESULTS AND DISCUSSION

Figure 2A shows the XRD patterns of NVPF@C and NVPF@C/CNTs samples. From **Figure 2A**, it is found that there is no obvious difference between the NVPF@C and NVPF@C/CNTs samples, and all diffraction peaks can be fully indexed as the tetragonal structure of $Na_3V_2(PO_4)_2F_3$ (PDF#89-8485) with space group $P4_2/mnm$, and no other impurity phases are detected. In addition, the element contents of both samples are also measured. It is found that the molar ratios of Na: V: P: F of NVPF@C and NVPF@C/CNTs are 2.99: 2: 2.01: 3.01 and 3.01: 2: 1.99: 2.98, respectively, which are close to their theoretical values. The above results indicate that the well-crystallized pure phase $Na_3V_2(PO_4)_2F_3$ can be successfully synthesized through water-based hydrothermal method, and the addition of CNTs does not affect the crystal structure of $Na_3V_2(PO_4)_2F_3$. For the sake of contrast, the XRD pattern of CNTs is also shown in **Figure 2B**. However, those diffraction peaks corresponding to CNTs are not clearly observed

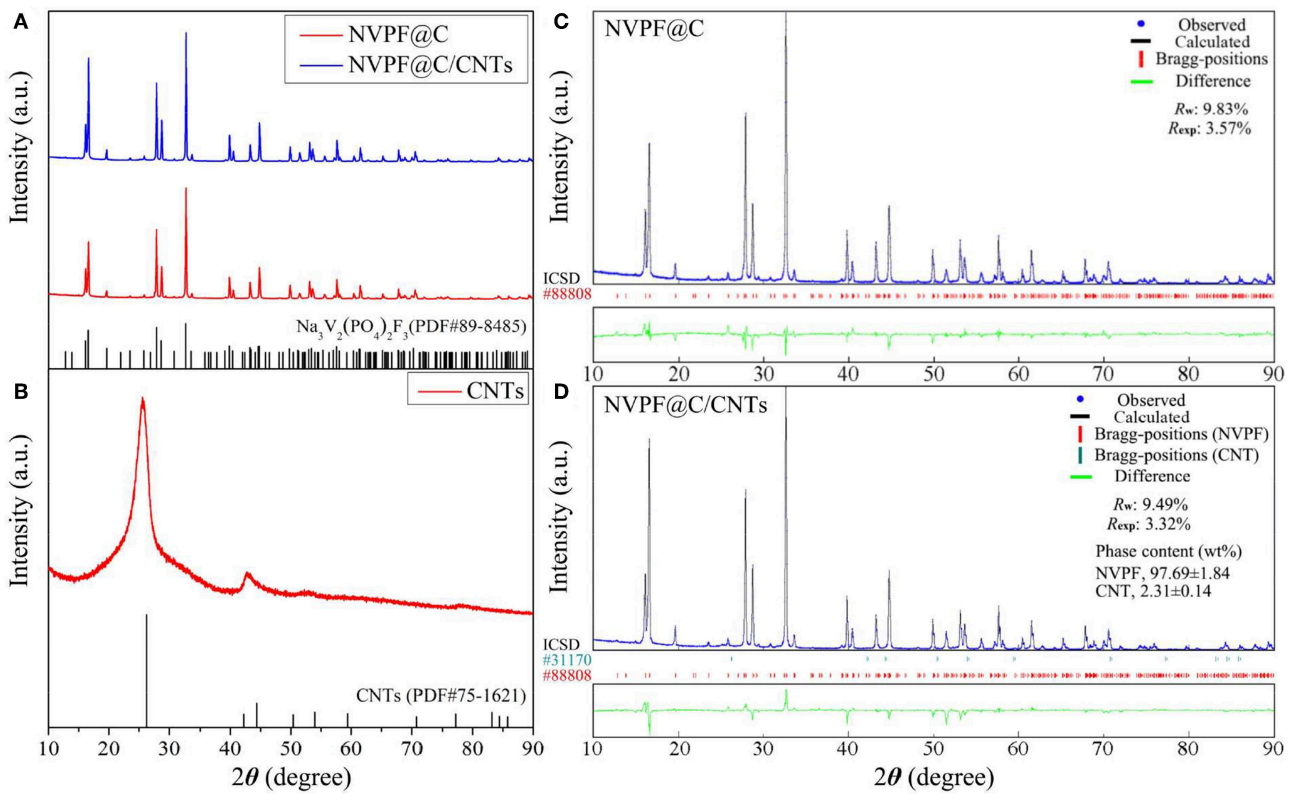

FIGURE 2 | XRD patterns of NVPF@C, NVPF@C/CNTs **(A)** and CNTs **(B)**. Rietveld refinement XRD patterns of NVPF@C **(C)** and NVPF@C/CNTs **(D)**.

TABLE 1 | Lattice parameters and crystallite size of NVPF@C and NVPF@C/CNTs samples obtained from XRD Rietveld refinement.

Samples	Lattice parameters				Crystallite size	Refinement error	
	a/Å	*b*/Å	*c*/Å	*V*/Å^3	*D*/nm	R_w/%	R_{exp}/%
NVPF@C	9.039	9.039	10.681	872.67	404.79	9.83	3.75
NVPF@C/CNTs	9.038	9.038	10.679	872.31	382.53	9.49	3.32

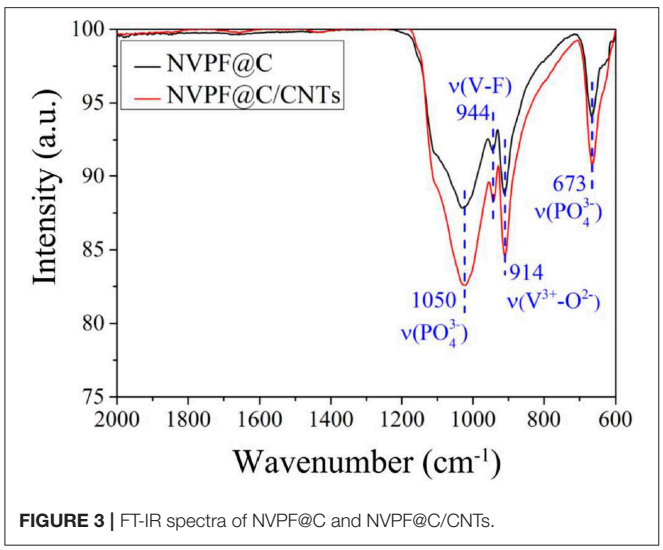

FIGURE 3 | FT-IR spectra of NVPF@C and NVPF@C/CNTs.

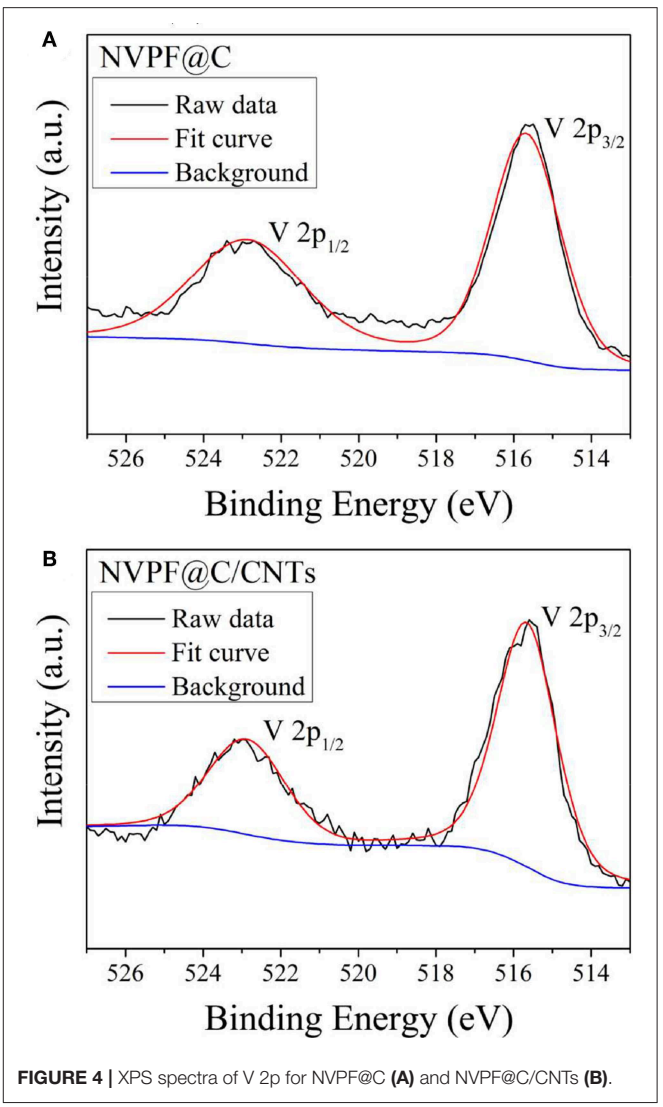

FIGURE 4 | XPS spectra of V 2p for NVPF@C **(A)** and NVPF@C/CNTs **(B)**.

in NVPF@C/CNTs. Therefore, in order to further clarify the structure of the samples, the XRD data of NVPF@C and NVPF@C/CNTs samples are refined by Rietveld method, and the refinement results are shown in **Figures 2C,D**, respectively. As shown, each fitting curve is well-matched with the measured data, and the refinement errors R_w and R_{exp} are acceptable, implying the results are reliable. The refinement results in **Figure 2D** demonstrate the presence of CNTs and indicate that the phase content of CNTs is about 2.31 ± 0.14 wt%. To verify the accuracy of CNTs content, the samples were subjected to C-S analysis. C-S test results reveal that the carbon content of NVPF@C and NVPF@C/CNTs is 3.04 wt% and 5.21 wt%, respectively. Compared with NVPF@C, the increased carbon content (2.17 wt%) of NVPF@C/CNTs should be ascribed to CNTs. This value (2.17 wt%) is close to the XRD refinement result. The above results reveal that CNTs are successfully compounded with NVPF@C. **Table 1** shows the lattice parameters and crystallite size of the two samples. As shown, the lattice parameters of both samples are similar, and all the values are consistent with those reported in the previous references (Gover et al., 2006; Shakoor et al., 2012; Cai et al., 2018). However, the crystallite size (*D* value) of NVPF@C/CNTs is smaller than that of NVPF@C. The results demonstrate that although the addition of CNTs does not affect the crystal structure of NVPF, it can restrict the growth of crystal in some degree, which is of great benefit to obtaining smaller NVPF crystals.

Infrared absorption spectroscopy (FTIR) analysis of the NVPF@C and NVPF@C/CNTs samples are shown in **Figure 3**. It is found that the peaks of both samples appear in the same band, but the absorption peaks of NVPF@C/CNTs are stronger. The band corresponding to the symmetric stretching vibration of PO_4^{3-} anion is located at 673 cm^{-1}, and the broadband at 1,050 cm^{-1} is ascribed to the asymmetric stretching of PO_4^{3-} anion. In addition, the band at 944 cm^{-1} manifests the presence of V–F (Qi et al., 2015; Li et al., 2018b). Moreover, the vibration from V^{3+}—O^{2-} bonds in isolated VO_4F_2 octahedra, is detected at 914 cm^{-1}. While, the typical bands of V^{5+} in the VO_4F_2 octahedron are not

detected at 760 cm^{-1} and 950 cm^{-1} (Song et al., 2014; Pineda-Aguilar et al., 2017; Cai et al., 2018), meaning that the V^{5+} ions in NH_4VO_3 have been reduced to V^{3+}.

In order to further determine the valence state of V^{n+} in the samples, XPS spectra of V 2p are shown in **Figure 4**. It can be observed that the peaks corresponding to V $2p_{3/2}$ and V $2p_{1/2}$ are present at binding energies of 515.7 and 522.9 eV, which are similar to the binding energies of V^{3+} in the previous literature (Ni et al., 2017; Li et al., 2018a). Based on the above analysis, V^{5+} is successfully reduced to V^{3+} by oxalate acid during the hydrothermal process, and well-crystallized NASICON-type $Na_3V_2(PO_4)_2F_3$ can be obtained by the one-step hydrothermal method. Most significantly, no additional heating process is required.

Figures 5a–d shows the SEM images of NVPF@C and NVPF@C/CNTs. As shown, both samples exhibit the tetragonal architecture, but the sample NVPF@C/CNTs shows more regular tetragonal architecture and smaller particle size than NVPF@C. The particle size of NVPF@C and NVPF@C/CNTs is about in the ranges of 30–50 and 5–10 μm, respectively. It is obvious that the NVPF@C grains are too large for the fast insertion/extraction of Na-ions. While the grain size of NVPF@C/CNTs is suitable and very close to those of commercial Li-ion battery materials, such as $LiCoO_2$ and $LiNi_{0.33}Co_{0.33}Mn_{0.33}O_2$. These changes in the shape and size of NVPF particles are mainly ascribed to the addition of CNTs, which is not only beneficial to restrict the NVPF particles over growth, but also can weave a 3D conductive network between the micro-sized tetragonal grains. This 3D network structure can be expected to greatly improve the conductivity of NVPF cathode materials. The tap densities of NVPF@C and NVPF@C/CNTs are 1.12 and 1.03 g cm^{-3}, respectively, which are higher than those of nanoscale powders.

TEM images of the NVPF@C and NVPF@C/CNTs samples are shown in **Figures 5e,h**, respectively. As can be seen, both samples show tetragon shape, but NVPF@C/CNTs sample exhibits smaller grain size than NVPF@C. Furthermore, NVPF crystals in NVPF@C/CNTs sample are intertwined with CNTs. From the HRTEM images (**Figures 5f,i**), it can be clearly seen that the surface of the NVPF crystal for both samples are uniformly coated with an amorphous nano-carbon layer (about 5 nm thick). The carbon layer is mainly derived from the carbonization of oxalic acid. The regular lattice fringes

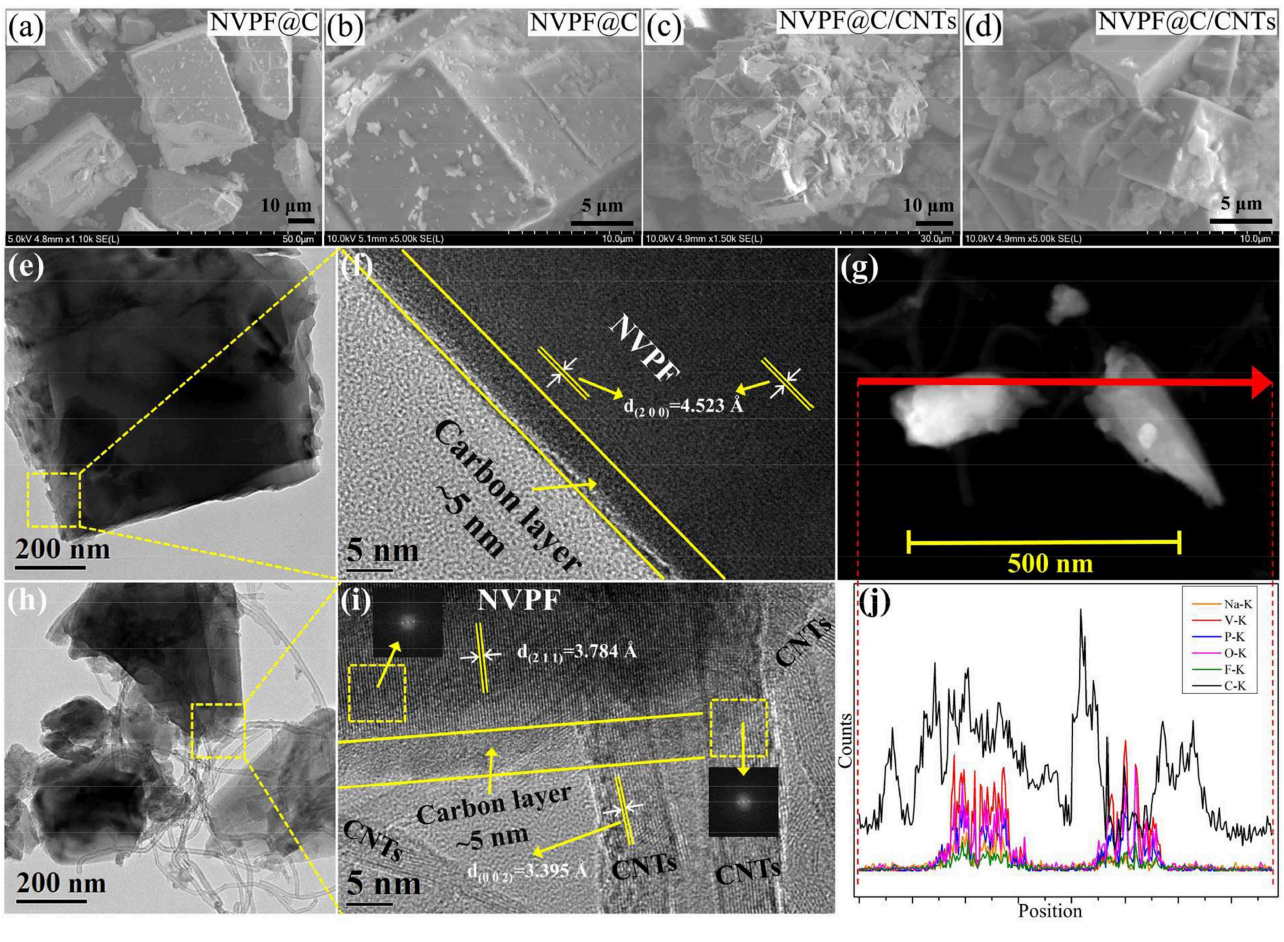

FIGURE 5 | SEM images of NVPF@C **(a,b)** and NVPF@C/CNTs **(c,d)**. TEM and HRTEM images of NVPF@C **(e,f)** and NVPF@C/CNTs **(h,i)**. TEM image of NVPF@C/CNTs **(g)** and corresponding EDS line-scanning curves of Na, V, P, O, F, and C elements **(j)**.

corresponding to the (2 0 0) and (2 1 1) crystal planes of NVPF can be observed in NVPF@C and NVPF@C/CNTs samples, respectively. In addition, the lattice fringes of CNTs [$d_{(002)}$ = 3.395 Å] can be clearly found in NVPF@C/CNTs, and some lattice fringes of CNTs embed in the lattice fringes of NVPF crystals. The above results confirm that some CNTs are embed into the NVPF crystals and the others wrap around the NVPF@C particles. As a result, the embedded and wrapped CNTs combined with the uniform nano-carbon layer construct a 3D conductive network for the transmission of electron and Na^+. Moreover, the illustrations in the upper left and lower right areas in **Figure 5i** are the fast Fourier transform (FFT) of the two selections. The upper left area corresponds to the diffraction spots of the NVPF, and the lower right area corresponds to the diffraction spots of the CNTs. The FFT images further prove the coexistence of NVPF and CNTs. For further study, we perform a EDS linear scanning analysis for NVPF@C/CNTs sample along the line marked in **Figure 5g**, and the results are shown in **Figure 5j**. As shown, the Na, V, P, O, and F elements are mainly distributed in the NVPF particles, and the carbon signal in the particles confirms the presence of the carbon layer on the surface of NVPF particles. Significantly, the location of the CNTs shows a very high carbon signal.

Figures 6A,B shows the charge and discharge curves of the samples at different C-rates. It is obvious that the NVPF@C/CNTs sample shows more flat voltage plateaus, smaller polarization and higher average working voltage than NVPF@C at various C-rates during charge and discharge processes. Furthermore, the initial discharge specific capacity of NVPF@C/CNTs (120.2 mAh g^{-1}) is higher than that of NVPF@C (105.8 mAh g^{-1}) at 0.1C rate. With the increasing of C-rate (from 1C to 10C), the discharge capacities of NVPF@C/CNTs also exhibit less decay than NVPF@C. For example, the ratio of 10C/0.1C discharge capacity for NVPF@C sample is only 37.6%, while the ratio for NVPF@C/CNTs is as high as 61.8%. **Figure 6C** shows the cycle performance of the two samples at various C-rates. It is distinct that NVPF@C/CNTs shows better rate capability and cycling performance than NVPF@C. Especially, the NVPF@C/CNTs sample exhibits a capacity retention rate of 99.5% after 20 cycles at 0.1 C rate, and shows almost no capacity fading when cycling at 1C, 2C, 5C, and 10C, respectively. After cycling at various C-rates for 80 cycles, the discharge

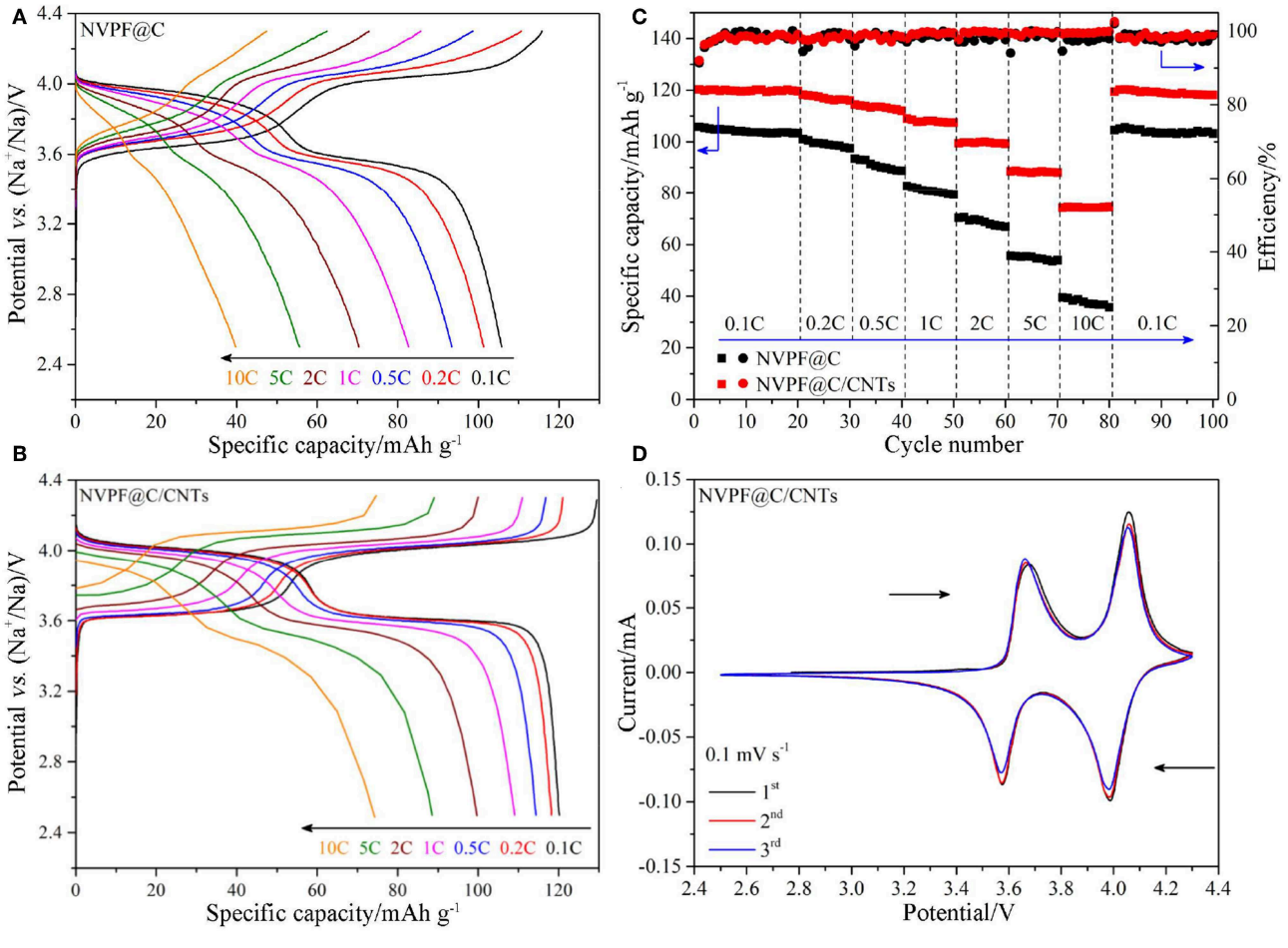

FIGURE 6 | The first charge/discharge curves of NVPF@C **(A)** and NVPF@C/CNTs **(B)** at various C-rates. Cycling performance of NVPF@C and NVPF@C/CNTs at various C-rates **(C)**. CV curves of NVPF@C/CNTs at a scan rate of 0.1 mV s^{-1} **(D)**.

specific capacity of NVPF@C/CNTs at 0.1C (the 81st cycle) can still holds 99.4% of its initial value of the first cycle (120.2 mAh g^{-1}), which indicates that the structure of NVPF is very stable. Moreover, the coulomb efficiency of each cycle is almost 100% at various C rates. **Figure 6D** presents the CV profiles of NVPF@C/CNTs sample at a sweep rate of 0.1 mV s^{-1}. As shown, the sample exhibits the oxidation and reduction peaks of 3.66/3.57 and 4.05/3.98 V, respectively. It should be noted that the 1st, 2nd, and 3rd CV curves overlap closely, which further proves the stable structure of NVPF. The excellent electrochemical performances of NVPF@C/CNTs should be owing to: (1) the well-crystallized NVPF can offer a stable crystal structure; (2) the addition of CNTs can effectively restrict the NVPF grains over growth, which is conducive to the migrating of Na-ions during the charge/discharge processes; (3) the uniform nano-carbon layer, embedded and wrapped CNTs together construct a highly conductive 3D network for the electron transmission.

CONCLUSIONS

Well-crystallized NVPF@C/CNTs cathode material with tetragonal architecture is successfully synthesized by a one-step water based hydrothermal method. In this method, the reduction and crystallization of materials are simultaneously accomplished in the hydrothermal process, no additional heat treatment is needed. The obtained NVPF crystals are coated with a uniform nano-carbon layer, and CNTs are embed into and wrapped around the NVPF grains. Both the coating layer and CNTs weave a highly conductive 3D network for the migration of electron and Na-ion, which leads to the excellent rate capability and cycling performance of the micron-sized (5–10 μm) NVPF@C/CNTs composite. Significantly, the raw materials used in this method are very ordinary, cheap and eco-friendly, the solvent is water and the synthesis temperature is only 180°C. Therefore, we believe that this is a green, low cost, efficient, and facile method for the synthesis of NVPF-based cathode materials.

DATA AVAILABILITY STATEMENT

All datasets generated for this study are included in the article/supplementary files.

AUTHOR CONTRIBUTIONS

HG and YH did the main experiment and wrote the manuscript. XZ, RZ, and YS envolved the discussion of the experiment and revised the manuscript. LW and DH made the research plan. LW also provided the financial support.

FUNDING

This study was financially supported by the National Natural Science Foundation of China (51574170, 51774210, and 51774207).

REFERENCES

Bianchini, M., Fauth, F., Brisset, N., Weill, F., Suard, E., Masquelier, C., et al. (2015). Comprehensive investigation of the $Na_3V_2(PO_4)_2F_3$-$NaV_2(PO_4)_2F_3$ system by operando high resolution synchrotron X-ray diffraction. *Chem. Mater.* 27, 3009–3020. doi: 10.1021/acs.chemmater.5b00361

Cai, Y., Cao, X., Luo, Z., Fang, G., Liu, F., Zhou, J., et al. (2018). Caging $Na_3V_2(PO_4)_2F_3$ microcubes in cross-linked graphene enabling ultrafast sodium storage and long-term cycling. *Adv. Sci.* 5:1800680. doi: 10.1002/advs.201800680

Chen, J., Li, L., Wu, L., Yao, Q., Yang, H., Liu, Z., et al. (2018). Enhanced cycle stability of $Na_{0.9}Ni_{0.45}Mn_{0.55}O_2$ through tailoring O3/P2 hybrid structures for sodium-ion batteries. *J. Power Sources* 406, 110–117. doi: 10.1016/j.jpowsour.2018.10.058

Chen, J., Zhong, S., Zhang, X., Liu, J., Shi, S., Hu, Y., et al. (2017). High performance of hexagonal plates P2-$Na_{2/3}Fe_{1/2}Mn_{1/2}O_2$ cathode material synthesized by an improved solid-state method. *Mater. Lett.* 202, 21–24. doi: 10.1016/j.matlet.2017.05.084

Choi, J. W., and Aurbach, D. (2016). Promise and reality of post-lithium-ion batteries with high energy densities. *Nat. Rev. Mater.* 1:16013. doi: 10.1038/natrevmats.2016.13

Delmas, C., Braconnier, J. J., Fouassier, C., and Hagenmuller, P. (1981). Electrochemical intercalation of sodium in Na_xCoO_2 bronzes. *Solid State Ionics* 3, 165–169. doi: 10.1016/0167-2738(81)90076-X

Doeff, M. M., Peng, M. Y., Ma, Y., and De Jonghe, L. C. (1994). Orthorhombic Na_xMnO_2 as a cathode material for secondary sodium and lithium polymer batteries. *J. Electrochem. Soc.* 141, L145–L147. doi: 10.1149/1.2059323

Eshraghi, N., Caes, S., Mahmoud, A., Cloots, R., Vertruyen, B., and Boschini, F. (2017). Sodium vanadium (III) fluorophosphate/carbon nanotubes composite (NVPF/CNT) prepared by spray-drying: good electrochemical performance thanks to well-dispersed CNT network within NVPF particles. *Electrochim. Acta* 228, 319–324. doi: 10.1016/j.electacta.2017.01.026

Ge, X., Li, X., Wang, Z., Guo, H., Yan, G., Wu, X., et al. (2019). Facile synthesis of $NaVPO_4F$/C cathode with enhanced interfacial conductivity towards long-cycle and high-rate sodium-ion batteries. *Chem. Eng. J.* 357, 458–462. doi: 10.1016/j.cej.2018.09.099

Gover, R. K. B., Bryan, A., Burns, P., and Barker, J. (2006). The electrochemical insertion properties of sodium vanadium fluorophosphates. $Na_3V_2(PO_4)_2F_3$. *Solid State Ionics* 177, 1495–1500. doi: 10.1016/j.ssi.2006.07.028

Guignard, M., Didier, C., Darriet, J., Bordet, P., Elkaïm, E., and Delmas, C. (2013). P2-Na_xVO_2 system as electrodes for batteries and electron-correlated materials. *Nat. Mater.* 12, 74–80. doi: 10.1038/nmat3478

Guo, B., Diao, W., Yuan, T., Liu, Y., Yuan, Q., Li, G., et al. (2018). Enhanced electrochemical performance of $Na_3V_2(PO_4)_2F_3$ for Na-ion batteries with nanostructure and carbon coating. *J. Mater. Sci. Mater. Electron.* 29, 16325–16329. doi: 10.1007/s10854-018-9722-8

Jiang, T., Chen, G., Li, A., Wang, C., and Wei, Y. (2009). Sol-gel preparation and electrochemical properties of $Na_3V_2(PO_4)_2F_3$/C composite cathode material for lithium ion batteries. *J. Alloy. Compd.* 478, 604–607. doi: 10.1016/j.jallcom.2008.11.147

Lee, E., Kim, D. H., Hwang, J., Kang, J. S., Minh, N. V., Yang, I. S., et al. (2013). Soft x-ray absorption spectroscopy study of prussian blue analogue $ACo[Fe(CN)_6]H_2O$ nano-particles (A=Na, K). *J. Korean Phys. Soc.* 62, 1910–1913. doi: 10.3938/jkps.62.1910

Leng, J., Wang, Z., Wang, J., Wu, H.-H., Yan, G., Li, X., et al. (2019). Advances in nanostructures fabricated via spray pyrolysis and their applications in energy storage and conversion. *Chem. Soc. Rev.* 48, 3015–3072. doi: 10.1039/C8CS00904J

Li, L., Xu, Y., Sun, X., Chang, R., Zhang, Y., Zhang, X., et al. (2018b). Fluorophosphates from solid-state synthesis and electrochemical ion

exchange: $NaVPO_4F$ or $Na_3V_2(PO_4)_2F_3$. *Adv. Energy Mater.* 8:1801064. doi: 10.1002/aenm.201801064

Li, L., Xu, Y., Sun, X., He, S., and Li, L. (2018a). High capacity-favorable tap density cathode material based on three-dimensional carbonous framework supported $Na_3V_2(PO_4)_2F_3$ nanoparticles. *Chem. Eng. J.* 331, 712–719. doi: 10.1016/j.cej.2017.09.012

Ni, Q., Bai, Y., Wu, F., and Wu, C. (2017). Polyanion-type electrode materials for sodium-ion batteries. *Adv. Sci.* 4:1600275. doi: 10.1002/advs.201600275

Park, Y. U., Seo, D. H., Kim, H., Kim, J., Lee, S., Kim, B., et al. (2014). A family of high-performance cathode materials for Na-ion batteries, $Na_3(VO_{1-x}PO_4)_2F_{1+2x}$ ($0 \leq x \leq 1$): combined first-principles and experimental study. *Adv. Funct. Mater.* 24, 4603–4614. doi: 10.1002/adfm.201400561

Pineda-Aguilar, N., Gallegos-Sánchez, V. J., Sánchez, E. M., Torres-González, L. C., and Garza-Tovar, L. L. (2017). Aluminum doped $Na_3V_2(PO_4)_2F_3$ via sol–gel Pechini method as a cathode material for lithium ion batteries. *J. Sol Gel Sci. Technol.* 83, 405–412. doi: 10.1007/s10971-017-4398-8

Qi, Y., Mu, L., Zhao, J., Hu, Y. S., Liu, H., and Dai, S. (2015). Superior Na-storage performance of low-temperature-synthesized $Na_3(VO_{1--x}PO_4)_2F_{1+2x}$ ($0 \leq x \leq 1$) nanoparticles for Na-ion batteries. *Angew. Chem. Int. Ed.* 54, 9911–9916. doi: 10.1002/anie.201503188

Qian, J., Zhou, M., Cao, Y., Ai, X., and Yang, H. (2012). Nanosized $Na_4Fe(CN)_6$/C composite as a low-cost and high-rate cathode material for sodium-ion batteries. *Adv. Energy Mater.* 2, 410–414. doi: 10.1002/aenm.201100655

Serras, P., Palomares, V., Rojo, T., Brandc, H. E. A., and Sharma, N. (2014). Structural evolution of high energy density V^{3+}/V^{4+} mixed valent $Na_3V_2O_{2x}(PO_4)_2F_{3-2x}$ (x=0.8) sodium vanadium fluorophosphate using in situ synchrotron X-ray powder diffraction. *J. Mater. Chem. A* 2, 7766–7779. doi: 10.1039/C4TA00773E

Shakoor, R. A., Seo, D. H., Kim, H., Park, Y. U., Kim, J., Kim, S. W., et al. (2012). A combined first principles and experimental study on $Na_3V_2(PO_4)_2F_3$ for rechargeable Na batteries. *J. Mater. Chem.* 22, 20535–20541. doi: 10.1039/c2jm33862a

Shen, C., Long, H., Wang, G., Lu, W., Shao, L., and Xie, K. (2018). $Na_3V_2(PO_4)_2F_3$@C dispersed within carbon nanotube frameworks as a high tap density cathode for high-performance sodium-ion batteries. *J. Mater. Chem. A* 6, 6007–6014. doi: 10.1039/C8TA00990B

Song, W., Ji, X., Chen, J., Wu, Z., Zhu, Y., Ye, K., et al. (2015). Mechanistic investigation of ion migration in $Na_3V_2(PO_4)_2F_3$ hybrid-ion batteries. *Phys. Chem. Chem. Phys.* 17, 159–165. doi: 10.1039/C4CP04649H

Song, W., Ji, X., Wu, Z., Zhu, Y., Li, F., Yao, Y., et al. (2014). Multifunctional dual $Na_3V_2(PO_4)_2F_3$ cathode for both lithium-ion and sodium-ion batteries. *RSC Adv.* 4, 11375–11383. doi: 10.1039/C3RA47878E

Vassilaras, P., Ma, X., Li, X., and Geder, G. (2013). Electrochemical properties of monoclinic $NaNiO_2$. *J. Electrochem. Soc.* 160, A207–A211. doi: 10.1149/2.023302jes

Wang, L., Lu, Y., Liu, J., Xu, M., Cheng, J., Zhang, D., et al. (2013). A superior low-cost cathode for a Na-ion battery. *Angew. Chem.* 125, 2018–2021. doi: 10.1002/ange.201206854

Wu, L., Hu, Y., Zhang, X., Liu, J., Zhu, X., and Zhong, S. (2018b). Synthesis of carbon-coated Na_2MnPO_4F hollow spheres as a potential cathode material for Na-ion batteries. *J. Power Sources* 374, 40–47. doi: 10.1016/j.jpowsour.2017.11.029

Wu, L., Shi, S., Zhang, X., Yang, Y., Liu, J., Tang, S., et al. (2018a). Room-temperature pre-reduction of spinning solution for the synthesis of $Na_3V_2(PO_4)_3$/C nanofibers as high-performance cathode materials for Na-ion batteries. *Electrochim. Acta* 274, 233–241. doi: 10.1016/j.electacta.2018.04.122

Xie, Y., Wang, H., Liu, R., Wang, Z., Wen, W., Jiang, Z., et al. (2017). In situ monitoring of structural and valence evolution during electrochemical desodiation/sodiation process of $Na_2Fe_{0.5}Mn_{0.5}PO_4F$. *J. Electrochem. Soc.* 164, A3487–A3492. doi: 10.1149/2.0281714jes

Xu, M., Xiao, P., Stauffer, S., Song, J., Henkelman, G., and Goodenough, J. B. (2014). Theoretical and experimental study of vanadium-based fluorophosphate cathodes for rechargeable batteries. *Chem. Mater.* 26, 3089–3097. doi: 10.1021/cm500106w

Yue, Y., Binder, A. J., Guo, B., Zhang, Z., Qiao, Z. A., Tian, C., et al. (2014). Mesoporous prussian blue analogues: template-free synthesis and sodium-ion battery applications. *Angew. Chem. Int. Ed.* 53, 3134–3137. doi: 10.1002/anie.201310679

Zhao, J., Mu, L., Qi, Y., Hu, Y. S., Liu, H., and Dai, S. (2015). A phase-transfer assisted solvo-thermal strategy for low-temperature synthesis of $Na_3(VO_{1-x}PO_4)_2F_{1+2x}$ cathodes for sodium-ion batteries. *Chem. Commun.* 51, 7160–7163. doi: 10.1039/C5CC01504A

Zheng, J., Yang, B., Wang, X., Zhang, B., Tong, H., Yu, W., et al. (2018). Comparative investigation of $Na_2FeP_2O_7$ sodium insertion material synthesized by using different sodium sources. *ACS Sustain. Chem. Eng.* 6, 4966–4972. doi: 10.1021/acssuschemeng.7b04516

Zhu, C., Wu, C., Chen, C. C., Kopold, P., Aken, P. A. V., Maier, J., et al. (2017). A high power–high energy $Na_3V_2(PO_4)_2F_3$ sodium cathode: investigation of transport parameters, rational design and realization. *Chem. Mater.* 29, 5207–5215. doi: 10.1021/acs.chemmater.7b00927

Conflict of Interest: The authors declare that the research was conducted in the absence of any commercial or financial relationships that could be construed as a potential conflict of interest.

frontiers in Chemistry

ORIGINAL RESEARCH
published: 27 November 2019
doi: 10.3389/fchem.2019.00748

Graphene-Modified 3D Copper Foam Current Collector for Dendrite-Free Lithium Deposition

Juan Yu[1,2], *Yangyang Dang*[1], *Maohui Bai*[3], *Jiaxin Peng*[1], *Dongdong Zheng*[1], *Junkai Zhao*[1,2], *Linbo Li*[1,2] *and Zhao Fang*[1,2]*

[1] School of Metallurgical Engineering, Xi'an University of Architecture and Technology, Xi'an, China, [2] Shaanxi Province Metallurgical Engineering and Technology Research Centre, Xi'an, China, [3] School of Metallurgy and Environment, Central South University, Changsha, China

Lithium (Li) metal is regarded as the ideal anode for rechargeable Li-metal batteries such as Li-S and Li-air batteries. A series of problems caused by Li dendrites, such as low Coulombic efficiency (CE) and a short circuit, have limited the application of Li-metal batteries. In this study, a graphene-modified three-dimensional (3D) Copper (Cu) current collector is addressed to enable dendrite-free Li deposition. After Cu foam is immersed into graphene oxide (GO) suspension, a spontaneous reduction of GO, induced by Cu, generates reduced graphene oxide on a 3D Cu (rGO@Cu) substrate. The rGO@Cu foam not only provides large surface area to accommodate Li deposition for lowering the local effective current density, but also forms a rGO protective layer to effectively control the growth of Li dendrites. As current collector, the rGO@Cu foam shows superior properties than commercial Cu foam and planar Cu foil in terms of cycling stability and CE. The rGO@Cu foam delivers a CE as high as 98.5% for over 350 cycles at the current density of 1 mA cm^{-2}. Furthermore, the full cell using $LiFePO_4$ as cathode and Li metal as anode with rGO@Cu foam as current collector ($LiFePO_4$/rGO@Cu-Li) is assembled to prove the admirable capacities and indicates commercialization of Li-metal batteries.

Keywords: Li metal anode, rGO@Cu foam, Li dendrite, current collector, $LiFePO_4$ cathode

OPEN ACCESS

Edited by:
Shengkui Zhong,
Soochow University, China

Reviewed by:
Yunjian Liu,
Jiangsu University, China
Xianwen Wu,
Jishou University, China

***Correspondence:**
Zhao Fang
fangzhao@xauat.edu.cn

Specialty section:
This article was submitted to Electrochemistry, a section of the journal Frontiers in Chemistry

Received: *21 August 2019*
Accepted: *21 October 2019*
Published: *27 November 2019*

Citation:
Yu J, Dang Y, Bai M, Peng J, Zheng D, Zhao J, Li L and Fang Z (2019) Graphene-Modified 3D Copper Foam Current Collector for Dendrite-Free Lithium Deposition. Front. Chem. 7:748. doi: 10.3389/fchem.2019.00748

INTRODUCTION

Electrical energy storage has garnered great attention when considering the problems of pollution and global warming from the burning of fossil fuels and biomass (Goodenough and Kim, 2010). One of the most important candidates is the rechargeable Li battery (Ji et al., 2011; Lu et al., 2014b; Zhao et al., 2015), since it offers higher stored volume and gravimetric energy density (Goodenough and Kim, 2010; Manthiram et al., 2012; Narayanan et al., 2012). Li metal is considered to be a very promising anode material, because it holds quite a higher theoretical specific capacity (3,860 mAh g^{-1}), lower density (0.53 g cm^{-3}), and a lowest redox potential −3.04 V vs. the standard hydrogen potential electrode) than other anode materials (Xu et al., 2014; Zhao et al., 2015). However, the safety hazards caused by the Li dendrite limit its real applications. Unlike the commercial "host" material, the Li metal anode undergoes the process of Li deposition/stripping during cycling, leading to uncontrollable dendritic Li *via* repeated charging and discharging (Ding et al., 2013; Yun et al., 2016; Li Q. et al., 2017; Ma et al., 2017). When Li is deposited on a planar substrate, the small dendrites are formed first, resulting in an electric field that is distributed unevenly, further promoting the Li^+ inhomogeneous concentrate (Yun et al., 2016; Li Q. et al., 2017). As the Li

dendrites grow, it can render the breakdown/repair of the solid electrolyte interphase (SEI) repeatedly, owing to continuous interfacial reactions (Liu et al., 2017; Gu et al., 2018; Yan et al., 2018). In this way much of the electrolyte is consumed, severely reducing the Coulombic efficiency and capacity decay (Lee et al., 2015; Ye et al., 2017). At the same time, Li dendrites can penetrate the separator further causing an irreversibly infinite volume change and even catastrophic safety hazards (Song et al., 2011; Cheng et al., 2017; Tang et al., 2018).

As noted above, multifarious strategies have been proposed in order to make the Li metal electrodes viable by controlling Li^+ flux to facilitate uniform deposition of Li and enable formation of a stable SEI (Wu et al., 2017; Li et al., 2018). A variety of electrolyte additives have been employed to modify electrolyte composition and to stabilize the SEI film (Haregewoin et al., 2016). Different kinds of polymeric and ceramic electrolytes have been proven to suppress Li dendrite growth effectively (Kamaya et al., 2011; Kotobuki et al., 2011; Bouchet et al., 2013; Han et al., 2017; Li et al., 2019), however, a series of problems such as chemical instability and low ionic conductivity for application still exists when in contact with Li metal (Li et al., 2015). $LiPF_6$ was mixed with LiTFSI-LiBOB dual-salt/carbonate-solvent-based electrolytes which can improve the charging capability and cycling stability of Li-metal batteries notably (Zheng et al., 2017), and which cannot achieve stability with the constant consumption of additives in long-term cycles. Another method to suppress Li dendrite growth is planting an artificial SEI layer by manipulating the formation process (Gao et al., 2017) or inserting an interface protective layer (Lu et al., 2014a; Kozen et al., 2015; Lin et al., 2016; Bobnar et al., 2018; Shi et al., 2019). While, there is not enough mechanical strength of the artificial film to suit large volume expansion in extended periods (Yan et al., 2018). It is reported that a flexible, interconnected, hollow amorphous carbon nanosphere coated on Li metal is desired to accommodate the volumetric expansion of Li deposition without mechanical damage (Zheng et al., 2014). In addition, a composite Li metal anode with an ion-conducting mesoscale skeleton can improve electrochemical performance significantly (Liang et al., 2019). Very recently, the other approach to inhibit Li dendrites by modifying the current collector has been widely discussed. It was found that by creating the CuO nanostructure on the Cu surface as a current collector, exhibits an improved capacity for Li batteries (Liu et al., 2016; So et al., 2018; Zhang et al., 2018). Moreover, the 3D conductive framework as a current collector can suppress the growth of dendrites, because of its large specific surface and low local current density for the Li metal anode (Xie et al., 2016; Yun et al., 2016; Li Q. et al., 2017). However, the pore size of the 3D substrate is thought to have a great impact on electrical conductivity. 3D Cu foam that is too large in size is considered unsuitable for current collectors (Yang et al., 2015).

Based on the above-mentioned discussion, we propose a spontaneous formation of rGO@Cu foam *via* the reaction of 3D Cu foam with graphene oxide to substitute the commercial Cu as a current collector. To prove the excellent properties of the rGO@Cu foam current collector, it was directly used to assemble a half-cell as an electrode with Li metal as the counter electrode. By contrast, 3D Cu foam and 2D planar Cu foil were also directly used separately to assemble batteries with a Li metal sheet as a counter electrode. Compared to three kinds of cells, the rGO@Cu foam inhibits the growth of Li dendrites effectively as well as exhibiting superior properties to 3D Cu foam and planar Cu foil current collectors. The 3D porous structure can reduce the effective electrode current density and provides more space to accommodate Li metal deposition because of its large specific surface. Furthermore, the rGO layer can enhance electrical conductivity and structural stability (Li G. et al., 2017). After cycling, there are minimal dendrites in the 3D Cu foam substrate and the maximum dendrites in the planar Cu foil. Furthermore, the $LiFePO_4$/rGO@Cu-Li full cell was fabricated to estimate the advantageous capabilities of the rGO@Cu foam current collector. The remarkable cycling stability and rate performance of the $LiFePO_4$/rGO@Cu-Li full cells make it possible to utilize in commercial.

EXPERIMENTAL SECTION

Materials Preparations

The schematic diagram for the preparation of the rGO@Cu foam is shown in **Figure 1a**. To begin this process, GO was prepared from purified natural graphite according to the Hummers' method (Hu et al., 2013; Zaaba et al., 2017; Bai et al., 2018) (details refer to the **Supplementary Material**). The commercial Cu foam was immersed into the 1 mg/ml graphene oxide (GO) suspension (**Figure S1**) for 12 h until the black reduced graphene oxide layer covered the whole surface. Then, the Cu foam was removed from the GO suspension and transferred to a vacuum drying oven (DZF-2B) for 24 h, after which, the rGO@Cu foam was obtained.

Material Characterizations

Morphologies of samples were conducted on a field-emission scanning electron microscope (FESEM, NOVA 450, USA). At the same time, Energy-dispersive (EDS) investigation was collected to analyze element distribution of the sample. X-ray photoelectron spectroscopy (XPS) was chosen to characterize the compound of samples. XPS analysis was conducted with the SDTQ600 Type thermo gravimetric analyzer and the XPS spectra were adopted using monochromatic Al Kα (1486.6eV) X-ray emission-spot size was 650 μm.

Electrochemical Characterizations

The bare Cu foil, 3D Cu foam and rGO@Cu foam were punched out into discs with a diameter of 12 mm and were tested as different current collectors. To evaluate the properties of repeated Li deposition/stripping in planar Cu foil, commercial Cu foam, and rGO@Cu foam current collectors, CR2016 coin cells were directly assembled using the three kinds of current collectors, with bare Li metal as counter electrodes. The separator was a Celgard-2325 microporous polypropylene film. The electrolyte was a 1 M lithium bis (trifluoromethanesulphonyl) imide (LiTFSI) in 1,3-dioxolane (DOL) and 1,2- dimethoxyethane (DME) (volume ratio 1:1) with 2% lithium nitrate ($LiNO_3$) without any additives. Before the symmetrical cell test, the current collectors were first initialized by cycling from 0 to 1 V at 50 μA for five cycles to remove

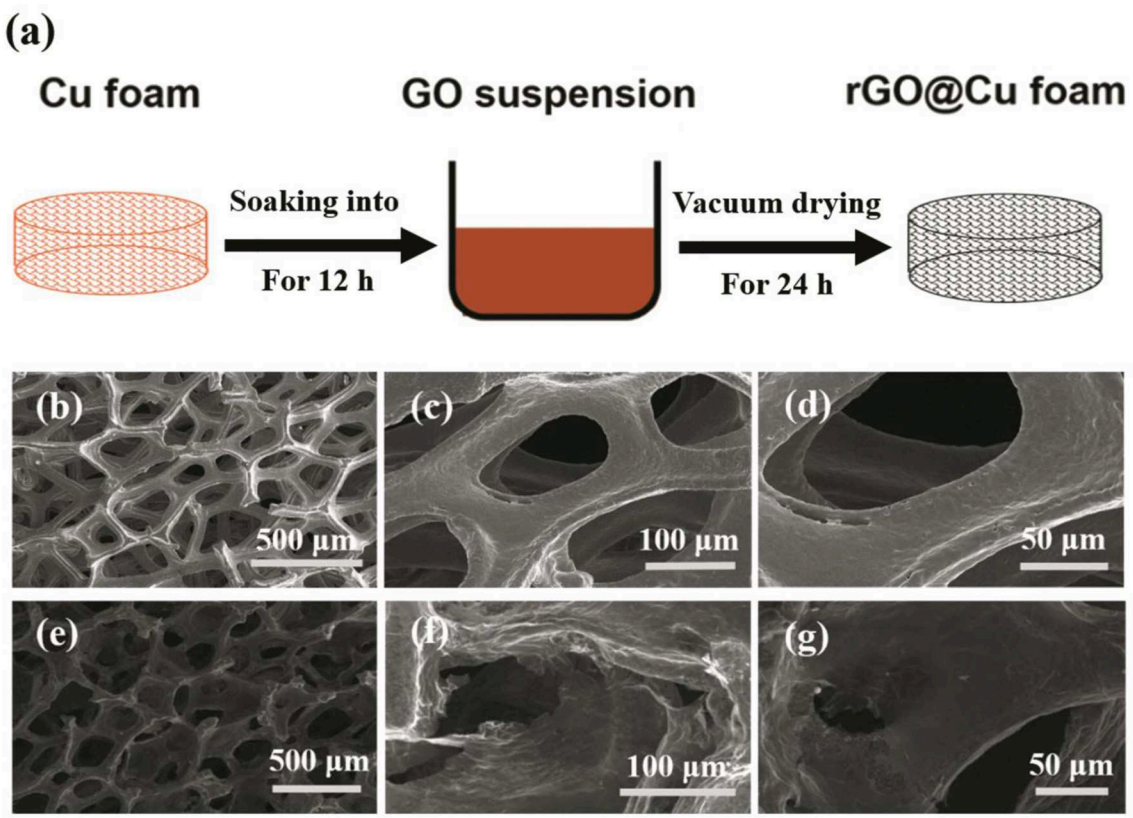

FIGURE 1 | Schematic illustration of the rGO@Cu foam formation process. **(a)** rGO@Cu foam obtained from Cu foam in the 1 mg/ml aqueous GO suspension for 12 h. SEM images of **(b–d)** Cu foam and **(e–g)** rGO@Cu foam.

surface contaminations and to stabilize the interface. Then 1 mAh cm^{-2} of Li was plated on the current collector at a current density of 1 mA cm^{-2} and the cutoff potential for the discharge process was set to 1.0 V. To confirm the possibility of a practical application of the modified current collector, the $LiFePO_4$ full cell was built using $LiFePO_4$ as a cathode and Li metal as an anode with 2D planar Cu foil ($LiFePO_4$/2D-Cu-Li), 3D Cu foam ($LiFePO_4$/3D-Cu-Li), or a rGO@Cu foam current collector. 1 mAh cm^{-2} of Li was first deposited onto the different Cu current collectors by a half-cell using Li foil as a counter electrode. The cell was then disassembled in an argon-filled glovebox and a new anode was reassembled into a full cell with $LiFePO_4$ as the cathode (for details refer to the **Supplementary Material**). The electrolyte was 1.0 M $LiPF_6$ in ethylene carbonate (EC)/dimethyl carbonate (DMC) (1:1 in volume). The $LiFePO_4$ full cells were cycled between 2.0 and 4.2 V at 1 C. All the cells were assembled in the argon-filled glovebox and were tested using the LANHE multi-channel battery testing system and PARSTAT 2273 Electrochemical System (Princeton Applied Research, USA).

RESULTS AND DISCUSSION

The pictures of planar Cu foil, bare Cu foam current collector and rGO@Cu foam are shown in **Figure S2**. A bare Cu foam of reddish brown changed into black after soaking in the GO suspension, showing that the graphene is evenly covered on bare Cu foam. The top view SEM images of commercial Cu foam at different magnifications are shown in **Figures 1b–d** and rGO@Cu foam is shown in **Figures 1e–g**. An abundance of pores can be observed in the SEM images of both commercial Cu foam and rGO@Cu foam, confirming the 3D porous structure of samples. Meanwhile, it can be clearly seen that rGO is attached to the Cu skeleton. **Figure 2a** displays the top view SEM images of a modified Cu foam current collector. Compared with the bare Cu foam, there is a layered structure connected to the Cu skeleton (**Figure S3**). This layered structure is considered to be rGO because the GO is spontaneously reduced by Cu, and Cu is oxidized to form CuO. The SEM image of the surface of the layered structure is magnified on **Figure 2b** and the corresponding elemental mappings are shown in **Figures 2c,d**. It can be discovered that only C (**Figure 2c**) and O (**Figure 2d**), as major elements, are distributed evenly and independently on the layered structure. To further illustrate the composite of Cu foam with GO, XPS spectra of samples are collected in **Figures 2e–h**. **Figure 2e** exhibits the XPS survey spectra measured in the range of binding energies from 0 to 1,361 eV and the peaks of C 1s, O 1s, and Cu 2p can be clearly observed. As shown in **Figure 2f**, the intensities of the C-O (286.25 eV) and C=O (288.38 eV) functional groups are significantly decreased compared with the

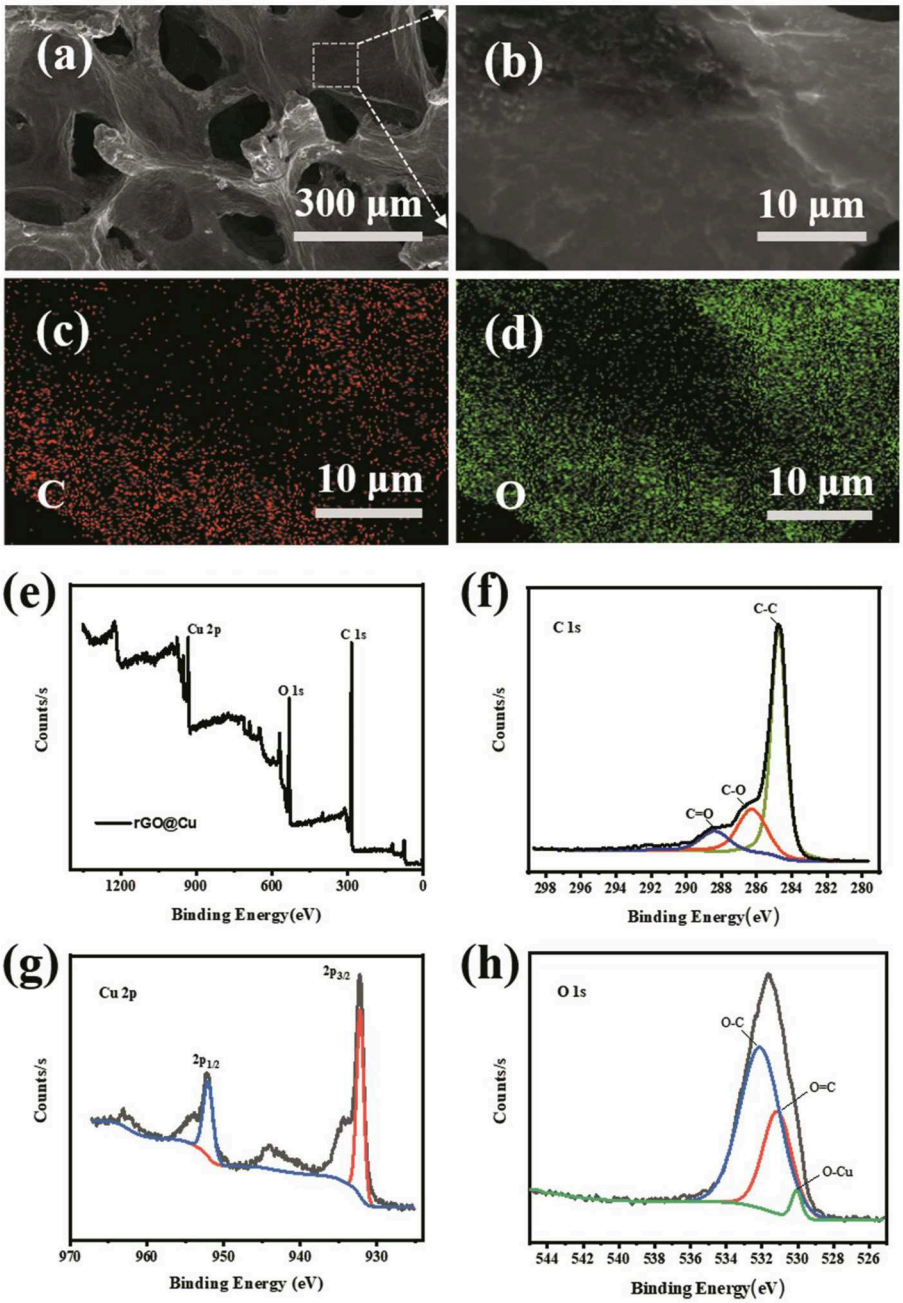

FIGURE 2 | (a) SEM images of the morphology of the rGO@Cu foam current collector. **(b)** Magnified view of the rGO from rGO@Cu foam and corresponding element mapping of **(c)** C, **(d)** O. **(e)** XPS spectra of rGO@Cu foam and the corresponding **(f)** C 1s, **(g)** Cu 2p, and **(h)** O 1s peaks.

spectra of GO (Stankovich et al., 2007; Luo et al., 2011; Kim et al., 2013). At the same time, the main peak at 284.75 eV indicates that most of the C-C functional group was formed (Stankovich et al., 2007). This result can be explained by the fact that GO is reduced to rGO. The high-resolution scan of Cu 2p is displayed in **Figure 2g**, a double peak with binding energies at 932.75 and 952.75 eV is attributed to Cu 2p3/2 and Cu 2p1/2 of Cu^{2+} in CuO, respectively. Also, the gap between the Cu 2p3/2 and Cu 2p1/2 energy levels is 20.0 eV, corresponding to the split orbit for Cu^{2+} (Soleimani and Moghaddami, 2017). These results can be considered to show that the Cu was oxidized to CuO. To further prove the existence of oxygen-containing functional groups and CuO, the O 1s core-level spectrum is shown in **Figure 2h**. There are mainly three peaks centered at 532.88, 531.82, and 530.7 eV, which is approximately consistent with the O-C, O=C, and O-Cu (Novakov and Prins, 1971; Mattevi et al., 2009). The peaks

of O 1s of the sample are significantly increased compared with GO, indicating that most of the oxygen functional groups are reduced and the rGO is formed (Kim et al., 2013). In addition, the existence of O-Cu further proves the formation of CuO. As a result, the existence of rGO and CuO without any external conditions proves that the spontaneous reaction is real.

The electrochemical performance of the coin cells with 2D planar Cu foil, 3D commercial Cu foam, and rGO@Cu foam as an electrode with Li metal as a counter electrode is displayed in **Figure 3**. The coin cells with three types of current collectors were first cycled five times from 0 to 1 V at 50 μA to remove surface impurities and to help form a stable SEI film. **Figures 3a–d** exhibit the galvanostatic cycling voltage profiles on the 2D planar Cu foil, 3D commercial Cu foam, and rGO@Cu foam electrode for cycles at 10th, 50th, 150th, and 300th. After the initial 10 cycles, 2D planar Cu foil and 3D commercial Cu foam display a higher discharge voltage plateau and a lower charge voltage plateau than rGO@Cu foam (**Figure 3a**), indicating a much lower polarization of planar Cu foil and 3D Cu foam compared to rGO@Cu foam. This might be attributed to the fact that the surface of rGO@Cu foam was not activated completely by the electrolyte, causing the accumulation of Li^+ on the current collector. Notice that this phenomenon disappears after fifty cycles (**Figure 3b**). In addition, compared with the 50th (**Figure 3b**), 150th (**Figure 3c**), and 300th (**Figure 3d**) cycles, a significant capacity decay of planar Cu foil is observed, which may be due to the growth of Li dendrites further leading to the formation of dead Li and the repeated consumption of the electrolyte caused by unstable SEI. For commercial Cu foam, the capacity decay appears about 300 cycles, illustrating that there is less irreversible Li deposition on the 3D Cu and more stable SEI than planar Cu. By contrast, the galvanostatic charge/discharge profiles of the rGO@Cu foam shows outstanding stability even after 300 cycles, and rGO@Cu foam also exhibits a superior capacity retention. These results demonstrate that the deposition of Li on rGO@Cu foam is more uniform and the formation of SEI is more stable than planar Cu and commercial Cu foam. To evaluate the long-term cycling stabilities of the Li anode with the three types of current collectors, the symmetric cells were assembled and examined at a current density of 1 mA cm^{-2} with a capacity of 1 mAh cm^{-2}. As shown in **Figure S4**, after 84 h, an abrupt voltage drop is detected for the planar Cu foil current collector with fluctuating voltage in the later hours. This could be explained by an internal soft short-circuit with Li dendrite penetration (Lin et al., 2016). A distinct decrease in polarization is observed in commercial Cu foam, in the initial 80 h, may be due to the gradual stabilization of the SEI layer. By contrast, the 3D rGO@Cu current collector maintains a much lower and more stable hysteresis after 400 h, illustrating that its extended reduced graphene layer can reduce the local current density and inhibit the growth of Li dendrites. The cycling Coulombic efficiencies of 2D Cu foil, 3D commercial Cu foam, and rGO@Cu foam current collectors were examined at a current density of 1 mA cm^{-2}. CE is computed by the ratio of the total amount of Li stripped away, vs. the deposited amount on the current collector in each cycle. As shown in **Figure 3e**, the CE of 2D Cu foil is stabilized at 97% during the 60 cycles, and then the CE is reduced gradually to <92% after 110 cycles. This may be ascribed to the irreversible Li deposition because of the formation of Li dendrites and dead Li. As for the commercial Cu foam current collector, the CE can reach more than 97% and be sustained during 225 cycles, showing that the Cu foam current collector with a special porous structure does help to accommodate more Li^+, hence hindering the growth of Li dendrites and extending the cycle life, whereas the CE of the 3D Cu foam becomes unstable after only 260 cycles and drops to below 96%. The rGO@Cu foam as current collector was conducted to further develop the cycling performance in comparison to 2D planar Cu foil and commercial Cu foam. The Columbic efficiency of rGO@Cu foam maintains a stability as high as 98.5% for over 350 cycles, which demonstrates that the covered reduced graphene oxide on the 3D Cu foam has significant effects and improves the Columbic efficiency and cycling stability in contrast to commercial Cu foam. To further explain the effect of the reduced graphene oxide layer on the improvement of the Cu foam interfaces, EIS was elected to evaluate the interfacial resistance of the planar Cu foil, commercial Cu foam, and rGO@Cu foam current collectors. The Nyquist plots of the three types of current collectors is displayed in **Figure 3f**. Comparing the intercept and the diameter of the first semicircle in each sample, the rGO@Cu foam possesses smaller SEI film resistance (4 Ω cm^2) than commercial Cu foam (5.9 Ω cm^2) and planar Cu foil (6.5 Ω cm^2), which could be attributed to the stable SEI film modified by the reduced graphene layer. In addition, the second semicircle reflects the charge transfer (interfacial) resistance Rct (Schipper et al., 2018; Wu et al., 2019). The rGO@Cu foam and commercial Cu foam have considerably smaller charge transfer resistance (24 and 30 Ω cm^2) compared with planar Cu foil (184 Ω cm^2). It suggests that a large amount of Li dendrites and dead Li are deposited on the surface of Cu foil. All the results confirm that the rGO@Cu foam current collector possesses superior properties such as higher electrochemical stability, better capacity retention, and Li dendrite suppression.

Figure 4 illustrates the behaviors of Li deposition on the 2D planar Cu, 3D commercial Cu foam, and rGO@Cu foam current collectors. Li is deposited on the substrate and unavoidably form some protuberances on the surface of planar Cu foil (**Figure 4a**), leading to the electric field being distributed unevenly, further promoting Li accumulation at the protuberances, finally growing into Li dendrites or even forming "dead Li." On the other hand, the formation of Li dendrites destroys SEI and further leads to the repeated formation of SEI film. Furthermore, these problems could deteriorate during cycling. In a Cu foam current collector (**Figure 4b**), owing to its special 3D porous structure, more space could be provided to accommodate Li. The porous current collector exhibits lower interfacial resistance and local current density compared to planar Cu, therefore Li^+ will distribute homogeneously on the surface of the 3D Cu foam and few Li dendrites will be formed. However, the phenomenon of Li dendrites still worsens after cycling. For the rGO@Cu foam current collector (**Figure 4c**), Li dendrites are restrained effectively. The rGO@Cu foam current collector displays outstanding electric conductive and mechanical strength for Li deposition. Li favors deposition on the inner surface of

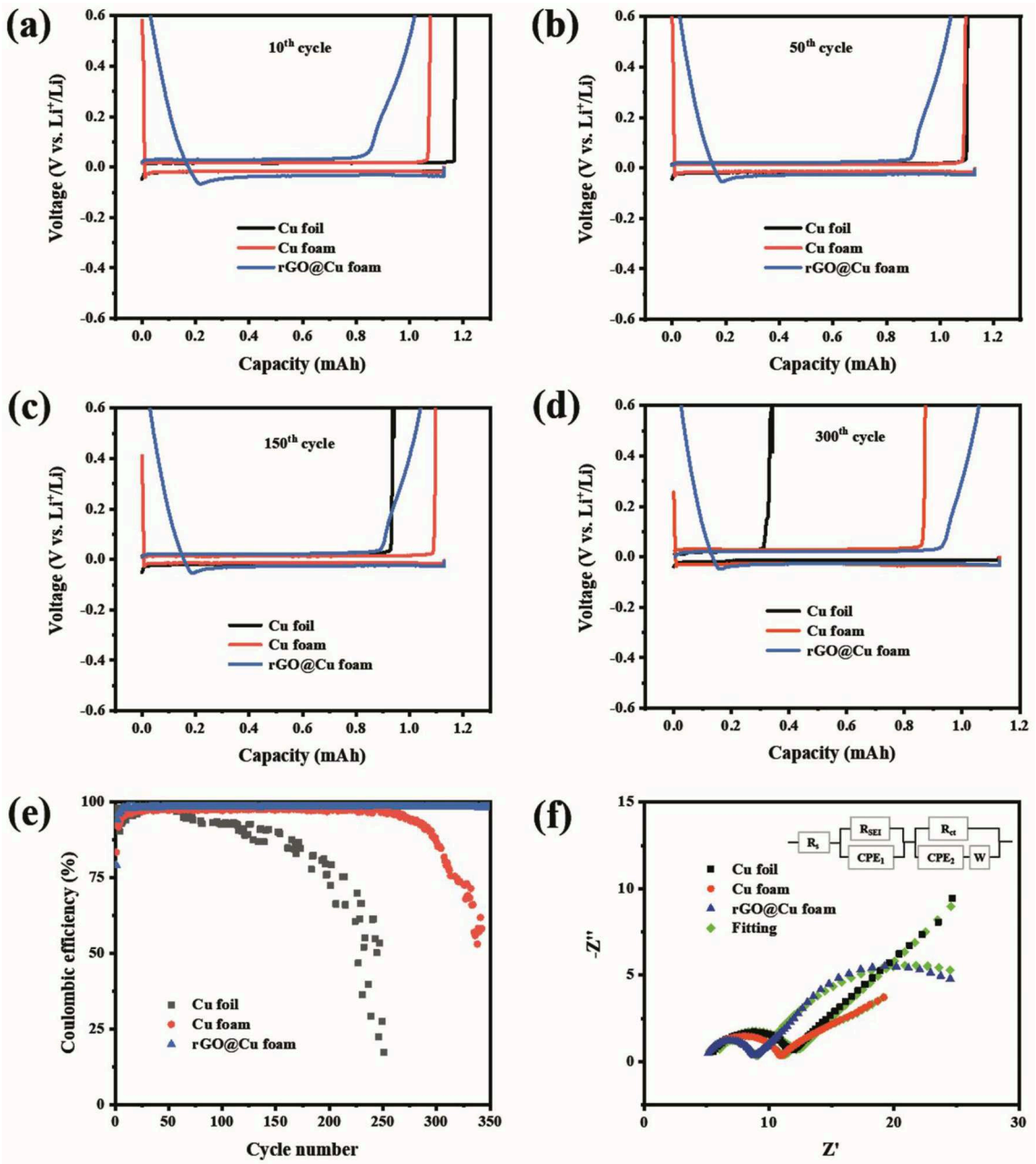

FIGURE 3 | The voltage profiles for the **(a)** 10th, **(b)** 50th, **(c)** 150th, and **(d)** 300th cycles with 2D planar Cu, 3D commercial Cu foam, and rGO@Cu foam as an electrode and Li metal as a reference electrode at a current density of 1.0 mA cm^{-2}. **(e)** CE of cells using Cu foil, Cu foam, or rGO@Cu foam as an electrode with Li metal as a counter electrode at a current density of 1 mA cm^{-2} with the deposition capacity at 1 mAh cm^{-2}. **(f)** Nyquist plots of Cu foil, Cu foam, and rGO@Cu foam. The impedance is obtained after 300 cycles with a current density at 1 mA cm^{-2} and a cycling capacity of 1 mAh cm^{-2}.

the rGO@Cu foam current collector. This obviously strengthens the stability of SEI and reduces the consumption of Li. In order to clearly observe the morphology of Li dendrite growth, the SEM images of the surfaces of current collectors are shown in **Figures 4d–f** with high magnifications. In the planar Cu foil, many Li filaments (**Figure 4d**) with lengths of $<3\,\mu m$ (**Figure S5**a) could be discovered after long-term cycling, leading to penetration of the separator and causing short circuiting of the cell. In addition, a loose structure is composed as a result of the formation of Li dendrites and dead Li. This loosely aggregated structure further gives rise to the electrical field being distributed unevenly and accelerates Li being deposited unequally. By contrast, for a 3D commercial Cu foam, there are only a few fibrous Li and some mossy Li formed on the

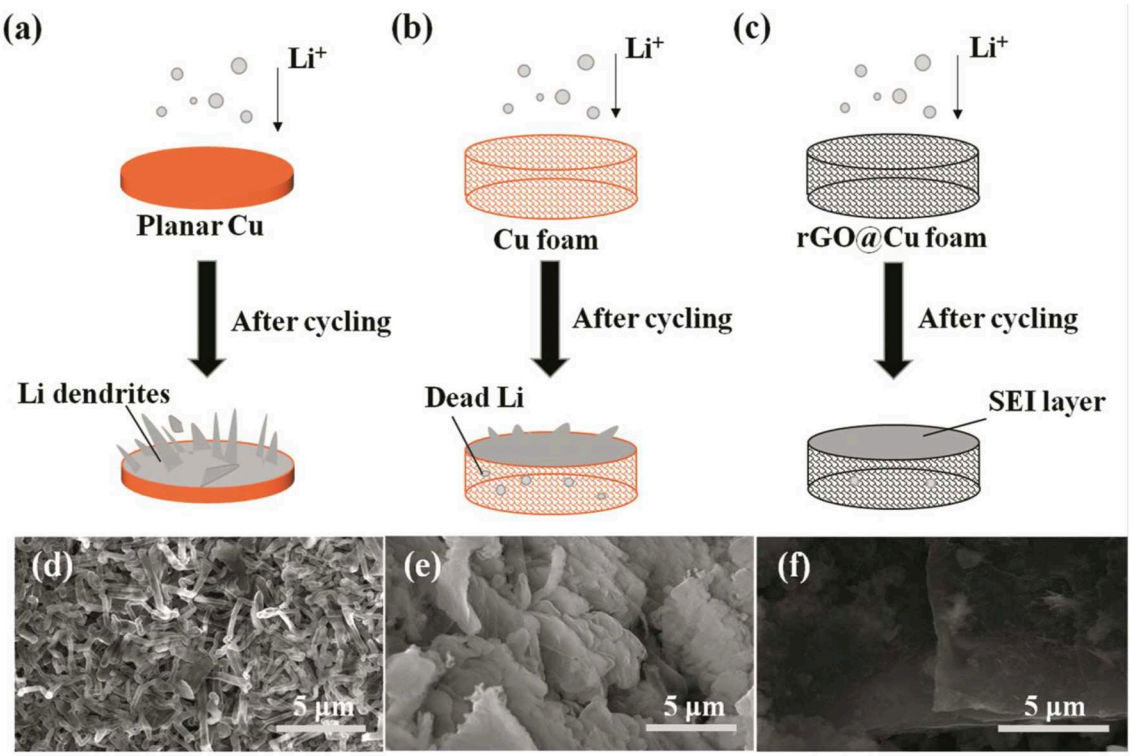

FIGURE 4 | Schematic representations showing the process of Li deposition on **(a)** bare planar Cu, **(b)** Cu foam, and **(c)** rGO@Cu foam. SEM images of surfaces of **(d)** bare planar Cu, **(e)** Cu foam and **(f)** rGO@Cu foam after cycles.

surface of the current collector (**Figure 4e**), indicating that the porous structure of the 3D Cu foam current collector revealed an excellent property to accommodate the expansion of the deposited Li. **Figure S5**b shows a magnified surface of 3D Cu foam after cycling, illustrating that it provides a more stable working electrode structure and interface than planar Cu foil. Moreover, compared with commercial Cu foam, the SEM images of rGO@Cu foam, as shown in **Figure 4f** and **Figure S5**c, clearly show that the surface of this composite electrode is remarkably smooth in general without obvious Li dendrites or mossy Li under the same conditions. This result may be explained by the fact that the rGO@Cu foam current collector can prevent the growth of Li dendrites and remove the potential of Li-metal battery hazards. This flat surface could be due to the rGO@Cu foam combined with the benefits of the rGO and 3D porous structure. rGO works as a protective layer to inhibit the growth of Li dendrites and the 3D porous structure promotes uniform deposition of Li into the interspace of the rGO@Cu foam current collector, improving cycling stability and the lifespan of Li-metal batteries.

To further investigate the battery performance under practical applications, the $LiFePO_4$/2D-Cu-Li, $LiFePO_4$/3D-Cu-Li, and $LiFePO_4$/rGO@Cu-Li full cells were assembled and galvanostatically cycled from 2.0 to 4.2 V at 1 C. **Figure 5a** exhibits the long-term cycling performance of the $LiFePO_4$/2D-Cu-Li, $LiFePO_4$/3D-Cu-Li, and $LiFePO_4$/rGO@Cu-Li full cells at 1 C. For $LiFePO_4$/2D-Cu-Li cells, the discharge capacity is about 132.2 mAh g^{-1} in the first cycle and starts to decrease obviously after 15 cycles. The reversible capacity of $LiFePO_4$/2D-Cu-Li cells is dropped to 57.6 mAh g^{-1} with a CE of 95.7% at 200 cycles. The depletion of the electrolyte is due to the continuous decomposition at Li metal and the formation of "dead Li." While as for the $LiFePO_4$/3D-Cu-Li cells, the reversible capacity degrades gradually from the beginning with 131.7 to 98.6 mAh g^{-1} and the CE is maintained at about 99% during 200 cycles. It can be seen that the cycling performance of $LiFePO_4$/3D-Cu-Li cells is greatly improved compared with $LiFePO_4$/2D-Cu-Li. By contrast, the $LiFePO_4$/rGO@Cu-Li cells exhibit a higher initial capacity of 132.9 mAh g^{-1} and better capacity retention with a discharge capacity of 126.2 mAh g^{-1} after 200 cycles. Moreover, it shows a more stable CE of 99% for more than 200 cycles, illustrating that the $LiFePO_4$/rGO@Cu-Li cells display outstanding capacity retention and cycling stability. **Figure 5b** shows the rate performance of these three kinds of $LiFePO_4$ full cells with 2D Cu, 3D Cu foam, and rGO@Cu foam current collectors under different current densities. The rate capability of cells was evaluated under cycling at rates varying from 0.2 C to 5 C with intervals of 10 cycles. It can be observed that the capacity almost goes back to the previous corresponding value when the rate is recovered to 0.5 C, and all the full cells display obvious capacity decay with current density increases. The $LiFePO_4$/rGO@Cu-Li cells exhibit a capacity of 88 mAh g^{-1} at 5 C, indicating its enhanced discharge capacity, especially at a high cycling rate. While under the same conditions,

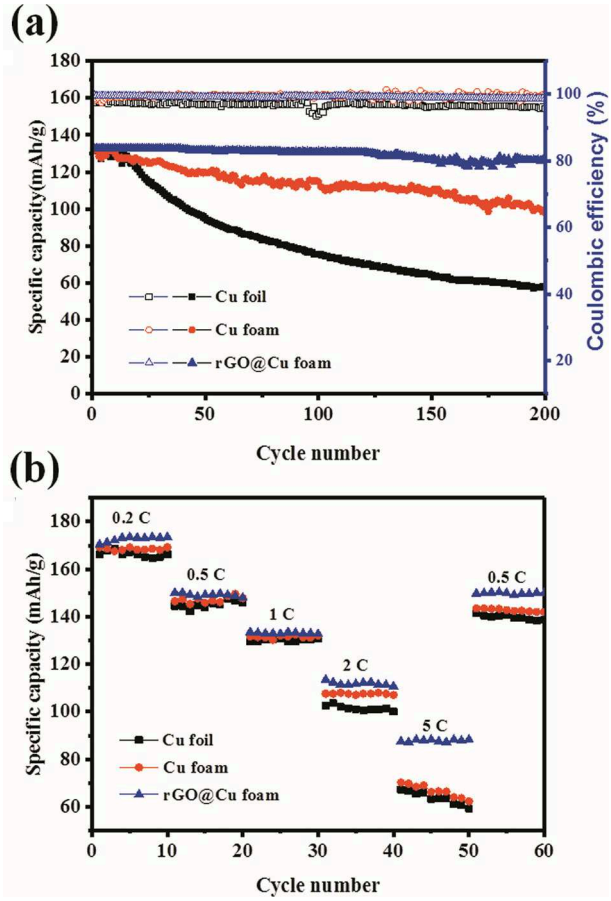

FIGURE 5 | Electrochemical characterization of full cells using a $LiFePO_4$ cathode and a Li metal anode with 2D planar Cu, 3D Cu foam, or rGO@Cu foam as a current collector. **(a)** Cycling performance of $LiFePO_4$/2D-Cu-Li, $LiFePO_4$/3D-Cu-Li, $LiFePO_4$/rGO@Cu-Li at 1 C. **(b)** Rate performance of $LiFePO_4$/2D-Cu-Li, $LiFePO_4$/3D-Cu-Li, $LiFePO_4$/rGO@Cu-Li from 0.2 to 5 C.

the capacity of $LiFePO_4$/2D-Cu-Li cells almost reach 67 mAh g^{-1} and $LiFePO_4$/3D-Cu-Li cells are 70 mAh g^{-1}, which is still less than the $LiFePO_4$/rGO@Cu-Li cells. In addition, the $LiFePO_4$/rGO@Cu-Li cells always remain at the highest capacity compared to $LiFePO_4$/2D-Cu-Li and $LiFePO_4$/3D-Cu-Li at different current densities. These results indicate that the $LiFePO_4$/rGO@Cu-Li shows excellent rate performance and a higher capacity, demonstrating its great potential for practical application.

CONCLUSIONS

In summary, in this study, we have reported a simple but effective strategy to suppress the growth of Li dendrites and to facilitate the uniform deposition of Li using a rGO@Cu foam as a current collector. After soaking in GO suspension, the commercial Cu foam is covered with a layered structure of rGO. The rGO@Cu foam exhibits superior performance because the rGO layer works as a protective film to inhibit the growth of Li dendrites. Furthermore, its special porous structure can provide more space to accommodate Li metal deposition and reduces the effective electrode current density. The half-cell using rGO@Cu foam as an electrode and Li metal as a counter electrode exhibits a high CE of above 98.5% after 350 cycles under the current density of 1 mA cm^{-2}. As for the $LiFePO_4$/rGO@Cu-Li full cells, the reversible capacity is maintained at 126.2 mAh g^{-1} and the CE can remain as high as 99% after 200 cycles at 1 C. The $LiFePO_4$/rGO@Cu-Li full cells also show a stable rate performance compared to $LiFePO_4$/2D-Cu-Li and $LiFePO_4$/3D-Cu-Li cells. The superior properties of the rGO@Cu foam current collector are beneficial in achieving the effective suppression of Li dendrites for next-generation Li-metal battery applications.

DATA AVAILABILITY STATEMENT

All datasets generated for this study are included in the article/**Supplementary Material**.

AUTHOR CONTRIBUTIONS

All authors contributed to manuscript revision, read, and approved the submitted version.

FUNDING

This study was funded by the National Natural Science Foundation of China (51974219, 51974222); Natural Science Basic Research Plan in Shaanxi Province (2019JQ-764, 2018JM5135); and Project (18JK0474) supported by Shaanxi Provincial Education Department, China.

SUPPLEMENTARY MATERIAL

The Supplementary Material for this article can be found online at: https://www.frontiersin.org/articles/10.3389/fchem.2019.00748/full#supplementary-material

REFERENCES

Bai, M., Xie, K., Yuan, K., Zhang, K., Li, N., Shen, C., et al. (2018). A scalable approach to dendrite-free lithium anodes via spontaneous reduction of spray-coated graphene oxide layers. *Adv. Mater.* 30:1801213. doi: 10.1002/adma.201801213

Bobnar, J., Lozinsek, M., Kapun, G., Njel, C., Dedryvere, R., Genorio, B., et al. (2018). Fluorinated reduced graphene oxide as a protective layer on the metallic lithium for application in the high energy batteries. *Sci. Rep.* 8:5819. doi: 10.1038/s41598-018-23991-2

Bouchet, R., Maria, S., Meziane, R., Aboulaich, A., Lienafa, L., Bonnet, J.-P., et al. (2013). Single-ion BAB triblock copolymers as highly efficient electrolytes for lithium-metal batteries. *Nat. Mater.* 12, 452–457. doi: 10.1038/nmat3602

Cheng, X.-B., Yan, C., Chen, X., Guan, C., Huang, J.-Q., Peng, H.-J., et al. (2017). Implantable solid electrolyte interphase in lithium-metal batteries. *Chem* 2, 258–270. doi: 10.1016/j.chempr.2017.01.003

Ding, F., Xu, W., Graff, G. L., Zhang, J., Sushko, M. L., Chen, X., et al. (2013). Dendrite-free lithium deposition via self-healing electrostatic shield mechanism. *J. Am. Chem. Soc.* 135, 4450–4456. doi: 10.1021/ja312241y

Gao, Y., Yi, R., Li, Y. C., Song, J., Chen, S., Huang, Q., et al. (2017). General method of manipulating formation, composition, and morphology of solid-electrolyte interphases for stable Li-alloy anodes. *J. Am. Chem. Soc.* 139, 17359–17367. doi: 10.1021/jacs.7b07584

Goodenough, J. B., and Kim, Y. (2010). Challenges for rechargeable Li batteries. *Chem. Mater.* 22, 587–603. doi: 10.1021/cm901452z

Gu, Y., Wang, W. W., Li, Y. J., Wu, Q. H., Tang, S., Yan, J. W., et al. (2018). Designable ultra-smooth ultra-thin solid-electrolyte interphases of three alkali metal anodes. *Nat. Commun.* 9:1339. doi: 10.1038/s41467-018-03466-8

Han, X., Gong, Y., Fu, K. K., He, X., Hitz, G. T., Dai, J., et al. (2017). Negating interfacial impedance in garnet-based solid-state Li metal batteries. *Nat. Mater.* 16, 572–579. doi: 10.1038/nmat4821

Haregewoin, A. M., Wotango, A. S., and Hwang, B.-J. (2016). Electrolyte additives for lithium ion battery electrodes: progress and perspectives. *Energy Environ. Sci.* 9, 1955–1988. doi: 10.1039/C6EE00123H

Hu, C., Zhai, X., Liu, L., Zhao, Y., Jiang, L., and Qu, L. (2013). Spontaneous reduction and assembly of graphene oxide into three-dimensional graphene network on arbitrary conductive substrates. *Sci. Rep.* 3:2065. doi: 10.1038/srep02065

Ji, L., Lin, Z., Alcoutlabi, M., and Zhang, X. (2011). Recent developments in nanostructured anode materials for rechargeable lithium-ion batteries. *Energy Environ. Sci.* 4, 2682–2699. doi: 10.1039/c0ee00699h

Kamaya, N., Homma, K., Yamakawa, Y., Hirayama, M., Kanno, R., Yonemura, M., et al. (2011). A lithium superionic conductor. *Nat. Mater.* 10, 682–686. doi: 10.1038/nmat3066

Kim, K. H., Yang, M., Cho, K. M., Jun, Y. S., Lee, S. B., and Jung, H. T. (2013). High quality reduced graphene oxide through repairing with multi-layered graphene ball nanostructures. *Sci. Rep.* 3:3251. doi: 10.1038/srep03251

Kotobuki, M., Kanamura, K., Sato, Y., and Yoshida, T. (2011). Fabrication of all-solid-state lithium battery with lithium metal anode using Al_2O_3-added $Li_7La_3Zr_2O_{12}$ solid electrolyte. *J. Power Sources* 196, 7750–7754. doi: 10.1016/j.jpowsour.2011.04.047

Kozen, A. C., Lin, C. F., Pearse, A. J., Schroeder, M. A., Han, X., Hu, L., et al. (2015). Next-generation lithium metal anode engineering via atomic layer deposition. *ACS Nano* 9, 5884–5892. doi: 10.1021/acsnano.5b02166

Lee, H., Lee, D. J., Kim, Y.-J., Park, J.-K., and Kim, H.-T. (2015). A simple composite protective layer coating that enhances the cycling stability of lithium metal batteries. *J. Power Sources* 284, 103–108. doi: 10.1016/j.jpowsour.2015.03.004

Li, G., Jing, M., Chen, Z., He, B., Zhou, M., and Hou, Z. (2017). Self-assembly of porous CuO nanospheres decorated on reduced graphene oxide with enhanced lithium storage performance. *RSC Adv.* 7, 10376–10384. doi: 10.1039/C6RA28724G

Li, N., Wei, W., Xie, K., Tan, J., Zhang, L., Luo, X., et al. (2018). Suppressing dendritic lithium formation using porous media in lithium metal-based batteries. *Nano Lett.* 18, 2067–2073. doi: 10.1021/acs.nanolett.8b00183

Li, Q., Zhu, S., and Lu, Y. (2017). 3D porous Cu current collector/Li-metal composite anode for stable lithium-metal batteries. *Adv. Funct. Mater.* 27:1606422. doi: 10.1002/adfm.201606422

Li, W., Yao, H., Yan, K., Zheng, G., Liang, Z., Chiang, Y. M., et al. (2015). The synergetic effect of lithium polysulfide and lithium nitrate to prevent lithium dendrite growth. *Nat. Commun.* 6:7436. doi: 10.1038/ncomms8436

Li, Y., Zhang, W., Dou, Q., Wong, K. W., and Ng, K. M. (2019). $Li_7La_3Zr_2O_{12}$ ceramic nanofiber-incorporated composite polymer electrolytes for lithium metal batteries. *J. Mater. Chem. A* 7, 3391–3398. doi: 10.1039/C8TA11449H

Liang, Z., Yan, K., Zhou, G., Pei, A., Zhao, J., Sun, Y., et al. (2019). Composite lithium electrode with mesoscale skeleton via simple mechanical deformation. *Sci. Adv.* 5:eaau5655. doi: 10.1126/sciadv.aau5655

Lin, D., Liu, Y., Liang, Z., Lee, H. W., Sun, J., Wang, H., et al. (2016). Layered reduced graphene oxide with nanoscale interlayer gaps as a stable host for lithium metal anodes. *Nat. Nanotechnol.* 11, 626–632. doi: 10.1038/nnano.2016.32

Liu, S., Wang, G., Hou, H., Liu, X., Duan, J., and Liao, Q. (2016). Binder-free combination of large area reduced graphene oxide nanosheets with Cu foil for lithium ion battery anode. *Diam. Relat. Mater.* 68, 102–108. doi: 10.1016/j.diamond.2016.06.013

Liu, Y., Lin, D., Yuen, P. Y., Liu, K., Xie, J., Dauskardt, R. H., et al. (2017). An artificial solid electrolyte interphase with high Li-ion conductivity, mechanical strength, and flexibility for stable lithium metal anodes. *Adv. Mater.* 29:1605531. doi: 10.1002/adma.201605531

Lu, J., Cheng, L., Lau, K. C., Tyo, E., Luo, X., Wen, J., et al. (2014a). Effect of the size-selective silver clusters on lithium peroxide morphology in lithium-oxygen batteries. *Nat. Commun.* 5:4895. doi: 10.1038/ncomms5895

Lu, J., Li, L., Park, J. B., Sun, Y. K., Wu, F., and Amine, K. (2014b). Aprotic and aqueous Li-O_2 batteries. *Chem. Rev.* 114, 5611–5640. doi: 10.1021/cr400573b

Luo, D., Zhang, G., Liu, J., and Sun, X. (2011). Evaluation criteria for reduced graphene oxide. *J. Phys. Chem. C* 115, 11327–11335. doi: 10.1021/jp110001y

Ma, L., Kim, M. S., and Archer, L. A. (2017). Stable artificial solid electrolyte interphases for lithium batteries. *Chem. Mater.* 29, 4181–4189. doi: 10.1021/acs.chemmater.6b03687

Manthiram, A., Fu, Y., and Su, Y.-S. (2012). Challenges and prospects of lithium-sulfur batteries. *Acc. Che. Res.* 46, 1125–1134. doi: 10.1021/ar300179v

Mattevi, C., Eda, G., Agnoli, S., Miller, S., Mkhoyan, K. A., Celik, O., et al. (2009). Evolution of electrical, chemical, and structural properties of transparent and conducting chemically derived graphene thin films. *Adv. Funct. Mater.* 19, 2577–2583. doi: 10.1002/adfm.200900166

Narayanan, S., Ramezanipour, F., and Thangadurai, V. (2012). Enhancing Li ion conductivity of garnet-type $Li_5La_3Nb_2O_{12}$ by Y- and Li-codoping: synthesis, structure, chemical stability, and transport properties. *J. Phys. Chem. C* 116, 20154–20162. doi: 10.1021/jp304737x

Novakov, T., and Prins, R. (1971). Band structure and the shakeup photoelectron spectra of copper and nickel halides and oxides. *Solid State Commun.* 9, 1975–1979. doi: 10.1016/0038-1098(71)90594-1

Schipper, F., Bouzaglo, H., Dixit, M., Erickson, E. M., Weigel, T., Talianker, M., et al. (2018). From surface ZrO_2 coating to bulk Zr doping by high temperature annealing of nickel-rich lithiated oxides and their enhanced electrochemical performance in lithium ion batteries. *Adv. Energy Mater.* 8:1701682. doi: 10.1002/aenm.201701682

Shi, P., Li, T., Zhang, R., Shen, X., Cheng, X. B., Xu, R., et al. (2019). Lithiophilic LiC_6 layers on carbon hosts enabling stable Li metal anode in working batteries. *Adv. Mater.* 31:1807131. doi: 10.1002/adma.201807131

So, J. Y., Lee, C. H., Kim, J. E., Kim, H. J., Jun, J., and Bae, W. G. (2018). Hierarchically nanostructured CuO-Cu current collector fabricated by hybrid methods for developed Li-ion batteries. *Materials* 11:1018. doi: 10.3390/ma11061018

Soleimani, E., and Moghaddami, R. (2017). Synthesis, characterization and thermal properties of PMMA/CuO polymeric nanocomposites. *J. Mater. Sci. Mater. Electron.* 29, 4842–4854. doi: 10.1007/s10854-017-8440-y

Song, M.-K., Park, S., Alamgir, F. M., Cho, J., and Liu, M. (2011). Nanostructured electrodes for lithium-ion and lithium-air batteries: the latest developments, challenges, and perspectives. *Mat. Sci. Eng. R.* 72, 203–252. doi: 10.1016/j.mser.2011.06.001

Stankovich, S., Dikin, D. A., Piner, R. D., Kohlhaas, K. A., Kleinhammes, A., Jia, Y., et al. (2007). Synthesis of graphene-based nanosheets via chemical reduction of exfoliated graphite oxide. *Carbon* 45, 1558–1565. doi: 10.1016/j.carbon.2007.02.034

Tang, Y., Shen, K., Lv, Z., Xu, X., Hou, G., Cao, H., et al. (2018). Three-dimensional ordered macroporous Cu current collector for lithium metal anode: uniform nucleation by seed crystal. *J. Power Sources* 403, 82–89. doi: 10.1016/j.jpowsour.2018.09.083

Wu, H., Cao, Y., Geng, L., and Wang, C. (2017). *In situ* formation of stable interfacial coating for high performance lithium metal anodes. *Chem. Mater.* 29, 3572–3579. doi: 10.1021/acs.chemmater.6b05475

Wu, X., Li, Y., Zhao, S., Zeng, F., Peng, X., Xiang, Y., et al. (2019). Fabrication of F-doped, C-coated $NiCo_2O_4$ nanocomposites and its electrochemical performances for lithium-ion batteries. *Solid State Ion* 334, 48–55. doi: 10.1016/j.ssi.2019.01.039

Xie, K., Wei, W., Yuan, K., Lu, W., Guo, M., Li, Z., et al. (2016). Toward dendrite-free lithium deposition via structural and interfacial synergistic effects of 3D graphene@Ni scaffold. *ACS Appl. Mater. Interfaces* 8, 26091–26097. doi: 10.1021/acsami.6b09031

Xu, W., Wang, J., Ding, F., Chen, X., Nasybulin, E., Zhang, Y., et al. (2014). Lithium metal anodes for rechargeable batteries. *Energy Environ. Sci.* 7, 513–537. doi: 10.1039/C3EE40795K

Yan, H., Shen, C., Yuan, K., Zhang, K., Liu, X., Wang, J.-G., et al. (2018). Hosting ultrahigh areal capacity and dendrite-free lithium via porous scaffold. *ACS Sustainable Chem. Eng.* 6, 4776–4783. doi: 10.1021/acssuschemeng.7b03910

Yang, C. P., Yin, Y. X., Zhang, S. F., Li, N. W., and Guo, Y. G. (2015). Accommodating lithium into 3D current collectors with a submicron skeleton towards long-life lithium metal anodes. *Nat. Commun.* 6:8058. doi: 10.1038/ncomms9058

Ye, H., Yin, Y.-X., Zhang, S.-F., Shi, Y., Liu, L., Zeng, X.-X., et al. (2017). Synergism of Al-containing solid electrolyte interphase layer and Al-based colloidal particles for stable lithium anode. *Nano. Energy* 36, 411–417. doi: 10.1016/j.nanoen.2017.04.056

Yun, Q., He, Y. B., Lv, W., Zhao, Y., Li, B., Kang, F., et al. (2016). Chemical dealloying derived 3D porous current collector for Li metal anodes. *Adv. Mater.* 28, 6932–6939. doi: 10.1002/adma.201601409

Zaaba, N. I., Foo, K. L., Hashim, U., Tan, S. J., Liu, W.-W., and Voon, C. H. (2017). Synthesis of graphene oxide using modified Hummers method: solvent influence. *Proc. Eng.* 184, 469–477. doi: 10.1016/j.proeng.2017.04.118

Zhang, C., Lv, W., Zhou, G., Huang, Z., Zhang, Y., Lyu, R., et al. (2018). Vertically aligned lithiophilic CuO nanosheets on a Cu collector to stabilize lithium deposition for lithium metal batteries. *Adv. Energy Mater.* 8:1703404. doi: 10.1002/aenm.201703404

Zhao, Y., Ding, Y., Li, Y., Peng, L., Byon, H. R., Goodenough, J. B., et al. (2015). A chemistry and material perspective on lithium redox flow batteries towards high-density electrical energy storage. *Chem. Soc. Rev.* 44, 7968–7996. doi: 10.1039/C5CS00289C

Zheng, G., Lee, S. W., Liang, Z., Lee, H. W., Yan, K., Yao, H., et al. (2014). Interconnected hollow carbon nanospheres for stable lithium metal anodes. *Nat. Nanotechnol.* 9, 618–623. doi: 10.1038/nnano.2014.152

Zheng, J., Engelhard, M. H., Mei, D., Jiao, S., Polzin, B. J., Zhang, J.-G., et al. (2017). Electrolyte additive enabled fast charging and stable cycling lithium metal batteries. *Nat. Energy* 2:17012. doi: 10.1038/nenergy.2017.12

Conflict of Interest: The authors declare that the research was conducted in the absence of any commercial or financial relationships that could be construed as a potential conflict of interest.

frontiers in Chemistry

ORIGINAL RESEARCH
published: 10 January 2020
doi: 10.3389/fchem.2019.00893

Effect of Aging-Induced Dioxolane Polymerization on the Electrochemistry of Carbon-Coated Lithium Sulfide

Lucas Lodovico[1,2], *Alberto Varzi*[1,2] *and Stefano Passerini*[1,2]*

[1] Helmholtz Institute Ulm (HIU), Ulm, Germany, [2] Karlsruhe Institute of Technology (KIT), Karlsruhe, Germany

Lithium sulfide-based materials have been considered as potential positive electrodes for the next generation batteries. Lithium sulfide is the fully lithiated form of sulfur, i.e., they share the same high theoretical capacity. However, it has the benefit of already containing lithium, which allows making cells with lithium-free negative electrodes. Lithium sulfide, however, shares with sulfur the polysulfide dissolution drawback upon cycling. One possible solution to this problem is to envelop the active material particles with carbonaceous materials. In this work, we investigate the effect of a nitrogen-rich carbon coating on lithium sulfide particles. The effect of such coating on the surface properties and electrochemistry of lithium sulfide cathodes is investigated in details, in particular, regarding its interaction with fresh vs. aged electrolyte. The polymerization of dioxalane (DOL) due to aging is found to affect the electrochemistry of lithium sulfide and, interestingly, to improve the cycling performance.

Keywords: lithium-sulfur battery, lithium sulfide, dioxalane, electrolyte aging, N-rich carbon-coating, ethylenediamine

OPEN ACCESS

Edited by:
Shengkui Zhong,
Soochow University, China

Reviewed by:
Donghai Wang,
Pennsylvania State University (PSU), United States
Yanwei Li,
Guilin University of Technology, China

***Correspondence:**
Stefano Passerini
stefano.passerini@kit.edu

Specialty section:
This article was submitted to Electrochemistry, a section of the journal Frontiers in Chemistry

Received: *13 September 2019*
Accepted: *11 December 2019*
Published: *10 January 2020*

Citation:
Lodovico L, Varzi A and Passerini S (2020) Effect of Aging-Induced Dioxolane Polymerization on the Electrochemistry of Carbon-Coated Lithium Sulfide. Front. Chem. 7:893. doi: 10.3389/fchem.2019.00893

INTRODUCTION

Lithium-sulfur batteries (LSBs) have attracted much attention in recent years, with the prospect of replacing lithium-ion batteries (LIBs) as energy source for automotive and, especially, flight applications as soon as 2030 (International and Agency, 2018). The main reason for this is the high theoretical capacity of sulfur, around 1,675 mAh g^{-1}, promising Li-S batteries with energy densities (based on the electrode materials only) as high as 2,600 Wh kg^{-1}. Sulfur-based cathodes, however, still possess a multitude of problems that need to be solved. The main challenge posed by sulfur is the high solubility of the intermediates formed during cycling (Xu et al., 2015). These intermediates take the form of polysulfides with general formula Li_2S_x, which are chain of sulfur atoms with x usually comprised between 3 and 8. At the end of discharge, solid discharge products (Li_2S and Li_2S_2) are finally formed. The first and most obvious consequences of polysulfides dissolution are low Coulombic efficiencies and loss of active material during battery operation.

In order to avoid these effects, a commonly used strategy is to physically constrain the polysulfides in the positive electrode (cathode), often by enveloping the active material's particles with an inert coating, such as carbon (Jeong et al., 2013; Agostini et al., 2014; Chen et al., 2014; Nan et al., 2014; Hwa et al., 2015; Wu et al., 2016). Carbon coating of sulfur, however, is all but trivial, owing to its low melting point and tendency to easily sublimate at moderate temperature. In these terms, the use of lithium sulfide as cathode active material presents interesting advantages. Besides being already in the lithiated state, which allows it to be paired with lithium-free negative (anode)

electrodes (Nanda et al., 2018), lithium sulfide is thermally stable up to rather high temperature allowing processing such as carbonization.

In this work, we investigate the effect of a nitrogen-rich carbon coating on lithium sulfide particles. Specifically, ethylenediamine-embedded lithium sulfide, previously reported by our group (Lodovico et al., 2019), is pyrolized in order to obtain carbon-coated lithium sulfide, with the ethylenediamine molecules serving as the carbon source. The use of this kind of diamine lead to a N-doped carbon coating with C:N weight ratios around 2:1. The effect of such coating on the surface properties and electrochemistry of lithium sulfide cathodes is investigated in details, in particular, regarding its interaction with fresh vs. aged electrolyte. It was found that upon prolonged storage (12+ months) the dioxolane-based electrolyte tends to polymerize, which greatly affects the behavior of Li_2S-based cathodes.

METHODS

Chemical and electrode preparations, infrared measurements, and cell assembly were carried out in a glove box (MBraun) filled with argon (O_2 and H_2O content below 0.1 ppm). The 1:1 volume ratio mixture of Dimethoxyethane (DME, Solvionic) and 1,3-Dioxolane (DOL, Solvionic) was used as the electrolyte solvent. Prior to mixing, the two solvents were individually dried using 3Å molecular sieves (Sigma Aldrich) to reach water contents below 20 ppm as determined via Karl-Fischer titration (Mettler-Toledo Titrator Compact C30). Appropriate amounts of lithium bis(trifluoromethanesulfonyl)imide (LiTFSI, Solvionic) and lithium nitrate ($LiNO_3$, Alfa Aesar) were dissolved into the DME-DOL solvent mixture to achieve concentration of 1 and 0.25 mol L^{-1}, respectively, using aluminum bottles. This electrolyte was used soon after its preparation (i.e., within 2 weeks; labeled as "fresh") or after storage (i.e., after more than 1 year, labeled "aged"). Besides the aging, both the electrolytes were stored in sealed aluminum bottle inside the glove box.

Carbon-coated lithium sulfide (Li_2S-CC) was prepared using ethylenediamine-containing lithium sulfide (Li_2S-En) as precursor. Li_2S-En synthesis, carbon coating procedure, and electrode preparation is described in a previous work (Lodovico et al., 2019). The final material possesses a particle coating with a C:N weight ratio of about 2:1.

Li_2S-CC was employed as active electrode materials. The electrodes were prepared by manually grind-mixing the active material (Li_2S-CC) with the conductive carbon (Super C65; Imerys Graphite & Carbon) and the binder (polyvinylidene fluoride; PVdF 6020 from Solvay). The respective weight ratios were 53:37:10. The mixed powders were then dispersed with N-Methyl-2-pyrrolidone (NMP, Sigma Aldrich), and the resulting slurry cast over aluminum current collectors using the doctor blade method. Finally, the electrode tapes were dried at 60 °C under Ar.

For the determination of the electrolyte electrochemical stability window, carbon electrodes composed of Super C65 and PVdF were prepared in the 85:15 weight ratio. NMP was added to prepare the slurry, which was cast over the aluminum current collector as well.

Carbon electrodes were also prepared using nitrogen-rich carbon derived from carbonization of 1-ethyl-3-methylimidazolium tricyanomethanide (EMImTCM, IoLiTec). In short, EMImTCM was placed in an alumina boat inside a horizontal tube furnace under argon flow. The temperature was raised to 500°C at a rate of 5°C min^{-1} and kept for 5 h. The resulting carbonized sample (N-rich carbon) was composed of 62% carbon, 33% nitrogen, 2% hydrogen, and 3% oxygen (all values given as weight percentages). This composition is rather similar to that of the carbon coating in Li_2S-CC. The N-rich carbon was used to prepare electrodes as well, in which Super C-65, N-rich carbon, and PVdF were mixed in a 70:15:15 weight ratio, dispersed in NMP, and cast over aluminum foil, and dried at 120°C under vacuum for 48 h.

Electrochemical tests were performed using three electrode T-type cells (Swagelok), with lithium metal as both the reference and counter electrodes. The cells were assembled using 100 μL of electrolyte soaked into glass fiber separators (Whatman GF/A). For the capacity retention experiments, the cells stored at 20°C in climatic chamber (Binder) were galvanostatically cycled using a battery tester (Maccor S4000). The Li_2S-CC based cells were activated by charge at a C/20 rate (1C = 1,165 mAh g^{-1}) up to 4 V vs. Li/Li^+, followed by cycling at C/10 between 1.9 and 3.0 V vs. Li/Li^+.

Electrochemical impedance spectroscopy (EIS) measurements were performed using a BioLogic VMP3 multi-channel potentiostat. For that, the cells were cycled using the same procedures as mentioned above. However, after each discharge, the cell was allowed to rest at open-circuit for 2 h prior to measuring impedance. Spectra were recorded between frequencies of 200 kHz and 100 mHz, using a 5 mV signal amplitude.

The anodic electrochemical stability of the electrolytes was studied by cyclic voltammetry (CV), where the potential was scanned from 3 to 4 V vs. Li/Li^+. After cycling, each cell was disassembled inside a glove box, and the electrolyte recovered by centrifuging the glass fiber separators at 6,000 rpm for 10 min. The recovered electrolytes were analyzed via ATR-IR.

RESULTS AND DISCUSSION

Figure 1A shows the capacity retention of Li_2S-CC-based electrodes when using either the fresh (Li_2S-CC_F) or the aged (Li_2S-CC_A) electrolyte. It is evident that the electrolyte aging has a large impact on the cell performance. Surprisingly, the aged electrolyte provides higher discharge capacity as well as capacity retention upon 100 cycles. In order to better understand the reason behind this effect, the discharge curves of the cathode in each electrolyte were closely examined. The inset of **Figure 1A** shows the typical discharge curve of a Li_2S-based electrode after the initial activation charge leading to fully oxidized S. The first region (I) shows a potential plateau (around 2.4 V vs. Li/Li^+) followed by a slopy region, both associated with the reduction of molecular sulfur (S_8) to medium chain polysulfides

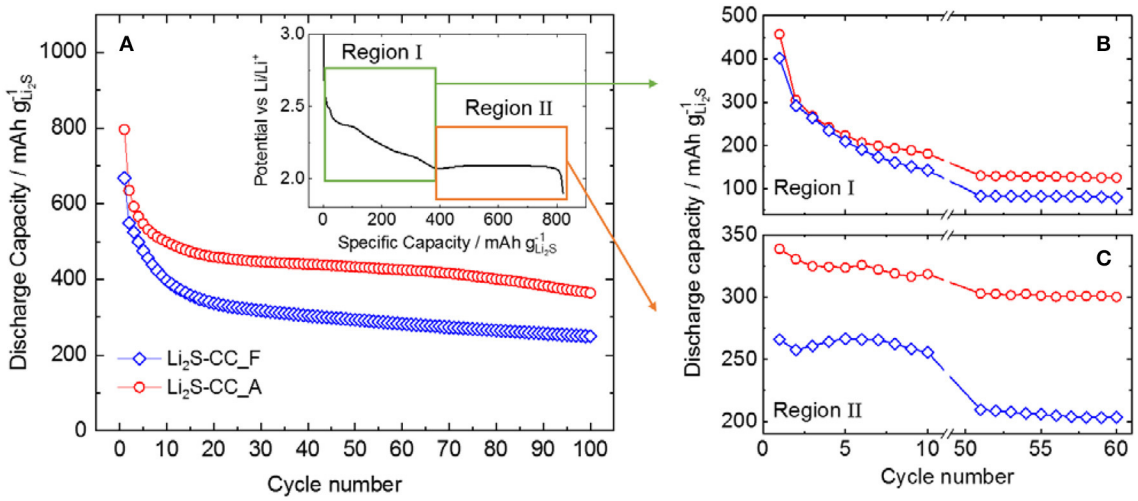

FIGURE 1 | (A) Capacity retention for cells using carbon-coated Li_2S either in fresh (Li_2S-CC_F) or aged electrolyte (Li_2S-CC_F). Inset: Typical discharge profile showing the two main discharge plateaus. Evolution of the capacity of **(B)** region I and **(C)** region II for selected cycles.

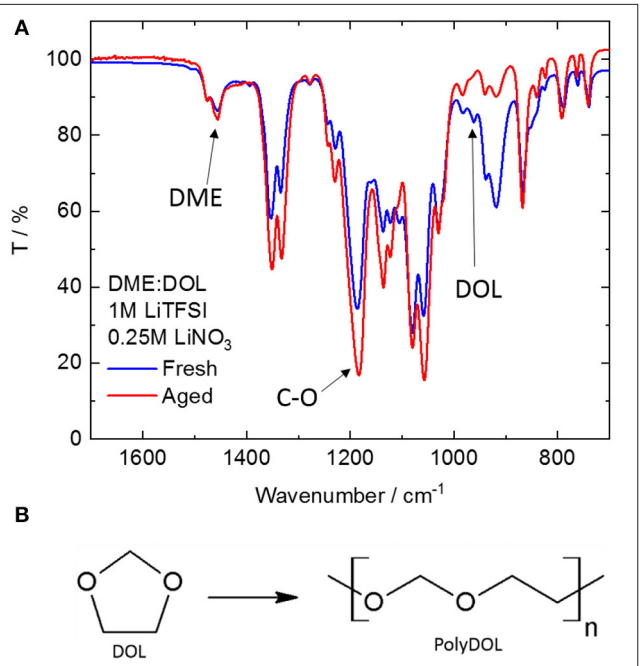

FIGURE 2 | (A) ATR-FTIR spectra of freshly prepared (blue line) and aged (red line). DME, DOL-based electrolyte. **(B)** Scheme of the polymerization reaction of DOL.

(Li_2S_x, x = 4–6). Afterwards, a second region (II) characterized by a long plateau at lower potential (around 2.1 V vs. Li/Li^+) appears, resulting from the reduction of lithium polysulfides to form the final solid discharge products (Li_2S_x, $1 \leq x \leq 2$) (Xu et al., 2015).

Figures 1B,C show the evolution of the capacity arising in regions I and II, respectively, for a few selected cycles (1st to 10th and 50th to 60th cycle). The individual capacity of each region is calculated as shown in the inset of **Figure 1A**. Namely, Region I is delimited between the beginning of discharge until the dip in potential before the low-potential plateau. Region II starts at the dip in potential until the end of discharge. As shown in **Figure 1B**, the capacity in the first region decrease sharply during the first 10 cycles to stabilize, however, after the 50th cycle. This indicates that, in both cells, less and less elemental sulfur (S_8) is formed in each charge, until a minimum is reached. In **Figure 1C**, the evolution of the capacity associated with the second region shows a considerably more peculiar behavior. It is clearly observed that the initial lower capacity of the fresh electrolyte cell with respect to that employing the aged one mostly arose from region II, where the solid discharge products are formed. In fact, while the Li_2S-CC_A cell delivered a stable capacity upon cycling, the Li_2S-CC_F cell showed a lower and more rapidly decreasing capacity in this region. This indicates that understanding the effect of the N-rich carbon-coating and the aged electrolyte on this voltage region is vital to a deeper comprehension of the lithium sulfide electrochemistry.

First of all, the electrolytes were studied by IR spectroscopy. **Figure 2** shows the infrared spectrum of a freshly prepared electrolyte (fresh), as well as that of one (with the same composition) after storage for at least 12 months (aged). Clearly, there are significant changes occurring during storage. The band at around 1,450 cm^{-1} due to the $-CH_3$ deformation in DME (Bailey, 1985) has a constant intensity before and after aging, showing that DME is stable. On the contrary, the band at 960 cm^{-1} due to the ring-breathing mode of DOL (Yang et al., 2005) shows an appreciable decrease upon storage. In fact, DOL is known to be relatively unstable (Okada et al., 1964), being prone to ring-opening reactions such as isomerization and polymerization (Okada et al., 1964). Isomerization of DOL leads to the formation of ethyl formate. However, no band corresponding to the vibration of the carbonyl group can be

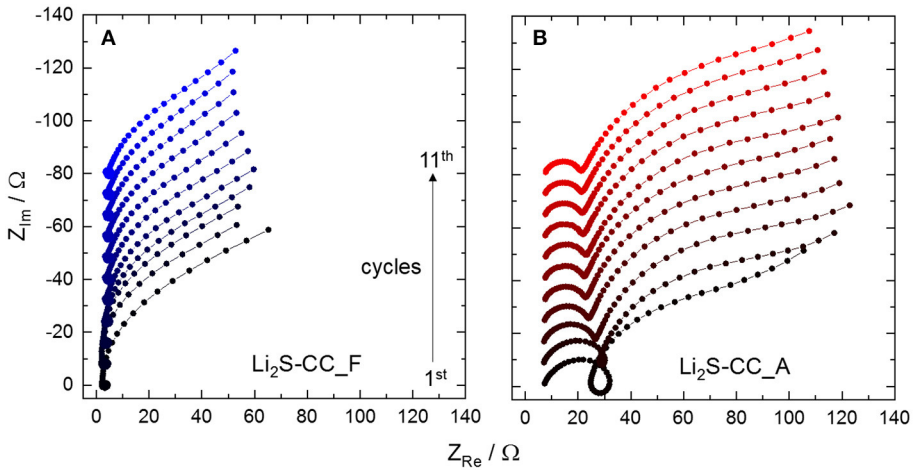

FIGURE 3 | Evolution of the electrochemical impedance spectra from the first to the eleventh cycle of **(A)** Li_2S-CC_F and **(B)** Li_2S-CC_A. The baselines of the spectra are shifted upward for clarity. All spectra were taken on 3-electrode cells in the discharged state.

detected in the aged electrolyte, thus ruling out this option. On the other hand, polymerization of DOL has been extensively studied and known to happen when a cationic initiator is present (Okada et al., 1964; Berman et al., 1969; Yang et al., 2005), leading to the formation of polydioxolane (polyDOL, **Figure 2B**), a polyether. The formation of polyDOL in the aged electrolyte is proven by the increase in the band at around 1,190 cm^{-1}, which is caused by the vibrations of the C-O bonds in linear molecules (Yoshida and Matsuura, 1998). Being a cyclic compound, C-O-C vibrations in DOL involve the whole ring and are thus heavily shifted (Makarewicz and Ha, 2001). The exact cause of this polymerization, in this case, is still unknown. Although DOL is known to be reactive, polymerization only happens in the presence of an appropriate initiator, usually one that can promote chain growth through a cationic mechanism. Analysis of the pure solvent mixture (1:1 DME:DOL) without addition of salt and stored under the same conditions for the same period of time shows no change in its spectrum, such that the culprit is likely the salts added to form the electrolyte ($LiNO_3$ and LiTFSI). Li^+ is known to coordinate the oxygen atoms in ether molecules (Blint, 1995), placing a partial positive charge on it. This weak initiating ability could explain the long storage times necessary to observe the polymerization appreciably.

In summary, the polymerization of DOL occurring upon prolonged storage of the electrolyte appears to be beneficial in Li_2S-CC_A cell, which shows a higher capacity than the Li_2S-CC_F cell (**Figure 1A**) mainly due to a higher and more stable capacity delivered in region II (**Figure 1C**). Similar results have been already reported in literature (Li et al., 2016). The comparison of electrolytes based on DME:DOL, TEGDME:DOL, and poly(ethylene glycol) dimethyl ether (PEGDME):DOL, for which the chain length increases in the aforementioned order, showed an increase in capacity of up to 2.5 times for the PEGDME:DOL based electrolyte compared to the DME:DOL based one. In order to better clarify the reason for the Li_2S-CC cell behavior, the EIS response of all electrodes in the discharged states upon cycling was collected.

The spectra of Li_2S-CC_F (**Figure 3A**) show a small high frequency (HF) semicircle evolving into a pseudo-inductive loop, followed by the beginning of a large, partially depressed, semicircle at low frequencies (LF). The pseudo-inductive loop has been related to intermediate species, i.e., polysulfides, adsorbed on the electrode's surface (Ding et al., 2013; Jeong et al., 2013; Lin et al., 2013; Xie et al., 2017). The depressed LF semicircle is typical of charge-transfer reactions, and corresponds to the reversible conversion of polysulfides to solid products. However, for Li_2S-CC_A (**Figure 3B**) some differences are clearly observed, the most relevant being the large HF semicircle before the pseudo-inductive loop. This feature may be associated to the presence of a surface layer on the electrode. The formation of a passivation layer is not unexpected. In fact, during the activation step the cathode is charged up to 4 V vs. Li/Li^+, while the electrolyte is only stable up to 3.6 V vs. Li/Li^+ (Yim et al., 2013). To test the effect of the N-rich carbon-coating on the electrode passivation, the anodic stability window of carbon electrodes (Li_2S-free) was investigated.

Figure 4 shows the anodic stability limit measurements of the electrolytes performed using carbon electrodes containing either the conductive carbon only (labeled as SC 65) or the mixture of conductive carbon and nitrogen-rich carbon (labeled as SC 65 + N-rich C), the latter mimicking carbon coating in Li_2S-CC electrodes. As seen in **Figures 4A,B**, the two electrolytes showed oxidation peaks above 3.5–3.6 V vs. Li/Li^+. For the fresh electrolyte, comparable peaks were observed with both kinds of carbon electrodes in the first cycle. The same occurred in the second cycle, where almost no oxidation current was recorded, indicating that the carbon electrodes underwent a passivation process upon the previous scan. However, the recorded peak current was substantially larger with the aged electrolyte,

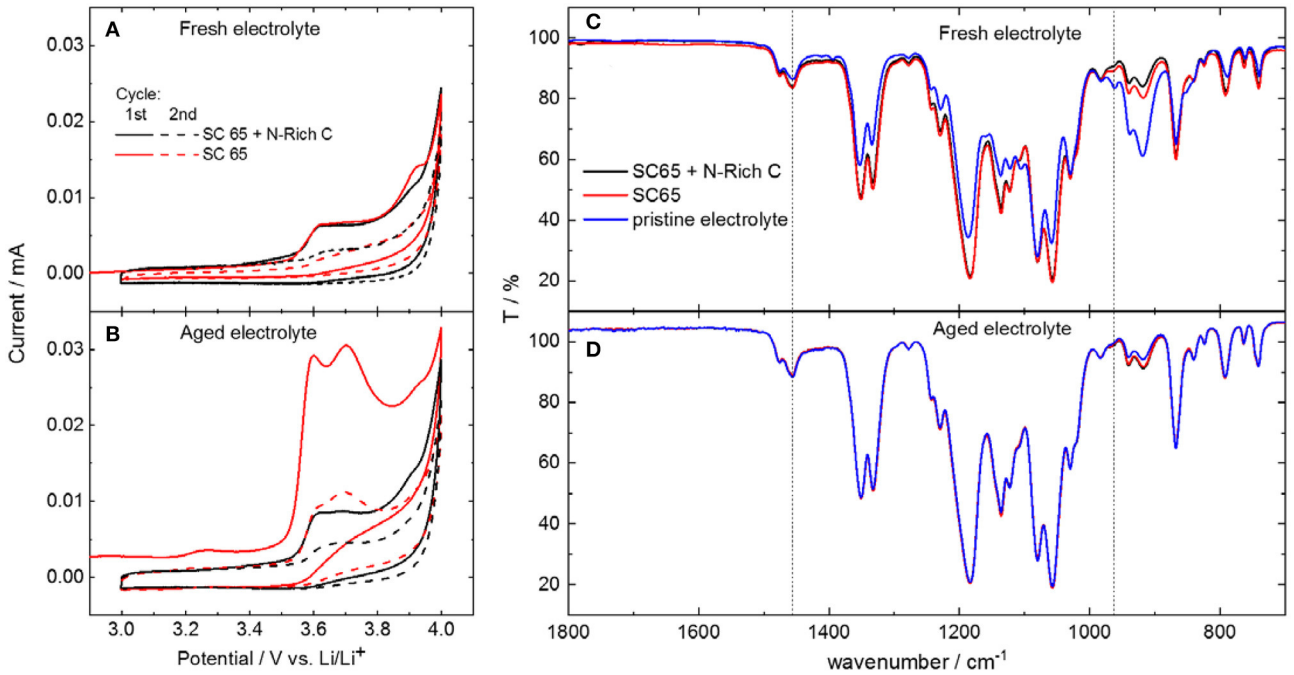

FIGURE 4 | Electrochemical stability window determined by cyclic voltammograms with different carbon-based electrodes, of **(A)** fresh and **(B)** aged electrolytes. IR spectra of **(C)** fresh and **(D)** aged electrolyte extracted from the cell. The spectra of the uncycled electrolyte is also shown for comparison.

especially for the electrode solely composed by SuperC 65 and the binder.

The electrolyte was then extracted from such cells and analyzed. The infrared spectra of the electrolytes after cycling (**Figure 4C**) show the disappearance of the DOL band, indicating its consumption to form the passivation layer on the carbon electrodes. The aged electrolyte (**Figure 4D**) contains less DOL than the fresh one even before cycling, due to the age-induced polymerization. However, there is only a little, if any, change in the spectra of the recovered aged electrolyte in comparison to the pristine aged electrolyte. Still, the cyclic voltammograms show pretty clearly that the oxidation current of the electrode using only Super C65 is much larger than that of the electrode containing also the N-rich carbon. This is a strong indication that the formation of a passivation layer still occurred, but at a much reduced extent on the electrode containing the N-rich carbon. Though the exact mechanism is not clear yet, it can be proposed that the N-rich carbon layer facilitates the anchoring of the PolyDOL from the aged electrolyte, resulting in the formation of a protective layer on the carbon-coated Li_2S, which leads to the improved performance of such electrodes in the aged electrolyte.

CONCLUSIONS

In summary, the effect of N-rich carbon-coating of Li_2S-based cathode was studied. The presence of polyDOL in the aged electrolyte has an unexpected, but appreciable impact on the performance of the Li_2S electrodes, improving the performance of the N-rich carbon-coated Li_2S electrodes. The obtained results suggest that PolyDOL can form a stable, hydrophilic passivation layer over the N-rich carbon-coating, which improves the lithium sulfide formation during discharge leading to larger discharge capacities.

DATA AVAILABILITY STATEMENT

The datasets generated for this study are available on request to the corresponding author.

AUTHOR CONTRIBUTIONS

LL performed the experiments. LL and AV analyzed the experimental data. All authors wrote the manuscript and conceived the work.

ACKNOWLEDGMENTS

LL would like to acknowledge the financial support from CNPq/Science without Borders program [205186/2014-9]. AV and SP acknowledge the financial support of the Helmholtz Association. The data presented here was partially used in LL's Doctorate dissertation (Lodovico, 2018).

REFERENCES

Agostini, M., Hassoun, J., Liu, J., Jeong, M., Nara, H., Momma, T., et al. (2014). A lithium-ion sulfur battery based on a carbon-coated lithium- sulfide cathode and an electrodeposited silicon-based anode. *ACS Appl. Mater. Interfaces* 6, 10924–10928. doi: 10.1021/am4057166

Bailey, W. J. (1985). Free radical ring-opening polymerization. *Die Makromol. Chem.* 13, 171–190. doi: 10.1002/macp.1985.020131985113

Berman, Y. L., Lyudvig, Y. B., Ponomarenko, V. A., and Medvedev, S. S. (1969). Mechanism of the polymerization of 1,3-dioxolane. *Polym. Sci. U.S.S.R.* 11, 225–231. doi: 10.1016/0032-3950(69)90028-8

Blint, R. J. (1995). Binding of ether and carbonyl oxygens to lithium ion. *J. Electrochem. Soc.* 142, 696–702. doi: 10.1149/1.2048519

Chen, L., Liu, Y., Ashuri, M., and Shaw, L. L. (2014). Li_2S encapsulated by nitrogen-doped carbon for lithium sulfur batteries†. *J. Mater. Chem. A* 2, 18026–18032. doi: 10.1039/C4TA04103H

Ding, F., Xu, W., Graff, G. L., Zhang, J., Sushko, M. L., Chen, X., et al. (2013). Dendrite-free lithium deposition via self-healing electrostatic shield mechanism. *J. Am. Chem. Soc.* 135, 4450–4456. doi: 10.1021/ja312241y

Hwa, Y., Zhao, J., and Cairns, E. J. (2015). Lithium sulfide (Li_2S)/graphene oxide nanospheres with conformal carbon coating as a high-rate, long-life cathode for Li/S cells. *Nano Lett.* 15, 3479–3486. doi: 10.1021/acs.nanolett.5b00820

International Energy Agency (2018). *Global EV Outlook 2018*. International Energy Agency.

Jeong, S., Bresser, D., Buchholz, D., Winter, M., and Passerini, S. (2013). Carbon coated lithium sulfide particles for lithium battery cathodes. *J. Power Sources* 235, 220–225. doi: 10.1016/j.jpowsour.2013.01.084

Li, Z., Zhang, J., Guan, B., Wang, D., Liu, L. M., Lou, X. W., et al. (2016). A sulfur host based on titanium monoxide@carbon hollow spheres for advanced lithium-sulfur batteries. *Nat. Commun.* 7, 1–11. doi: 10.1038/ncomms13065

Lin, Z., Liu, Z., Fu, W., Dudney, N. J., and Liang, C. (2013). Phosphorous pentasulfide as a novel additive for high-performance lithium-sulfur batteries. *Adv. Funct. Mater.* 23, 1064–1069. doi: 10.1002/adfm.201200696

Lodovico, L. (2018). *The Role of the Electrolyte on the Lithium-Sulfur Battery Electrochemistry*. Karlsruhe: Karlsruher Institut fuer Technology.

Lodovico, L., Milad Hosseini, S., Varzi, A., and Passerini, S. (2019). Amorphous lithium sulfide as lithium-sulfur battery cathode with low activation barrier. *Energy Technol.* 7, 1801013. doi: 10.1002/ente.201801013

Makarewicz, J., and Ha, T. (2001). *Ab initio* study of the pseudorotation in 1,3-dioxolane. *J. Mol. Struct.* 599, 271–278. doi: 10.1016/S0022-2860(01)00830-4

Nan, C., Lin, Z, Liao, H., Song, M.-K., Li, Y., Cairns, E. J. (2014). Durable carbon-coated Li_2S core-shell spheres for high performance lithium/sulfur cells. *J. Am. Chem. Soc.* 136, 4659–4663. doi: 10.1021/ja412943h

Nanda, S., Gupta, A., and Manthiram, A. (2018). A lithium – sulfur cell based on reversible lithium deposition from a Li 2 S cathode host onto a hostless- anode substrate. *Adv. Energy Mater.* 8:1801556. doi: 10.1002/aenm.201801556

Okada, M., Yamashita, Y., and Ishii, Y. (1964). Polymerization of 1,3-dioxolane. *Makromolekulare* 80, 196–207. doi: 10.1002/macp.1964.020800117

Wu, F., Lee, J. T., Xiao, Y., and Yushin, G. (2016). Nanostructured Li_2Se cathodes for high performance lithium-selenium batteries. *Nano Energy* 27, 238–246. doi: 10.1016/j.nanoen.2016.07.012

Xie, K., You, Y., Yuan, K., Lu, W., Zhang, K., Xu, F., et al. (2017). Ferroelectric-enhanced polysulfide trapping for lithium–sulfur battery improvement. *Adv. Mater.* 29:1604724. doi: 10.1002/adma.201604724

Xu, R., Lu, J., and Amine, K. (2015). Progress in mechanistic understanding and characterization techniques of Li-S batteries. *Adv. Energy Mater.* 5:1500408. doi: 10.1002/aenm.201500408

Yang, Y., Mikeš, F., and Okamoto, Y. (2005). Polymerization of cyclic acetals by a free radical initiator, perfluorodibenzoyl peroxide, in the presence of oxygen. *Macromolecules* 38, 5841–5843. doi: 10.1021/ma050568y

Yim, T., Park, M. S., Ju, J. S., Kim, K. J., Im, K. Y., Lim, J. H. (2013). Effect of chemical reactivity of polysulfide toward carbonate-based electrolyte on the electrochemical performance of Li–S batteries. *Electrochim. Acta* 107, 454–460. doi: 10.1016/j.electacta.2013.06.039

Yoshida, H., and Matsuura, H. (1998). Density functional study of the conformations and vibrations of 1, 2-dimethoxyethane. *J. Phys. Chem. A* 102, 2691–2699. doi: 10.1021/jp9800766

Conflict of Interest: The authors declare that the research was conducted in the absence of any commercial or financial relationships that could be construed as a potential conflict of interest.

frontiers in Materials

ORIGINAL RESEARCH
published: 24 January 2020
doi: 10.3389/fmats.2019.00341

Fluorine-Doped Carbon Coated $LiFePO_{3.938}F_{0.062}$ Composites as Cathode Materials for High-Performance Lithium-Ion Batteries

Zhixiong Yan[1,2], *Dequan Huang*[1,2], *Xiaoping Fan*[1,2], *Fenghua Zheng*[1,2]*, *Qichang Pan*[1,2], *Zhaoling Ma*[1,2], *Hongqiang Wang*[1,2], *Youguo Huang*[1,2] *and Qingyu Li*[1,2]*

[1] School of Chemical and Pharmaceutical Sciences, Guangxi Normal University, Guilin, China, [2] Guangxi Key Laboratory of Low Carbon Energy Materials, Guangxi Normal University, Guilin, China

OPEN ACCESS

Edited by:
Feixiang Wu,
Central South University, China

Reviewed by:
Dianlong Wang,
Harbin Institute of Technology, China
Jin Tao Zhang,
Nanyang Technological University, Singapore
Wang Ding,
Kunming University of Science and Technology, China
Jia Feng Zhang,
Central South University, China

***Correspondence:**
Fenghua Zheng
zhengfh870627@163.com
Qingyu Li
liqingyu62@126.com

Specialty section:
This article was submitted to Energy Materials, a section of the journal Frontiers in Materials

Received: 30 August 2019
Accepted: 17 December 2019
Published: 24 January 2020

Citation:
Yan Z, Huang D, Fan X, Zheng F, Pan Q, Ma Z, Wang H, Huang Y and Li Q (2020) Fluorine-Doped Carbon Coated $LiFePO_{3.938}F_{0.062}$ Composites as Cathode Materials for High-Performance Lithium-Ion Batteries. Front. Mater. 6:341. doi: 10.3389/fmats.2019.00341

Fluorine-doped carbon coated olivine $LiFePO_{3.938}F_{0.062}$ composite (LFPF/CF) is synthesized by a simple solid-state reaction method, and the Tween40 and polyvinylidene fluoride (-$(CH_2$-$CF_2)_n$-, PVDF) were used as carbon source and fluorine sources, respectively. Benefiting from the Tween40 ($C_{22}H_{42}O_6(C_2H_4O)_n$) is attributed to formation a homogeneous carbon layer on the surface of $LiFePO_4$ particles. And polyvinylidene fluoride could produces fluoride in the thermal decomposition process, which is doped into carbon and $LiFePO_4$ to form fluoride-doped carbon layer and $LiFePO_{3.938}F_{0.062}$, respectively. In this constructed architecture, the F-doped carbon layer acts as conductive network for LFP, which can enhance the electronic conductivity of overall electrode. Furthermore, the crystal lattice of LFP was enlarged by the F doping, which facilitates the Li^+ intercalation/deintercalation. On the other hand, a strong electronic coupling between F-doped carbon and $LiFePO_{3.938}F_{0.062}$ can effectively suppress the shedding of carbon layer during cycling process, which keep stabilized of the reaction interface, and thus enhance the cycling stability. As a result, LFPF/CF composite shows superior rate performance (164.8, 159.2, 148.6, 135.8, and 102.3 mAh g^{-1} at 0.1, 0.5, 1, 5, and 10 C), and excellent cycling stability (high capacity retention of 95.6% after 500 cycles at high rate of 5 C).

Keywords: lithium ion batteries, cathode materials, $LiFePO_{3.938}F_{0.062}$, fluorine-doped carbon, electrochemical performance

INTRODUCTION

Lithium ion batteries (LIBs) have been considered as one of the promising power sources in practical applications, for examples, electric vehicles (EVs), hybrid electric vehicles (HEVs) (Armand and Tarascon, 2008; Van Noorden, 2014; Whittingham, 2014). The energy storage mechanism of LIBs is the extraction/insertion of Li^+ in the electrode materials during charge/discharge process, and all of the Li^+ from cathode materials (Dunn et al., 2011). Therefore, cathode materials are very important for lithium ion battery (Zheng et al., 2015; Pan et al., 2017). Among commercial cathode materials, lithium iron phosphate ($LiFePO_4$) has aroused great

interest because of its high theoretical capacity (170 mAh g^{-1}), high safety, stability, low cost, and environment friendly (Park et al., 2007; Huang and Goodenough, 2008; Liu et al., 2009; Wu et al., 2011; Li et al., 2015, 2018; Zheng et al., 2015). However, $LiFePO_4$ shows poor rate performance, resulting in lower mass, and charge transport kinetics, which caused by its low electronic conductivity and Li-ion diffusivity at room temperature (Wang et al., 2005; Sun et al., 2011; Yang et al., 2012; Kuss et al., 2017).

Many strategies have been proposed to improve the rate performance, such as cationic doping and surface coating. Cationic doping is a effective method to expand lithium ion diffusion channels of cathode materials, e.g., cations include Al^{3+}, Mg^{2+}, Co^{2+}, Zn^{2+}, Al^{3+}, and anions include F^-, S^{2-}, Cl^- (Chung and Chiang, 2003; Ni et al., 2005; Hui and Zhou, 2006; Liu et al., 2006; Sun et al., 2010; Chiang et al., 2012; Gao et al., 2017; Gupta et al., 2017). On the other hand, surface coating have been confirmed is another strategy to improve rate performance which due to surface coating can improve the electronic conductivity of materials (Belharouak et al., 2005; Shin et al., 2006; Liu et al., 2008; Lu et al., 2009; Wagemaker et al., 2009; Wu et al., 2013; Lepage et al., 2014; Wang B. et al., 2016; Wang L. L. et al., 2016; Wang et al., 2019). Zheng et al. synthesized carbon coated $LiFePO_4$ by solid-state reaction method, which shows higher capacity of 125 mAh g^{-1} at 5 C (Huang et al., 2013). Zhang et al. prepared Li_4SiO_4-coated $LiFePO_4$ by sol-gel method and microwave heating, delivers reversible capacity of 100 mAh g^{-1} at 5 C (Zhang et al., 2012). Therefore, these results indicate that the cationic doping or surface coating is effective approach to improve rate performance of $LiFePO_4$. However, the electrochemical potential of $LiFePO_4$ cannot be completely realized only by cationic doping or surface coating. Thus, an upgrade strategy combined with cationic doping and carbon coating is used to enhance the rate performance of $LiFePO_4$. Nevertheless, the common strategy combined with cationic doping and the carbon coating is very complicated, which must via a two or three steps including the preliminary synthesis of lithium iron phosphate and subsequent surface coating and cationic doping (Shu et al., 2014; Li et al., 2015). In addition, the carbon was only modified on the surface of $LiFePO_4$, which shows weak interaction between $LiFePO_4$ and the carbon layers, resulting in poor rate performance and cycling stability. Therefore, it is necessary to develop simple and effective strategies to modified $LiFePO_4$ by the combined with surface coating and cationic doping.

In this study, fluorine-doped carbon coated $LiFePO_{3.938}F_{0.062}$ was synthesized by facile one step solid phase method. And choice carbon source and fluorine sources is very important for the electrochemical performance. The Tween40 surfactant contain hydrophobic group and hydrophilic group. Therefore, Tween40 surfactant without impurity elements could uniformly mix with materials in aqueous solution and adsorb on the particle surface to form a carbon layer during heat treatment, which can coat tightly on the surface of the cathode material. While, PVDF only contains two elements of carbon and fluorine, and the fluorine content is 59%, which can contribute to form fluorine doping successfully in the heat process. The incorporation of fluorine (F) into carbon materials could tailor their electron-donor properties, which could further enhanced electronic conductivity of carbon layer and increase bonding force between carbon layer and $LiFePO_4$. Meanwhile, fluorine (F) doped into $LiFePO_4$ could enlarge lithium ion diffusion channel, and thus facilitates the Li^+ intercalation/deintercalation. We focus on study the effect of the F-doped carbon coating and cationic doping on electrochemical performance. In addition, the physical, structural, and electrochemical properties of the F-doped carbon coat $LiFePO_{4-x}F_x$ composites were systematically investigated. As a result, benefiting from combined the advantages of surface coating and cationic doping, the obtained LFPF/CF exhibits high reversible capacity, excellent cycling stability, and rate performance.

EXPERIMENTAL

Preparation of Materials

F-doped carbon coat $LiFePO_{3.938}F_{0.062}$ composites (LFPF/CF) were prepared by one step solid phase method, using Tween40 and PVDF as carbon sources and fluorine sources, respectively. The stoichiometric amount of $FePO_4$, Li_2CO_3, Tween40, and PVDF were mixed by ball milling for 2 h and using deionized water as the liquid medium (The mass ratio of Tween40 and PVDF equal to 2:0.60). The obtained mixture was dried at 80°C for 12 h and disintegrated by crusher to obtain the precursor powders. As-prepared precursors were calcined at 750°C for 10 h to obtain F-doped carbon coat $LiFePO_{3.938}F_{0.062}$ composites (LFPF/CF). The same procedure was also used to synthesize carbon modified $LiFePO_4$ in the absence of the polyvinylidene fluoride (PVDF) and pure $LiFePO_4$ in the absence of the Tween40 and polyvinylidene fluoride (PVDF). Pure $LiFePO_4$, carbon coated $LiFePO_4$, and fluorine-doped carbon coated $LiFePO_{3.938}F_{0.062}$ are denoted as LFP, LFP/C, and LFPF/CF, respectively.

Characterizations

An X-ray diffraction (XRD: Rigaku, D/max 2500v/pc, Cu Kα radiation) was used to analysis the structure of all samples. In order to observe the microstructure of the powder, the scanning electron microscopy (SEM: Philips, FEI Quanta 200 FEG) and transmission electron microscopy (TEM: JEM-2010, JEOL) were carried out. Thermo gravimetric analysis (TGA) was determined by thermal analyzer (SDTO600) in air flow with temperature rising of 5°C min^{-1}. X-ray photoelectron spectroscopy (XPS) measurements were carried out by a Phi X-Tool XPS system to determine the valence state of an element on the surface of all samples. Raman measurement of the composite was performed using a laser Raman spectrometer (Jobin Yvon, T6400).

Electrochemical Evaluation

The electrochemical performances of all samples were evaluated using CR2032 coin cells. The active materials, acetylene black, and polyvinylidene fluoride (PVDF) at a weight ratio of 8:1:1 were mixed for 2 h in an N-methyl-2-pyrrolidene (NMP) solvent, and finally obtain the cathode slurry. The slurry were coated on aluminum foil and dried in vacuum at 120°C for 24 h. Then the CR2032-type half coin cells was assembled in a Ar-filled

glovebox (Etelux LAB2000). The components of the CR2032-type half coin cells are as prepared samples as cathode, lithium metal as the counter electrode, Celgards 2200 separator and A 1:1 volumetric ratio mixture of ethylene carbonate (EC) and dimethyl carbonate (DMC) containing 1 M $LiPF_6$ as the electrolyte. The LAND CT2001A battery testing system (Wuhan, China) was used to test electrochemical performance at voltage range of 2.3–4.3 V under different rates. The cyclic voltammetry (CV) measurements were carried out on IM6 electrochemical workstation at a scan rate of 0.1 mV s^{-1}. Electrochemical impedance spectroscopy (EIS) of the cell was measured by using IM6 electrochemical workstation, with the 5 mV amplitude of the AC signal at the frequency range between 100 kHz and 0.01 Hz.

RESULTS AND DISCUSSION

Scheme 1 illustrates the detailed formation process of F-doped carbon coated $LiFePO_{3.938}F_{0.062}$ composites (LFPF/CF). First, the $FePO_4$, Li_2CO_3, Tween40, and PVDF were mixed through a ball mill method. In this process, Tween40 could bonded with the raw materials, and adsorbed their surface, which could form obstructer film. While, PVDF exists between $FePO_4$ and Li_2CO_3. Subsequently, the obtained precursor was sintered at 750°C in Ar atmosphere, and LFPF/CF composite was obtained. Tween40 form a homogenous carbon layer on the surface of particles, and fluoride from PVDF decomposition at high temperature process is doped into carbon layer and bulk materials to form F-doped carbon coat $LiFePO_{3.938}F_{0.062}$ composite. Hence, the optimal *x* value, *F* content of F-doped carbon layer and the carbon content were chosen in the follow-up investigation (**Table S5** and **Figures S5, S6**).

Figure 1A shows the XRD patterns of pure LFP, LFP/C, and LFPF/CF composite. The characteristic peaks of all samples belong to single phase of orthorhombic olivine-type structure $LiFePO_4$ with the Pnma space group (**Figure 1D**) (Choi and Kumta, 2007). There are no other characteristic peaks in the LFP/C and LFPF/CF sample, suggesting that carbon content is extremely low, and have little effect on the structure. In order to analysis the XRD data of all samples (**Figure 1B** and **Figures S1A,B**), the Rietveld refinement method was implemented, and the crystallographic data were summarized in **Table S1**. A slight decrease of the lattice parameter a, b, and c indicated that F has been successfully doped into the crystal lattice. Concerning fluorine ion, some references suggest that it is substituted for the oxygen rather than the whole PO_4^{3+} group. Meanwhile, PO_4^{3+} group has very high formation energy, so it can't be replaced by fluorine (Liao et al., 2007; Pan et al., 2011; Milovic et al., 2013). The lattice parameters evolution inferred that the average bond lengths of P-O in the PO_4^{3+} group decrease after F doped, which due to the ionic size of F^- (1.33 Å) is smaller that of O^{2-} (1.40 Å) and fluorine are highly electronegative (Shannon and Prewitt, 1969). Therefore, the contractions of the PO_4^{3+} group enlarged the lithium ion diffusion tunnel after F doped, which lead to the lithium ions deintercalate/intercalate more easily in the tunnel (**Figure 2**).

Raman spectroscopy was used to study the exist of carbon and the effect of F-doped on the structure of carbon layer. **Figure 1C** exhibits the Raman spectra of pure LFP, LFP/C, and LFPF/CF. All samples shows a relatively small band at about 948 cm^{-1}, which is assigned to the symmetric PO_4 stretching vibration of the $LiFePO_4$. The bands below 400 cm^{-1} are assigned to vibration of Fe-O (Wu et al., 2013). In addition, two bands at 1,350 and 1,605 cm^{-1} for both LFP/C and LFPF/CF composite are related to the D and G bands of carbon, respectively. The D and G bands are ascribed to the sp^2 graphite-like structure and the sp^3 type carbon, respectively (Tian et al., 2015). Furthermore, LFPF/CF composite shows higher I_D/I_G (0.975) value than that of LFP/C (0.911), which are assigned to increase the defects in carbon layer after fluorine doped. Therefore, the F-doping carbon layer provides sufficient electronic pathways, and consequently enhances the kinetic process. In addition, The carbon content of LFP/C and LFPF/CF composites are analyzed by TGA, and the carbon content in the samples is about 1.83 and 2.02%, respectively (**Figure S2**).

In order to analyze the chemical states and compositions of pure LFP, LFP/C, and LFPF/CF, the X-ray photoelectron spectroscopy (XPS) was carried out, and the results are shown in **Figure 3**. The high-resolution of Fe 2p for pure LFP splits two peaks at 709.2 and 723.2 eV along with two satellite peaks at 713.6 and 727.6 eV, corresponding to Fe $2p_{3/2}$ and Fe $2p_{1/2}$, which proved that iron is oxidation state of +2 (Zhou et al., 2016). For LFP/C, there is no different in the position of the Fe 2p spectrum compare to pure LFP. While, the main peaks of Fe 2p for LFPF/CF composite shows a lower binding energy shifted compared to that of pure LFP, which due to the density of electron clouds increase around $LiFePO_4$. As illustrated in **Figure 4**, Fluorine doping can make the carbon atom in the electron-rich state, and electron cloud tends to LFP, forming a strong electronic coupling between carbon layer and bulk material. The C1s high resolution XPS spectrum is de-convoluted into three peaks at 284.6, 285.4, and 287.9 eV, which belong to the C-C (sp^3-C), C=O (sp^2-C) and C-F bonds, respectively (Wu et al., 2018). Moreover, there are two peaks at 686.2 and 688.2 eV in the fitting of F1s high revolution XPS spectrum, which correspond to F-Li and F-C, respectively (Feng et al., 2017). Therefore, above results indicated that F was doped into the LFP lattice and carbon, respectively.

The effect of F-doped on the microstructure was studied by SEM. **Figure 5** exhibits the SEM images of pure LFP, LFP/C, and LFPF/CF. As seen in **Figure 5A**, pure LFP shows agglomerated particles with a larger diameter of about 600–800 nm. However, for LFP/C and LFPF/CF, the size of particles are smaller than that of pure LFP, suggesting that carbon and F-doped carbon coated could effectively inhibit the growth of particles. **Figures 5D$_1$–D$_4$** shows the EDX elemental mapping images of LFPF/CF. As seen **Figures 5D$_1$–D$_4$**, Fe, C, and F elements shows uniform distribution in the LFPF/CF composite, which indicated that F-doped carbon layer is homogeneously coated on the surface of the LFP particles. In addition, the tap densities of pure LFP, LFP/C, and LFPF/CF are 1.25, 1.22, and 1.20 g/cm^3 (**Table S2**), suggesting that tap density not vary after surface modified.

Meanwhile, the microstructures of pure LFP, LFP/C, and LFPF/CF composite were further investigated by the TEM and

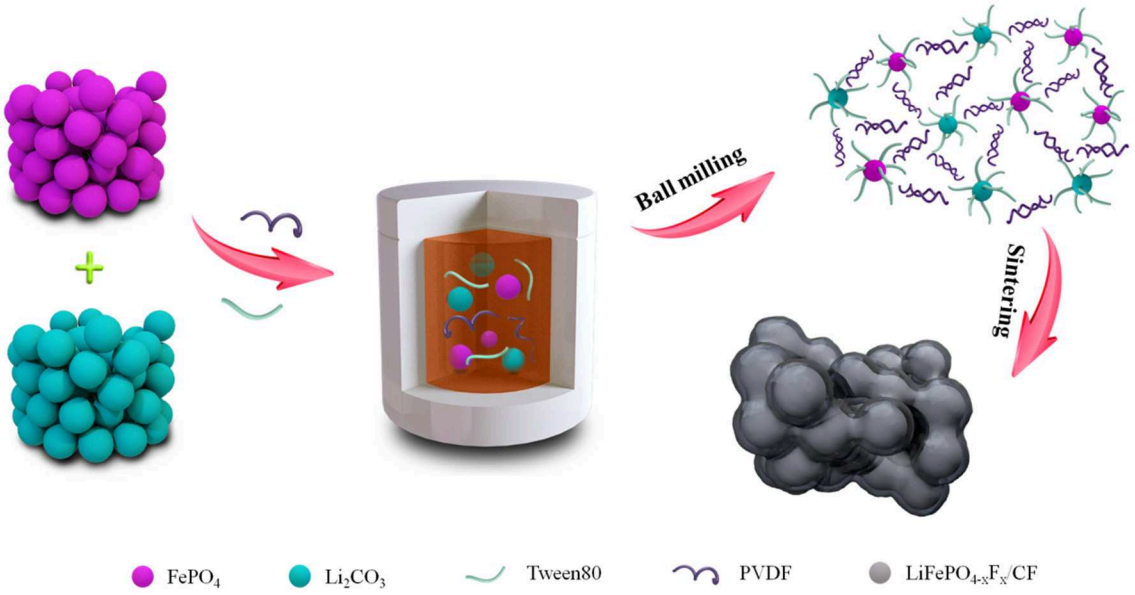

SCHEME 1 | Schematic illustration of the fabrication of fluorine doped carbon coated $LiFePO_{4-x}F_x$ composite.

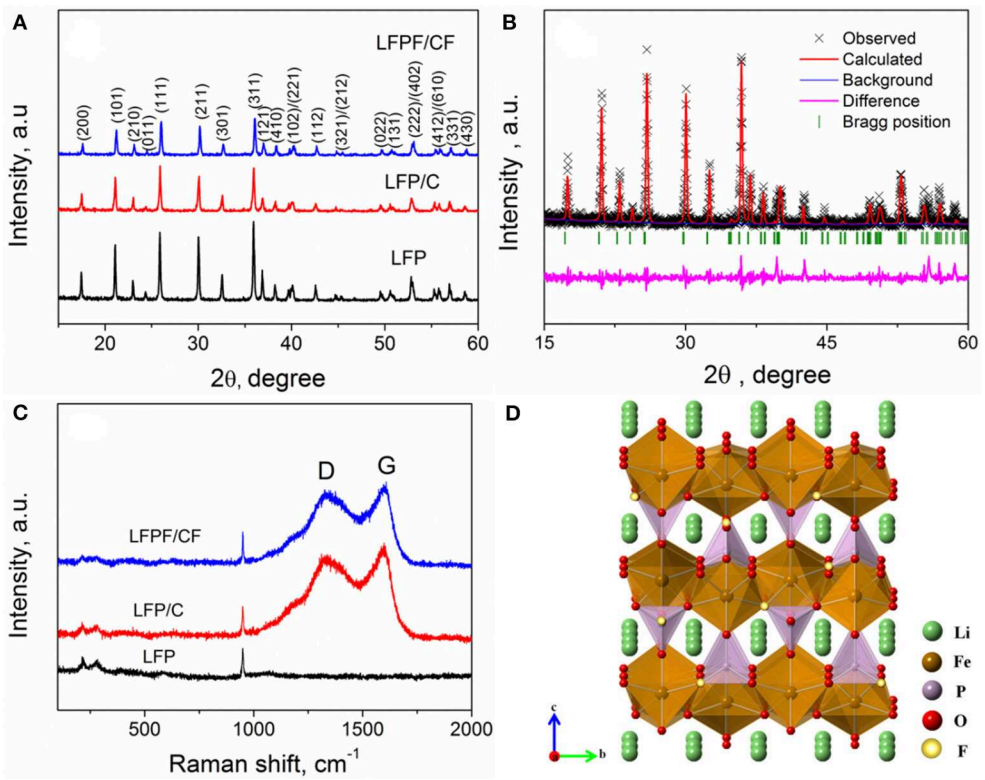

FIGURE 1 | (A) XRD pattern of LFP, LFP/C, and LFPF/CF composite, **(B)** Rietveld refinement plot of LFPF/CF, **(C)** Raman patterns of LFP, LFP/C, and LFPF/CF composite, and **(D)** The crystal structure of LFPF/CF composite.

HRTEM, and the results are shown in **Figure 6**. **Figure 6A$_1$** shows that the pure LFP particles with size range of 600–800 nm, which is in consistent with the SEM results. In addition, the HRTEM image shows that pure LFP exhibits a smooth surface without carbon layer (**Figure 6A$_2$**). **Figures 6B$_1$,B$_2$** shows the TEM and HRTEM images of LFP/C. The particles

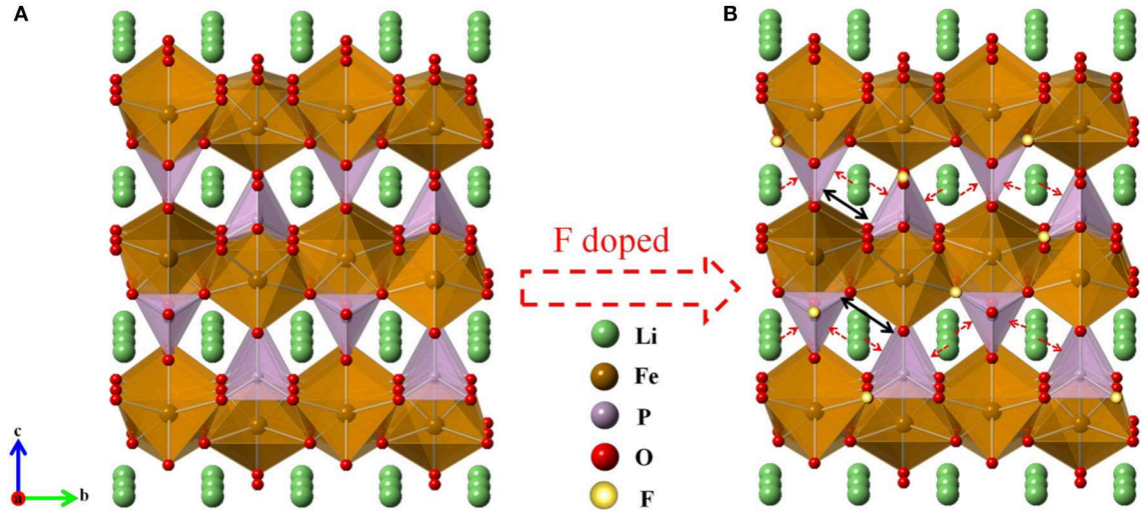

FIGURE 2 | Refined crystal structure of each material of **(A)** pure LFP and **(B)** Fluorine-doped carbon coated olivine $LiFePO_{3.938}F_{0.062}$.

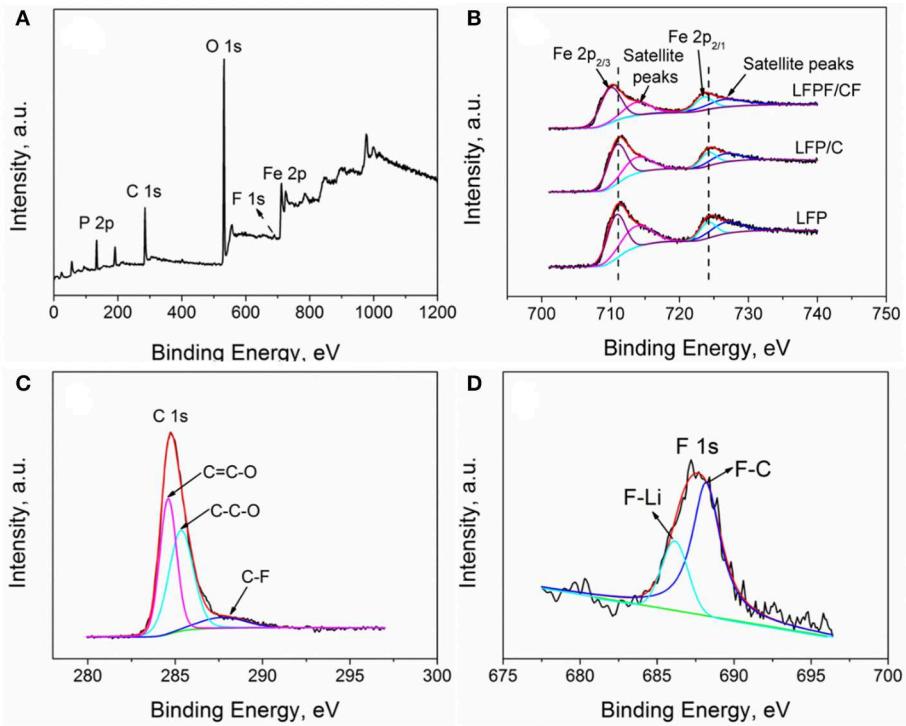

FIGURE 3 | XPS patterns of **(A)** survey spectrum of LFPF/CF composites, **(B)** Fe 2p of LFP, LFP/C, and LFPF/CF composite, **(C)** C 1s, and **(D)** F 1s of LFPF/CF composite.

size of LFP/C are smaller than that of pure LFP, whereas thin carbon layer with the thickness of 2–5 nm on the surface of LFP particles were observed. Moreover, as shown in **Figure 6C$_1$**, LFPF/CF shows smaller particles size than that of pure LFP, and there are F-doped carbon between LFP particles. HRTEM image of the LFP@CF (**Figure 6C$_2$**) shows the F-doped carbon layer with 2–5 nm were coated on the surface of LFP particles. Meanwhile, it is observed that the d-spacing of lattice fringes for LFP and LFP/C are almost 0.272 nm, corresponding to the (102) plane of the LFP. While, LFPF/CF composite show the d-spacing of lattice fringes of 0.274 nm, which is higher than that of LFP and LFP/C. Obviously, the interlayer spacing was enlarged with fluorine doping into $LiFePO_4$ lattice.

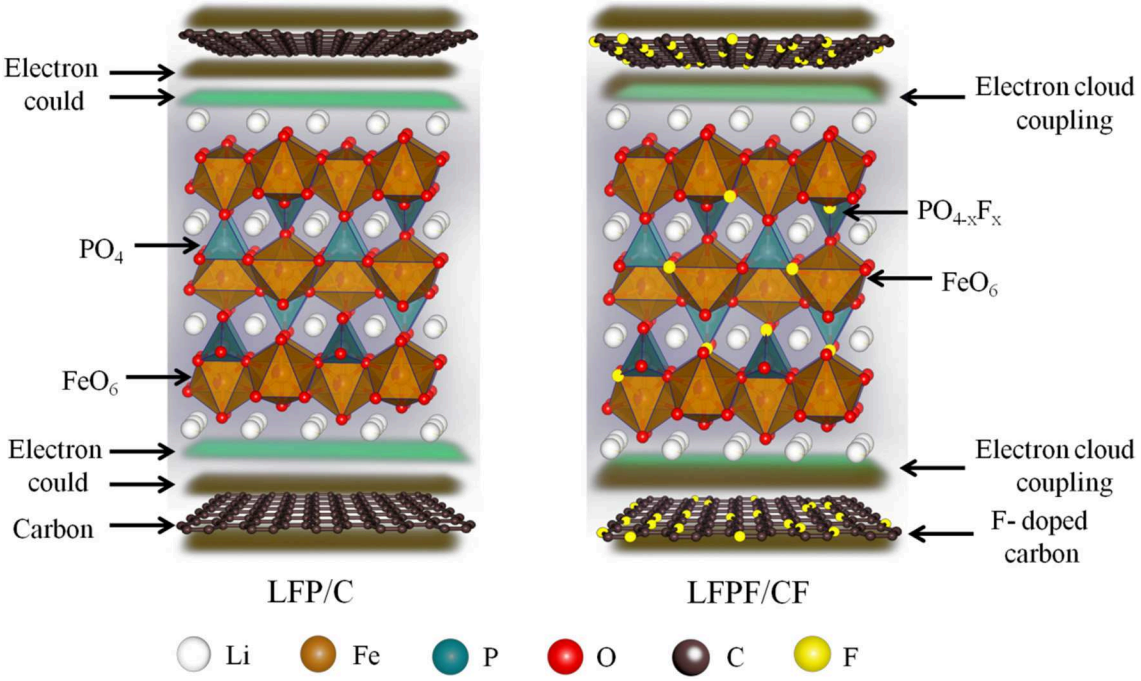

FIGURE 4 | Illustration of the strong interaction between $LiFePO_{4-x}F_x$ and F-doped carbon.

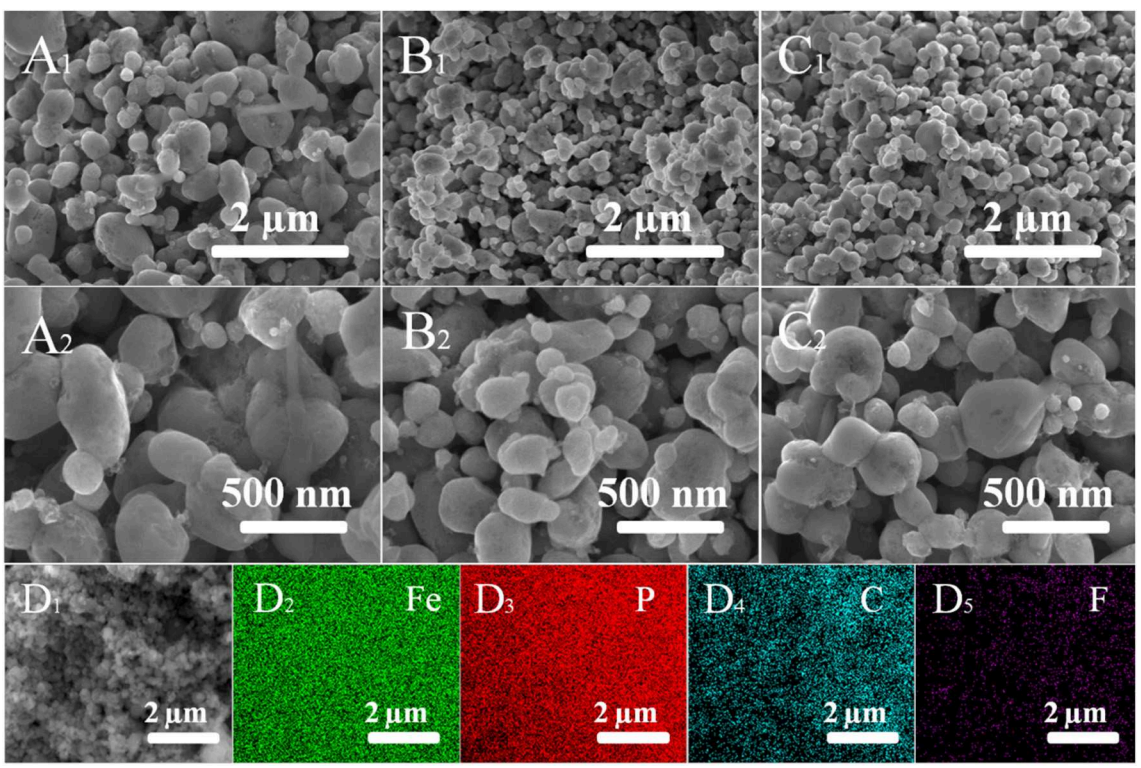

FIGURE 5 | SEM images of pure LFP **(A_1,A_2)**, LFP/C **(B_1,B_2)**, LFPF/CF **(C_1,C_2)**, and corresponding EDX elemental mapping images of Fe, P, C, and F **(D_1–D_4)**.

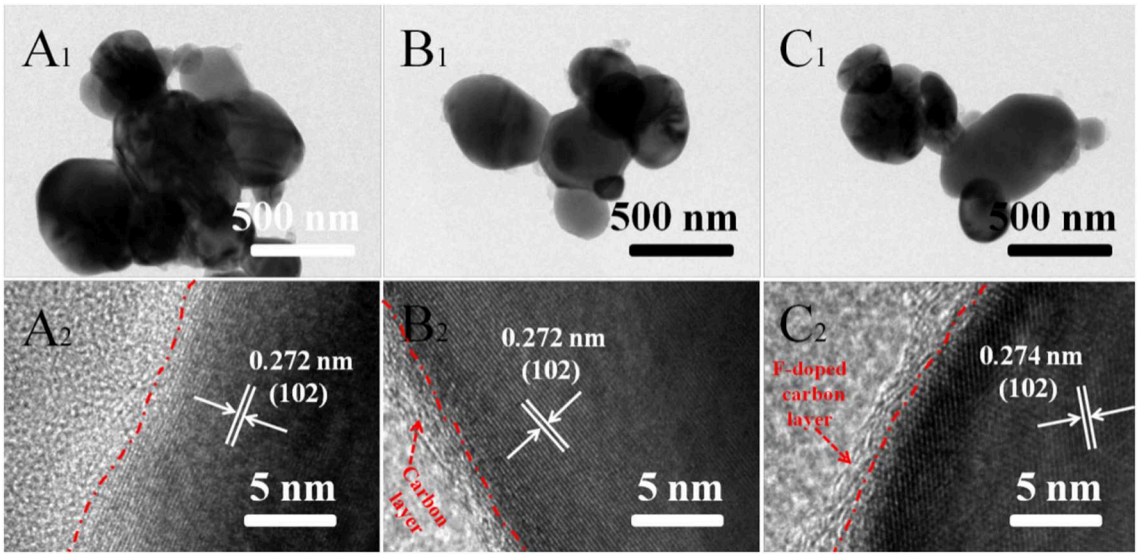

FIGURE 6 | TEM images and HRTEM images of pure LFP **(A_1,A_2)**, LFP/C **(B_1,B_2)**, and LFPF/CF **(C_1,C_2)**.

Figure 7A shows the initial charge/discharge curves of pure LFP, LFP/C, and LFPF/CF at 0.1 C. There are two plateaus for charge/discharge curves of pure LFP, LFP/C, and LFPF/CF, which is ascribed to Li^+ intercalation/deintercalation from $LiFePO_4$, accompanied by the oxidation/reduction of Fe^{2+}/Fe^{3+} (Wang et al., 2018). Pure LFP delivers a discharge capacity of 131.8 mAh g^{-1} with a coulombic efficiency of 85.8%. However, the LFP/C exhibits slightly higher coulombic efficiency of 91.2%, which due to the carbon coated can increase the electronic conductivity. However, for LFPF/CF, the discharge capacity reach to 164.8 mAh g^{-1} with a high coulombic efficiency of 97.5%, which is higher than that of pure LFP and LFP/C. Meanwhile, LFPF/CF exhibits a lower charge voltage plateau and a higher discharge voltage plateau compared with the pure LFP and LFP/C, suggesting that LFPF/CF has lower polarization. Therefore, these results confirmed that the LFPF/CF with better ion transport ability and high electronic conductivity compare to pure LFP and LFP/C.

Figure 7B and **Figure S3** shows the rate performance of pure LFP, LFP/C, and LFPF/CF. As seen **Figure S3**, the discharge capacity of LFPF/CF are 164.8, 159.2, 148.6, 135.8, and 102.3 mAh g^{-1} at 0.1, 0.5, 1, 2, 5, and 10 C, respectively, which shows excellent rate performance. However, the pure LFP and LFP/C delivers lower discharge capacity of 131.8, 121.7, 103.4, 83.2, and 41.6 mA h g^{-1} and 147.8, 139.5, 123.3, 106.8, and 72.8 mA h g^{-1} at 0.1, 0.5, 1, 5, and 10 C. In order to study the common effect of the F doped into LFP lattice and F-doped carbon coated the kinetic process, the cyclic voltammograms of pure LFP, LFP/C, and LFPF/CF composite at different scanning rate were performed out, and the results are provided in **Figure 7C** and **Figure S4**. The potential intervals (ΔV) are increased between the anodic peak and cathode peak of all samples with the increased scanning rate, which can be attributed to the kinetic process limitations (Huang et al., 2014). However, the LFPF/CF (**Figure 7C**) shows lower potential interval (ΔV) than that of pure LFP (**Figure S4B**) and LFP/C (**Figure S4A**) at different sweeping rates. Meanwhile, the redox peak current value of all samples also increases with the increase of scanning rate. The LFPF/CF exhibits higher redox peaks current than that of pure LFP and LFPF/CF composite. Above result indicated that LFP/CF has excellent kinetic process, which are attributed to the introduction of F into the lattice could enlarged interlayer spacing and F-doped carbon coated could form an electronic conductive network.

Figures 7D,E shows the cycling performance of pure LFP, LFP/C, and LFP/CF at 0.5 C and 5 C, respectively. Pure LFP can deliver a discharge capacity of 124.7 mAh g^{-1} with capacity retention of 82.1% after 100 cycles at 0.5 C. Nevertheless, low capacity retention of 43.5% were achieved after 500 cycles at 5C. The poor cycling stability is attributed to the kinetic process limitations, which lead to Li^+ are irreversibly intercalation/deintercalation from $LiFePO_4$ during charge/discharge process. However, LFP/C shows a capacity retentions of 92.7 and 82.3% after 100 cycle at 0.5 C and 500 cycles at 5 C, respectively, which is higher than that of pure LFP. Therefore, these results suggested that carbon coated can effective increase electronic conductivity, resulting in increased kinetic process, as well as suppress the capacity degradation to some extent during cycling process. On the other hand, the LFPF/CF can deliver outstanding cycling stability compare to that of LFP/C. The LFPF/CF deliver high specific capacity of 158.7 mAh g^{-1} after 100 cycles, and a high capacity retention of 98.6% is maintained. More importantly, a high capacity retention of 91.4% can be achieved even over 500 cycles at 5 C. Such excellent cycling stability can be ascribed to the introduction of F into the lattice and F-doped carbon coated enhance lithium ion diffusion and electron transport, so that more lithium ions can reversibly de/intercalate into $LiFePO_4$ during long cycling at high rate. Meanwhile, a strong electronic coupling form the binding force between F-doped carbon layer and bulk material, which could keep the reaction interface stability of LFPF/CF.

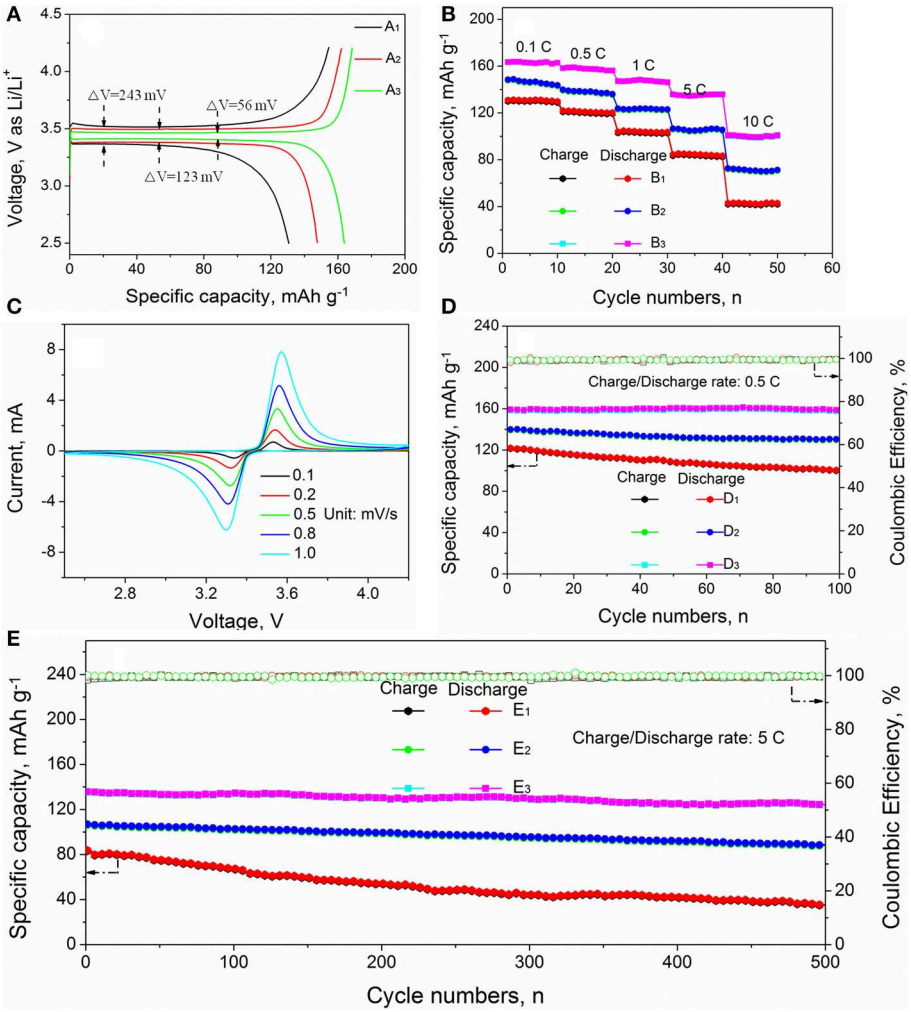

FIGURE 7 | (A) The initial voltage profiles of (A_1) pure LFP, (A_2) LFP/C, and (A_3) LFPF/CF composites; **(B)** rate performance of (B_1) pure LFP, (B_2) LFP/C, and (B_3) LFPF/CF composites, **(C)** the CV curves of LFPF/CF composites at different scanning rates and cycling performance at 0.5 C rate **(D)** and 5 C rate **(E)** of (D_1,E_1) pure LFP, (D_2,E_2), LFP/C, and (D_3,E_3) LFPF/CF composite.

To better explore the reasons for the improved cycling stability of LFPF/CF compare to pure LFP and LFP/C, the ICP and TEM analysis after cycling were carried out, and the results as shown in **Table 1** and **Figure 8**. As seen **Table 1**, the lithium content for pure LFP in charge/discharge state are 28.53 and 72.32% after 300 cycles, suggesting lithium ion are irreversibly from the $LiFePO_4$ lattice. Above results indicated that the irreversible deintercalation/intercalation of lithium ion increase as the increased cycles. **Figures 8A$_1$,A$_2$** exhibits the TEM images of pure LFP after 300 and 500 cycles, and the surface and structure of pure LFP have not change, suggesting that the deterioration of cycling stability which be attributed to poor the kinetic process that cause lithium ions be irreversibly intercalated/deintercalated from $LiFePO_4$ lattice at high rate. The lithium percentage in charge/discharge state for the LFP/C after cycling are lower/higher than that of pure LFP, suggesting that carbon coated could enhance the kinetic process. However, after 500 cycles, the lithium ion percentage after charge/discharge of LFP/C show a certain degree of increase/decrease (12.3%/85.38%). Through TEM observation, it was found that the expansion and contraction of $LiFePO_4$ led to the shedding of carbon layer during the charge/discharge process at high rate (**Figures 8B$_1$,B$_2$**), which was caused by the different expansion coefficients of the two materials. The shedding of carbon layer directly decreases the electrical conductivity of LFP/C. By contrast, the lithium ion percentage of the LFPF/CF not vary much with the increased cycles. While we observe that the F-doped carbon layer still coated on surface of $LiFePO_4$ after 300 and 500 cycles (**Figures 8C$_1$,C$_2$**). The difference between LFP/C and LFPF/CF is attributed to a strong electronic coupling form the binding force between F-doped carbon layer and bulk material, so as to prevent the carbon layer shedding from $LiFePO_4$ surface, and stabilized the reaction interface of LFPF/CF composite.

Figure 9A exhibits the Nyquist plots of pure LFP, LFP/C, and LFPF/CF before and after cycling. As seen **Figure 9A**, the

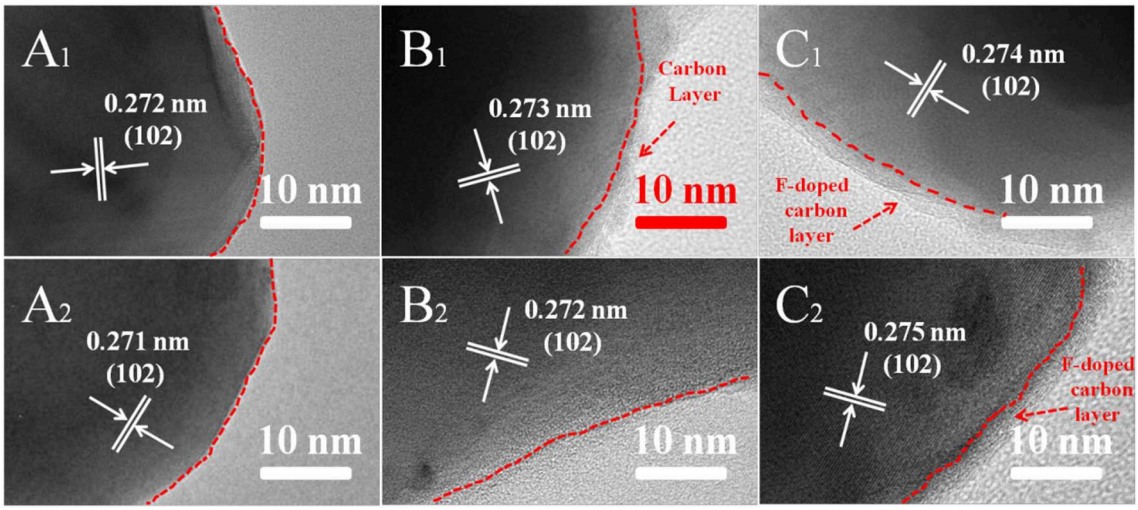

FIGURE 8 | TEM images of all samples of pure LFP: **(A_1)** after 300 cycles, **(A_2)** after 500 cycles, LFP/C: **(B_1)** after 300 cycles, **(B_2)** after 500 cycles and LFPF/CF: **(C_1)** after 300 cycles, **(C_2)** after 500 cycles at 5 C rate, respectively.

TABLE 1 | The ICP analysis of pure LFP, LFP/C, and LFPF/CF composite after cycling, respectively (fully charged/discharge).

Samples	Percentage of lithium in $LiFePO_4$/wt/%	
	After 300 cycles (charge/discharge)	After 500 cycles (charge/discharge)
Pure LFP	28.53/72.32	22.81/61.65
LFP/C	12.34/91.56	16.63/85.38
LFPF/CF	2.51/98.37	3.12/96.82

impedance spectrum is consist of an intercept at high frequency, a depressed semicircle at medium frequency and a straight line in the low frequency region, which relates to the ohmic resistance (R_Ω), the charge transfer resistance (R_{ct}) and the Warburg impedance (W), respectively. These impedance spectra were analyzed by the equivalent circuit model (**Figure 9E**), and corresponding parameters are shown in the **Tables S3, S4**. Meanwhile, the Li^+ ion diffusion coefficiency (D_{Li}^+) is calculated by the following equations (Li et al., 2010; Wang L. L. et al., 2016; Wang et al., 2017):

$$D_{Li}^+ = \frac{R^2T^2}{2A^2n^4F^4C_{Li}^2\sigma^2} \quad (1)$$

$$Z' = R_\Omega + R_{ct}\sigma\omega^{-1/2} \quad (2)$$

where T, R, A, F, n, C, ω is constant temperature, gas constant, surface area of cathode, Faraday constant, number of involved electrons, Li^+ ions concentration, and angular frequency in the low frequency region, respectively. Meanwhile, σ is the Warburg coefficient, it is associated with Z′ against $\omega^{-1/2}$.

The LFPF/CF composite shows R_{ct} value of 178.6 *Omega*, which is lower than that of pure LFP (558.8 Ω) and LFP/C (339.2 Ω) before cycling. In addition, the Li^+ diffusion coefficiency of LFPF/CF composite is 2.72×10^{-12} cm^2 s^{-1}, which is higher that of pure LFP (0.87×10^{-12} cm^2 s^{-1}) and LFP/C (1.43×10^{-12} cm^2 s^{-1}). The results suggest that the introduction of F-doped carbon coated could greatly improve the charge and Li^+ ion diffusion transport coefficiency.

Figures 9B–D show the Nyquist plots of pure LFP, LFP/C and LFPF/CF at 5 C after different cycles, respectively. For pure LFP, when the number of cycles goes from 1st to 500th, the R_{ct} values increase from 629.8 Ω and 1372.9 Ω, and the D_{Li}^+ value decreased from 0.77×10^{-12} cm^2 s^{-1} to 0.35×10^{-12} cm^2 s^{-1}. The LFP/C show the increased R_{ct} values and the decreased D_{Li}^+ value after 300 and 500 cycles, which are lower than that of pure LFP. While, for LFPF/CF, the R_{ct} values is 254.7 Ω after 300 cycles, and increased to 314.8 Ω after 500 cycles which are lower than those of pure LFP and LFPF/CF composite. Meanwhile, the D_{Li}^+ value of LFPF/CF composite not vary much as the increased cycle numbers. This case clearly shows that the F-doped carbon coated can significantly keep the stability of resistance and Li^+ diffusion coefficient during cycling, which is attributed to a strong electronic coupling form the binding force between F-doped carbon layer and bulk material to stabilize the reaction interface.

CONCLUSIONS

In summary, the F-doped carbon coated $LiFePO_{3.938}F_{0.062}$ composite (LFPF/CF) were synthesized by a simple solid-state reaction method. The surface of $LiFePO_4$ particles is uniformly coated by F-doped carbon layer, and a strong electronic coupling was formed between LFP and F-doped carbon layers, which resulting in enhanced electronic conductivity and reaction interfacial stability. In addition, minor F fluorine doped into the $LiFePO_4$ lattice, which can enlarge the lithium ion diffusion

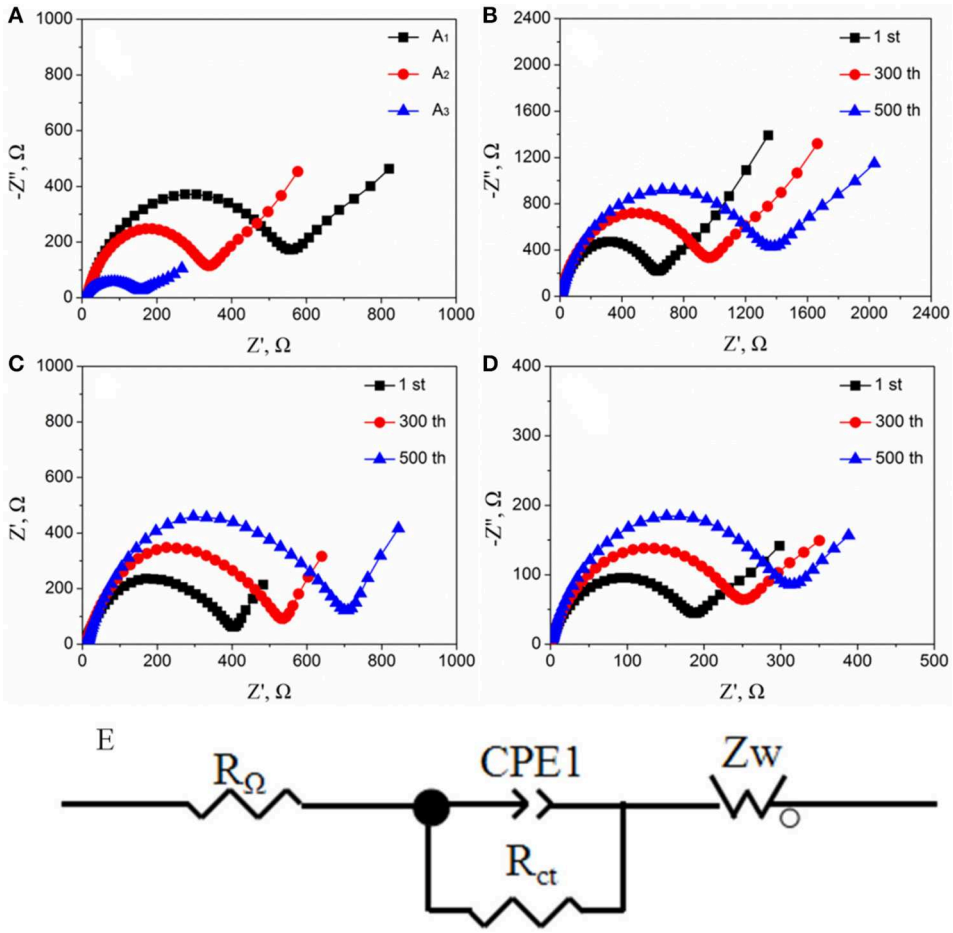

FIGURE 9 | (A) Nyquist plots of all samples [(A_1) pure LFP, (A_2) LFP/C, and (A_3) LFPF/CF] before cycling, **(B)** pure LFP, **(C)** LFP/C, and **(D)** LFPF/CF after cycling at 5 C, **(E)** equivalent circuit models.

channel. As a result, the LFPF/CF shows excellent rate capability (164.8, 159.2, 148.6, 135.8, and 102.3 mAh g^{-1} at 0.1, 0.5, 1, 2, 5, and 10 C, respectively) and high cycling stability (high capacity retention reach 91.4% after 500 cycles at 5 C). Therefore, we believe that as-prepared F-doped carbon coated LFPF/CF composite could be one of an advanced cathode materials for Li-ion battery technology.

DATA AVAILABILITY STATEMENT

The raw data supporting the conclusions of this article will be made available by the authors, without undue reservation, to any qualified researcher.

AUTHOR CONTRIBUTIONS

ZY conducted the experiments. QL is the supervisor of this research work. ZY and FZ helped writing. ZY, DH, XF, FZ, QP, and ZM performed the characterization and data analysis. All authors involved the analysis of experimental data and manuscript preparation.

FUNDING

This research was supported by National Natural Science Foundation of China (51864007), Guangxi Key Research and Development Program of Science and Technology (GUIKE AB17195065 and AB17129011), and Guangxi Technology Base and Talent Subject (GUIKE AD18126001).

SUPPLEMENTARY MATERIAL

The Supplementary Material for this article can be found online at: https://www.frontiersin.org/articles/10.3389/fmats.2019.00341/full#supplementary-material

REFERENCES

Armand, M., and Tarascon, J. M. (2008). Building better batteries. *Nature* 451, 652–657. doi: 10.1038/451652a

Belharouak, I., Johnson, C., and Amine, K. (2005). Synthesis and electrochemical analysis of vapor-deposited carbon-coated $LiFePO_4$. *Electrochem. Commun.* 7, 983–988. doi: 10.1016/j.elecom.2005.06.019

Chiang, C. Y., Su, H. C., Wu, P. J., Liu, H. J., Hu, C. W., Sharma, N., et al. (2012). Vanadium substitution of $LiFePO_4$ cathode materials to enhance the capacity of $LiFePO_4$-based lithium-ion batteries. *J. Phys. Chem. C* 116, 24424–24429. doi: 10.1021/jp307047w

Choi, D. W., and Kumta, P. N. (2007). Surfactant based sol-gel approach to nanostructured $LiFePO_4$ for high rate Li-ion batteries. *J. Power Sources* 29, 1064–1069. doi: 10.1016/j.jpowsour.2006.09.082

Chung, S. Y., and Chiang, Y. M. (2003). Microscale measurements of the electrical conductivity of doped $LiFePO_4$. *Electrochem. Solid-State Lett.* 6, A278–A281. doi: 10.1149/1.1621289

Dunn, B., Kamath, H., and Tarascon, J. (2011). Electrical energy storage for the grid: a battery of choices. *Science* 334, 928–935. doi: 10.1126/science.1212741

Feng, T., Jiang, W., Zong, Z., and Wu, M. (2017). Investigation of the electrochemical performance of polyvinylidene fluoride-derived $LiFePO_4$/C composite nanospheres. *J. Mater. Sci.* 53, 1279–1285. doi: 10.1007/s10853-017-1585-5

Gao, L., Xu, Z., Zhang, S., Xu, J., and Tang, K. (2017). Enhanced electrochemical properties of $LiFePO_4$ cathode materials by Co and Zr multi-doping. *Solid State Ionics* 305, 52–56. doi: 10.1016/j.ssi.2017.04.021

Gupta, R., Saha, S., Tomar, M., Sachdev, V. K., and Gupta, V. (2017). Effect of manganese doping on conduction in olivine $LiFePO_4$. *J. Mater. Sci. Mater. Electron.* 28, 5192–5199. doi: 10.1007/s10854-016-6175-9

Huang, Y. G., Zheng, F. H., Zhang, X. H., Li, Q. Y., and Wang, H. Q. (2014). Effect of carbon coating on cycle performance of $LiFePO_4$/C composite cathodes using Tween80 as carbon source. *Electrochimica Acta* 130, 740–747. doi: 10.1016/j.electacta.2014.03.091

Huang, Y. G., Zheng, F. H., Zhang, X. H., Li, Y. H., Yin, J. C., and Li, Q. Y. (2013). Tween40 surfactant effect on the formation of nano-sized $LiFePO_4$/C powder via a solid state reaction and their cathode properties. *Solid State Ionics* 249, 158–164. doi: 10.1016/j.ssi.2013.08.015

Huang, Y. H., and Goodenough, J. B. (2008). High-rate $LiFePO_4$ lithium rechargeable battery promoted by electrochemically active polymers. *Chem. Mat.* 20, 7237–7241. doi: 10.1021/cm8012304

Hui, X., and Zhou, Z. (2006). Physical and electrochemical properties of mix-doped lithium iron phosphate as cathode material for lithium ion battery. *Electrochim. Acta* 51, 2063–2067. doi: 10.1016/j.electacta.2005.07.014

Kuss, C., Trinh, N. D., Andjelic, S., Saulnier, M., Dufresne, E. M., Liang, G. X., et al. (2017). Structural transformation of $LiFePO_4$ during ultrafast delithiation. *J. Phys. Chem. Lett.* 24, 6160–6164. doi: 10.1021/acs.jpclett.7b02569

Lepage, D., Sobh, F., Kuss, C., Liang, G., and Schougaard, S. B. (2014). Delithiation kinetics study of carbon coated and carbon free $LiFePO_4$. *J. Power Sources* 256, 61–65. doi: 10.1016/j.jpowsour.2013.12.054

Li, Q. Y., Zheng, F. H., Huang, Y. G., Zhang, X. H., Wu, Q., Fu, D. J., et al. (2015). Surfactants assisted synthesis of nano-$LiFePO_4$/C composite as cathode materials for lithium-ion batteries. *J. Mater. Chem. A* 3, 2025–2035. doi: 10.1039/C4TA03293D

Li, Z., Du, F., and Bie, X. (2010). Electrochemical kinetics of the $Li[Li_{0.23}Co_{0.3}Mn_{0.47}]O_2$ cathode material studied by GITT and EIS. *J. Phys. Chem. C* 114, 22751–22757. doi: 10.1021/jp1088788

Li, Z. J., Yang, J. X., Li, C. J., Wang, S. C., Zhang, L., Zhu, K. J., et al. (2018). Orientation-dependent lithium miscibility gap in $LiFePO_4$. *Chem. Mater.* 3, 874–878. doi: 10.1021/acs.chemmater.7b04463

Liao, X. Z., He, Y. S., Ma, Z. F., Zhang, X. M., and Wang, L. (2007). Effects of fluorine-substitution on the electrochemical behavior of $LiFePO_4$/C cathode materials. *J. Power Sources* 174, 720–725. doi: 10.1016/j.jpowsour.2007.06.146

Liu, H., Cao, Q., Fu, L. J., Li, C., Wu, Y. P., and Wu, H. Q. (2006). Doping effects of zinc on $LiFePO_4$ cathode material for lithium ion batteries. *Electrochem. Commun.* 8, 1553–1557. doi: 10.1016/j.elecom.2006.07.014

Liu, H., Wang, G. X., Wexler, D., Wang, J. Z., and Liu, H. K. (2008). Electrochemical performance of $LiFePO_4$ cathode material coated with ZrO_2 nanolayer, *Electrochem. Commun.* 10, 165–169. doi: 10.1016/j.elecom.2007.11.016

Liu, J., Wang, J., Yan, X., Zhang, X., Yang, G., Jalbout, A. F., et al. (2009). Long-term cyclability of $LiFePO_4$/carbon composite cathode material for lithium-ion battery applications. *Electrochim. Acta* 54, 5656–5659. doi: 10.1016/j.electacta.2009.05.003

Lu, C. Z., Kuo, G. T., Fey, T. K., and Kao, H. M. (2009). Study of $LiFePO_4$ cathode materials coated with high surface area carbon. *J. Power Sources* 189, 155–162. doi: 10.1016/j.jpowsour.2008.10.015

Milovic, M., Jugovic, D., Cvjeticanin, N., Uskokovic, D., Milosevic, A. S., Popovic, Z. S., et al. (2013). Crystal structure analysis and first principle investigation of F doping in $LiFePO_4$. *J. Power Sources* 241, 70–79. doi: 10.1016/j.jpowsour.2013.04.109

Ni, J. F., Zhou, H. H., Chen, J. T., and Zhang, X. X. (2005). $LiFePO_4$ doped with ions prepared by co-precipitation method. *Mater. Lett.* 59, 2361–2365. doi: 10.1016/j.matlet.2005.02.080

Pan, M., Lin, X., and Zhou, Z. (2011). Electrochemical performance of $LiFePO_4$/C doped with F synthesized by carbothermal reduction method using NH_4F as dopant. *J. Solid State Electrochem.* 16, 1615–1621. doi: 10.1007/s10008-011-1564-8

Pan, Q. C., Zheng, F. H., Ou, X., Yang, C. H., Xiong, X. H., and Liu, M. L. (2017). MoS_2 encapsulated SnO_2-SnS/C nanosheets as a high performance anode material for lithium ion batteries. *Chem. Eng. J.* 316, 393–400. doi: 10.1016/j.cej.2017.01.111

Park, K. S., Schougaard, S. B., and Goodenough, J. B. (2007). Conducting-polymer/iron-redox-couple composite cathodes for lithium secondary batteries. *Adv. Mater.* 19, 848–851. doi: 10.1002/adma.200600369

Shannon, R. D., and Prewitt, C. T. (1969). Effective ionic radii in oxides and fluorides. *Acta Crystallogr. B* 25, 925–946. doi: 10.1107/S0567740869003220

Shin, H. C., Cho, W. I., and Ho, J. (2006). Electrochemical properties of carbon-coated $LiFePO_4$ cathode using graphite, carbon black, and acetylene black. *Electrochim. Acta* 52, 1472–1476. doi: 10.1016/j.electacta.2006.01.078

Shu, H. B., Chen, M. F., Fu, Y. Q., Yang, X. K., Yi, X., Bai, Y. S., et al. (2014). Improvement of electrochemical performance for spherical $LiFePO_4$ via hybrid coated with electron conductive carbon and fast Li ion conductive $La_{0.56}Li_{0.33}TiO_3$. *J. Power Sources* 252, 73–78. doi: 10.1016/j.jpowsour.2013.11.036

Sun, C., Rajasekhara, S., Goodenough, J. B., and Zhou, F. (2011). Monodisperse porous $LiFePO_4$ microspheres for a high power Li-ion battery cathode. *J. Am. Chem. Soc.*133, 2132–2135. doi: 10.1021/ja1110464

Sun, C. S., Zhang, Y., Zhang, X. J., and Zhou, Z. (2010). Structural and electrochemical properties of Cl-doped $LiFePO_4$/C. *J. Power Sources* 195, 3680–3683. doi: 10.1016/j.jpowsour.2009.12.074

Tian, R., Liu, H., Jiang, Y., Chen, J., Tan, X., Liu, G., et al. (2015). Drastically enhanced high-rate performance of carbon-coated $LiFePO_4$ nanorods using a green chemical vapor deposition (CVD) method for lithium ion battery: a selective carbon coating process. *ACS Appl. Mater. Interfaces* 7, 11377–11386. doi: 10.1021/acsami.5b01891

Van Noorden, R. (2014). A better battery. *Nature* 207, 26–28. doi: 10.1038/507026a

Wagemaker, M., Mulder, F. M., and Van der Ven, A. (2009). The role of surface and interface energy on phase stability of nanosized insertion compounds. *Adv. Mater.* 21, 2703–2709. doi: 10.1002/adma.200803038

Wang, B., Liu, T., Liu, A., Liu, G., Wang, L., Gao, T. T., et al. (2016). A hierarchical porous C@$LiFePO_4$/carbon nanotubes microsphere composite for high-rate lithium-ion batteries: combined experimental and theoretical study. *Adv. Energy Mater.* 6:1600426. doi: 10.1002/aenm.201600426

Wang, B., Ruan, T., Chen, Y., Jin, F., Peng, L., Zhou, Y., et al. (2019). Graphene-based composites for electrochemical energy storage. *Energy Storage Mater.* 24, 22–51. doi: 10.1016/j.ensm.2019.08.004

Wang, D. Y., Wu, X. D., Wang, Z. X., and Chen, L. Q. (2005). Cracking causing cyclic instability of $LiFePO_4$ cathode material. *J. Power Sources.* 140, 125–128. doi: 10.1016/j.jpowsour.2004.06.059

Wang, H. Q., Pan, Q. C., Wu, Q., Zhang, X. H., Huang, Y. G., Li, Q. Y., et al. (2017). Ultrasmall MoS_2 embedded in carbon nanosheets coated Sn/SnO_x as anode material for high-rate and long life Li-ion batteries. *J. Mater. Chem. A* 5, 4576–4582. doi: 10.1039/C6TA10932B

Wang, L. L., Hu, Z. Y., Zhao, K. N., Luo, Y. Z., Wei, Q. L., Tang, C. J., et al. (2016). Hollow spherical $LiNi_{0.5}Mn_{1.5}O_4$ built from polyhedra with high-rate performance via carbon nanotube modification. *Sci. China Mater.* 59, 95–103. doi: 10.1007/s40843-016-0120-3

Wang, X., Feng, Z., Huang, J., Deng, W., Li, X., Zhang, H., et al. (2018). Graphene-decorated carbon-coated $LiFePO_4$ nanospheres as a high-performance cathode material for lithium-ion batteries. *Carbon* 127, 149–157. doi: 10.1016/j.carbon.2017.10.101

Whittingham, M. S. (2014). Ultimate limits to intercalation reactions for lithium batteries. *Chem. Rev.* 114, 11414–11443. doi: 10.1021/cr5003003

Wu, J., Dathar, G. K., Sun, C., Theivanayagam, M. G., Applestone, D., Dylla, A. G., et al. (2013). *In situ* Raman spectroscopy of $LiFePO_4$: size and morphology dependence during charge and self-discharge. *Nanotechnology* 24:424009. doi: 10.1088/0957-4484/24/42/424009

Wu, Y. M., Wen, Z. H., and Li, J. H. (2011). Hierarchical carbon-coated $LiFePO_4$ nanoplate microspheres with high electrochemical performance for Li-ion batteries. *Adv. Mater.* 23, 1126–1129. doi: 10.1002/adma.201003713

Wu, Z., Li, P., Qin, Q., Li, Z., and Liu, X. (2018). N-doped graphene combined with alloys (NiCo,CoFe) and their oxides as multifunctional electrocatalysts for oxygen and hydrogen electrode reactions. *Carbon* 139, 35–44. doi: 10.1016/j.carbon.2018.06.028

Yang, K., Deng, F. H., and Suo, J. S. (2012). Synthesis and characterization of $LiFePO_4$ and $LiFePO_4$/C cathode material from lithium carboxylic acid and Fe^{3+}. *J. Power Sources* 201, 274–279. doi: 10.1016/j.jpowsour.2011.11.019

Zhang, Q., Jiang, W. W., Zhou, Z. F., Wang, S. M., Guo, X. S., Zhao, S., et al. (2012). Enhanced electrochemical performance of Li_4SiO_4-coated $LiFePO_4$ prepared by sol-gel method and microwave heating. *Solid State Ionics* 218, 31–34. doi: 10.1016/j.ssi.2012.05.006

Zheng, F. H., Yang, C. H., Xiong, X. H., Xiong, J. W., Hu, R. Z., Chen, Y., et al. (2015). Nanoscale surface modification of lithium-rich layered-oxide composite cathodes for suppressing voltage fade. *Angew. Chem. Int. Ed.* 54, 13058–13062. doi: 10.1002/anie.201506408

Zhou, Y. K., Lu, J. M., Deng, C. J., Zhu, H. X., Chen, G. Z., Zhang, S. W., et al. (2016). Nitrogen-doped graphene guided formation of monodisperse microspheres of $LiFePO_4$ nanoplates as the positive electrode material of lithium-ion batteries. *J. Mater. Chem. A* 4, 12065–12072. doi: 10.1039/C6TA03440C

Conflict of Interest: The authors declare that the research was conducted in the absence of any commercial or financial relationships that could be construed as a potential conflict of interest.

frontiers in Chemistry

ORIGINAL RESEARCH
published: 20 March 2020
doi: 10.3389/fchem.2020.00072

High Efficient and Environment Friendly Plasma-Enhanced Synthesis of Al_2O_3-Coated $LiNi_{1/3}Co_{1/3}Mn_{1/3}O_2$ With Excellent Electrochemical Performance

Xinzhi Wang[1†], *Qianqian Jiang*[1,2*†], *Yichi Zhang*[1], *Nannan Yuan*[1] *and Jianguo Tang*[1*]

[1] *Institute of Hybrid Materials, National Center of International Research for Hybrid Materials Technology, National Base of International Science and Technology Cooperation, College of Materials Science and Engineering, Qingdao University, Qingdao, China,* [2] *School of Chemical and Biomedical Engineering, Nanyang Technological University, Singapore, Singapore*

OPEN ACCESS

Edited by:
Junchao Zheng,
Central South University, China

Reviewed by:
Jin Tao Zhang,
Nanyang Technological University, Singapore
Lingjun Li,
Changsha University of Science and Technology, China

***Correspondence:**
Qianqian Jiang
kaiqian2008@163.com
Jianguo Tang
jtang951@163.com

[†] *These authors have contributed equally to this work*

Specialty section:
This article was submitted to Electrochemistry, a section of the journal Frontiers in Chemistry

Received: *27 June 2019*
Accepted: *22 January 2020*
Published: *20 March 2020*

Citation:
Wang X, Jiang Q, Zhang Y, Yuan N and Tang J (2020) High Efficient and Environment Friendly Plasma-Enhanced Synthesis of Al_2O_3-Coated $LiNi_{1/3}Co_{1/3}Mn_{1/3}O_2$ With Excellent Electrochemical Performance. Front. Chem. 8:72. doi: 10.3389/fchem.2020.00072

PLA-1-Al_2O_3@LNCM synthesized using an efficient and facile plasma-enhanced method exhibits markedly improved capacity retention of 98.6% after 100 cycles, which is much larger than that of LNCM at 80% after 100 cycles. What is more, it also exhibits significantly enhanced cyclicity compared to that of 1-Al_2O_3@LNCM cathodes prepared using the normal solid state method, which further illustrates the efficiency and superiority of this plasma-enhanced method. More importantly, the rate performance of PLA-1-Al_2O_3@LNCM is improved because of the better electrolyte storage of the assembled hierarchical architecture of the Al_2O_3 coating layer according to unimpeded Li+ diffusion from electrode to electrolyte. When cycling at 55°C, the PLA-1-Al_2O_3@LNCM shows 93.6% capacity retention after 100 cycles, which is greatly enhanced due to the uniform Al_2O_3 layer. Further, growth of polarization impedance during cycling can be effectively suppressed by the Al_2O_3 layer, which can further confirm the effect the Al_2O_3 layer coated on the surface of the LNCM. The enhanced cycling performance and thermal stability illustrates that this facile surface modification, using the plasma-enhanced method, can form an effective structured coating layer, which indicates its prospects as an application in the modification of other electrode materials.

Keywords: plasma-enhanced method, Al_2O_3 layer, LNCM, elevated temperature performance, Li-ion batteries

INTRODUCTION

With the development of the global energy demand and the urgency of protecting the environment, there is a growing need to develop clean and more efficient power sources like lithium ion batteries (LIBs) (Tang et al., 2013; Chen et al., 2016), which have become the most feasible power source for portable electronic devices, mainly due to their high gravimetric and volumetric energy densities (Xu et al., 2017; Lv et al., 2019) Considering that the specific capacity of LIBs heavily relies on cathode materials, efforts have been made to develop cathode materials with a high energy density and large power capability (Lee et al., 2014; Zhang et al., 2018).

Until now, in cathode materials, such as layered $LiCoO_2$ (Zhao et al., 2015), spinel $LiMn_2O_4$ (Jiang et al., 2016b), $LiNiO_2$, and olivine $LiFePO_4$ have been widely applied for commercial LIBs

in electrical vehicles (EVs) or hybrid electric vehicles (HEVs). Among them, $LiCoO_2$ is the earliest commercialized cathode material which cannot meet the increasing practical demand due to its low practical capacity, relatively high cost, toxicity of cobalt, and unreliable safety. Researchers have therefore focused on finding alternative cathode materials to satisfy the required environmental, safety, and cost standards for LIBs (Ohzuku and Makimura, 2001; Deng et al., 2008; Makkus et al., 2010). In comparison with $LiCoO_2$, layered $LiNi_xCo_yMn_zO_2$ ($x + y + z = 1$) is considered an excellent candidate as a cathode for commercial LIBs. In 2001, $LiNi_{1/3}Co_{1/3}Mn_{1/3}O_2$ (LNCM) was successfully implemented, and has the same layered α-$NaFeO_2$ structure with overall hexagonal symmetry (space group R-3 m) as $LiCoO_2$ (Xia et al., 2014) but with a much higher capacity, better thermal stability, is more environmental friendly and costs less (Lee et al., 2004; Luo et al., 2006; Cho et al., 2011). Nevertheless, LNCM still has some disadvantages, such as an inferior cycle performance at high working voltage, relatively poor conductivity, and irreversible side reactions with electrolytes and cation a disorder between Li^+ and Ni^{2+}, which leads to some technical challenges related to cyclability and rate capability, seriously affecting its large-scale applications (Yao et al., 2013; Cui and Xu, 2015; Zhu et al., 2015). Researchers worldwide have proposed various solutions to overcome these disadvantages. For example, surface coating is an easy and effective way to improve the electrochemical performances of cathodes. Various coating materials such as carbon and metal oxides (Al_2O_3, Li et al., 2014; Li_2TiO_3, Lu et al., 2013; ZrO_2, Hu et al., 2009; TiO_2, Li et al., 2006; AlF_3, Myung et al., 2010; $AlPO_4$, Wang et al., 2013, etc.) have been studied, which can increase the electronic conductivity and inhibit the side reactions between cathode and electrolyte (Jiang et al., 2018). Among the metal oxides mentioned above, Al_2O_3 is regarded as a desirable surface coating material due to its excellent chemical and thermal stability, which is good for the electrochemical performance cathode material. However, the normal method used for coating Al_2O_3 is solid-state (Kim et al., 2006) or solution methods (Qiu et al., 2014), which often result in no uniform elemental distribution and inferior electrochemical performance (Yan et al., 2016). In addition, the experimental conditions (pH, temperature, and mixing speed) should be carefully controlled to synthesize homogeneous hydroxide or carbonate precipitates, making this method complicated (Manthiram et al., 2016). Therefore, it becomes challenging to develop a facile and general approach for the preparation of coating on the LNCM with favorable structures and excellent electrochemical performance.

Herein, we first report a novel facile plasma-enhanced low-temperature approach in $LiNi_{1/3}Co_{1/3}Mn_{1/3}O_2$ coated with Al_2O_3 with a superior hierarchical structure, as illustrated in **Scheme 1**. This method produces a simple, uniform coating, which can delay the cathode/electrolyte interfacial reactions and facilitate Li-ion diffusion in the batteries. The cell made of $LiNi_{1/3}Co_{1/3}Mn_{1/3}O_2$ coated with Al_2O_3 delivers a high specific reversible capacity of 213.8 (0.2°C), 208.4 (0.5°C), 199.6 (1°C), and 189.0 (2°C) mAhŁEg^{-1}, respectively. More importantly, all the $LiNi_{1/3}Co_{1/3}Mn_{1/3}O_2$ coated with Al_2O_3 composite electrodes show improved cycling performance and rate capability, especially in an elevated temperature, compared to the pristine $LiNi_{1/3}Co_{1/3}Mn_{1/3}O_2$ electrode, which further illustrates the effect of the Al_2O_3 layer as a medium of preventing the material from degradation during cycling.

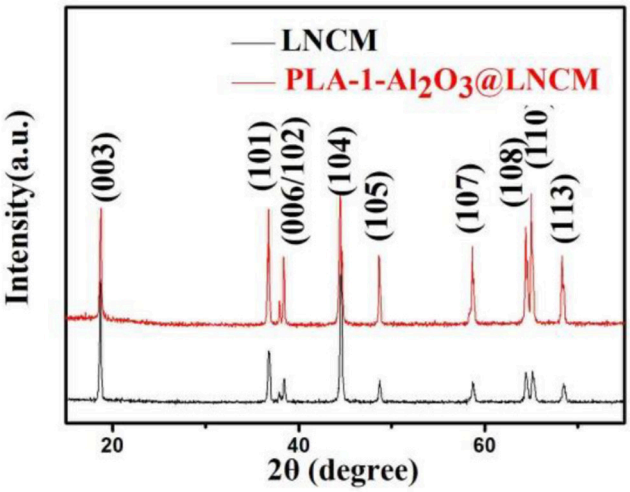

FIGURE 1 | Powder X-ray diffraction patterns of LNCM and PLA-1-Al_2O_3@LNCM.

EXPERIMENTAL

Synthesis of PLA-1-Al_2O_3@LNCM and 1-Al_2O_3@LNCM Cathode Electrodes

The $LiNi_{1/3}Co_{1/3}Mn_{1/3}O_2$ coated with Al_2O_3 layer was prepared by an efficient plasma-enhanced method. In order to make the uniform mixture, the $LiNi_{1/3}Co_{1/3}Mn_{1/3}O_2$ (denoted as LNCM) powder was supplied by one Tech. Company. Aluminum isopropoxide ($C_9H_{21}AlO_3$, purchased from Aladdin official online mall) was chosen as the source of aluminum, and the Al content was set at molar ratios of Al:(Ni + Co + Mn) = 0, 0.5, 1.0, and 1.5% by controlling the amount of $C_9H_{21}AlO_3$. First, the mixture was transferred into the plasma-enhanced tube furnace. The oxygen gas was introduced into the reactor for about 20 min to remove the air in the tube. The temperature of the tube furnace was set to 350°C with the heating rate at 10°/min. Then the pressure was controlled under 50 Pa. During the process, the applied RF power was set to 200 W. The plasma treatment time was controlled for 20 min. The samples of $LiNi_{1/3}Co_{1/3}Mn_{1/3}O_2$, coated with Al_2O_3 synthesized by the plasma-enhanced method using $C_9H_{21}AlO_3$ as the Al source, was defined as PLA-X Al_2O_3@LNCM (X represents the Al content: 0.5, 1.0, and 1.5%). For comparison, the conventional annealing method was also utilized to prepare $LiNi_{1/3}Co_{1/3}Mn_{1/3}O_2$ coated with a Al_2O_3 layer using $C_9H_{21}AlO_3$ for the Al source. The mixed powders with an Al content of 1% were sintered at 500°C for 6 h. Finally, the Al_2O_3-coated $LiNi_{1/3}Co_{1/3}Mn_{1/3}O_2$ was obtained after naturall cooling the product to room temperature (denoted as 1-Al_2O_3@LNCM).

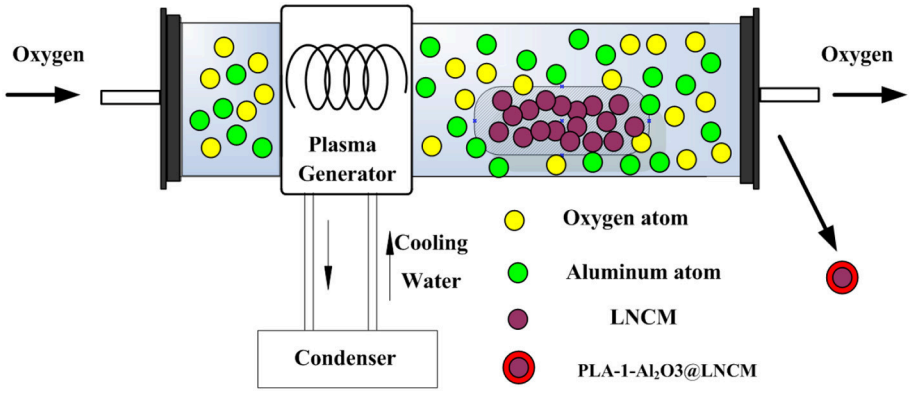

SCHEME 1 | Schematic diagrams for PLA-1-Al_2O_3@LNCM.

Materials Characterizations

The crystalline phases and morphologies of the samples were characterized by an X-ray diffractometer (D/MAX-2200V, Rigaku, Japan) using Cu Kα radiation (k = 0.15406 nm) and scanning electron microscopy (JEOL JSM-7800F, Japan) equipped with an energy dispersive spectrometer (EDS) for elemental analysis. X-ray diffraction studies were carried out using Cu-Kα radiation. The morphology, crystal lattice, and the micro-region structure of the sample coating layer were characterized by the HR-TEM (HR-TEM, JEOL JEM-2100Plus, Japan).

Cell Fabrication and Electrochemical Measurements

Electrochemical experiments performed in R2032 coin type cells were assembled in an argon-filled glove box, using lithium metal as the counter electrode. The electrolyte consisted of a solution of 1 M $LiPF_6$ in ethylene carbonate (EC), dimethyl carbonate (DMC), and ethyl methyl carbonate (EMC) solution (1:1:1 by volume). The composite electrodes were made from the active materials powder (80 wt.%), acetylene black (10 wt.%), and polyvinylidene fluoride (PVDF) binder (10 wt.%), homogeneously mixed in Nmethyl pyrrolidinone (NMP) solvent. The slurry was then coated onto the aluminum foil current collector and dried under a vacuum at 100°C for 12 h. The mixed slurry was pasted on Al foil and subsequently dried at 120°C for 12 h under a vacuum and then roll-pressed. All cells were assembled in an argon filled gloved box. The galvanostatic charge and discharge cycle tests were carried out at 25 and 55°C between 2.8 and 4.3 V using a battery tester at the current density of 0.2°C (1°C = 1,675 $mAhŁEg^{-1}$) (LAND CT2001A, China). The electrochemical impedance spectra (EIS) were conducted on UT85794 (made in the Netherland) in the range from 100 kHz to 10 mHz.

RESULTS AND DISCUSSION

The X-ray diffraction patterns of the bare LNCM and PLA-1-Al_2O_3@LNCM are shown in **Figure 1**. All the peaks of the two samples in the XRD patterns can be indexed to the $NaFeO_2$ structure using space group R-3m without impurity phases, and matched well with those reported in the literature (Li et al., 2018). Furthermore, distinct splitting (006)/(102) and (108)/(110) peaks were observed in all the XRD patterns, indicating that a well-formed layered structure was obtained, illustrating that the thin Al_2O_3 surface coating did not change the structure of the LNCM. No peak of Al_2O_3 was observed due to the low quantity, which reveals that only Al_2O_3 exists and no other impurity presents during the plasma-enhanced coating process. To confirm the differences between PLA-1-Al_2O_3@LNCM and LNCM, the lattice parameters calculated by Rietveld refinement programs are shown in **Table S1**. From this data, it can be seen that a slight difference is noted for PLA-1-Al_2O_3@LNCM, which has a slight increase in the a and c axes. In addition, there is no shift in the peaks, indicating that Al-doping does not take place during the plasma-enhanced process, further illustrating the efficiency of the plasma-enhanced method for the preparation of PLA-1-Al_2O_3@LNCM electrode materials.

The morphologies of LNCM and Al_2O_3 coated LNCM are shown in **Figure 2**. The two samples fall under a similar size range of 0.5–0.8 μm. It can however, clearly be seen that the surface of PLA-1-Al_2O_3@LNCM becomes rough and loses its smooth contours, due to the Al_2O_3 grown on the surface of LNCM with layermorphology. When analyzed using EDS during SEM analysis, as-prepared Al_2O_3 coated electrodes, clearly revealed that the molar ratios of Ni, Co, and Mn of the two samples are both close to 1:1:1, which agrees with the ideal layer structure LNCM. In addition, it exhibits an increase in Al and O content compared to that of pristine LNCM as shown in **Figure S1**, which can further confirm that the Al_2O_3 has successfully grown on the surface of LNCM. At the same time, the SEM images of the LNCM with different Al_2O_3 consent, have been invested as shown in **Figure S2**. We can see that when the consent of Al_2O_3 is 1 wt.%, it shows a uniform morphology, which will be good for the electrochemical performance of the material. When the consent of Al_2O_3 is less or more, it may not grow uniformly or may aggregate on the surface of LNCM, which will hinder the speed of the lithium ion insert/disinsert during cycles. SEM images of the PLA-1-Al_2O_3@LNCM and LNCM,

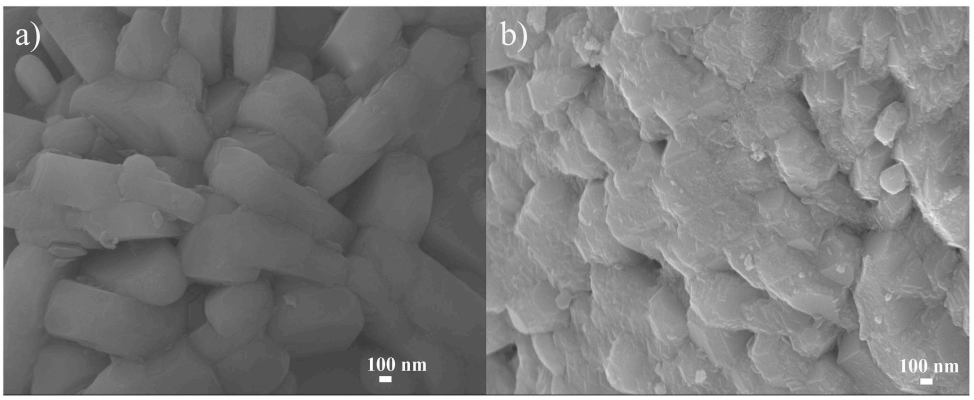

FIGURE 2 | SEM images of **(a)** LNCM and **(b)** PLA-1-Al_2O_3@LNCM.

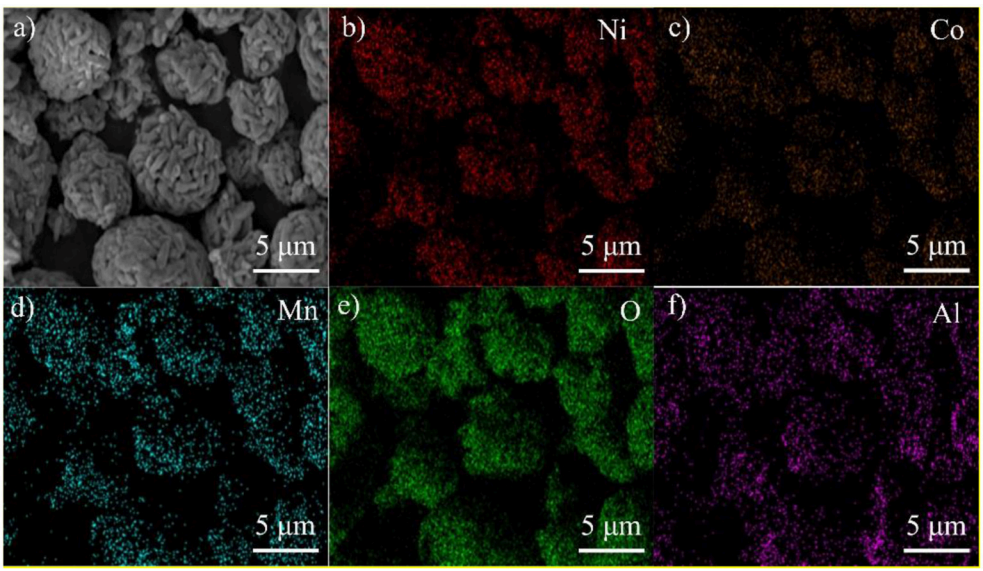

FIGURE 3 | EDS maps for PLA-1-Al_2O_3@LNCM: **(a)** SEM image PLA-1-Al_2O_3@LNCM powders, corresponding elemental mappings images of **(b)** Ni, **(c)** Co, **(d)** Mn, **(e)** O, and **(f)** Al.

after cycling at 0.2°C, are shown in **Figure S3**. It can be clearly seen that the SEM image of PLA-1-Al_2O_3@LNCM presents no obvious changes in the morphology, which further illustrates the stability of sample PLA-1-Al_2O_3@LNCM due to the uniform Al_2O_3 layer.

In order to check the uniformity of the Al_2O_3 coating layer on the surface of LNCM, EDS mapping was performed, as shown in **Figure 3**. The bright dots assigned to the elements O and Al are similar to the SEM of the PLA-1-Al_2O_3@LNCM sample, which indicates that Al_2O_3 has uniformly dispersed on the surface of LNCM. This result is consistent with that of XRD patterns, SEM, and EDAX, which further confirms that the Al_2O_3 layer has successfully grown on the surface of LNCM.

In order to further analyze the thickness and microstructure of Al_2O_3 on the surface coating layer, TEM of LNCM and PLA-1-Al_2O_3@LNCM materials at different magnification are shown in **Figure 4**. Because the coating carbon layer is very thin, it is difficult to find any obvious differences in **Figures 4a,b**. However, the HR-TEM image in **Figure 4c** clearly shows that the host LNCM with interplanar distances of the parallel lattice value of 0.47 nm, indexed to the distance of the closely packed (003) plane of the R3m-layered structure (Guo et al., 2015), which illustrates that the Al atom has not changed the structure of LNCM and only grows on the surface of LNCM. In addition, it can be seen that the Al_2O_3 coating layer with an amorphous phase is about 5 nm, and is clearly distinguishable from the crystalline LNCM, which is consistent with XRD and SEM analysis. TEM analysis demonstrates that the coating method is an effective way to coat the Al_2O_3 layer on the surface of LNCM, which can reduce the contact area between the electrode and electrolyte, and further protects the cathode material from dissolving into the electrolyte.

The initial charge-discharge capacity of PLA-1-Al_2O_3@LNCM at the rate of 0.2°C in the voltage of 2.8–4.3 V

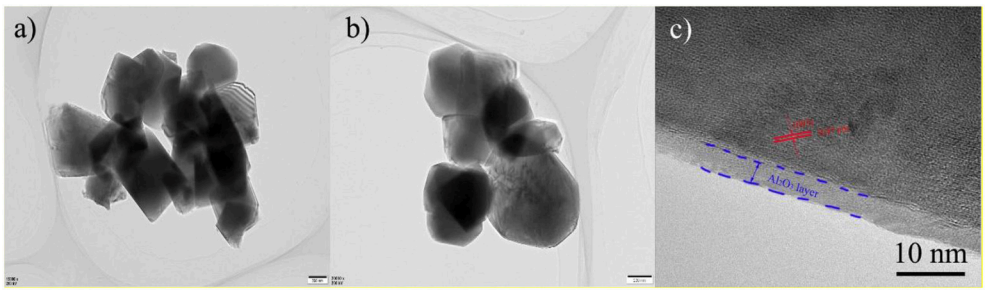

FIGURE 4 | TEM image of **(a)** LNCM and **(b)** PLA-1-Al_2O_3@LNCM, **(c)** HR-TEM image PLA-1-Al_2O_3@LNCM.

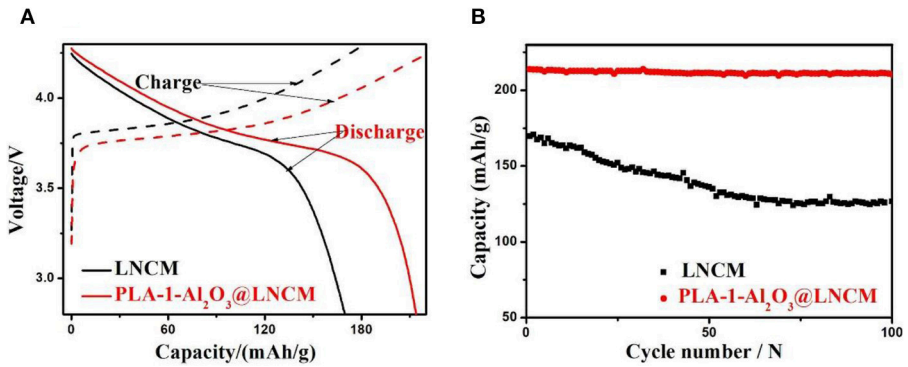

FIGURE 5 | (A) The initial discharge curves and **(B)** Discharge capacities vs. cycle number of LNCM and PLA-1-Al_2O_3@LNCM at the rate of 0.2°C in the voltage of 2.8–4.3 V at room temperature.

at room temperature are compared with LNCM as shown in **Figure 5A**. It can be seen that the initial discharge capacity of PLA-1-Al_2O_3@LNCM is much higher than that of bare LNCM, probably due to the uniform Al_2O_3 layer, which can improve the electrical conductivity of the material and even prohibit the Jahn-Teller distortion occurring at the surface under non equilibrium conditions (Jiang et al., 2016a). At the same time, LNCM coated with different Al_2O_3 consent are also characterized in Li-ion batteries (as shown in **Figure S4A**). Among the three samples, PLA-1-Al_2O_3@LNCM shows the highest initial discharge performance, due to the suitable thickness of Al_2O_3 formed only with the consent Al of 1%. In order to further make sure the efficient of this plasma-enhanced method, the initial discharge performance of Al_2O_3@LNCM synthesized form the normal solid state method are invested as shown in **Figure S5A**. The initial discharge of Al_2O_3@LNCM is 196.9 $mAh{\cdot}g^{-1}$, which is lower than that of PLA-1-Al_2O_3@LNCM. This result illustrates this method not only can improve the efficient of this coated experiment, but also can improve the electrochemical performance of the material, indicating that the plasma-enhanced method can synthesized the coated LNCM with suitable Al_2O_3 layer with lower temperature and less reaction time.

Figure 5B summarizes cycling performances of LNCM and coated LNCM cathodes cycled at 0.2°C in a potential range of 2.8–4.3 V at room temperature. Capacity retention of PLA-1-Al_2O_3@LNCM upon cycling between 4.3 and 2.8 V is 98.46%, which is much higher than that of LNCM (74.66%). In other words, the discharge capacity of LNCM only maintained 74.66% of its initial capacity; while the discharge capacities of PLA-1-Al_2O_3@LNCM only decrease slightly from 213.8 to 210.5 $mAhŁEg^{-1}$ after 100 cycles, maintaining 98.46% of its initial capacity, which may be associated with cobalt dissolution and structural deterioration at the high operating voltage, resulting in increased interfacial resistance. At the same time, LNCM coated with different Al_2O_3 consent are also characterized in Li-ion batteries as shown in **Figure S4B**. The capacity of The PLA-0.5-Al_2O_3@LNCM and PLA-1.5-Al_2O_3@LNCM samples suffers 11.51 and 10.54% capacity loss, respectively, while PLA-1-Al_2O_3@LNCM has the highest capacity retention of 98.46% after 100 cycles at 0.2°C between 2.8 and 4.3 V. It can be seen that when the mass concentration of Al_2O_3 is less or more than 1 wt.%, the capacity loss also undergoes a certain fading, which further illustrates that the suitable consent of Al content is 1 wt.%. For the PLA-1-Al_2O_3@LNCM sample with a proper coating amount, the hierarchical nanosheets of metal oxide can sequester HF in electrolytes containing $LiPF_6$. The rich pores improve the ionic conductivity of the coating layer and the suitable thin film of Al_2O_3 can strongly inhibit the electronic conductivity (Jung and Han, 2013). Additionally, to confirm the efficiency of this plasma enhanced method, the cycling performance of Al_2O_3@LNCM, synthesized form the normal solid state method,

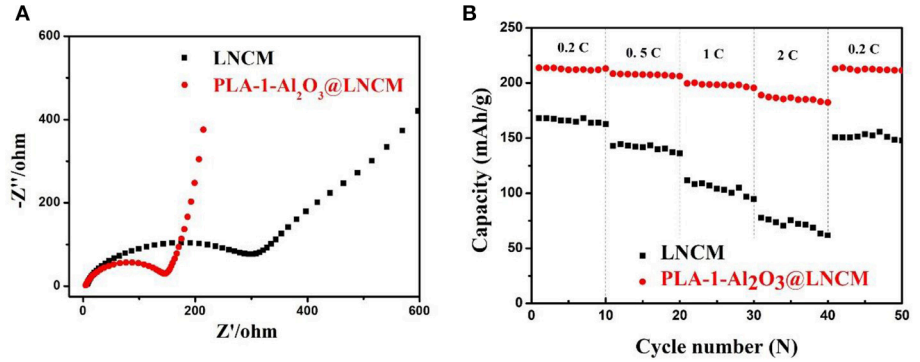

FIGURE 6 | (A) Nyquist plots of bare LNCM and PLA-1-Al_2O_3@LNCM. **(B)** Rate capabilities vs. cycle number for bare LNCM and PLA-1-Al_2O_3@LNCM electrodes cycled at 0.2, 0.5, 1, 2, 0.2°C rates between voltage limits of 2.8 and 4.3 V.

is also invested, as shown in **Figure S5B**. Compared to PLA-1-Al_2O_3@LNCM, 1-Al_2O_3@LNCM, reaches a discharge capacity of only 181.8 mAhŁEg^{-1} after 100 cycles, which only represents 92.38% of its initial discharge capacity (196.9 mAhŁEg^{-1}). However, PLA-1-Al_2O_3@LNCM shows much higher capacity retention (98.46%) after 100 cycles, which further illustrates that the plasma-enhanced method has higher efficiency than that of the normal solid state method. These results clearly indicate that the materials obtained by the plasma-enhanced strategy can be used as a promising cathode material in lithium-ion batteries.

To further investigate the effect of the Al_2O_3-coating on the electrochemical performance, the AC impedance curves of all the cycled samples were performed as shown in **Figure 6A**. The EIS plot consists of a depressed semi-circle in the high-medium frequency region that is attributed to the lithium-ion migration, through the SEI film and charge transfer reaction, and a straight line in the low frequency region attributed to the lithium-ion diffusion in the bulk electrode (Wang et al., 2014). A more detailed analysis of the impedance spectra was studied on the basis of the proposed equivalent circuit, where Rs represents the solution resistance and R_{ct} represents charge transfer resistance during the electrochemical reactions. The inclined line in the low-frequency region represents the Warburg impedance (Zw) associated with Li-ion diffusion in the electrode active material (Liu et al., 2004). EIS plots in **Figure 6A** were fitted using the equivalent circuit model. During cycling, the formation of the solid-state interface layer may lead to raised impedance. From the fitted impedance parameters, it can be seen that the charge transfer resistance (R_{ct}) of PLA-1-Al_2O_3@LNCM is much smaller ($R_{ct} \approx$ 152.78 Ł) than that of the pristine LNCM (Rct $\approx$ 343.97 Ł), which indicates that the Al_2O_3 layer can enhance Li+ transportation with enlarged interlayer. Moreover, it may be due to the removal of the unidentified phase in the precycled electrode or the influence of a native passivation layer on the electrodes (Lin et al., 2014). Therefore, the decrease of impedance illustrates the effect of the Al_2O_3 layer on restraining the process during cycling, which further verifies the fact that the Al_2O_3 layer is responsible for the good performance of PLA-1-Al_2O_3@LNCM. In addition, the impedance reduction exhibits an enhancement in the kinetics of the lithium-ion diffusion through the surface layer, and an obvious increase in rate capability as shown in **Figure 6B**. During rate capability testing, the effect of the coating layer on improving capacity retention is relatively apparent. Rate measurement is performed as the currents gradually increase to 2°C, finally returning back to 0.2°C, as shown in **Figure 6B**. The pristine LNCM delivers a capacity of 168.2, 142.9, 111.8, and 77.8 mAhŁEg^{-1} at 0.2, 0.5, 1, and 2°C, respectively. For PLA-1-Al_2O_3@LNCM, the corresponding capacity is 213.8, 208.4, 199.6, and 189.0 mAhŁEg^{-1}, respectively, which shows an obvious improved rate performance than that of the pristine LNCM. Moreover, when the current returns back to 0.2°C, the PLA-1-Al_2O_3@LNCM electrodes recover 99.58% of their original 0.2°C discharge capacity, compared to 89.66% for the uncoated electrode due to the attack from the electrolyte, further concluding that coating LNCM with Al_2O_3 can significantly improve its rate performance. The superior retention capability is due to the coating which improves the homogeneity of near-surface current density on the coated electrodes and uniform Al_2O_3 layer for the improvement transfer of lithium ions between the electrode and electrolyte. Therefore, the excellent rate performance can be attributed to the uniform coating, which can cut off contact with the electrolyte and suppress the dissolution of active substances.

The cyclic performances of bare LNCM and PLA-1-Al_2O_3@LNCM at 0.2°C in a potential range of 2.8–4.3 V at a high temperature (55°C) are shown in **Figure 7**. The initial discharge capacity of bare LNCM is 165.2 mAhŁEg^{-1}, whereas that of the PLA-1-Al_2O_3@LNCM is 209.1 mAhŁEg^{-1}. There is a lot of difference between the LNCM and PLA-1-Al_2O_3@LNCM sample, indicating that the 5 nm Al_2O_3 coating layer affects the Li+ diffusion between the LNCM particles and the electrolyte during the first cycle. More importantly, there are significant differences in cyclic performance between LNCM and PLA-1-Al_2O_3@LNCM as shown with the increasing cycling numbers. After 100 cycles, the discharge capacities of bare LNCM is only maintained at 86.6 mAhŁEg^{-1}, suggesting that the material suffers stronger destruction as compared to the side reaction aggravated under a higher temperature. PLA-1-Al_2O_3@LNCM shows better capacity retention with 85.08% of the initial discharge, presumably to an inhibiting effect of

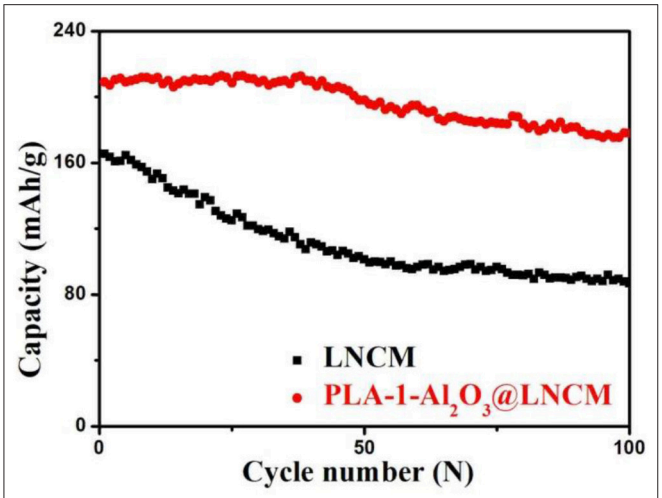

FIGURE 7 | Cyclic performances at 0.2°C of LNCM and PLA-1-Al_2O_3@LNCM at 55°C.

the Al_2O_3 coating layer on the metal ion dissolution from the LNCM electrode to the electrolyte. In order to further confirm the effect of the plasma-enhanced method on the material, the cyclic performances of 1-Al_2O_3@LNCM are invested, as shown in **Figure S6**. The initial discharge capacity of PLA-1-Al_2O_3@LNCM is much higher than that of 1-Al_2O_3@LNCM, which indicates that the different synthesis methods have many differences on the first discharge cycle. Moreover, PLA-1-Al_2O_3@LNCM exhibited much better cyclic performance than that of 1-Al_2O_3@LNCM, which further confirms the superiority of the plasma-enhanced method in synthesizing the LNCM with the uniform Al_2O_3 layer. The proper coating using a special synthesis method can also suppress the formation of the passive film of the solid state electrolyte acting as a highly effective lithium ion conductor, which consequently improves the rate capability even at an elevated temperature. In addition, we can clearly see that PLA-1-Al_2O_3@LNCM exhibits excellent electrochemical performances compared to many relevant references as shown in **Table S2**.

CONCLUSION

A novel and effective Al_2O_3 coating has been successfully achieved via a facile plasma-enhanced route method, investigating the effects of the Al_2O_3 coating on the high temperature cyclic performance of LNCM. From the physical test, it can clearly be seen that the Al_2O_3 uniformly grows on the surfaces of LNCM particles with a thickness of about 5 nm, causing no changes on the structure of LNCM. Futhermore, PLA-1-Al_2O_3@LNCM exhibited a better cyclic performance and its discharge capacity was 213.8 mAhŁEg^{-1} at 0.2°C, and its capacity retention was 98.46% after 100 cycles, which is much higher than that of bare LNCM and 1-Al_2O_3@LNCM synthesized using the normal solid state method. What's more, PLA-1-Al_2O_3@LNCM shows better rate capability and cycling stability, which can be attributed to the uniform coating of Al_2O_3. When cycling at 55°C, PLA-1-Al_2O_3@LNCM shows 85.08% capacity retention after 100 cycles, which is much higher than that of bare LNCM only, with a 52.42% capacity retention. The enhanced electrochemical performance further illustrates the efficiency and superiority of the Al_2O_3 layer, which is achieved using the plasma-enhanced method, and which can protect cathode material thus alleviating the severe dissolution of metal ions from dissolving in the electrolyte and reduces decomposition of the electrolyte at the cathode. This facile and efficient surface modification with low-cost starting material and an effective coating layer structure can be adopted to enhance the cycling performance and thermal stability for other electrode materials, which can be used to synthesize other candidate cathode materials for lithium ion batteries.

DATA AVAILABILITY STATEMENT

The datasets generated for this study are available on request to the corresponding author.

AUTHOR CONTRIBUTIONS

QJ and XW wrote and modified the manuscript. YZ tested the performances of materials. NY synthesized the materials. JT modified the manuscript.

ACKNOWLEDGMENTS

The work was supported by the National Natural Science Foundation of China (Grant Nos. 51473082, 51273096, and 51603109), the programme of Introducing Talents to the Universities (111 plan), the National One-Thousand Foreign Expert Program (Grant No. WQ20123400111), the Natural Science Foundation of Shandong province (Grant Nos. ZR2017BEM047, ZR2019BB002), and the postdoctoral science foundation of China (Grant No. 2017M610408).

SUPPLEMENTARY MATERIAL

The Supplementary Material for this article can be found online at: https://www.frontiersin.org/articles/10.3389/fchem.2020.00072/full#supplementary-material

REFERENCES

Chen, Z., Wang, J., Chao, D., Tom, B., Bai, L., Chen, S., et al. (2016). Hierarchical porous $LiNi_{1/3}Co_{1/3}Mn_{1/3}O_2$ nano-/micro spherical cathode material: minimized cation mixing and improved Li^+mobility for enhanced electrochemical performance. *Sci. Rep.* 6:25771. doi: 10.1038/srep25771

Cho, M. Y., Roh, K. C., Park, S. M., and Lee, J. W. (2011). Effects of CeO_2 coating uniformity on high temperature cycle life performance of $LiMn_2O_4$. *Mater. Lett.* 65, 2011–2014. doi: 10.1016/j.matlet.2011.03.100

Cui, Y., and Xu, S. (2015). High tap density of $Ni_3(PO_4)_2$ coated $LiNi_{1/3}Co_{1/3}Mn_{1/3}O_2$ with enhanced cycling performance at high cut-off voltage. *Chin. J. Chem. Eng.* 23, 315–320. doi: 10.1016/j.cjche.2014.03.001

Deng, C., Liu, L., Zhou, W., Sun, K., and Sun, D. (2008). Effect of synthesis condition on the structure and electrochemical properties of $LiNi_{1/3}Co_{1/3}Mn_{1/3}O_2$ prepared by hydroxide co-precipitation method. *Electrochim. Acta* 53, 2441–2447. doi: 10.1016/j.electacta.2007.10.025

Guo, X., Cong, L. N., Zhao, Q., Tai, L. H., Wu, X. L., Zhang, J. P., et al. (2015). Enhancement of electrochemical performance of $LiNi_{1/3}Co_{1/3}Mn_{1/3}O_2$ by surface modification with MnO_2. *J. Alloy. Compd.* 651, 12–18. doi: 10.1016/j.jallcom.2015.06.270

Hu, S. K., Cheng, G. H., Cheng, M. Y., Hwang, B. J., and Santhanam, R. (2009). Cycle life improvement of ZrO_2-coated spherical $LiNi_{1/3}Co_{1/3}Mn_{1/3}O_2$ cathode material for lithium ion batteries. *J. Power Sources* 188, 564–569. doi: 10.1016/j.jpowsour.2008.11.113

Jiang, Q., Chen, N., Liu, D., Wang, S., and Zhang, H. (2016a). Efficient plasma-enhanced method for layered $LiNi_{1/3}Co_{1/3}Mn_{1/3}O_2$ cathodes with sulfur atom-scale modification for superior-performance Li-ion batteries. *Nanoscale* 8, 11234–11240. doi: 10.1039/C6NR02589G

Jiang, Q., Peng, L., Jie, L., and Tang, J. (2018). Improving the elevated-temperature behaviors of $LiNi_{1/3}Co_{1/3}Mn_{1/3}O_2$ by surface modification with Nano-La_2O_3. *J. Alloy. Compd.* 742, 549–554. doi: 10.1016/j.jallcom.2018.01.354

Jiang, Q., Zhang, H., and Wang, S. (2016b). Plasma-enhanced low-temperature solid-state synthesis of spinel $LiMn_2O_4$ with superior performance for lithium-ion batteries. *Green Chem.* 18, 662–666. doi: 10.1039/C5GC01563D

Jung, S. C., and Han, Y.-K. (2013). How do Li atoms pass through the Al_2O_3 coating layer during lithiation in Li-ion batteries? *J. Phys. Chem. Lett.* 4, 2681–2685. doi: 10.1021/jz401231e

Kim, Y., Kim, H. S., and Martin, S. W. (2006). Synthesis and electrochemical characteristics of Al_2O_3-coated $LiNi_{1/3}Co_{1/3}Mn_{1/3}O_2$ cathode materials for lithium ion batteries. *Electrochim. Acta* 52, 1316–1322. doi: 10.1016/j.electacta.2006.07.033

Lee, J., Urban, A., Li, X., Su, D., Hautier, G., and Ceder, G. (2014). Unlocking the potential of cation-disordered oxides for rechargeable lithium batteries. *Science* 343, 519–522. doi: 10.1126/science.1246432

Lee, M. H., Kang, Y. J., Myung, S. T., and Sun, Y. K. (2004). Synthetic optimization of $Li[Ni_{1/3}Co_{1/3}Mn_{1/3}]O_2$ via co-precipitation. *Electrochim. Acta* 50, 939–948. doi: 10.1016/j.electacta.2004.07.038

Li, J., Fan, M., He, X., Zhao, R., Jiange, C., and Wan, C. (2006). TiO_2 coating of $LiNi_{1/3}Co_{1/3}Mn_{1/3}O_2$ cathode materials for Li-ion batteries. *Ionics* 12, 215–218. doi: 10.1007/s11581-006-0034-2

Li, X., He, W., Chen, L., Guo, W., Chen, J., and Xiao, Z. (2014). Hydrothermal synthesis and electrochemical performance studies of Al_2O_3-coated $LiNi_{1/3}Co_{1/3}Mn_{1/3}O_2$ for lithium-ion batteries. *Ionics* 20, 833–840. doi: 10.1007/s11581-013-1041-8

Li, Y., Hou, X., Zhou, Y., Han, W., Liang, C., Wu, X., et al. (2018). Electrochemical performance of structure-dependent $LiNi_{1/3}Co_{1/3}Mn_{1/3}O_2$ in aqueous rechargeable lithium-ion batteries. *Energy Technol.* 6, 391–396. doi: 10.1002/ente.201700528

Lin, H. B., Hu, J. N., Rong, H. B., Zhang, Y. M., Mai, S. W., Xing, L. D., et al. (2014). Porous $LiMn_2O_4$ cubes architectured with single-crystalline nanoparticles and exhibiting excellent cyclic stability and rate capability as the cathode of a lithium ion battery. *J. Mater. Chem. A* 2, 9272–9279. doi: 10.1039/c4ta01474j

Liu, H., Zhang, Z., Gong, Z., and Yang, Y. (2004). A comparative study of $LiNi_{0.8}Co_{0.2}O_2$ cathode materials modified by lattice-doping and surface-coating. *Solid State Ionics* 166, 317–325. doi: 10.1016/j.ssi.2003.11.010

Lu, J., Peng, Q., Wang, W., Nan, C., Li, L., and Li, Y. (2013). Nanoscale coating of $LiMO_2$ (M = Ni, Co, Mn) nanobelts with Li^+-conductive Li_2TiO_3: toward better rate capabilities for Li-ion batteries. *J. Am. Chem. Soc.* 135, 1649–1652. doi: 10.1021/ja308717z

Luo, X., Wang, X., Liao, L., Wang, X., Gamboa, S., and Sebastian, P. J. (2006). Effects of synthesis conditions on the structural and electrochemical properties of layered $LiNi_{1/3}Co_{1/3}Mn_{1/3}O_2$ cathode material via the hydroxide co-precipitation method. *J. Power Sources* 161, 601–605. doi: 10.1016/j.jpowsour.2006.03.090

Lv, C., Yang, J., Peng, Y., Duan, X., Ma, J., Li, Q., et al. (2019). 1D Nb-doped $LiNi_{1/3}Co_{1/3}Mn_{1/3}O_2$ nanostructures as excellent cathodes for Li-ion battery. *Electrochim. Acta* 297, 258–266. doi: 10.1016/j.electacta.2018.11.172

Makkus, R. C., Hemmes, K., and Wit, J. H. W. D. (2010). ChemInform abstract: a comparative study of NiO(Li), $LiFeO_2$, and $LiCoO_2$ porous cathodes for molten carbonate fuel cells (MCFC). *Cheminform* 26:10012. doi: 10.1002/chin.199510012

Manthiram, A., Knight, J. C., Myung, S. T., Oh, S. M., and Sun, Y. K. (2016). Nickel-rich and lithium-rich layered oxide cathodes: progress and perspectives. *Adv. Energy Mater.* 6:1501010. doi: 10.1002/aenm.201501010

Myung, S.-T., Lee, K.-S., Yoon, C. S., Sun, Y.-K., Amine, K., and Yashiro, H. (2010). Effect of AlF_3 coating on thermal behavior of chemically delithiated $Li_{0.35}Ni_{1/3}Co_{1/3}Mn_{1/3}O_2$. *J. Phys. Chem. C* 114, 4710–4718. doi: 10.1021/jp9082322

Ohzuku, T., and Makimura, Y. (2001). Layered lithium insertion material of $LiNi_{1/2}Mn_{1/2}O_2$: a possible alternative to $LiCoO_2$ for advanced lithium-ion batteries. *Chem. Lett.* 2001, 744–745. doi: 10.1246/cl.2001.744

Qiu, Q., Huang, X., Chen, Y., Tan, Y., and Lv, W. (2014). Al_2O_3 coated $LiNi_{1/3}Co_{1/3}Mn_{1/3}O_2$ cathode material by sol–gel method: preparation and characterization. *Ceram. Int.* 40, 10511–10516. doi: 10.1016/j.ceramint.2014.03.023

Tang, W., Zhu, Y., Hou, Y., Liu, L., Wu, Y., Loh, K. P., et al. (2013). Aqueous rechargeable lithium batteries as an energy storage system of superfast charging. *Energy Environ. Sci.* 6, 2093–2104. doi: 10.1039/c3ee24249h

Wang, J.-H., Wang, Y., Guo, Y.-Z., Ren, Z.-Y., and Liu, C.-W. (2013). Effect of heat-treatment on the surface structure and electrochemical behavior of $AlPO_4$-coated $LiNi_{1/3}Co_{1/3}Mn_{1/3}O_2$ cathode materials. *J. Mater. Chem. A* 1, 4879–4884. doi: 10.1039/c3ta00064h

Wang, Y., Zhang, H., Chen, W., Ma, Z., and Li, Z. (2014). Gel-combustion synthesis and electrochemical performance of $LiNi_{1/3}Co_{1/3}Mn_{1/3}O_2$ as cathode material for lithium-ion batteries. *RSC Adv.* 4, 37148–37156. doi: 10.1039/C4RA06386D

Xia, H., Wan, Y., Assenmacher, W., Mader, W., Yuan, G., and Lu, L. (2014). Facile synthesis of chain-like $LiCoO_2$ nanowire arrays as three-dimensional cathode for microbatteries. *NPG Asia Mater.* 6:126. doi: 10.1038/am.2014.72

Xu, J., Ma, J., Fan, Q., Guo, S., and Dou, S. (2017). Recent progress in the design of advanced cathode materials and battery models for high-performance lithium-X (X = O_2, S, Se, Te, I_2, Br_2) batteries. *Adv. Mater.* 29, 1606454–1606473. doi: 10.1002/adma.201606454

Yan, P., Zheng, J., Zheng, J., Wang, Z., Teng, G., Kuppan, S., et al. (2016). Ni and Co segregations on selective surface facets and rational design of layered lithium transition-metal oxide cathodes. *Adv. Energy Mater.* 6, 1502455–1502410. doi: 10.1002/aenm.201502455

Yao, Y., Liu, H., Li, G., Peng, H., and Chen, K. (2013). Synthesis and electrochemical performance of phosphate-coated porous $LiNi_{i1/3}Co_{1/3}Mn_{1/3}O_2$ cathode material for lithium ion batteries. *Electrochim. Acta* 113, 340–345. doi: 10.1016/j.electacta.2013.09.071

Zhang, Y., Jia, D., Tang, Y., Huang, Y., Pang, W., Guo, Z., et al. (2018). *In situ* chelating synthesis of hierarchical $LiNi_{1/3}Co_{1/3}Mn_{1/3}O_2$ polyhedron assemblies with ultralong cycle life for Li-ion batteries. *Small* 14, 1704354–1704360. doi: 10.1002/smll.201704354

Zhao, F., Tang, Y., Wang, J., Tian, J., Ge, H., and Wang, B. (2015). Vapor-assisted synthesis of Al_2O_3-coated $LiCoO_2$ for high-voltage lithium ion batteries. *Electrochim. Acta* 174, 384–390. doi: 10.1016/j.electacta.2015.05.180

Zhu, G., Wen, K., Lv, W., Zhou, X., Liang, Y., Yang, F., et al. (2015). Materials insights into low-temperature performances of lithium-ion batteries. *J. Power Sources* 300, 29–40. doi: 10.1016/j.jpowsour.2015.09.056

Conflict of Interest: The authors declare that the research was conducted in the absence of any commercial or financial relationships that could be construed as a potential conflict of interest.

Advantages of publishing in Frontiers

OPEN ACCESS
Articles are free to read for greatest visibility and readership

FAST PUBLICATION
Around 90 days from submission to decision

HIGH QUALITY PEER-REVIEW
Rigorous, collaborative, and constructive peer-review

TRANSPARENT PEER-REVIEW
Editors and reviewers acknowledged by name on published articles

Frontiers
Avenue du Tribunal-Fédéral 34
1005 Lausanne | Switzerland

Visit us: www.frontiersin.org
Contact us: info@frontiersin.org | +41 21 510 17 00

REPRODUCIBILITY OF RESEARCH
Support open data and methods to enhance research reproducibility

DIGITAL PUBLISHING
Articles designed for optimal readership across devices

FOLLOW US
@frontiersin

IMPACT METRICS
Advanced article metrics track visibility across digital media

EXTENSIVE PROMOTION
Marketing and promotion of impactful research

LOOP RESEARCH NETWORK
Our network increases your article's readership